Mesoporous Bioactive Glass and Alginate Composite Scaffolds for Tissue Engineering

Jian Ping Fan

Dissertation submitted for the degree of

Doctor of Philosophy

Department of Mechanical Engineering
University College London
U.K.

June 2014

Declaration

I, Jian Ping Fan, confirm that the work presented in this thesis is my own. Where information has been derived from other sources, I confirm that this has been indicated in the thesis.

Jian Ping Fan

June 2014

Abstract

Sol-gel derived, silica-based bioactive glasses of a ternary system (SiO_2 – CaO – P_2O_5) has the potential to promote hard and soft tissue regeneration. Compared to melt-derived glasses, glasses synthesised from the sol-gel process has the advantage of low processing temperatures, high specific surface areas (SSA) and tailorable porous nanostructures. Using scaffolds as a strategy for tissue engineering, the application of sol-gel derived bioactive glasses in combination with alginate polymers as scaffold composite materials has great potential and therefore requires further study.

This thesis investigates the synthesis of bioactive glasses via the sol-gel (acidic) route and the multi-step (alkali) route, through the sol → drying → sintering stages. Sol-gel route nanoparticles derived were heterogeneous in shape, while the multi-step route produced spherical (30 – 90 nm diameter) nanoparticles. Increases in calcium content of the sol led to an increase in pore size and a decrease in SSA. Three dehydration methods: oven, vacuum and freeze drying were devised to control the morphology of nanoparticles. Freeze dried nanoparticles were found to have a rough surface texture, with an aligned ordered porous nanostructure. This led to faster apatite formation when compared to oven dried nanoparticles immersed in simulated body fluid (SBF).

A novel internal ionic diffusion cross-linking method of alginate was developed, utilising the glass nanoparticles as nanocarriers, for the synthesis of alginate-bioactive glass composite scaffolds. Strontium chloride ($SrCl_2$) and copper chloride ($CuCl_2$), which provided therapeutic ions, were impregnated into the nanocarriers, and were compared to calcium chloride ($CaCl_2$), as the control. Impregnation efficiency was in the order of $CuCl_2 > SrCl_2 \approx CaCl_2$, attributed to Cu^{2+} having the smallest ionic radii and its interaction with silinol groups on the nanocarrier surfaces. Scaffold gelation time was correlated to the type of cross-linking salt, its loading concentration and glass to alginate (G/A) ratio. It was observed that $SrCl_2$ loaded nanocarriers (BGSr) were most efficient in cross-linking when compared to $CuCl_2$ and $CaCl_2$ loaded nanocarriers (BGCu and BGCa respectively), due to Sr^{2+} having a greater affinity towards alginate. Results showed that nanocarriers with the highest SSA possessed the highest impregnation efficiency; however nanocarriers with the largest pore diameter and volume led to the fastest scaffold gelation time.

BGCa and BGSr scaffolds showed significant improvements in maintaining stiffness (Young's modulus) and shear resistance (maximum shear stress) after incubation in aqueous solutions for up to 28 days, which were in contrast to the deterioration in mechanical properties of conventional $CaCl_2$ cross-linked scaffolds. Calcium ions were detected in the range above 260 ppm in BGCa nanocarrier supernatant, suggesting the gradual release of ions from the nanocarriers, internally diffusing into the scaffold matrix, leading to continuous cross-linking over time. Meanwhile, *in vitro* biological studies showed fast apatite formation on BGCa cross-linked scaffolds in SBF, with the scaffolds capable of supporting the attachment, growth and proliferation of human osteoblast cells, thus indicating their high bioactivity. Control over glass nanoparticle morphology was achieved and through specific ionic impregnation, the successful synthesis of alginate-bioactive glass composite scaffolds was demonstrated, producing bioactive scaffolds with improved mechanical properties.

Papers and communications

Publications

1. Memarzadeh K., Vargas M., Huang J., **Fan J.P.**, Allaker R.P., Nano metallic-oxides as antimicrobials for implant coatings. Key Engineering Materials, 2012. 493-494: p. 489-494.

2. **Fan J.P.**, Kalia P., Di Silvio L., Huang J., *In vitro* response of human osteoblasts to multi-step sol–gel derived bioactive glass nanoparticles for bone tissue engineering. Materials Science and Engineering: C, 2013. 36(0): p. 206-214.

3. Kalia P., Viscay-Barenna G., **Fan J.P.**, Warley A., Di Silvio L., Huang J., Nanohydroxyapatite shape and its potential role in bone formation: an analytical study. Journal of the Royal Society Interface, 2014. 11(93).

4. **Fan J.P.**, Mimicking the microstructure of nacre for bone tissue engineering. Mollusc World, 2014. 34(0): p. 4-5.

5. **Fan J.P.**, Zhu B., Li X., Guo Z.X., Wojcik A., Huang J. Tailoring of mesoporous bioactive glass nanoparticle morphology at the nanoscale for enhanced bioactivity. Submitted, June 2014.

Patent application

1. **Fan J.P.**, Wojcik A., Huang J. Novel ionically cross-linked composites for tissue engineering and methods for production. In preparation, 2014.

Key conference contributions

1. **Fan J.P.**, Huang J., A novel cross-linked Bioglass-Alginate composite scaffold for tissue engineering. Poster presentation, European Society of Biomaterials 2011, Ireland.

2. **Fan J.P.**, Kalia P., Sinha J., Di Silvio L., Huang J., Development and characterisation of a novel nanocomposite scaffold for tissue engineering. Oral presentation, Chelseden Club King's College London 2012, United Kingdom.

3. Kalia P., **Fan J.P.**, Sinha J., Di Silvio L., Huang J., Novel osteochondrol scaffold-multicell constructs for cartilage repair. Oral presentation, Orthopeadic Research United Kingdom 2012, United Kingdom.

4. Kalia P., Viscay-Barenna G., **Fan J.P.**, Warley A., Di Silvio L., Huang J., Primary human osteoblast self-organisation and ultrastructural response to hydroxyapatite nanoparticles of different shapes. Poster presentation, United Kingdom Society of Biomaterials 2012, United Kingdom.

5. **Fan J.P.**, Kalia P., Di Silvio L., Huang J., Development and characterisation of a novel bioglass-hydroxyapatite-alginate nanocomposite scaffold for tissue engineering. Oral presentation, 9th World Biomaterials Congress 2012, China.

Awards

1. Major Travel Award for Conferences, UCL Graduate School, 2012.

2. Best Oral Presentation Award, PhD Research Forum, UCL, 2012. Presentation title: Development and characterisation of a novel bioglass-hydroxyapatite-alginate nanocomposite scaffold for tissue engineering.

For my mother, with appreciation, gratitude and love.

Acknowledgement

First and foremost, I would like to express my sincere appreciation to my supervisor, Dr. Jie Huang for her meticulous supervision, support and intellectual contribution throughout my research. I am indebted to her for her challenging discussions and constructive suggestions, for her unstinting interest and enthusiasm.

I would also like to express my gratefulness towards my second supervisor, Dr. Adam Wojcik, for his invaluable advice, generous support and passion over all aspects. I must also thank Professor Lucy Di Silvio for the opportunity to work in her lab and for the valuable input, effort and thought towards the biological aspects of my research. Further appreciation is accorded to Dr. Priya Kalia and Ms. Paula Coward (Biomaterials, Tissue Engineering and Imaging, King's College London) for their assistance and guidance in cellular work.

I would also like to acknowledge a number of people for technical assistance rendered. Mr. Binjun Xiao (Department of Chemistry, UCL) is thanked for his tremendous help with XRD sample preparation and guidance. Dr. David Martin (Department of Chemistry, UCL) is thanked for his patience and generous assistance with nitrogen sorption testing. Mr. Mark Turmaine (Department of Anatomy and Developmental Biology, UCL), Mr. Kevin Reeves (Department of Archaeology, UCL) and Dr. Ee Zhuan Chong (3Bs Group, King's College London Dental Institute) are thanked for their generous support with imaging and microscopy and Dr. Xiang Li (Department of Materials Science and Engineering, Zhejiang University) for producing some excellent HRTEM images of bioactive glass nanoparticles.

The staff members of Mechanical Engineering, UCL, have been amazing to work with and a special mention to Dr. Gillian Munir, for her insightful discussions and good humour and to Dr. Ding Zhao, for his camaraderie over long days in the lab and sincere friendship. I am ever grateful to my housemate, for his patience, especially whilst I was writing up. To my family and friends, thank you for all your support and encouragement.

Last, but most importantly, my utmost gratitude is accorded to my mother, Professor Siew Nooi Phang, whom without, I will have not been able to pursue my passion.

Table of contents

List of figures

List of tables

Chapter 1
Introduction

1.1 Background

The need for bone implants have increased drastically over the past few decades. Although having the ability to self-heal, damaged bone tissue exceeding a critical size requires an alternative pathway of treatment either via implantation or transplantation. In the case of bone transplantation, two main options available are autografting and allografting, in which the former uses bones harvested from the patient, while the latter uses bone tissue from a donor [1, 2]. However, with the increase in life expectancy and a general ageing population, the need for implant materials to replace, repair and regenerate body parts which we are now outliving is increasing. With the severe increase in demand for autologous bone grafts, the need for new bone regenerative materials has become an element of global significance and importance.

The creation of an ideal implant substitute for bone tissue regeneration has proven elusive even though extensive research and effort has been put into its development. One widely accepted strategy is the use of scaffolds as templates for cells to adhere and proliferate, and at the same time provide some form of mechanical support to the host tissue. The requirements for creating successful implant substitutes is to design a structure which uses nontoxic, biodegradable materials, by which under selected synthesis methods can form scaffolds which are able to provide an architectural path for cells to adhere, proliferate and produce extracellular matrix along the scaffold geometry [3]. The complication which leads to the elusive creation of this ideal scaffold arises due to the wide array of materials and methods available for synthesis. The combination of thousands of materials and methods available make it at present rather impossible to determine the ideal recipe for the synthesis of such a scaffold.

The progression of materials for bone tissue engineering can be differentiated into three generations. The first generation showed bioinert materials, such as zirconia and alumina, which failed to integrate with native bone tissue, and over time became loose

and separated from the surrounding tissue. The second generation progressed towards bioactive, biodegradable and resorbable materials, such as calcium phosphate ceramics, bioactive glasses and composites. Although clinically used, prostheses made of these materials had a limited working lifespan of 10 – 20 years, before requiring revision surgery [2, 4, 5]. Currently in the third generation of biomaterial research, the focus would be on biomaterials capable of up-regulating the expression of specific genes [6]. One such material is bioactive glass, which was first introduced by Larry Hench in 1969. Bioactive glasses have been widely used in both research as well as commercially, due to its osteoconductive and osteoinductive properties, and its ability to encourage rapid bone formation compared to other bioceramics [7].

Two decades ago, bioactive glasses were synthesised via the sol-gel process [8]. The sol-gel process is a relatively low temperature method of obtaining bioactive glasses from the hydrolysis and polycondensation of metal hydroxides, alkoxides and inorganic salts. Further benefits, such as better bone bonding, higher degradation rates and the ability to incorporate various cation inclusions into the sol-gel network, have made this method of bioactive glass synthesis very attractive [9]. Recent papers on the development of sol-gel bioactive glass nanoparticles have pointed towards new potential functions of these biomaterials [9-11]. One of these new potentials is the idea of capitalising on its mesoporous structure for various applications in the fields of imaging and sensing, carrier-delivery therapeutic systems and filtration [12-16]. Furthermore, these mesoporous nanoparticles have also been found to demonstrate improvements in its bioactive and biological responses [15]. Bioactive glasses and bioceramics have been earmarked as suitable materials, but due to their inherent brittle nature, they fail to provide compatible mechanical properties. To overcome this, polymers are used in combination with these brittle materials to form composites, which combine the bioactive properties of the bioactive glasses and bioceramics with the mechanical properties of polymers. Nevertheless, issues such as stress shielding and a mismatch in resorption rates between the glass and polymer phases hinder its use in bone tissue engineering [17-19].

1.2 Aims and objectives

This thesis explores the use of third generation biomaterials for the synthesis of composite scaffolds, to address the need for new bone regenerative materials and its pertaining shortfalls. This work investigates the development and characterisation of bioactive glass nanoparticles via two routes (sol-gel and multi-step routes) and the ability to tailor nanoparticle morphology by varying composition, drying procedures and heat treatment regimes. The synthesis of an alginate-bioactive glass composite scaffold through the use of the tailored mesoporous bioactive glass nanoparticles as nanocarriers for ionic cross-linking forms the next aim of this thesis. The feasibility of this novel method will be investigated, with the objective of establishing a specific system by which combinations of different cross-linking ions, nanocarrier morphology and alginate concentrations can be employed. The next aim of this research is to evaluate the microstructure, mechanical properties and biological response of these composite scaffolds, to determine its suitability for bone tissue engineering applications.

1.3 Thesis outline

This thesis is composed of seven chapters, in which the first chapter provides an introduction into the main problem faced – the need for regenerative bioactive materials in the form of scaffolds to address the shortage for bone implants. The concept of scaffolds and bioactive glasses is briefly described.

Chapter 2 proceeds with the literature review of the work. The current issues and treatments available for damaged bone tissue, with the fundamental physiology and properties of bone discussed. Subsequently, the use of scaffolds for bone tissue engineering and scaffold fabrication techniques are detailed. The biomaterials employed in the synthesis of scaffolds are reviewed, with the emphasis on the alginate polymer and bioactive glasses.

Chapter 3 provides a detailed description of the materials used, the synthesis routes of various bioactive glass nanoparticles and composite scaffolds. The characterisation techniques, principles and protocols of nanoparticles and scaffold microstructure are

detailed. Furthermore, the standard protocols for *in vitro* bioactivity, cellular responses and mechanical property evaluation on the synthesised materials are outlined.

The next three chapters describe the major findings of this thesis. Chapter 4 studies the influence of processing through the sol-gel (acidic) route and the multi-step (alkali) route on nanoparticle morphology, in terms of nanoparticle surface areas, pore sizes, shapes and volumes. Additionally, variation in glass composition, drying stages and sintering regimes on final bioactive glass nanoparticle morphology is also investigated. The *in vitro* bioactive response from the changes to nanoparticle morphology is evaluated.

Chapter 5 investigates the feasibility of using the mesoporous bioactive glass nanoparticles derived in Chapter 4, as nanocarriers, for the ionic cross-linking of alginate, subsequently to synthesise alginate-bioactive glass composite scaffolds. Therapeutic ions, provided by strontium chloride, copper chloride and calcium chloride are impregnated into the nanocarriers to evaluate the fabrication of these hybrid composite scaffolds in terms of gelation time and scaffold microstructure.

Chapter 6 assesses the bioactivity and biological response of the hybrid composite scaffolds developed in Chapter 5. The hybrid composite scaffolds were also compared with those prepared by conventional cross-linking using $CaCl_2$ solutions, particularly the long term stability in mechanical properties.

Chapter 7 discusses and concludes the findings of the entire thesis. Future work is proposed based on the expansion of the investigation carried out from the results and discussions related to the field of bone tissue engineering.

Chapter 2

Literature Review

2.1 Overview

This literature survey provides the background pertaining to the issue at hand – the need for bone implants. Hence, the fundamental micro- and macrostructure of bone, its function and characteristics are firstly described. Subsequently, the concept of tissue engineering is introduced with the focus on scaffolds as the strategy for bone tissue repair and regeneration. Scaffold design challenges, fabrication biomaterials, and manufacture routes available are discussed. Finally, an in-depth review of the two biomaterials (alginate and bioactive glasses) used for the synthesis of these three-dimensional composite scaffolds is presented, with sections devoted to material molecular structure, synthesis, characterisation and application.

2.2 Bone

2.2.1 Function and structure

Bone forms the structural frame in which our body is built on. It plays the vital role in our body as a form of locomotion, load bearing, homeostasis and protection. It is biologically dynamic, continuously remodelling throughout the lifetime of an individual [2]. Bones have a diverse micro- and macrostructure, each carefully tailored to suit the many demands and functions of the body. Bone tissue is arranged in either the compact pattern (cortical bone) or the trabecular pattern (cancellous bone) [20]. The cortical bone, which is of dense structure provides the mechanical and load bearing ability of bone while the cancellous bone provides the porous supporting structural network of struts [21]. Cancellous bone consists of a connected porous network of rod and plate like cellular material. This low density and thus low stress bearing part of bone is protected by a hard outer shell of compact bone, which is the cortical bone [22].

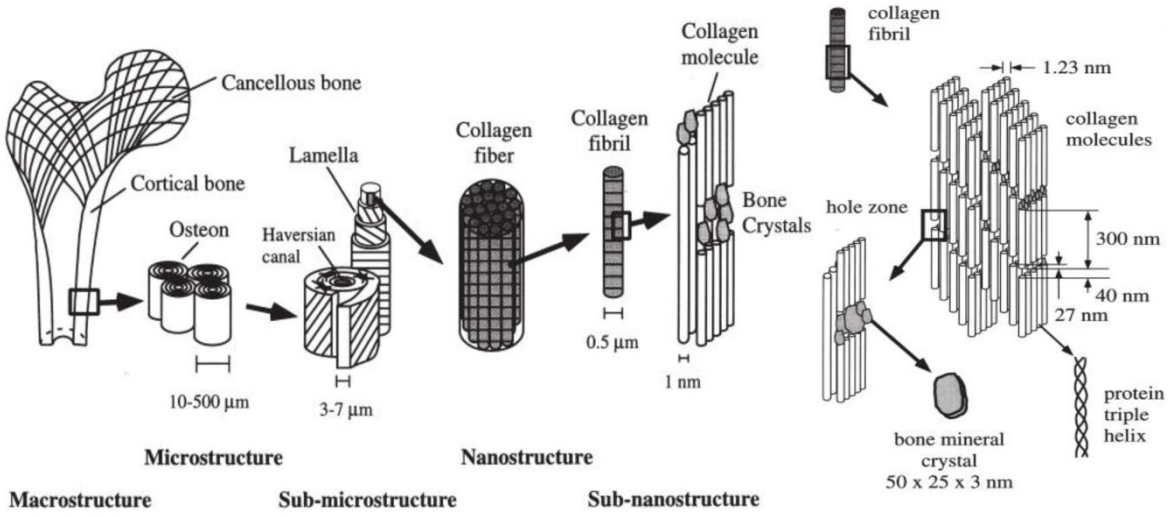

Figure 2.1: The hierarchical structure of bone. Modified after reference [23].

The micro- and macroscopic detail of each part of the bone structure is depicted in Figure 2.1. Microscopically, bone comprises of an organic and inorganic component. Collagen type I fibres of 100 – 2000 nm in diameter, which forms the matrix of the bone is the organic component. These fibres consist of fibrils which can be identified by a distinctive periodic cross-band. The collagen present in bone is synthesised by osteoblast cells and deposited in a lamella or layered form [24]. Rod- or plate-shaped bone mineral crystallites, mostly in the form of hydroxyapatite (HA) of 40 – 60 nm in length and 5 nm in diameter forms the inorganic component of bone. These crystallites are deposited and arranged in parallel to the collagen fibres thus providing the rigidity and stiffness to the bone [24, 25]. These nanofibres are arranged in lamellar sheets of about 3 – 7 µm in thickness. When grouped together in stacks of 4 – 20 lamellae, they are arranged in concentric rings around the haversian canal, thus forming an osteon [23]. The osteon rings which appear as alternating bright and dark layers on the cross-section are due to the differing orientation of each successive lamella.

The ratio of organic to inorganic phases in bone affects the mechanical properties. The collagen fibres in bone retain similar characteristics to polymers which gives bone the flexural resilience and toughness by decreasing the brittleness of the mineralised phase HA. On the other hand, the mineral material gives bone the mechanical strength and stiffness. Both cortical and cancellous bone display very different mechanical

properties. For instance, the compressive strength of cortical bone is 130 – 200 MPa and has a Young's modulus of 7 – 30 GPa while cancellous bone has a compressive strength of approximately 0.1 – 16 MPa and a Young's modulus of 0.05 – 0.5 GPa [26-29].

2.2.2 Current issues and treatments

Bone is the most commonly replaced tissue in the body and the global orthopaedic implants market is estimated to approach $41.8 billion by 2016 [30, 31]. Currently in the U.K., there are over 600,000 bone and joint related operations annually [2]. There are various causes for bone replacement operations, such as bone trauma resulting from significant lost in bone tissue, osteoporosis, arthritis, bone tumours and brittle bone disease [32, 33].

The use of bioinert implants made of metal alloys, alumina or polyethylene have been widely applied to stabilise fractures and as orthopaedic implants [34]. Although these implants have superb mechanical properties, they are biologically inert and thus unable to regenerate. Furthermore, the issue of stress shielding arises due to the mismatch in mechanical properties between bone and the implant material. This leads to elevated levels of bone resorption at the interface between implant and natural bone, and over time, the implant will become loose and fail. Risk of infection and allergy is also a cause for concern when the implants begin to wear and release debris [6, 21].

The current gold standard for bone regeneration treatment is autografting, whereby the patient's own bones are harvested and implanted into the patient [1]. Although this type of treatment has the capacity to guide new bone tissue growth over the defect site, this procedure has various limitations such as patient site morbidity, anatomical and structural problems from the removal of bone tissue [2, 6]. Allografting is another option used, in which bone tissue from a donor is harvested and implanted into the patient. However, this option also has further limitations such as viral contamination and transmission and a mismatch in compatibility between donor and patient, which will lead to rejection of the implant [35].

Thus far, it can be seen that, although there are a variety of options available for bone repair and replacement operations, the limitations of each method and the risk posed to the patient is of significance. Therefore, the need for improved materials and alternative repair methods to alleviate the problems currently faced by both surgeons and their patients is required.

2.3 Scaffolds for bone tissue engineering

One route scientists have focused their attention, to address this issue of the severe need for bone, is tissue engineering [17, 36, 37]. Tissue engineering is an interdisciplinary field, which encompasses both the principles of engineering and the life sciences, for the development of biological substitutes, which can maintain, replace or regenerate tissue and its functions [3]. The strategies of tissue engineering typically involve the use of signalling molecules, cells as therapeutics and three-dimensional (3D) scaffolds [3]. Scaffolds are 3D structures which form a site for which cells can adhere and proliferate, to repair bone defects and regenerate lost bone tissue. Scaffolds can be synthesised from different materials such as ceramics, polymers, metallic alloys or a combination of any one as a composite [17, 29, 37, 38]. The materials used should provide sufficient mechanical support at the implanted site, over the period of new tissue growth. If biodegradable materials are used, time-dependent changes in its mechanical properties have to be considered, to ensure sustained structural support is provided over time [17, 37].

Fundamentally, scaffolds for tissue engineering have to be of comparable mechanical properties to the tissue it is fabricated to replace. Additionally, good interconnectivity, substantial pore sizes and pore homogeneity is essential. Good interconnectivity is important for nutrient transport, cell attachment and proliferation and cell in-growth. The porosities of the scaffolds have to be well interconnected with a minimum porosity of 50%, for successful cell in-growth. Pore size should be a minimum of 100 µm to enable cell penetration [26, 39]. The preponderance in scaffold manufacture is, there will be a decrease in mechanical properties with an increase in pore size and porosity, and *vice-versa,* as pores under significant loading will coalesce with one another, propagating a crack, causing the material to fail. Furthermore, the ease of

manufacture and reproducibility also has to be considered when designing a scaffold for tissue engineering [37].

2.3.1 Scaffold biomaterials

Over the past few decades, ceramics in the field of bone tissue engineering have seen a great transformation from being bioinert to bioactive and resorbable [40]. A bioactive material is a material capable of stimulating an advantageous biological response from the body when introduced [41]. Since the discovery of Bioglass® 45S5, which incidentally also led to the coining of the term 'bioactive materials', a whole host of hybrid ceramics, glasses and glass-ceramics have been synthesised and used as novel biomaterials for bone tissue engineering. Currently, the focus has become creating materials which demonstrate the ability to stimulate specific responses at a cellular level and capable of inducing osteogenesis on undifferentiated cells to follow a bone cell lineage [6, 42].

Polymers also play an important role in the study of bone tissue engineering. In the search for improved materials to achieve the objective of creating an ideal scaffold for bone tissue engineering, many natural and synthetic polymers, of various degrees of mechanical properties and degradation rates have been tested [29, 43]. The polymers have a wide range of medical applications, such as drug delivery, imaging, medical devices and tissue engineering scaffolds [43]. Over the recent years, biodegradable polymers have been the subject of research because of its suitability in drug delivery as well as templating agents for the manufacture of micro and macro structures. Its desirability is further enhanced by the fact that many biodegradable polymers have been found to repair and regenerate tissue and yet not become permanent fixtures in the body [3, 38].

The most widely used polymers for tissue engineering include polylactic acid (PLA), polyglycolic acid (PGA) and copolymeric polyglycolic acid (PLGA). These polymers come from the family of poly- (α-hydroxy esters), are biodegradable and biocompatible, making them highly suitable for medical applications [38, 43, 44]. Apart from synthetic polymers, natural polymers are also highly desired for its low

toxicity, high biocompatibility and cost efficiency [45-47]. Most commonly used natural polymers include alginate, chitosan, silk and collagen [48].

A list of the more widely used ceramics and polymers are compiled in Table 2. 1. These biomaterials can be found used individually, or as a combination of two or more chemically distinct phases as a composite biomaterial. In summary, there are numerous biomaterials employed for the fabrication of scaffolds for tissue engineering. However, the selection of biomaterials most suitable for tissue engineering scaffold development would require further in-depth understanding and discussion of the materials on a molecular level, its structural behaviour and its interaction when introduced to physiological environments.

Table 2. 1: Biomaterials used for bone tissue engineering [17, 48-50].

Ceramics/Glasses	**Polymers**
Demineralised bone matrix (DBM)	Alginate
Melt-derived bioactive glass: Bioglass® (45S5)	Chitosan
Silica-based sol-gel bioactive glass: binary, ternary, quaternary systems.	Collagen
	Silk
Phosphate-based sol-gel bioactive glass: binary, ternary, quaternary systems.	Polylactic acid (PLA)
	Polyglycolic acid (PGA)
Glass-ceramic: apatite-wollatonite (A-W)	Polylactic-coglycilide (PLGA)
Calcium phosphate based ceramic: hydroxyapatite (HA), tricalcium phosphate (TCP)	PLA variants: PLLA, PDLA and PDLLA
Commercial graft: Collagraft (HA+TCP+fibrillar collagen)	Polycaprolactone (PCL)
	Polytetrafluroethylene (PTFE)
	Polymethylmethacrylate (PMMA)
	Polyhydroxyalkonoates (PHA) and variant: polyhydroxybutyraate-cohydroxyvalerate (PHBV)
	Poly-3- hydroxybutyraate-cohydroxyvalerate (P3HB)

2.3.2 Scaffold fabrication techniques

Various methods of producing scaffolds for bone tissue engineering are currently available, with comprehensive reviews provided in the literature [7, 17, 36, 50]. Specifically for alginate and bioactive glass scaffold synthesis, the common methods used, such as freeze drying, gel casting, gas foaming, thermally induced phase separation (TIPS), microsphere or short fibre sintering and solid freeform fabrication aim to meet the criteria of possessing both interconnected pores of suitable size with sound mechanical properties [17, 29, 37, 51, 52]. The different scaffold pore architecture from the various fabrications routes is depicted in Figure 2. 2.

For scaffolds fabricated through gel casting, the intended bioactive slurry is thoroughly mixed with a monomer solution, to which a surfactant (porogen) is added to create a foam mixture. Once the foam structure has solidified, it is heated in a furnace to burn off all polymers, leaving a porous bioceramic scaffold [53]. This technique has been employed to create open-channelled scaffolds with porosities of 72 – 90% and pore sizes of 17 – 122 µm [53]. Sol-gel bioactive glass scaffolds with porosities of approximately 82% and an average pore size of 325 µm were also obtained from this method [54]. However, poor interconnection and a heterogeneous pore distribution compounded by the introduction of foreign substances and free radicals from the surfactants and monomers suggest this method has its limitations [55]. Furthermore, residue organic solvents introduced were found to be toxic and caused an inflammatory response [56].

Another method used for scaffold synthesis which also involves the foaming of the biomaterials is gas foaming. This method differs from the method above in that it does not require an organic solvent to create a porous structure, instead, gas is utilised. Hydrogen peroxide (H_2O_2) or citric acid with bicarbonate salt is typically used as the gassing agents to create foam. In various studies, H_2O_2 was used to create porous scaffolds of calcium-phosphate bioceramics or bioactive glasses [57, 58]. Although porosities in excess of 70% were obtained from this method, the reproducibility and controllability of pore sizes were difficult and poor pore interconnectivity was obtained.

Solid freeform fabrication (SFF) is a computer aided method which is capable of manufacturing highly reproducible scaffolds. The designs of the scaffolds to meet the criteria of high interconnectivity and good pore homogeneity can be fabricated using this method. Initially, a computer aided design (CAD) or computer aided manufacture (CAM) is laid out, then through various fabrication routes, such as stereo lithography, selective laser sintering, 3D printing and ballistic particle manufacturing, the scaffold is fabricated [37, 59].

This method uses the same principle of transferring or removing the scaffold material either in powder or liquid form on the surface repeatedly until the desired shape is obtained. Hydroxyapatite and sol-gel bioactive glass scaffolds fabricated using the 3D printing route were found to provide a good template for human osteoblast (HOB) cell attachment and proliferation [9, 60]. Scaffolds with tailored microstructures have been achieved using SFF, with scaffolds synthesised with tuneable pore sizes. Specifically, bioactive glass scaffolds manufactured using this route had a porosity range of 50 – 60% and pore range of 300 – 1000 µm [36, 61, 62]. Although this method is reproducible, and macrostructures of the scaffolds can be specifically tailored, the entire process from designing to fabrication is time consuming and involves high equipment cost [59].

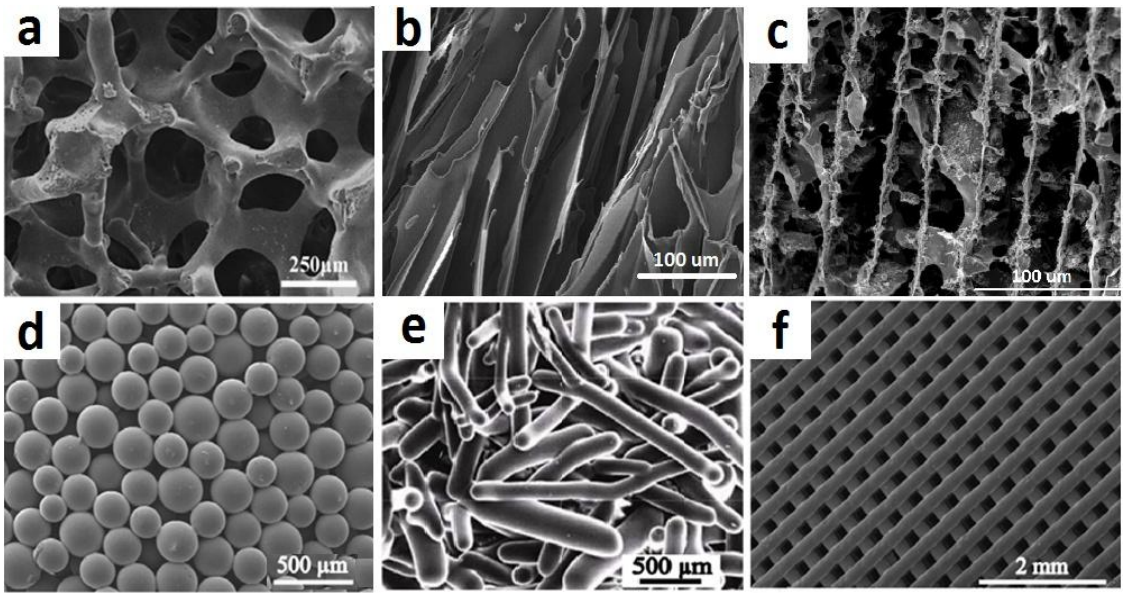

Figure 2. 2: Microstructure of bioactive glass and composite scaffolds fabricated by (a) foaming [36], (b) thermally induced phase separation [63], (c) unidirectional freeze drying [64], (d) microsphere sintering [36], (e) short fibre sintering [36] and (f) solid freeform fabrication [36].

Freeze drying has been seen as a promising approach for the fabrication of porous scaffolds [19, 65-67]. Freeze drying is a dehydration method in which a material (scaffold) is frozen and then pressure is reduced to achieve a region below the triple point. During this process, heat is transferred into the product, causing the frozen water trapped within the scaffold matrix to sublime directly from the solid phase to the gas phase, leaving a porous structure [68]. The triple point of water is achieved at a temperature of 0.009 °C and a pressure of 6.1×10^{-4} MPa (4.58 Torr.) [69]. Heat energy transferred onto the product through conduction, convection and radiation is necessary for the phase change (solid to gas) to take place [66, 68].

Hong *et al*. [10] fabricated poly-L-lactide (PLLA) composites with bioactive glass nanoparticles using this method, in which porous and interconnected scaffolds with controlled degradability and good biocompatibility was observed. Via freeze drying, Wu *et al*. [66] demonstrated that controlled orientation with tuneable pore size and extremely high porosity of 98% could be obtained from unidirectional freeze drying of gelatine scaffolds. Unidirectional freezing was carried out via insulating the specimen at its sides and exposing one surface of the specimen to the cold finger. Hence, the ice crystals would grow from this ice front upwards along an axis, thus creating directionality [66].

Scaffold architecture containing pore directionality has been shown to improve mechanical properties. Studies into the fabrication of bioactive glass composite scaffolds with orientated microstructures have found that, by aligning the microstructure of the scaffolds in lamellar or columnar directions, superior directional mechanical properties can be obtained [17]. This was observed from unidirectional bioactive glass scaffolds fabricated from a silica-based bioactive glass (BG13-93) via freeze drying, which demonstrated improved compressive strength as compared to scaffolds fabricated from other methods (Table 2. 2).

Additionally, pore sizes can be controlled by varying cooling rates using the fundamentals of the physics of ice formation to explain the manipulation of pore shape and sizes through cooling rates. The nucleation of ice crystals begin with the arrangement of a few water molecules in a crystal structure. As energy is lost, the

crystal structure continues to grow, fusing with other ice crystals until all the liquid is frozen [70]. For scaffold fabrication, understanding the parameters involved in the process of ice crystal formation is important in designing a suitable freezing regime.

Under slow cooling rates, the scaffold cools uniformly. Hence, the formation of ice crystals is homogeneous, resulting is relatively homogenous pore sizes. Furthermore, large ice crystals form since small amounts of heat from super cooling, which is a highly exothermic process is released, melts the small ice crystals, and allows for the ice crystals to connect with neighbouring crystals [65-67, 71]. On the other hand, Deville *et al*. [19] showed that for scaffolds which were cooled rapidly using liquid nitrogen, there was no provision for a uniform cold environment to allow the scaffold to cool gradually and form homogenous and directional pores.

There are a few reasons freeze drying would be preferred to create the scaffold as opposed to some other methods discussed above. Mainly, freeze drying allows for the control and the creation of scaffolds with homogenous pore sizes, directional pore orientation and scaffolds with high porosity. This is done through careful selection of freezing rates and pressures. Furthermore, the introduction of foaming agents and surfactants is eliminated, since the porous structure of the scaffold is fabricated through the removal of ice, which in itself acts as pore templates.

Table 2. 2: Characteristics of similar material (bioactive glass 13-93) scaffolds fabricated by different techniques.

Technique	**Compressive strength (MPa)**	**Pore size (µm)**	**Porosity (%)**	**Reference**
Gas foaming	11 ± 1	100 – 500	75 – 85	[72]
	5 ± 0.5	100 – 500	80 – 85	[73]
Solid freeform fabrication	15 ± 1	700 – 1000	58 – 60	[36]
	20.4	300 – 800	50	[61]
Unidirectional freeze	25 ± 3	90 – 110	53 – 57	[74]
drying	27 ± 8	60 – 120	50 – 55	[75]

2.4 Alginate

2.4.1 Polymer structure

Alginate is a naturally occurring anionic polysaccharide which is typically extracted from marine brown algae (Phaeophyceae). Apart from brown algae being the most desired source of extraction, due to high yield efficiency (> 40% of dried algae consists of alginate), alginate can also be extracted from bacteria [76, 77]. Alginates are linear copolymers containing (1⟶4) glycosidically-linked β-D-mannuronic acid (M) and α-L-guluronic acid (G) residues, as shown in the Haworth monomer formulas (Figure 2. 3). From the brown algae family of Laminaria, G-block-rich alginate has been extracted from the stipes of Laminaria hyperborean, while M-block-rich alginate has been extracted Laminaria digitata [78, 79]. Separately, alginate from bacterial sources has been found to be extremely rich in M-blocks, with alginates extracted from Pseudomonas sp. containing no G-blocks [77]. Depending on the source of the alginate, the amount of G and M monomers as well as their arrangement along the polymer chain can differ widely. The typical M to G ratio of the alginate ranges from 0.45 to 1.6, depending on the source of the algae. The molecular weight of sodium alginate range between 32000 – 400000 g/mol and has a density of 0.9 gcm^{-3} [46, 80].

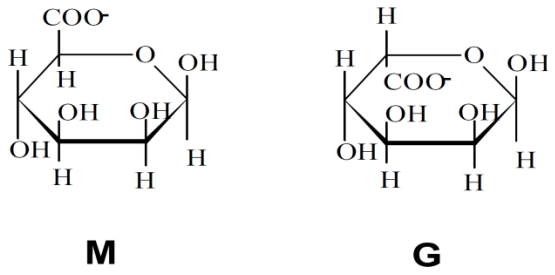

Figure 2. 3: The chemical structure of the M and G alginate monomers [76].

The molecular structure of the alginate consists of blocks of similar (MMMMMM, GGGGGG) or strictly alternating (GMGMGMGM) residues, of which each have different conformational preferences and behaviour (Figure 2. 4) [46, 79, 81, 82]. The structure of G-blocks differs from M-blocks, which affect the overall mechanical properties of the polymer. The linkages between two gluronate units in G-blocks are axial-axial, making the linkages shorter between each unit, thus making the overall structure less flexible and more susceptible to buckling. On the other hand, the

mannuronate units in M-blocks are equatorial-equatorial linked, forming a flat, ribbon-like structure, thus providing the polymer with increased flexibility. Interestingly, GM-blocks contain a mixture of axial-equatorial and equatorial-axial linkages which provide greater flexibility than the equatorial-equatorial link found in M-blocks through an increase in the degrees of freedom associated with this type of linkage [81, 83, 84]. As shown in Figure 2. 5, the G-, M- and GM-blocks can coexist on a single polymer chain, taking on various block sequences [46].

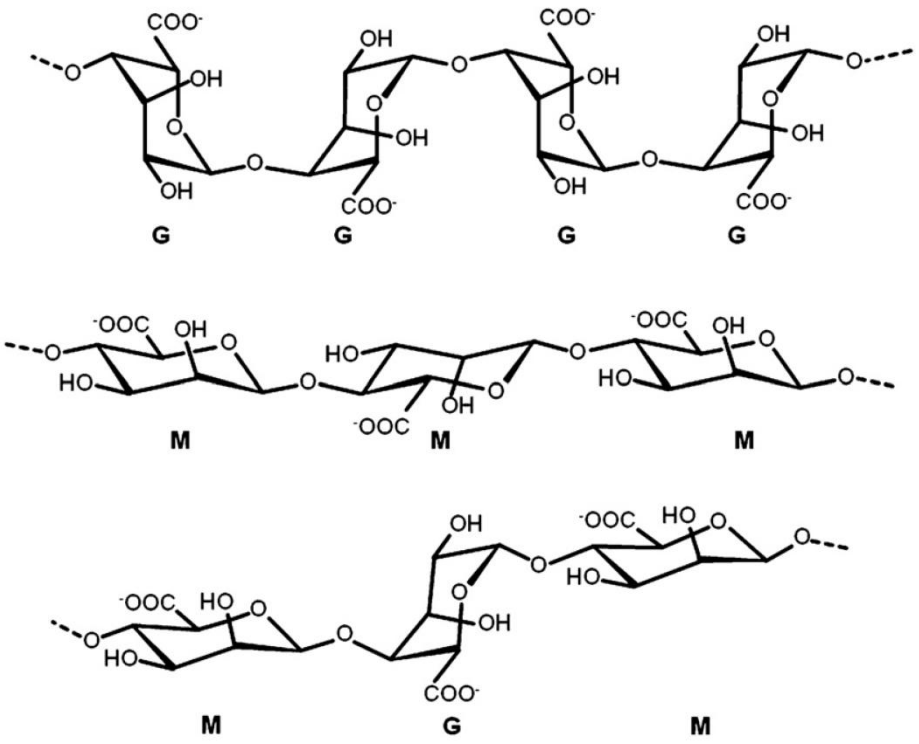

Figure 2. 4: The molecular structure of G-blocks, M-blocks and GM-blocks, showing the different linkage arrangements [46, 80].

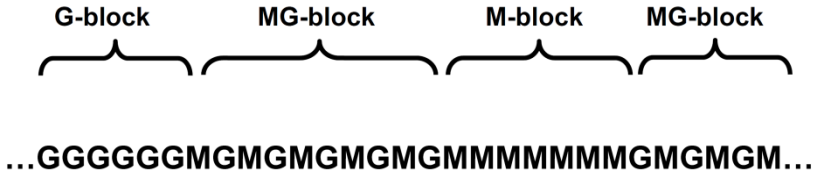

Figure 2. 5: Composition of an alginate polymer chain containing different block type combinations [76].

2.4.2 Alginate hydrogels

It is widely accepted that alginate is a biocompatible polymer, suitable for use in the biomedical industry. *In vitro* and *in vivo* studies have shown that alginate does not induce significant inflammatory responses or foreign body reaction when implanted in animal models [46, 85, 86]. However, there have also been reports of immunogenic responses from alginate implants, partly attributed to the impurities found in commercially produced alginate especially since various impurities, such as heavy metals, endotoxins and proteins could be present in the alginate extracted from the many natural sources [46].

The physical properties of alginate gels are highly dependent on its molecular weight and chemical composition (M to G ratio). Alginate, commonly supplied in the form of sodium alginate, is soluble in water. However, its solubility is highly dependent on pH, as this will affect the electrostatic charges on the uronic acid residues [87]. As such, as pH decreases to between pH 3 – 3.5, the alginate becomes protonated and forms hydrogen bonds, thus taking the form of the insoluble alginic acid [46]. The molecular weight and concentration play an important part in the viscosity of the alginate solution. The higher the molecular weight or concentration, the more viscous is the resultant alginate solution.

Although alginate solutions have little use in biomedical applications, after cross-linking, alginate hydrogels have been used in applications such as drug delivery, wound dressing and three dimensional scaffolds synthesis. Cross-linking is a process in which the loose polymer chains are linked together with adjacent chains to form a solid structure, consisting of networks of hydrophilic polymers intermittent by water, also known as a hydrogel. Common cross-linking methods include ionic cross-linking, covalent cross-linking, thermal cross-linking and cell cross-linking [46].

2.4.3 Hydrogel formation

Ionic cross-linking is the most common approach used for hydrogel formation. It takes place when divalent ions introduced, bind to the G-blocks of the polymer chain and form junctions, which attach to the other junctions formed with adjacent polymer

chains [88]. The mechanisms of cross-linking of alginate blocks are typically described using an egg-box model, wherein the axial-axial linked G residues form interstices to which the binding ion assembles, as illustrated with Ca^{2+} ions in Figure 2. 6. Once the many sequences of G-blocks form bonds with other sequences, a gel network is formed [46, 86]. The length of the G-blocks is crucial in the formation of stable junctions during cross-linking. Stokke *et al*. [89] reported that a minimum length of G-blocks consisting of at least 8 – 20 G residues is required for stable junctions to form.

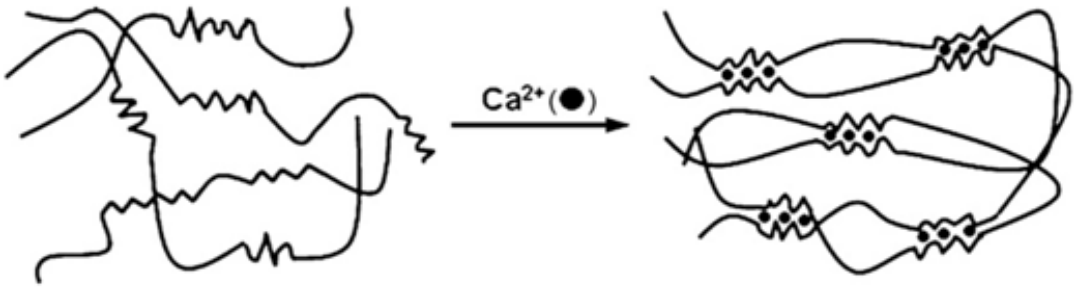

Figure 2. 6: Alginate polymer chains cross-linked using calcium ions, following the egg-box model to form a gel structure [46].

One frequently used ionic cross-linker is calcium chloride ($CaCl_2$) [47, 88]. $CaCl_2$ is a salt which is solid at room temperature but readily soluble in water, releasing Ca^{2+} ions in the process. Other sources of Ca^{2+} ions can also be obtained from calcium carbonate ($CaCO_3$) or calcium sulphate ($CaSO_4$) [46].

The process of Ca^{2+} ion cross-linking to form hydrogels involves the diffusion of ions from a calcium rich source into the alginate solution. This process of diffusion can be separated into two distinct routes: I) external diffusion and II) internal diffusion. The external diffusion route involves the gelation from the extremities of the alginate solution, progressing inward, and is widely used in alginate bead synthesis [90]. For the synthesis of alginate hydrogel scaffolds, the direct use of readily soluble Ca^{2+} sources through external diffusion for cross-linking often causes rapid and uncontrolled gelation, leading to heterogeneous structures with varying cross-linking density and polymer concentration gradients [47, 82].

To overcome this problem, the internal diffusion route can be employed, in which Ca^{2+} is introduced from within the hydrogel. Often used between a low solubility source of calcium ions such as calcium carbonate ($CaCO_3$) or calcium sulphate ($CaSO_4$) together with chelating agents such as, ethylenediaminetetraacetic acid (EDTA) or glucono delta-lactone (GDL), the internal diffusion route slowly dissociates the Ca^{2+}, releasing the ions into the surrounding alginate solution [47, 91, 92]. Kuo *et al*. [47] successfully demonstrated the gelation of uniform and mechanically improved alginate hydrogels through the combined use of $CaCO_3$ and GDL. In this approach, the $CaCO_3$ and GDL solution is mixed into alginate, the pH of the alginate solution is lowered by the hydrolisation of lactone, causing Ca^{2+} to gradually disassociate from $CaCO_3$ and cross-link the alginate. Similarly, Zmora *et al*. [67] prepared alginate scaffolds by intensively mixing calcium gluconate solutions with alginate, successfully producing alginate scaffolds with tailored pore architecture. It has been agreed that the control of the gelation rate of the hydrogels is essential in producing homogenous hydrogels and consequently improving the strength and mechanical properties of the gel structure [46]. However, due to the limited availability of cross-linking ions, the internal diffusion method often results in gels of lower strength as compared to the external diffusion method, where cross-linking is not limited [93].

2.4.4 Cross-linking ion affinity and functions

Apart from Ca^{2+} ions, various other divalent ions have been used for the ionic cross-linking of alginate [90, 94, 95]. Interestingly, it has been shown that the affinity of ions towards alginate follows a rigid series. The movement and redistribution of charges of divalent ions in alginate solutions was documented by Thiele *et al*. [96, 97] in the 1950s and showed that an ionotropic order existed. Subsequent research, employing the equilibrium dialysis of alginate involving various divalent ions allowed for a more detailed listing of the affinity series (Table 2. 3). Understanding the affinity of different divalent ions towards alginate is important, as a correlation between the gel modulus of rigidity (G) and cross-linking ion type had been shown. Smidsrod *et al*. [98] demonstrated that, the G of alginate gels decreased in the same order as the affinity series, summarised in Table 2. 4.

Additionally, the affinity of divalent ions was also found to be influenced by alginate composition (G-, M- and GM-block ratios). The affinity of these ions were found to follow the sequences of G-blocks: $Ba^{2+} > Sr^{2+} > Ca^{2+} > Mg^{2+}$; M-blocks: $Ba^{2+} > Sr^{2+} \approx Ca^{2+} \approx Mg^{2+}$; GM-blocks: $Ba^{2+} \approx Sr^{2+} \approx Ca^{2+} \approx Mg^{2+}$, through the study of its binding strength to alginate fragments [99]. Essentially, these results showed that the G-blocks highly influenced the affinity of ions towards alginate, with M- and GM-blocks showing almost no influence on ion affinity [76, 99].

Table 2. 3: Key changes and additions to the affinity series, measured through equilibrium dialysis of cations to alginate (M/G ratio: 0.45 - 2.1) over the years.

Affinity series	Year	Reference
$Pb^{2+} > Cu^{2+} > Ca^{2+} > Co^{2+} \approx Zn^{2+} \approx Ni^{2+} > Mn^{2+}$	1958	[100]
$Pb^{2+} > Cu^{2+} > Cd^{2+} > Zn^{2+} \approx Ni^{2+} \approx Co^{2+} > Mn^{2+}$	1961	[96]
$Ba^{2+} > Sr^{2+} > Ca^{2+} > Mg^{2+}$	1965	[101]
$Pb^{2+} > Cu^{2+} > Cd^{2+} > Ba^{2+} > Sr^{2+} > Ca^{2+} > Co^{2+} \approx Ni^{2+} \approx Zn^{2+} > Mn^{2+}$	2006	[90]

Table 2. 4: The correlation between the affinity series and modulus of rigidity of alginate gels with different divalent ions [96, 98].

Affinity series:	$Pb^{2+} > Cu^{2+} > Cd^{2+} > Zn^{2+} \approx Ni^{2+} \approx Co^{2+} > Mn^{2+}$						
Ion type	Pb^{2+}	Cu^{2+}	Cd^{2+}	Zn^{2+}	Ni^{2+}	Co^{2+}	Mn^{2+}
Modulus of rigidity (Ncm^{-2})	17.3	14.7	7.8	5.8	9.7	3.7	2.8

Other divalent ions such as Sr^{2+}, Zn^{2+} and Ba^{2+} have also been used in the ionic cross-linking of alginate to form hydrogels for biomedical applications [90, 94]. Morch *et al*. [90] studied the formation of microcapsule alginate beads via Sr^{2+}, Ba^{2+} and Ca^{2+} ionic cross-linking. The selection of Sr^{2+} and Ba^{2+} ions was based on the affinity series, which suggested that due to the higher affinity of these ions to alginate, the microbeads formed will have a higher degree of stability than Ca^{2+} cross-linked beads. More recently, Place *et al*. [94] employed alginate hydrogels cross-linked via a mixture of zinc-calcium and strontium-calcium ions for bone tissue engineering

applications. The results showed that, as the hydrogels degraded over time, a sustained release of the cross-linking ions led to favourable response of the osteoblast cells. Noticeable improvements in osteogenic properties, as well as increased levels of alkaline phosphotase (ALP) activity were observed from hydrogels cross-linked with zinc or strontium ions.

The study by Place *et al*. [94] is important because it points towards a dual-function usage of these divalent ions. Not only are these divalent ions employed to ionically cross-link alginate with physical improvements to the hydrogel properties, the added biological benefits from these ions could also be harnessed. The biological effects of divalent ions such as strontium (Sr^{2+}) have been found to be beneficial in promoting bone formation. Studies have shown that strontium can simultaneously increase osteoblast cell proliferation and ALP activity and inhibit osteoclasts resorption of calcium phosphate [102-104]. Magnesium and zinc ions have both been found to play a role in bone development and calcification of tissue. Studies have shown that, with the inclusion of these ions, ALP activity in osteoblast-like cells increased, and acts as cofactors to enzymes involved in bone formation [94, 105-108].

Furthermore, silver and copper ions have also been used for bone tissue engineering application, nevertheless, for its antimicrobial properties. Silver substituted bioactive glasses have been found to show antimicrobial effects across a whole range of bacterial types, while copper has also been found to significantly reduce bacterial activity [95, 109-112]. Heliopoulos *et al*. [95] recently demonstrated the excellent bactericidal effect of copper-alginate treated wool fibres. In the study, the treated wool fibres inhibited the growth and proliferation of E. coli bacteria and further showed that copper-alginate treatment increased the sustainability of its antimicrobial properties as compared to copper treated wool fibres. The benefits of employing different divalent ions for cross-linking alginate are huge, especially with the dual-functional usage of these divalent ions for the synthesis of scaffolds being relatively unexplored, further investigation is necessary.

2.4.5 Mechanical properties of alginate hydrogels

The study of the mechanical properties is imperative for various reasons. Mainly, it provides a better understanding of the material and suitability in various applications and requirements, the possibility to predict unacceptable levels of use to avoid failure and the ability to tailor and modify its chemical structure to improve on its mechanical characteristics.

For bone tissue engineering applications, it is important that the mechanical properties of the implant match that of the native tissue it replaces. Although the mechanical properties of alginate hydrogels to date are inferior to that of bone, many attempts to characterise its mechanical properties have been carried out. This would include the gels' permeability, swelling properties, stability and degradability. The permeability and consequently the degree of swelling of the gels when immersed in water or physiological solutions is an important parameter to consider. Under physiological conditions, the ion rich environment accelerates the chelating effects on the ionic cross-links, leading to osmotic swelling of the gels [90]. These expanded gels, with increased pore sizes, encourage further permeation of fluids, causing a significant reduction in gel stability and mechanical properties [113].

The degradation of ionically cross-linked alginate gels occur either through ionic exchange with its surroundings or by enzymatic cleaving. Enzymatic degradation of alginate requires alginase, which is not present in mammals [46]. As such, for biomedical applications, the degradation of alginate gels is reliant on the ionic exchange between the ionic cross-linking ions within the gel with that of the surrounding media [46, 86, 88]. Therefore, the process of alginate gel degradation in most *in vitro* and *in vivo* studies, which does not involve the use of alginase, is dissolution. The limited long term stability of ionically cross-linked alginate hydrogels in a physiological environment have been a cause of concern, since the gels are susceptible to cationic exchange reactions [46]. Hence, other forms of cross-linking have been explored to improve on the physical properties of the hydrogels.

Compared to ionically cross-linked gels, alginate hydrogels with controlled swelling properties and elasticity have been prepared by covalent cross-linking using

poly(ethylene glycol)-diamines. The improvements were a result of the difference in bonding mechanism [46, 114]. Zhao *et al.* [115] observed the different stress relaxation behaviour of alginate hydrogels from the onset of constant strain between ionically and covalently cross-linked alginate. Their results showed that stress relaxes occurred from the disassociation and reformation of ionically cross-linked bonds in the gel while stress relaxes occurred through the migration of water for covalently cross-linked hydrogels. Although improvements in the mechanical behaviour of the hydrogels were noted, covalent cross-linking reagents have been found to be toxic and thorough removal difficult [46].

A stress-strain test is routinely conducted to ascertain the mechanical behaviour of alginate hydrogels [17, 18, 47, 67, 86, 116]. Both tension and compression test can be carried out to obtain the stress-strain behaviour of the material [117]. The relationship between stress and strain for a linear elastic solid such as a metal or a ceramic is known as Hooke's law. For most polymers, over regions of low stress, stress and strain are proportional to each other, in which the constant of proportionality is the modulus of elasticity or commonly known as the Young's modulus (E). This region of elastic deformation or non-permanent deformation determined from the maximum stress applied to the material in which when the applied load is released, it can return to its original shape, the stress-strain curve results in a linear relationship. E is therefore a measure of stiffness; the material's ability to resist deformation [117].

The stiffness of alginate gels have been found to be influenced by alginate composition (ratio of G, M and G-M blocks), concentration, molecular weight, cross-linking ion type and the degree of cross-linking [79]. Since G-blocks are solely involved in the gelation mechanisms, alginates which were G-block rich have been found to possess higher levels of stiffness than its GM- and M-block-rich counterparts [76, 116]. As for the alginate concentration, it has been found that alginate stiffness increased with concentration [47]. Similarly, an increase in molecular weight was found to increase the hydrogel's stiffness, although, a limit was identified by Martinsen *et al.* [118] to be in the region of 600 mL/g in alginate solution intrinsic viscosity. Beyond this, the stiffness remained constant.

Rupture, the failure of a material through significant plastic deformation is another important mechanical behaviour of alginate hydrogels, typically measured by compressing cylindrical alginate constructs till the point of collapse, and recording the force required to do so [47, 117, 119]. Similar to stress-strain behaviour, rupture strength is influenced in the same way by concentration, molecular weight, cross-linking ion type and the degree of cross-linking of the alginate hydrogel. Studies have shown that, M-block rich alginate gels display higher rupture strength as compared to G-block rich gels. This is because, the equatorial-equatorial links found in M-blocks are longer, giving higher elasticity to the gel, while the shorter axial-axial links found in G-blocks form stiffer and more brittle gels, thus reducing the gel rupture strength [79, 118]. Through compressive testing, rupture of alginate gels have been recorded in the form of its compressive modulus and shear stress [120].

2.5 Bioactive glass

Bioactive glass is an amorphous material which has a disordered arrangement of atoms due to the rapid cooling of the molten ceramic. For bone tissue engineering, bioactive glasses can be silica-based, phosphate-based or borate-based amorphous material [4, 7, 121]. Among the various types of bioactive glasses, the most common and readily used in clinical applications is Bioglass® 45S5 (46.1% SiO_2, 24.4% NaO, 26.9% CaO and 2.6% P_2O_5; mol %). The term 45S5 signifies that the composition consist of 45% weight of SiO_2, S for silica as the network former, and a 5 to 1 molar ratio of Ca to P (in the form of CaO and P_2O_5) [122]. When Larry Hench invented Bioglass®, the first test conducted in 1969 showed that Bioglass® was able to not only bond to bone, but the interfacial bond between the bioactive glass and the host tissue was also greater than the host bone [123, 124].

There are two processing routes for bioactive glasses: the melt-derived processing route and the sol-gel route. Bioglass® 45S5 is an example of melt-derived glass. The sol-gel route is a relatively low temperature method of obtaining bioactive glasses from the hydrolysis and polycondensation of metal hydroxides, alkoxides and inorganic salts [8]. Although sol-gel processes have been known since the 1880s, it was not until a hundred years later when it began receiving interest within the

scientific community [125]. The first sol-gel derived bioactive glasses of the ternary system (SiO_2 – CaO – P_2O_5) with a silica range of 50 – 95 mol % were developed by Li *et al.* [8] in 1990.

2.5.1 The bioactivity of bioactive glass

The bioactivity of a material can be classified using the bioactivity index (I_B) which considers the time taken for 50% of the material interface to bond to bone. A material is considered Class A if it has an I_B of more than 8 and is able to bond to both hard and soft tissue. On the other hand, a Class B material has an I_B between 0 and 8 and is only able to bond to hard tissue [126-128].

Another important factor about Class A biomaterials is its ability to stimulate both osteoconduction and osteoinduction. Osteoconduction is the property of materials which allows bone growth on its surface or in the context of three dimensional objects, bone growth will be observed along the surface of the pores and channels of the material. On the other hand, osteoinduction is the stimulation of undifferentiated mesenchymal cells into a bone-forming cell lineage [128, 129]. The differences in both terms are crucial, osteoconduction is the formation of bone at the surfaces between the implant and the host bone, which is a characteristic of a second generation biomaterial, while osteoinduction involves the gene activation and cell signalling, is characteristic of third generation biomaterials [6, 42].

2.5.2 Bioactive glass – melt-derived route

The traditional melt-derived route of bioactive glass synthesis (Bioglass® 45S5) begins with the melting of the oxides (SiO_2, Na_2CO_3, $CaCO_3$, P_2O_5) in a crucible at 1370 °C. Crucibles of platinum or graphite are used to ensure no contamination of the molten glass [123]. The molten ceramic is then quench immediately in water, allowing no time for the atoms to arrange in a crystalline form, thus forming the amorphous material, also known as frit. Various oxides and multivalent cations can be added during the melting stage, to obtain various compositions of glass [122]. The amount of SiO_2 affects the rate of bone bonding. The most bioactive composition lies in the region of around 45 wt. % SiO_2. It has been found that 52 – 60 wt. % of SiO_2 in the

system (P_2O_5 is kept constant at 6 wt. %) reduces the rate of bone bonding, while a composition of more than 60 wt. % of SiO_2 in the system renders the glass bio-inert [128].

2.5.3 Bioactive glass – sol-gel route

Sol-gel bioactive glasses were firstly derived by Li *et al*. [8] and Pereira *et al*. [130] in the early 90s. The bioactive glasses were synthesised in room temperature and the proposed 58S glass (60% SiO_2 – 36% CaO – 4% P_2O_5; mol %) contained a composition close to 45S5, without the sodium oxide component. The research demonstrated a wider bioactive range for sol-gel bioactive glasses (up to 80 mol % of SiO_2), increased rate of hydroxy-carbonate apatite (HCA) formation and that an increase in silica led to an increase in specific surface area (SSA) of the glass which affected the bioactive response of the glass [8]. A binary system, 70S30C glass (70% SiO_2 – 30% CaO; mol %) was subsequently developed by Saravanapavan and Hench [131], which was a simplified phosphate-free system derived due to the rapid dissolution of P_2O_5 in the 58S glass. The HCA formation rate of the 70S30C glass was found to behave similarly to the 58S glass [132].

Focus on bioactive glass synthesis has been centred on the sol-gel route due to various advantages over the melt-derived route. Crucially, sol-gel derived bioactive glasses have been found to be more bioactive than the traditional melt-derived bioglasses. Studies have shown that these glasses exhibited high rates of HCA formation when exposed to simulated body fluids (SBF), fast bone bonding rates and improved degradation and resorption characteristics [133]. This is partly due to the high specific surface areas (SSA) of the nanoparticles, which have been reported to contain pores [134, 135]. The SSA of sol-gel glass was found to be two-fold larger than melt-derived glass. The pores within the nanostructure of sol-gel bioactive glass nanoparticles significantly increases the SSA of the glasses and hence increases the rate of dissolution [136].

The low processing temperature of the sol-gel route (600 – 700 °C) as compared to the melt-derived route (1250 – 1400 °C) is also attractive, since this process allows for better control in the homogenisation of the components, and reduces the cost of

processing in terms of energy, equipment and labour [8]. Furthermore, when compared to melt-derived bioactive glass, the range of SiO_2 content for sol-gel bioactive glass to achieve a bioactive response is vastly broader, with sol-gel glasses reported to be bioactive between 50 – 85 wt. % of SiO_2 in the system as compared to 45 – 60 wt. % SiO_2 for melt-derived glass [9, 136].

2.5.4 Synthesis of sol-gel bioactive glass

The stages involved in sol-gel bioactive glass synthesis are shown in Figure 2. 7. The sol-gel process begins with a two stage reaction of the hydrolysis and polycondensation of alkoxide, metal hydroxide and inorganic salt precursors [8, 9].

For a silica-based bioactive glass, the alkoxide precursor used to obtain the silica component is tetraethylorthosilicate (TEOS). TEOS is firstly reacted with water in which a colloidal suspension in a liquid called the sol is formed. During this stage, hydrolysis occurs through the nucleophilic attack of water on the alkoxide. This reaction is usually catalysed through the addition of acids or alkalis. Subsequently, condensation of the silanol groups (Si – OH) occurs, producing silixone bonds (Si – O – Si). Hence, TEOS acts as the network former and polycondensates upon aging to form the silicate network Si – O – Si, releasing water and ethanol as the by-product from this reaction [125, 137, 138]. The two main stages of sol-gel chemistry are summarised in Equations 2.1 and 2.2. Firstly, hydrolysis occurs in which water replaces the alkoxide group (OR) with the hydroxyl group (OH). Then, condensation takes place, in which silinol groups link together to form Si – O – Si bonds, releasing water and alcohol [138].

$$Si—OR + HOH \rightleftharpoons Si—OH + ROH \qquad \text{Equation 2.1}$$

$$Si—OH + Si—OH \rightleftharpoons Si—O—Si + HOH \qquad \text{Equation 2.2a}$$

And/or

$$Si—OR + Si—OH \rightleftharpoons Si—O—Si + ROH \qquad \text{Equation 2.2b}$$

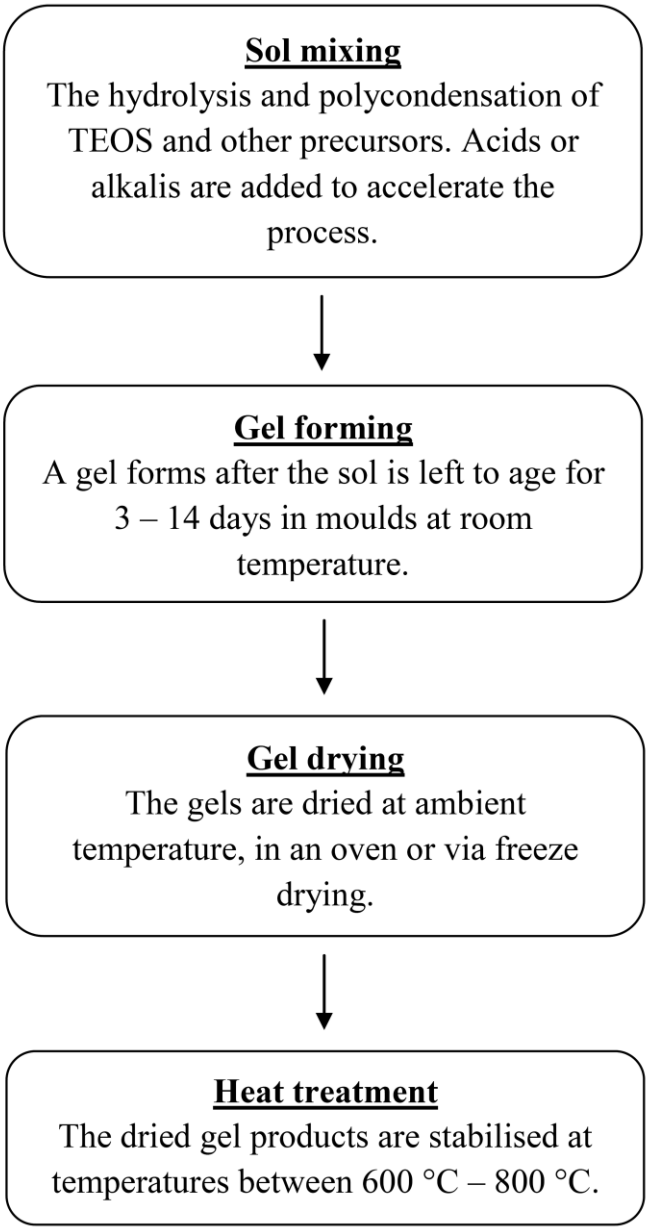

Figure 2. 7: The different stages involved in the synthesis of sol-gel bioactive glass.

Sol-gel bioactive glasses exist in the form of binary, ternary or quaternary systems. For instance, the precursors of calcium nitrate tetrahydrate ($Ca(NO_3)_2$) is added to form a binary glass (SiO_2 – CaO) or triethyl phosphate (TEP) can be added to the sol to form a ternary system bioactive glass (SiO_2 – CaO – P_2O_5). Further cation inclusions, such as MgO, Ag_2O and ZnO can also be added to enhance or provide novel properties to the bioactive glass [105, 110, 139]. The silica-based bioactive glasses used in this research are of the ternary system. Hence, it is important to understand the atomic structure of these silica glasses, which would provide for a

clearer understanding of the properties of the glass, such as dissolution rates, which influences the formation of hydroxy-carbonate apatite (HCA).

Silica-based glasses are composed of many units of the SiO_4 tetrahedron, connected through the oxygen atom to form a 3D network structure [121, 140]. The SiO_4 tetrahedral is classified by the number of oxygen atoms shared with other silicate tetrahedral. These shared oxygen atoms are commonly referred to as bridging oxygen (O – Si – O). The four oxygen atoms per silicate suggest up to four possible bridging oxygen bonds, which are classified by $Q^{(0\text{-}4)}$, as shown in Figure 2. 8. The type and relative amount of Q structures within a glass can be determined by magic angle spinning solid-state nuclear magnetic resonance (NMR) [135, 141].

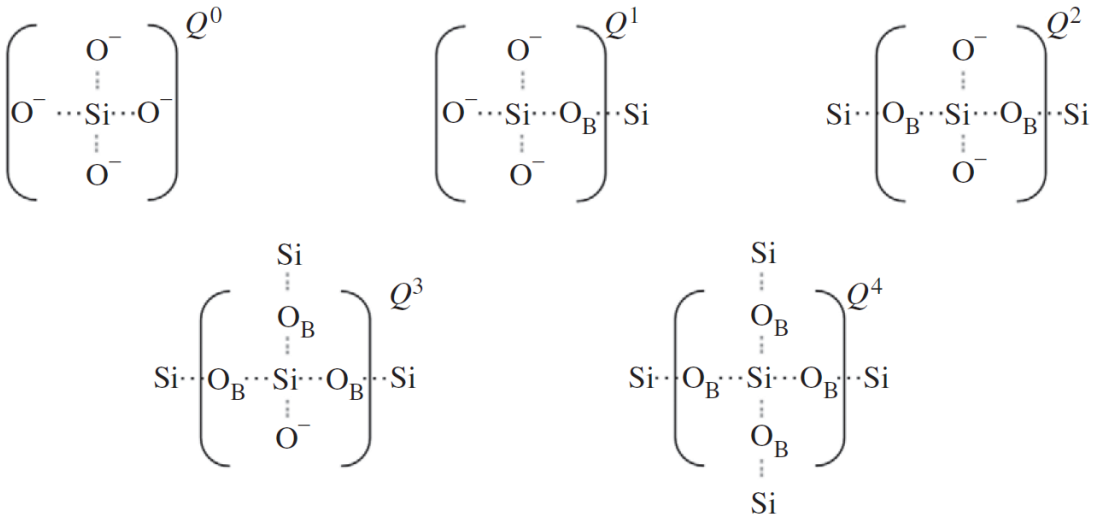

Figure 2. 8: The Q structures assigned to the silicate network, where O_B represents bridging oxygen bonds [140].

For both melt-derived and sol-gel glasses, the Q value can be used to explain the network connectivity of the glasses. By understanding the average value of Q in a structure, the dissolution of the glass network can be determined. Lin *et al.* [135] determined through NMR that sol-gel glasses have a mixture of Q structures (Q^4, Q^3 and Q^2), which was unlike melt-derived glasses which typically displayed a single Q^2 structure. Hill *et al.* [141] suggested that, by taking the average of the total Q structures measured, if the average Q value was too high (> 2.4), the high network connectivity in the glass will inhibit the breaking of bonds and thus inhibit ion

exchange when introduced in physiological fluid. On the other hand, too low a Q value would lead to extremely rapid dissolution [140].

However, to base the dissolution of the sol-gel glass system wholly on the Q value model is insufficient. Heat treated sol-gel glasses have been found to still contain hydroxyl groups (OH) due to the aqueous synthesis of the sol-gel glass. These – OH groups form silinol (Si – OH) bonds in the silicate tetrahedral, reducing the network connectivity of the glass which leads to rapid dissolution of the glass. A recent study determined that even after heat treatment of 700 °C, there was still 0.38 – OH bonds per silicon atom, which suggest that the effects of the – OH group in glass dissolution rates are quite significant [7, 135].

Calcium oxide (CaO), the second component of the ternary glass in this study, provides Ca^{2+} ions which are crucial for osteogenesis [42]. At the atomic structural level, the calcium introduced into the glass acts as a network modifier, forming non-bridging oxygen bonds (Si – O – Ca). This diffusion of Ca^{2+} ions occurs at temperatures between 400 °C and 560 °C [135, 142]. The incorporation of Ca^{2+} ions in the glass reduces network connectivity, causing an increase in dissolution. Li *et al.* [8] found that with a compositional range of 1 – 45 mol % CaO, an increase in CaO in sol-gel glasses led to an increase in HCA formation, attributed to lower network connectivity of the glass, which promoted its dissolution rate.

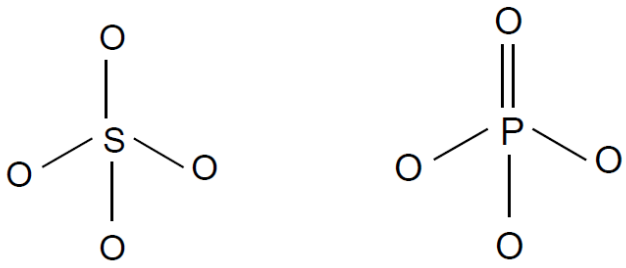

Figure 2. 9: The SiO_4 tetrahedral and the phosphate tetrahedral with the terminal double bond [121].

The third component, phosphorus pentoxide (P_2O_5), is also a network former. With an affinity to oxygen, phosphorus (PO_4) forms a tetrahedral, which link together with many tetrahedrons to form a phosphate 3D network. However, the difference between

a silicate glass network and a phosphate glass network is that the building blocks (SiO_4 tetrahedral units) are able to share all four oxygen atoms whilst phosphorus (PO_4) is unable to share all four oxygen atoms, whereby the unshared oxygen atoms between phosphate tetrahedrons form terminal double bonds [121]. This terminal end of oxygen reduces the connectivity of the phosphate glass network, hence increase the dissolution of the glass in aqueous environments [121, 143].

In the ternary system of bioactive glass, the P_2O_5 is found in the form of orthophosphate, and does not form any bonds with the silicate network [144, 145]. Even after heat stabilisation treatment, the phosphorus is found to be a separate entity from the silicate network. Thus, when the glass is exposed to a physiological environment, the phosphate is lost rapidly [136]. However, the isolated P_2O_5 component of ternary glass has been found to be instrumental in the formation of HCA [121, 146]. NMR studies have demonstrated that the introduction of P_2O_5 in the glass network led to the formation of amorphous calcium phosphate (ACP), isolated from the network and consequently acted as nucleation sites for HCA formation [9, 15, 147].

2.5.5 The sol

Across the different stages of sol-gel bioactive glass synthesis (Figure 2. 7), various factors, such as sol composition and pH levels, drying and heat treatment temperatures can affect the rate of reaction, the textural and structural properties of the final glass product [125, 148]. Changes in sol composition have been found to affect the final specific surface area (SSA), pore size and pore volume of the bioactive glass nanoparticles. Studies have shown that the introduction of calcium and phosphorus into the glass system decreases the nanoparticle SSA and pore volume [15, 149, 150]. The effects of compositional changes on pore diameters remain unclear with researchers reporting that an increase in calcium led to higher pore volumes and wider pore diameters, while other reports suggest a decrease in both pore diameter and volume [8, 15, 134, 150]. Table 2. 5 summarises the compositional effects on ternary glass nanoparticle morphology, without the influence of surfactants or structure-directing agents.

The process of hydrolysis occurs through the replacement of the alkoxide group in silinol with the hydroxyl group in water. However, the rate at which this process takes place is highly dependent on the pH levels, with increasing rates of hydrolysis away from pH 7 [138]. The sol, which has been homogenously mixed with all the precursors, is typically required to age for a period of 3 – 14 days for gelation to occur [8]. During this period, nanoparticles are formed from the polymerisation of the monomers in the sol. The particles grow throughout this process, linking together into chains and subsequently a network is formed throughout the sol resulting in gelation.

To accelerate this process, an acidic or basic catalyst, such as nitric acid is added to the reaction [8]. However, differences in polymer formation and growth using acid or base catalyst were observed by Brinker *et al.* [125]. Briefly, it was observed that linearly branched polymers were formed when acid was used, while, clustered or highly branched polymers formed under alkali conditions. Figure 2. 10 illustrate the differences between the two systems.

In 1968, Stober *et al.* [151] derived monodispersed silica particles by means of acid hydrolysis of TEOS and condensation via alcoholic solutions. This method, known as the Stober method, successfully synthesised spherical particles ranging from 50 nm – 2000 nm in diameter. Basified water was used as a morphological catalyst; without it, the silica colloid was found to agglomerate into heterogeneous shaped and sized particles. More recently, a faster alkali-mediated method of producing sol-gel bioactive glass has also been reported, wherein gelation time of the sol could be reduced to 2 min by the addition of ammonia hydroxide [152].

Table 2. 5: The effects of composition on bioactive glass nanoparticle morphology.

Glass composition (mol %)	Surface area (m^2/g)	Pore diameter (nm)	Pore volume (cm^3/g)	Ref.
80% SiO_2 – 15% CaO – 5% P_2O_5	127	4.4	0.13	[150]
60% SiO_2 – 35% CaO – 5% P_2O_5	79	12	0.25	
100% SiO_2	384	4.9	0.4	
80% SiO_2 – 15% CaO – 5% P_2O_5	351	4.8	0.36	[153]
70% SiO_2 – 25% CaO – 5% P_2O_5	303	4.8	0.33	

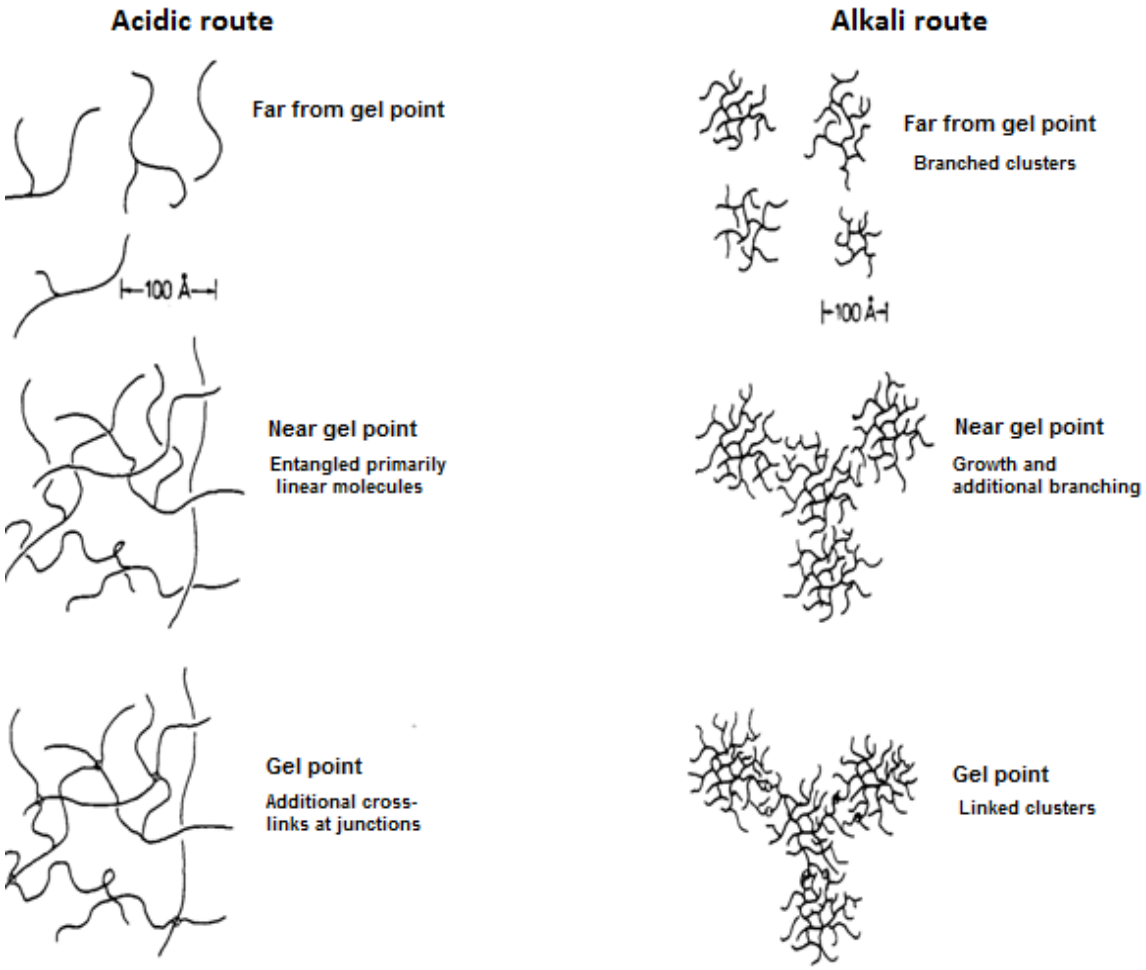

Figure 2. 10: The progression of polymer growth of hydrolysed TEOS either via acid or base catalyst [154].

Furthermore, Hong *et al*. [155] demonstrated the synthesis of extremely fine bioactive glass nanoparticles (< 80 nm in diameter) from a two step sol-gel and co-precipitation route in which the sol containing TEOS and calcium nitrate was slowly dripped into ammoniated water containing ammonium dibasic phosphate. The bioactive glass nanoparticles obtained from this were found to be homogenously spherical. Although this method was reminiscent of the Stober method, the results demonstrated that bioactive glass of the ternary system could be synthesised by this route. However, the effects of employing this synthesis route on the textural, structural and bioactive properties of the bioactive glasses were not characterised. Hence, an aim of this current study is to improve on the homogeneity of nanoparticle morphology and understand the nanostructure of nanoparticles derived from an alkali route.

2.5.6 Drying processes

A series of bioactive glass products from the sol-gel process can be obtained, as illustrated in Figure 2. 11. A dense bioactive glass film can be produced from the coating of the sol on a flat surface to initially form a porous dry gel (xerogel) film [154, 156]. Thin fibres of bioactive glass in the nanometre range can also be prepared by electrospinning the sol [48, 157]. Aerogels can be formed by carefully drying the block gel using supercritical CO_2, keeping the 3D network of the structure. Via freeze drying, pore liquor (by-products of the polycondensation reaction of the sol) within the gel can be sublimated without affecting the macrostructure of the block hydrogel, hence forming an aerogel [158]. From the description of the various routes employed to modify the end product of the sol-gel, it is obvious that drying forms an integral stage in bioactive glass processing, in which pore liquor is removed.

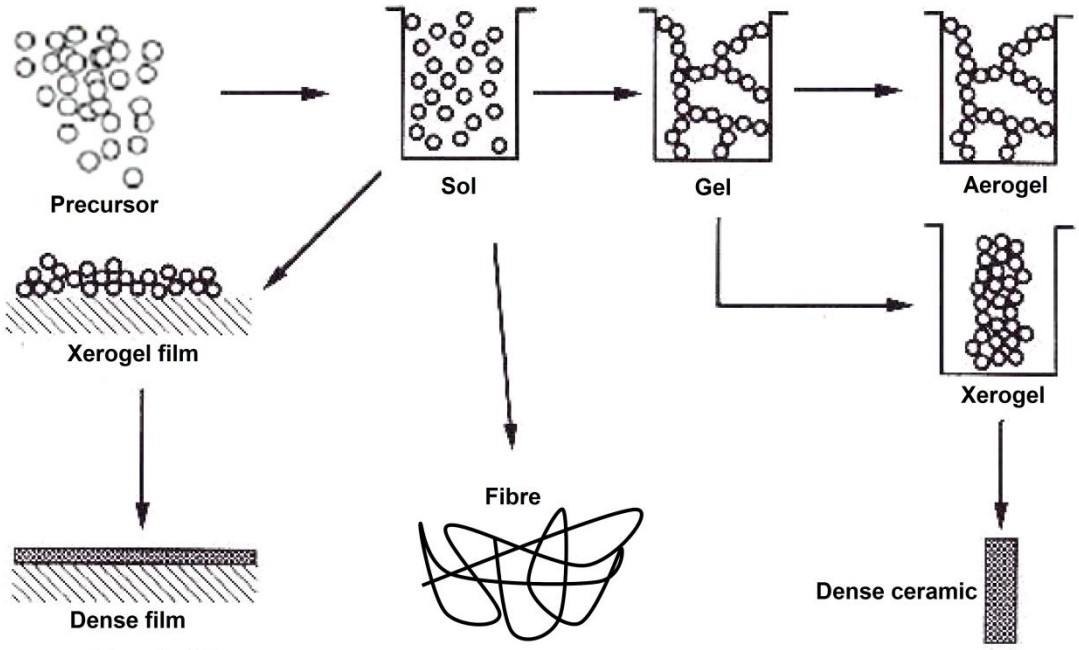

Figure 2. 11: Illustration of the various routes of processing the sol and gel [125].

The drying process has been carried out by evaporation at room temperature, heating in an oven or by lyophilisation [8, 10, 71, 131]. For the preparation of glass particles, Li *et al*. [8] employed oven drying, with temperatures of between 60 – 180 ºC to obtain bioactive glass powders with a wide range of surface areas (203 – 627 m^2/g), pore sizes (1.4 – 5.7 nm) and pore volumes (0.45 – 0.57 cm^3/g). Oven drying was also

used for the preparation of binary glass (70S30C: 70% SiO_2 – 30% CaO; mol %) and pure silica glass (S100), which demonstrated homogenous nanoparticle morphology, as shown in Table 2. 6 [135].

Zhong *et al*. [159] also studied a novel method of using a high humidity environment to dry ternary sol-gel bioactive gels (58S: 58% SiO_2 – 33% CaO – 9% P_2O_5 and 77S: 77% SiO_2 – 14% CaO – 9% P_2O_5). A drying oven, with a relative humidity maintained at 90 – 95%, was used to dry the gels over 3 days with a temperature of 180 ºC. Results showed that homogenous and stable glass powder was produced. Furthermore, a comparison between particles produced via ambient drying and high humidity drying revealed that high humidity drying led to an increase in pore diameter and pore volume of these particles, with a decrease in surface area (Table 2. 6). The increase in pore size and pore volume of these particles was attributed to the gradual evaporation of pore liquor, thus reducing the shrinkage and the collapse of the gel structure. The usage of freeze drying for the synthesis of bioactive glass particles was demonstrated by Hong *et al*. [155], however, the morphological properties of the glass were unclear.

Table 2. 6: The particle morphology of bioactive glasses processed using different drying routes.

Drying route	Glass type	Surface area (m^2/g)	Pore diameter (nm)	Pore volume (cm^3/g)	Ref.
Oven	S70C30	135	9	0.3	[135]
	100S	400	< 2	0.28	
Ambient	58S	289	3.4	0.49	[159]
	77S	431	3.0	0.32	
	100S	650	2.6	0.3	
High humidity	58S	151	13.2	0.45	[159]
	77S	389	4.0	0.41	
	100S	471	3.0	0.33	

2.5.7 Sintering regimes

The gel network is a mixture of silica colloidal particles surrounded by calcium and phosphate groups and pore liquor [135, 160]. After the drying process, the calcium is deposited on the surface of the silica nanoparticles. At this stage, the particles, with structural units either taking the form of chain-like clusters or discrete particles are described as secondary particles, with dimension of 5 – 8 nm [161, 162].

Studies have shown that a minimum temperature of 450 ºC is required for the fusion of calcium into the silicate network, while temperatures above 500 ºC is required to remove the organic phase, and a temperature of 600 ºC and above is required to eliminate any residual substances of nitrates and silanol groups [142, 163, 164]. However, above 800 ºC, the amorphous state of the glass would transition into a crystalline phase [165]. Lin *et al*. [166] have demonstrated that after heat treatment, the secondary particles would coalesce with one another from viscous flows caused by the sintering at high temperatures to form tertiary particles. Due to the random nature of viscous flow and particle fusion, nanoparticle shape, pore size and pore volume was suggested to be heterogeneous. This was in contrast with the findings of Saravanapavan and Hench [134], which pointed to some form of ordered nanoparticle morphology. The study demonstrated that tubular pores, taking the shape of 'inkbottles', were present within the nanoparticles. Throat sizes of the 'inkbottle'-shaped pores were found to be approximately 16.6 nm in diameter, with a cavity size of approximately 29 nm in diameter [134].

2.5.8 Bioactive glass nanoparticle morphology

Unlike the dense melt-derived bioactive glasses, one attractive feature of sol-gel bioactive glasses is its inherent porous structure [15, 134, 167, 168]. Characterisation of the nanoparticle textural features (nanoparticle shape, specific surface area, density and pore size, shape, volume) have been carried out using techniques such as transmission electron microscopy (TEM), nitrogen (N_2) sorption, mercury porosimetry and helium pyconometry [15, 134, 150]. TEM is used to provide visual results of the nanoparticles, while nitrogen sorption, mercury porosimetry and helium pyconometry techniques provide results of a quantitative nature. Helium pyconometry is a useful

technique for the characterisation of nanoparticle density and its porosity. Since these materials are porous, helium gas is able to penetrate into the porous structure, thus providing accurate measurements of the nanoparticles' true density. Additionally, the bulk density of the nanoparticle, which is the mass over the total volume (including the pores), can also be measured. Thus, the difference between bulk density and true density would give the nanoparticles porosity [169].

N_2 sorption and mercury porosimetry are useful techniques for the characterisation of nanoparticle specific surface area, pore size, pore volume and pore shape. In mercury porosimetry, mercury is used to penetrate particles, and data obtained from the differences in the intrusion and extrusion of mercury can be interpreted to determine nanoparticle morphology. One drawback of this technique is that, characterisation is limited to pores of sizes greater than 50 nm [170]. Therefore, N_2 sorption is the most appropriate technique for the characterisation of sol-gel bioactive glass nanoparticles, since characterisation of pore sizes can be carried out within the domains of 2 – 50 nm [169-171].

Although characterisation of the textural features of bioactive glass nanoparticles are widely carried out using N_2 sorption and mercury porosimetry techniques, visual verification by means of TEM is seldom reported. Lin *et al*. [135] studied the evolution of bioactive glass nanoparticles through different sintering temperatures using both N_2 sorption and TEM. Their TEM results were successfully verified through N_2 sorption measurements, and hence suggested that both methods are essential for nanoparticle characterisation. Suteewong *et al*. [172] similarly showed the verification of N_2 sorption measurements with TEM. A correlation was drawn between the isotherms from N_2 sorption and TEM, in which hexagonal and cubic pore structures were observed within pure silica mesoporous nanoparticles.

2.5.9 Application of mesoporous bioactive glass nanoparticles

The interesting textural features of sol-gel bioactive glasses have led to further exploration on various possibilities in bringing together multifunctional mesoporous bioactive glasses, which are able to induce a bioactive response and act as reservoir carriers of drugs for controlled delivery [15, 173]. The benefits of mesoporous

nanoparticles was noticed two decades ago in the form of a silica-based mesoporous nanoparticle (MCM-41) [12], which have led to a surge in the discovery for novel synthesis methods and application. Currently, the benefits of these mesoporous nanoparticles include application as catalysis, carrier-delivery systems, filtration and sensing [12-16].

The use of mesoporous nanoparticles as vehicles to store and deliver desired cargo, such as drug molecules, antibacterial agents and imaging sensors for biomedical applications on a nanoscale has been documented [13, 14, 174-176]. Largely this work has been carried out on silica nanoparticles, with few studies focused on bioactive glasses. The loading of mesoporous silica nanoparticles with cargo of various sizes and properties, have been carried out using the impregnation method, whereby, the to-be-loaded nanoparticles are immersed in solutions containing the desired loading material [168]. The efficiency of loading is typically dependent on the morphology of the silica nanoparticle (surface area, pore volume and pore size) but also its chemical properties [15]. Higher surface areas will allow for more attachment sites for the intended loading cargo, while increased pore volumes will permit higher amounts of cargo to be stored within the mesoporous structure [15, 173]. More interestingly, pore size also highly influences the efficiency of the load, acting as a 'gatekeeper' [173, 177]. Depending on cargo size, these pores can effectively filter out molecules which are larger than the pore size, allowing only the size-selected molecules to impregnate. Menaa *et al*. [178] effectively showed the selective loading of apomyoglobin with a size of 4.1 nm on mesoporous bioactive glass with pore sizes of 4 – 5 nm while albumin (8.5 – 11 nm) was not loaded due to its larger size.

As mentioned, the chemical properties of the nanoparticles also affect its loading capabilities. Silica-based bioactive glasses contain negative charges from the free SiO^- on its surface and also contain the –OH functional group from silinol (SiOH) [177]. The effective loading is thus affected by the interaction between the chemical properties of these nanoparticles and its host cargo. Through electrostatic interactions, polyethylenimine (PEI) can be electrostatically attached to negatively charged MCM-41 silica nanoparticles for CO_2 capturing applications, or to provide binding sites for nucleic acid [177, 179]. Covalent bonding is also used to bind the cargo onto the

surfaces of the nanoparticles. The organic functional group –OH, in the form of SiOH can be readily modified via functionalisation to allow for the attachment of cargo with various organic functional groups [14, 15, 173, 176]. For instance, the loading of drug molecules onto mesoporous bioactive glass nanoparticles was demonstrated by Lopez-Noriega *et al*. [167] through the functionalisation of its surfaces to incorporate a hydrophobic drug, Ipriflavone, which is used to reduce the rate of bone resorption. Similar to silica mesoporous nanoparticles, the silica-based bioactive glass nanoparticle also permit functionalisation through covalent anchoring between the silinol groups and the organic functions, allowing for the loading and controlled release of different drugs [15].

In the biomedical field, the use of mesoporous bioactive glass nanoparticles has suggested various improvements in terms of its *in vitro* bioactive responses. Additionally, the desirability of these mesoporous nanoparticles are due to their nanoscale size, allowing the nanoparticles to be efficiently internalised by plant and animal cells [14]. Using an evaporation-induced self-assembly (EISA) process, Yan *et al*. [180, 181] used a non-ionic block copolymer surfactant to structurally direct the mesopores within the nanostructure of bioactive glass, successfully synthesising a range of ternary glasses with a compositional range between 60 – 100 mol % of silica in the system, with highly ordered cylindrical pores and controlled pore sizes of 5.0 – 5.6 nm. *In vitro* bioactivity studies demonstrated that glass with a composition of 85 mol % silica was the most bioactive, contrary to conventional sol-gel glasses, which was reported to be most bioactive around the region of 60 mol % silica. Since an increase in calcium within the glass system led to an increase in pore size and pore volume, without specific control of the mesoporous structure, the definition of the ideal bioactive region is questionable [8, 181].

Arcos *et al*. [182] further showed that the rate of hydroxy-carbonate apatite (HCA) formation between a highly ordered cylindrical mesoporous structure and disordered mesoporous bioactive glass nanoparticles significantly improved. Although the mesopore sizes were not specified, the results showed the formation of HCA on the ordered glass was detected after 16 h of immersion in SBF, while the disordered mesoporous glass required 5 days of immersion before HCA was detected [182].

Recently, ordered mesoporous glass nanoparticles were found to have a faster bioactive response than conventional sol-gel glasses, observed through the rapid formation of HCA crystals when reacted with SBF [15, 147]. Vallet-Regi *et al*. [15] discovered that mesoporous ternary bioactive glass with an ordered nanostructure consisting of three-dimensional bicontinuous cubes developed HCA layer only after 1 h of immersion in SBF. This rapid formation of HCA crystallites, claimed to be the fastest recorded thus far, was attributed to the intrinsic textural and structural features of the ordered mesopores, which encouraged ionic exchange with the surrounding medium through efficient mass transport and diffusion processes.

In summary, the ability to modify the textural and structural properties of these bioactive glass nanoparticles to allow for higher surface areas, larger pore volumes, with a narrow pore size distribution and ordered nanostructure is important in enhancing the benefits of mesoporous materials. Various strategies have also been employed to tailor these properties. However, there remain gaps in the literature regarding the control of ternary mesoporous bioactive glass nanoparticle morphology by processing under different composition and pH conditions for carrier-delivery applications [15, 180, 183]. Furthermore, it is difficult to determine the exact compositional combination of glass for the optimum bioactive response, although both the composition and morphology of these nanoparticles play an important role in its bioactivity responses [149, 150]. As such, further work is needed to verify the influence of both composition and morphology on *in vitro* bioactivity

Chapter 3

Experimental details

3.1 Overview

This chapter explains the experimental details involved in the synthesis of the materials used throughout this thesis, the fundamentals behind experimental techniques and the protocols involved. However, as the focus of each chapter is different, certain materials and methods employed specifically to that particular chapter will be described within that respective chapter.

Unless stated otherwise, all chemicals used throughout the synthesis of materials were purchased from Sigma-Aldrich, U.K. All experiments employed ultra-pure deionised water, obtained from a Purelab UHQ water polishing unit (UHQ-PS-MK3; Elga, U.K.) to ensure purity and consistency of the synthesised materials.

3.2 Bioactive glass synthesis

3.2.1 Sol preparation

The synthesis of bioactive glass nanoparticles followed the sequence of: sol preparation → drying → sintering. For the studies conducted in this thesis, the composition and the pH conditions of the sols were varied during its preparation. Bioactive glass nanoparticles from two routes were synthesised which were: I) sol-gel (acidic) route and II) multi-step (alkali) route.

The weight of precursors used for each composition was determined by iterating the weight of the precursor with its respective molar weight across the three different precursors used, to obtain the moles of each precursor for the desired glass composition. The mol % of the glass composition was subsequently converted to wt. %.

I) Sol-gel route

Four types of sol-gel bioactive glasses of the ternary system SiO_2 – CaO – P_2O_5 with different compositions were synthesised. Table 3. 1 lists the sample codes associated with each type of glass composition and summarises the amounts of precursors used in the synthesis. The sol-gel glasses were prepared according to the method as reported elsewhere with modification [121].

For a glass composition of 65% SiO_2 – 30% CaO – 5% P_2O_5 (wt. %), 23.53 g of tetraethyl orthosilicate (TEOS) was added to 60 mL of 0.1 M nitric acid and allowed to react under stirring. Then a series of reagents was added in the following sequence, allowing 60 min for each reagent to react completely: 1.82 g triethylphosphate (TEP) and 10.85 g calcium nitrate tetrahydrate ($Ca(NO_3)_2$). The resultant solution was kept in sealed plastic containers for 14 days at ambient temperature to allow gelation to occur [8].

Table 3. 1: Composition of sol-gel route derived bioactive glass with corresponding weight of each precursor.

Sample	Glass composition (wt. %)	Weight (g)		
		TEOS	**$Ca(NO_3)_2$**	**TEP**
BG35	35%SiO_2 – 60%CaO – 5%P_2O_5	12.54	21.46	1.82
BG50	50%SiO_2 – 45%CaO – 5%P_2O_5	18.38	16.56	1.82
BG65	65%SiO_2 – 30%CaO – 5%P_2O_5	23.53	10.85	1.82
BG80	80%SiO_2 – 15%CaO – 5%P_2O_5	29.00	5.43	1.82

II) Multi-step route

A multi-step bioactive glass of the ternary system SiO_2 – CaO – P_2O_5 was synthesised by modifying the methods described elsewhere [151, 165]. Table 3. 2 list the sample code associated with the type of glass composition and summarises the amounts of precursors used in the synthesis.

For the glass composition of 65% SiO_2-30% CaO-5% P_2O_5 (wt. %), briefly, 34.05 g of tetraethyl orthosilicate (TEOS) was added to 120 mL of ethanol and stirred. 0.1 M nitric acid was added to the solution to (pH 1.9) and stirred. Separately, 17.81 g of

calcium nitrate ($Ca(NO_3)_2$) was dissolved in 200 mL of deionized water and then mixed together with the TEOS solution. 1.66 g of ammonium dibasic phosphate ($(NH_4)_2HPO_4$) was dissolved in 3 L of deionized water, the pH was adjusted to pH 11 using ammonium hydroxide (NH_3 28% in H_2O). Using a peristaltic pump, the solution containing TEOS and calcium nitrate was slowly dripped into the ammonium dibasic phosphate solution and stirred vigorously. During this process, the pH value of the solution was maintained at pH 11 using ammonium hydroxide. The resultant mixture was aged for 48 h before drying.

Table 3. 2: Composition of multi-step route derived bioactive glass and weight of each precursor.

Sample	Glass composition (wt. %)	Weight (g)		
		TEOS	**$Ca(NO_3)_2$**	**$NH_4(PO_4)_2$**
nBG65	$65\%SiO_2 – 30\%CaO – 5\%P_2O_5$	34.05	17.81	1.66

3.2.2 Drying

Drying is an important stage in the processing of bioactive glass nanoparticles for the control of nanoparticle morphology (specific surface area, pore size, shape and volume). The bioactive glass nanoparticles obtained from both the sol-gel and multi-step routes were subjected to different drying processes (Route A, B and C respectively).

Route A – Oven drying is a common method of air drying the gels in an open container, accelerated by means of heating the materials in an oven [159]. In this study, both types of bioactive glasses were placed in a drying oven with a temperature maintained at 150 °C for 24 h.

Route B – Vacuum drying employed the concept of lowering the external pressure applied over the drying gels by creating a vacuum environment. The lowering of external pressure would create an equilibrium between the external pressure acting on the gel and the capillary pressure formed from the liquid within the pores, which would continuously pull the gel network inward during evaporation, allowing gradual evaporation of the samples. Samples were transferred into drying vessels, with the

open end covered with a perforated film. This ensured the contents did not spew out when the pressure was reduced. The drying vessels were then placed in a sealed chamber and subjected to a vacuum for 24 h.

Route C – Freeze drying removed the frozen solvents trapped within the bioactive glass products through sublimation, which is a process of converting the ice directly into vapour (solid to gas phase transition). Samples were placed into drying vessels, and frozen from room temperature to -25 °C at a freezing rate of 1 °C/min. Manufacturer guidelines suggested that the appropriate pressure for freeze drying should be set between 20 – 30% of the vapour pressure of ice [68]. For a temperature of -25 °C, the recommended pressure was between 95 – 142 mTorr. Hence, the samples were held at -25 °C for 6 h, to ensure the entire sample was at the setting temperature before lyophilisation was carried out in a freeze-dryer (VirTis wizard 2.0) at a pressure of 100 mTorr for 24 h.

3.2.3 Sintering

Sintering is the next stage in the processing of bioactive glass to ensure the incorporation of calcium into the silicate network and the removal of nitrate and other impurities [142]. Once the drying step was completed, the bioactive glass nanoparticles were removed from their respective environments and heat treated in inert alumina crucibles using an Elite-Eurotherm (2116/2416) oven. The products were heat treated to 150 °C, 400 °C, 500 °C and 680 °C using a holding time of 16 h, with a heating and cooling rate of 1 °C/min from room temperature.

3.3 Bioactive glass composition and crystal structure analysis

3.3.1 Scanning electron microscopy and energy-dispersive spectroscopy

A scanning electron microscope (SEM) was used to obtain a selected area of interest for energy-dispersive X-ray (EDX) analysis. An SEM obtains an image through the detection of secondary electrons which are emitted from the surface of the sample

having been excited by the primary electron beam. Detectors pick up the emitted secondary electrons from various positions and builds up an image.

For the EDX analysis carried out, each element within a selected area of interest can be associated with a characteristic X-ray. The energy level of this characteristic X-ray is determined by the atomic number of the element. During spectroscopy, the area of interest is excited with an accelerating voltage. The accelerating electrons generated bombard the specimen, resulting in the emission of an X-ray spectrum. The accelerating electrons which are incident upon the elements' electrons eject them from the inner shell, and are subsequently filled by electrons from the outer shell. The surplus energy created from the ejection and filling of electrons create the characteristic X-ray [184, 185]. The X-ray spectrum generated is then detected by the EDX detector.

The compositional elements of the nanoparticles produced were verified by a SEM (JEOL JSM-6301F field emission SEM) equipped with an energy-dispersive spectroscope (INCA X-sight Oxford Instruments) detector. All samples selected for analysis were adhered onto aluminium stubs and carbon coated (Gatan 681 high resolution ion beam coater). An accelerating voltage of 20 kV was selected based on 2.5 times the highest excitation energy of the material analysed. INCA energy software was used to identify and quantify the elements present in the specimen. The spectrum obtained was quantitatively analysed by measuring the peak intensities (peak area) of the characteristic X-ray. Details of peak deconvolution and area calculation is detailed in the manufacturer's operating guidelines [185].

To improve on the accuracy of the results (error $< \pm 2$ %), standardisation was carried out. Standard material with accurately known intensity and concentration (Micro Analysis Consultants Ltd.) were used to evaluate the concentration of elements in the unknown sample. Hydroxyapatite and wollastonite, with known concentration were used as controls to further ensure any error from the results obtained which had developed over time was corrected for. The quantitative results obtained were normalised and were obtained from at least an average of 5 measurements over different sample sites ($n = 5$).

3.3.2 X-ray diffraction

X-ray diffraction (XRD) works on the principle of the diffraction of a monochromatic X-ray beam of wavelength (λ) which is transmitted into a material at an angle (θ). Atoms within the material cause the beam to scatter, and re-radiate the beam at different directions. If the atoms are arranged in a symmetrical order (crystalline structure), the re-radiated beams from varying angles of incidence will scatter in similar directions and will constructively build up, resulting in diffraction peaks. The relationship between the spacing between diffracting planes and the angle of incidence is described by Bragg's Law in Equation 3.1 [186]. The crystallographic structure of the nanoparticles synthesised was measured by XRD, using an X-ray diffractometer (Bruker D4 Endeavor) with copper Kα radiation. 2θ values were varied between 5º and 80º with a step size of 0.05º and a count rate of 2 s/step.

$$d = \frac{n\,\lambda}{2sin\theta} \qquad \text{Equation 3.1}$$

where d is the distance between diffracting planes, n is an integer, λ is the wavelength of monochromatic X-ray and θ is the angle of incidence.

3.3.3 Transmission electron microscopy

A transmission electron microscope (TEM) was employed to study bioactive glass crystal structure and nanoparticle morphology. Within a TEM, the accelerating high voltage electron beam generated by the electron gun transmits the electrons through the specimen which is then focused onto a photographic plate through the aid of a series of condenser, objective and projector lenses. Once the image is formed on the photographic plate, a charge couple device (CCD) camera is used to obtain the image [187]. The high accelerating voltage used in TEM allows the beam to transmit through the samples; therefore, TEM images capture the projection of the object. High magnification characterisation of nanoparticle morphology was carried out using a TEM (JEOL 1010 TEM) at an accelerating voltage of 100 kV. The TEM specimens were prepared by suspending the nanoparticle powder in ethanol using a sonicator (Branson 250 Sonicator) before being collected on TEM copper grids for imaging.

The short-range structure of amorphous states and nanocrystalline states of the bioactive glass nanoparticles was characterised by high resolution transmission electron microscopy (HRTEM). HRTEM is in fact another mode of transmission electron microscopy, in which the interference between scattered and unscattered electron beam which passes through the sample is used. When the electron wave passes through a sample, the electrons interact with the atom columns, causing a phase shift in the wave-front. For crystalline materials, the interference from the phase shift leads to the formation of bright and dark stripes recorded by a CCD camera. These stripes are known as lattice fringes, in which the dark lines represent the atoms while the bright lines represent the projection of electrons between the atom columns [186, 188].

Samples were analysed by HRTEM (FEI Tecnai G2 F20) at 200kV. The micrographs obtained were processed through Image J (NIH, United States). The lattice fringe distance for crystalline phases were calculated using the fast Fourier transform (FT) algorithm in Image J, in which a FT diffraction pattern was created, and the distance measured between the bright dots [188, 189].

3.3.4 Fourier transform infrared spectroscopy

Fourier transform infrared spectroscopy (FTIR) is a technique which uses the principles that each molecular structure absorbs and transmits infrared radiation differently. Each different material is built from a unique combination of atoms. Hence, the spectrum, resulting from the different transmitted peaks (energy), as the infrared beam passes through a sample, is unique. These peaks correspond to the frequencies of vibration between the bonds of the atoms. Fourier transformation is then used to interpret the different transmitted frequencies [190].

A Fourier transform infrared spectroscope (FTIR; Perkin Elmer Spectrum 2 IR Spectroscope) equipped with an attenuated total reflectance (ATR) accessory was utilised to characterise the functional groups present in the materials. Samples selected for analysis were pressed against a diamond crystal using the pressure arm to ensure good contact between the diamond and the sample. A diamond crystal was selected for its high refractive index, allowing the generated infrared beam to internally reflect

the beam upwards into the sample and back into the detector. A beam penetration of a few microns as suggested by the manufacturer was suitable for the nanoparticle samples tested [190]. FTIR spectra were collected from an accumulation of 32 scan, with a wavelength resolution of 2 cm^{-1}, between the frequencies of 2000 cm^{-1} and 400 cm^{-1}.

3.4 Nitrogen sorption analysis

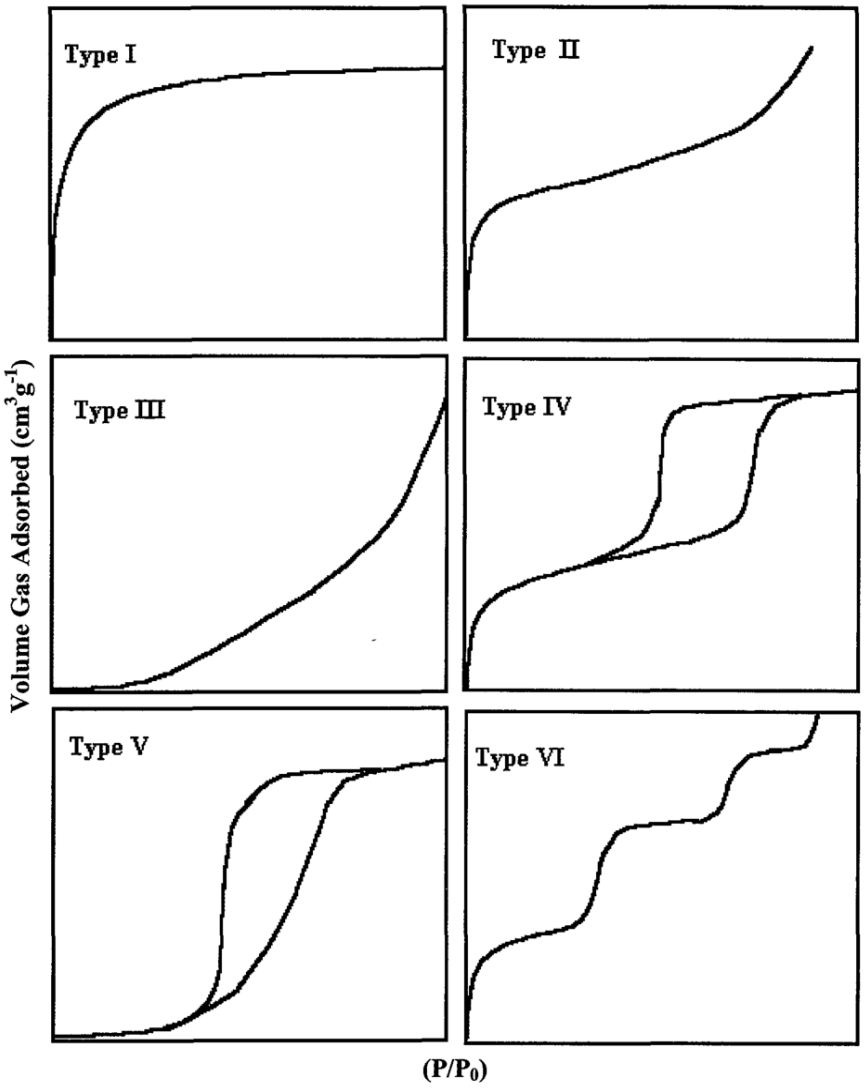

Figure 3. 1: Isotherm types according to the IUPAC report [191].

Quantitative measurements of the specific surface area (SSA) and pore morphology were carried out using the nitrogen (N_2) sorption technique. This technique analyses

the interaction between the adsorbent (bioactive glass nanoparticles) and adsorbate (N_2). As the N_2 is adsorb onto the surface of the adsorbent, a monolayer is formed which covers the surface of the samples. With further addition of N_2 and a gradual increase in pressure step-wise, multiple layers are formed. For porous materials, the N_2 begins to fill the pores. An isotherm can then be plotted as a function of equilibrium pressure (P) over saturation pressure (P_0); P/P_0 against the volume of adsorbate. The international union of pure and applied chemistry (IUPAC) describes six isotherms (Figure 3. 1), each reflecting a unique condition. Additionally, with porous structures, hysteresis appears as monolayer coverage of the nanoparticle surface progresses to multilayer coverage [169, 191]. Four hysteresis loops can be identified in this multilayer region of the sorption isotherm, shown in Figure 3. 2.

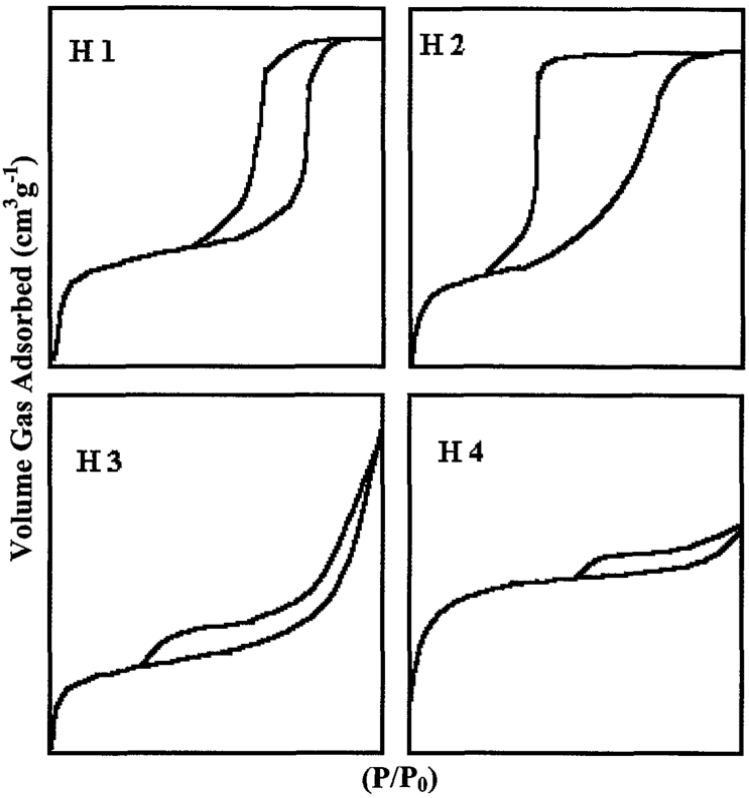

Figure 3. 2: Hysteresis loop types according to the IUPAC report [191].

The SSA of the nanoparticles was calculated using the Brunauer – Emmett – Teller (BET) theory. This theory uses the first part of the adsorption isotherm in the relative pressure region of $0.05 < P/P_0 < 0.35$ which corresponds to the monolayer formation, to predict the number of adsorbate molecules required to cover the adsorbent with a

monolayer of molecules [192]. Although, there exists no pressure at which the entire surface of the adsorbent can be covered by exactly one monolayer of molecules, the BET theory allows for the experimental determination of the number of molecules required to form a monolayer [169]. The BET equation is expressed in Equation 3.2.

$$\frac{1}{W\left[\left(\frac{P}{P0}\right)-1\right]} = \frac{1}{W_m C} + \frac{C-1}{W_m C}\left(\frac{P}{P_0}\right) \qquad \text{Equation 3.2}$$

where W is the weight adsorbed; W_m is the weight adsorbed in a monolayer and C is the BET constant.

To obtain the total surface area (S_t) of the nanoparticles can be calculated using Equation 3.3.

$$S_t = \frac{W_m N_a A}{M_a} \qquad \text{Equation 3.3}$$

where N_a is Avogadro constant; A the cross-sectional area of each nitrogen molecule; M_a molecular weight of the adsorbate.

Pore size and volume distribution measurements were carried out using the Barrett – Joyner – Halenda (BJH) analysis based on the Kelvin equation which relates the equilibrium vapour pressure of a liquid in a curved surface area to the equilibrium vapour pressure of the liquid on a plane surface [193].

$$ln\frac{P}{p_0} = -\frac{2\Upsilon V_l}{rRT}cos\theta \qquad \text{Equation 3.4}$$

where P is the equilibrium vapour pressure of the adsorbate liquid in a narrow pore; p_0 is the equilibrium pressure of the adsorbate liquid exhibiting a plane surface; Υ is the surface tension; V_l is the molar volume of liquid adsorbate; r radius of droplet; R universal gas constant; T temperature and θ is the contact angle between the adsorbate liquid and the pore wall.

Pores on a porous adsorbent material are filled with liquid adsorbate at saturated pressure. Hence, total pore volume (V_p) can be calculated by measuring the volume of adsorbate at the pressure approaching saturation as shown in Equation 3.5 [169].

$$V_p = \frac{PV_S V_l}{RT} \qquad \text{Equation 3.5}$$

where P is the ambient pressure and V_s is the volume of adsorbate at pressure approaching saturation.

The assumption used in the calculation of Equation 3.6 is that no surface other than the inner walls of the pore exists. For the calculation of average pore diameter (r_p), it is assumed that the pores are of cylindrical geometry. However, in reality, different hysteresis loops have been associated with different pore shapes [191, 194]. By considering these two assumptions, r_p can be calculated from the ratio of total pore volume and the BET surface area.

$$\frac{V_p}{S_{BET}} = \frac{r_p}{2} \qquad \text{Equation 3.6}$$

where S_{BET} is the BET calculated surface area, and V_p nanoparticle total pore volume.

For N_2 sorption tests, samples of approximately 1 g were firstly weighed and filled into round base glass tubes for degassing. The tubes were placed onto a heating rack, to which nitrogen was introduced into the tubes over 24 h at a temperature of 150 °C to remove contaminants and moisture. Once degassed, the nanoparticle powder was reweighed and transferred into the analysis port where the adsorbate (N_2) was injected into the glass cells containing the samples (adsorbent) for analysis.

The SSA of the nanoparticles was measured by nitrogen sorption at 77 K (Micromeritics Tristar 3000) using the BET method, while pore size distribution and pore volume of the nanoparticles was determined using the BJH method. The SSA of the sample was then calculated by dividing S_t with the sample weight used in the

analysis. At least five adsorption points in the relative pressure (P/P_0) range of between 0.05 and 0.35 were used to obtain a BET plot. The gradient (m) and the intercept (C) of each linear BET plot was positive with a linear regression correlation coefficient (R^2) no less than 0.99991 [134, 191].

3.5 Ion-selective electrode detection

The ion-selective electrodes (ISE) setup consisted of 2 electrodes, the calcium ion-specific electrode and a reference electrode. The permeable membrane of the electrodes respond to the presence of ions in a solution, measuring the potential difference generated between the 2 electrodes which are attached to a voltmeter. This potential difference is then matched with the calibration curve to obtain the corresponding ionic concentration of the solution.

Calibration of the system was carried out using standard $CaCl_2$ solutions of 1, 10, 100 and 1000 ppm. A standard solution of 1000 ppm was made up by dissolving 2.7692 g of $CaCl_2$ into 1 L of deionised water. Subsequently a series of dilutions was carried out to obtain a further 3 standard solutions. A linear relationship (calibration curve) between the electrical potential developed by the ISE and standard solution concentration was obtained before measurements were taken. The calcium ion concentration released over time was tracked using calcium ion-selective electrodes (ELIT 1801) and measured by converting the potential difference recorded by the electrodes into concentration units (ppm or mg/L) using ion analysing software (Nico2000 ISE/pH Ion Analyser).

In Chapter 4, the dissolution of bioactive glass nanoparticles was monitored through Ca^{2+} concentration changes of the supernatant. Similarly, in Chapter 6, the ionic release of Ca^{2+} from loaded nanocarriers (BG0.5Ca and BG0.8Ca) was quantitatively tracked by ISE measurements. Nanoparticles were firstly weighed before being immersed in deionised water and incubated at 37 ºC. A working concentration of 0.03 g/mL bioactive glass nanoparticles or loaded nanocarriers to deionised water was incubated at 37 ºC over 1, 2, 24 h and 7, 14, 21 and 28 day time points.

3.6 *In vitro* accellular studies

The simulated body fluid (SBF) model proposed by Kokubo *et al*. [195] was used for bioactivity testing of materials. The preparation of SBF was tailored specifically to obtain the ionic concentrations listed in Table 3. 3 which closely resembled the ionic concentration of blood plasma.

For the preparation of 1000 mL SBF, firstly, a thoroughly cleaned polyethylene beaker was filled with 800 mL deionsed water and placed in a water bath set at a temperature of 36.5 °C. Next, the following chemicals were added one by one following the respective order of listing: 7.996 g of NaCl, 0.35 g of $NaHCO_3$, 0.224 g of KCl, 0.228 g of $K_2HPO_4 \cdot 3H_2O$, 0.305 g of $MgCl_2 \cdot 6H_2O$, 40 mL of 1M HCl, 0.278 g of $CaCl_2$, 0.071 g of Na_2SO_4 and 6.057 g of $(CH_2OH)_3CNH_2$. Each chemical was left to stir until completely dissolved before the subsequent chemical was added. The pH of the solution was carefully monitored during the addition of $(CH_2OH)_3CNH_2$ to ensure the pH did not go beyond pH 7.5. The pH of the final solution at 36.5 °C was adjusted to pH 7.45 using 1M HCl. Once completed, the solution was made up to 1000 mL with deionised water and cooled to room temperature before being stored in a refrigerator.

Table 3. 3: Ionic composition of SBF compared to human blood plasma [7].

Ion	Concentration (mmol/L)	
	Simulated body fluid (SBF)	Human blood plasma
Na^+	142.0	142.0
K^+	5.0	5.0
Mg^{2+}	1.5	1.5
Ca^{2+}	2.5	2.5
Cl^-	147.8	103.0
HCO_3^-	4.2	27.0
HPO_4^{2-}	1.0	1.0
SO_4^{2-}	0.5	0.5

The bioactive response of the nanoparticles was tested by immersion in SBF with a final nanoparticle to SBF concentration of 0.1 mg/mL. The nanoparticles were incubated at 37 °C, monitored at 2 h intervals up to 12 h, and then at 24 h, 48 h and 96 h time points. After each time point, the reacted nanoparticles were removed, rinsed in

deionised water and dried in an air circulation drying oven. Changes in chemical composition of the nanoparticles pre and post immersion were analysed by EDX. SEM (Hitachi S-3400N) and FTIR were employed to examine surface changes.

For the testing of composite scaffolds, equally sized cylindrical scaffolds of 7.0 ± 0.5 mm radius and 5.5 ± 0.5 mm in height with a surface to SBF volume ratio of 0.04 were incubated at 37 ºC over a period of 1, 3, 7 and 14 days. After each time point, the samples were removed, gently rinsed in deionised water and freeze dried. Changes in surface structure of the scaffolds after immersion in SBF were characterised by SEM and Fourier transform infrared spectroscopy (FTIR).

3.7 *In vitro* cellular studies

3.7.1 Cell culture

Primary human osteoblast bone (HOB) cells model was used to evaluate the biological responses to the nanoparticles and scaffolds synthesised in this thesis. HOB cells, obtained by a method previously described [196] were cultured in 25 cm^2 sterile tissue culture flasks at 37 °C in a humidified air atmosphere of 5% CO_2. The culture medium used was Dulbecco's modified Eagle medium (DMEM), supplemented with 10% fetal calf serum (FCS), L-ascorbic acid (150 g/mL), L-glutamine (2 mM), penicillin and streptomycin (100 units/mL).

Once confluent, the HOB cells were collected by trypsinising adherent cells. Culture media was removed from the flask and the cells rinsed with PBS to completely remove any residue serum which would prevent the effects of trypsin on the cells. Once rinsed, trypsin is added to dislodge the cells from the flask. The cell suspension was then centrifuged and the pellet resuspended in fresh DMEM. Cell viability was assessed using the Trypan blue exclusion test. The cell concentration was measured using a cell counter (Biorad TC10 Automated Cell Counter). From the live cell count concentration obtained, the original cell suspension was then diluted by adding appropriate amounts of DMEM to the required cell concentration of 4×10^4 cells/mL.

Prior to seeding, the scaffolds were sterilised by ultraviolet light exposure for 5 h. Afterwards, the scaffolds were conditioned in Dulbecco's modified Eagle medium (DMEM) for 24 h before seeding. The scaffolds were then placed individually into 24-well culture plates and 1 mL of HOB cells in DMEM (4×10^4 cells/mL) was seeded onto each well. The plates were then incubated at 37 ºC in a humidified air atmosphere of 5% CO_2 for a period of 1, 4 and 7 days. Two-photon confocal and SEM microscopy were used to observe cell morphology on the seeded scaffolds.

3.7.2 Cell morphology characterisation

Two-photon confocal was used to observe cell morphology on the seeded scaffolds in Chapter 6. Prior to imaging, scaffolds were rinsed in phosphate buffer solution (PBS) to remove residual DMEM and then stained using Cy3 Cyanine nucleic acid dye. Stained samples were then placed onto glass slides and scanned using a two-photon confocal microscope (Nikon Eclipse Ti), with a laser wavelength of 820 nm and a band pass filter range of 580 – 620 nm.

Samples selected for SEM imaging were fixed in a glutaraldehyde solution (2.5% in H_2O) for 24 h before Osmium tetroxide (OsO_4) was added. The osmium stained samples were then rinsed in 0.01 M PBS to remove residual OsO_4. Ethanol was then added at increasing purity of 30%, 50% and then 100% onto the samples to gradually remove all PBS. The prepared constructs were dehydrated in a CO_2 exchanger, gold coated (Gatan 681 high resolution ion beam coater) for 2 min at 80 mA before imaged using a field emission SEM (JEOL JSM-7401F) with a beam voltage range of 2 – 3 kV.

3.8 Ionic cross-linker preparation

3.8.1 Ionic cross-linker solutions

The source of divalent ions employed for nanocarrier impregnation and subsequent cross-linking experiments in Chapter 5 were from strontium chloride ($SrCl_2$), copper chloride ($CuCl_2$) and calcium chloride ($CaCl_2$). The properties of each chemical are

shown in Table 3. 4. The mass of solute for each chemical was calculated using Equation 3. 7.

$$m_s = \frac{M \times M_w \times v}{1000} \qquad \text{Equation 3.7}$$

where m_s is the mass of solute; $M$is the molar concentration; $M_w$is the molar weight; v the volume (mL) of solution prepared.

Table 3. 4: Properties of cross-linker chemicals.

Properties	**Chemicals**		
	$SrCl_2$	**$CuCl_2$**	**$CaCl_2$**
Colour	White	Brown	White
Molecular weight (g/mol)	266.6	268.9	110.9
Purity (%)	> 99	99	99

3.8.2 Physical properties of cross-linker solutions

The density, surface tension and viscosity of the cross-linker were evaluated. All measurements carried out with the cross-linker solutions were maintained at 20 ºC by immersion in a water bath. A digital thermometer was used to verify the temperature of the solutions. At least 3 repeated measurements were recorded and the average taken.

I) Density

Density is the mass of the substance per unit volume [197]. The density (ρ) of cross-linker solutions were determined by Equation 3.8.

$$\rho = \frac{M_{DI} + M_S}{V} \qquad \text{Equation 3.8}$$

where M_{DI} is the mass of deionised water for a given volume V, and M_S is the mass of solute for a given volume V.

II) Surface tension

Surface tension is a measure of the cohesive force between the liquid molecules on the surface [198]. The surface tension (γ) of cross-linker solutions were evaluated using the capillary rise method. The experimental setup was such that a small bore glass capillary tube was inserted into the cross-linker solution of which its surface tension was to be determined. The height to which the liquid rose was used to calculate the surface tension using Equation 3.9.

$$\gamma = \frac{dghr}{2} \qquad \text{Equation 3.9}$$

where d is the density of the cross-linker solution, g the gravitational acceleration (9.81 ms^{-2}), h the change in height within the capillary tube and r the inner radius of the capillary tube.

Before analysis, the r of the capillary tube was measured by using deionised water at 20 ºC, since the known surface tension of water at that temperature is 72.75×10^{-3} Nm^{-1} [199]. Measurements were recorded after allowing the inserted capillary tube to stand in the liquid for at least 10 min to ensure an equilibrium temperature was achieved

III) Viscosity

Viscosity is the measure of the liquid's resistance to flow from shear stress [198]. The viscosity of the cross-linker solutions were measured using a U-Tube Viscometer (BS/U Size A VWR Viscometer). The viscosity was determined using Equation 3.10.

$$\eta = k\rho t \qquad \text{Equation 3.10}$$

where k is the viscometer constant, ρ the density of the cross-linker solution to be examined and t the time taken for the fluid to flow between 2 predetermined points.

Prior to testing, the viscometer was cleaned using deionised water. The viscometer constant (k = 0.00643) was determined using deionised water at 20 ºC, given that the dynamic viscosity of water is 1002 µPa.s [200]. The viscometer was clamped

vertically with a retort stand, and immersed partially in a water bath, ensuring the water level was above the level of liquid to be tested. A syringe was used to fill the viscometer with the testing fluid and stabilised for 15 min in the water bath. A pipette filler was then used to raise the fluid up to the reservoir. The time taken for each cross-linker fluid of similar amounts to flow between two predetermined points on the viscometer was recorded using a stop watch [201].

3.9 Scaffold fabrication

3.9.1 Alginate and composite hydrogels preparation

Alginate sodium salt was used to produce composites studied in Chapters 5 and 6. Its properties are shown in Table 3. 5. A series of alginate solutions with concentrations of 2, 4 and 6 wt. % were prepared. Typically, for the preparation of 2 wt. % alginate solution, 2 g of alginate powder was weighed and dissolved in 98 mL of deionised water.

Table 3. 5: Specifications of the alginate used [202].

Parameter	Specification
Alginate source	Brown algae
Colour	Off white, brown
Solubility in water	100 mg/mL
Viscosity (2 wt. % solution at 25 °C)	100 – 300 cps

In Chapter 6, pure alginate (Alg) and alginate-bioactive glass composite (AlgBG) scaffolds were used as controls. Alg scaffolds were made of 2 wt. % alginate solution (100% organic component) while AlgBG scaffolds were made of 2 wt. % alginate solution and 3 wt. % bioactive glass nanoparticles (BG65), therefore having a glass to alginate (G/A) ratio of 60:40). Both scaffolds were synthesised by external diffusion using the ionic cross-linker calcium chloride ($CaCl_2$) [90]. Firstly, 2 mL of slurry was poured into a mould (mould size: 15.5 mm diameter, 40 mm height) and cross-linked with 0.045 M $CaCl_2$. Then the gels were left to cure for 24 h before removal from moulds for subsequent testing. Based on preliminary studies in which $CaCl_2$ cross-

linkers with molarities of 0.015, 0.03, 0.045 and 0.09 M were used for the development of alginate composite scaffolds, it was found that 0.045 M cross-linked scaffolds were most homogenous [203]. Therefore, scaffolds synthesised by external cross-linking (Alg and AlgBG) were cross-linked using 0.045 M $CaCl_2$. The mass of the required reagent (mass of solute) to produce the specific molar concentration required was calculated using Equation 3.7.

3.9.2 Freeze drying of hydrogels

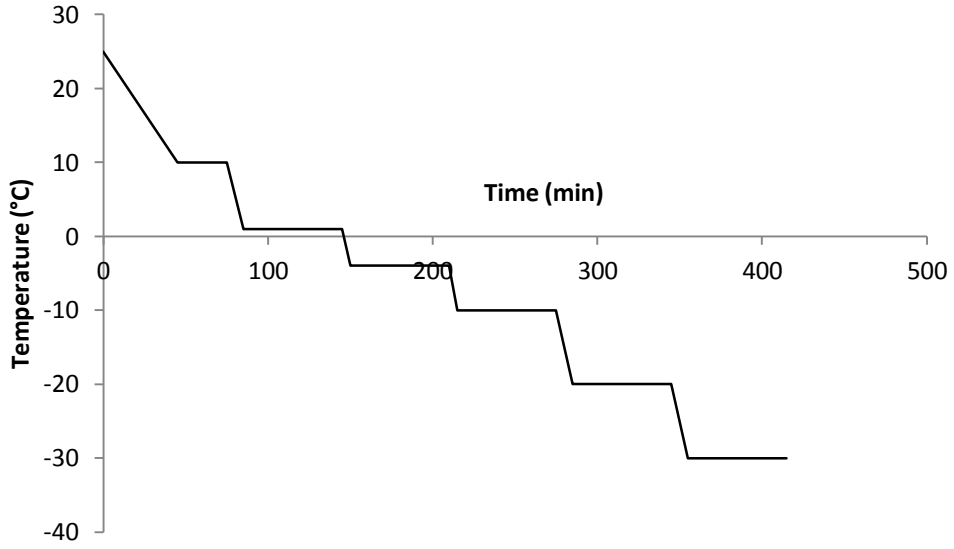

Figure 3. 3: Freezing regime used to freeze the scaffolds prior to drying.

Scaffolds were fabricated by freeze drying the synthesised hydrogels. The hydrogels were firstly frozen to a temperature of -25 °C under a controlled and gradual freezing rate of 1 °C/min with holding times in between each 'ramping' stage, to ensure the entire sample was at the setting temperature, as shown in Figure 3. 3. As previously discussed in the literature, a gradual freezing regime had been reported to produce a controlled and uniform ice crystal formation, leading to the formation of homogenous pores within the scaffold [19]. Hence, this freezing regime was selected to ensure all scaffolds were dried under controlled conditions. Once frozen, samples were freeze dried at a pressure of 100 mTorr for 24 h.

3.10 Scaffold microstructure analysis

The homogeneity of material distributed within the cylindrical scaffolds produced was determined using dry to wet weight ratios [47]. This method was used to measure the consistency of material throughout different sections of the scaffold, by evaluating the loss of water from each section before and after drying. Changes in the dry to wet weight ratio between sections of the scaffold would suggest that material distribution was not uniform.

The as-prepared scaffolds were sectioned perpendicular to the cylindrical axis into 3 disks of equal thickness. The wet weights of each disk were measured before dehydration by freeze drying (Section 3.9.2). After drying, the disks were weighed again, and the dry to wet weight ratios were calculated. At least 3 repeated measurements were recorded for each section and the averages and standard deviations reported ($n \geq 3$; ± SD). Additionally, the distribution of scaffold material of the synthesised cylindrical scaffolds was characterised using energy-dispersive X-ray (EDX). For EDX analysis, the elemental concentration of BGX within each disk was measured ($n = 5$; ± SD).

The surface morphology of the cylindrical scaffolds was studied with the aid of a scanning electron microscope (Hitachi S-3400N SEM) with a beam voltage of 20 kV. Samples were cut parallel to the cylindrical axis, and surfaces coated with gold (Gatan 681 high resolution ion beam coater) for 2 min at 80 mA. Furthermore, the micrographs were processed through Image J (NIH, United States). Pore diameters of each disk section were measured using the line function with a minimum of 50 measurements recorded ($n = 50$; ± SD).

3.11 Scaffold mechanical properties evaluation

3.11.1 Scaffold degradation

The *in vitro* degradation rate of scaffolds was monitored in phosphate buffer saline solution (PBS). PBS was prepared by dissolving one tablet of PBS (Sigma-Aldrich) in 200 mL of deionised water to obtain a final pH of 7.45 with a concentration of 0.01 M

phosphate buffer, 0.0027 M potassium chloride and 0.137 M sodium chloride. The *in vitro* degradation, $D\,(\%)$ of scaffolds was calculated using Equation 3.11.

Equally sized scaffolds of 7.0 ± 0.5 mm in radius and 5.5 ± 0.5 mm in height were incubated in PBS at 37 ºC for 10 h. At each hourly interval, the samples were removed, gently wiped with blotting paper and weighed. The pH of the PBS was also recorded at each time point.

$$D(\%) = \frac{W_a - W_b}{W_b} \times 100\% \qquad \text{Equation 3.11}$$

where W_a is weight after immersion and W_b is weight before immersion.

3.11.2 Scaffold structural integrity

Swelling, $S(\%)$ as a percentage change in volume was calculated using the Equation 3.12 and water absorption, $W(\%)$ as a percentage change in weight was calculate using the Equation 3.13. Scaffolds were immersed in deionised water at 37 ºC over 0, 7, 14 and 28 day time points. At each time point, samples were removed, gently wiped with a blotting paper and the dimensions measured using a vernier caliper. Additionally, the weight of the scaffolds was recorded using a high precision balance.

$$S(\%) = \frac{V_a - V_b}{V_b} \times 100\% \qquad \text{Equation 3.12}$$

where V_a is volume after immersion and V_b is volume before immersion.

$$W(\%) = \frac{W_a - W_b}{W_b} \times 100\% \qquad \text{Equation 3.13}$$

where W_a is weight after immersion and W_b is weight before immersion.

3.11.3 Compression test

For its application as scaffolds for tissue engineering, the synthesised composite scaffolds would be subjected to load-bearing situations. Since its in-service forces would largely be of a compressive nature, compression test was conducted to determine the stress and strain of all scaffolds [29]. Stress is defined as the instantaneous load applied to a specimen divided by its cross-sectional area while strain is the change in length of a specimen in the direction of the applied stress divided by its original length [117]. Using compression test, the sample is deformed along the direction of the applied stress, as such the output recorded will be the force applied against the change in sample length. From this, engineering stress and engineering strain can be calculated, which takes into account the geometrical changes of the sample during compression. This is because, as the sample is compressed, the cross-sectional area of the sample increases while contracting along the direction of the force, thus requiring a greater force to deform it.

Elastic deformation, which is the deformation of a material where stress and strain are proportional, was initially determined from a series of 5 repetitive deformation tests between 0.3 mm – 1 mm, in which the maximum distance the applied load could compress the scaffold without permanently deforming it was measured to be 0.5 mm. The Young's modulus or modulus of elasticity (E) of the scaffolds, which describes its stiffness, or resistance to elastic deformation was calculated from the ratio of stress to strain [117]. The Young's modulus was determined by subjecting the scaffolds to unconfined parallel plate compression over the first 0.5 mm of deformation (elastic deformation) using a mechanical tester (Hounsfield Materials Tester H5KS) equipped with a 100 N load cell. Test samples were subjected to compression at a rate of 1 mm/min, to minimise any strain-rate dependence.

3.11.4 Puncture test

Due to the elastic nature of the scaffolds, preliminary studies using parallel plate compression testing demonstrated that the determination at which point maximum compression strength had been achieved was arbitrary [203]. Therefore, a puncture test was used to determine the maximum shear stress (τ_{max}) of the scaffolds [204].

Shear stress is a measure of the force applied parallel to the surface of a material [117]. This method provided an absolute value (maximum force) which could be applied to the scaffold prior to failure. τ_{max} was calculated using Equation 3.14. Samples were placed on a sample holder and were punctured using a custom designed probe (Figure 3. 4) at a rate of 2 mm/min.

$$\tau_{max} = \frac{F}{A} \qquad \text{Equation 3.14}$$

where F is the maximum force applied to the scaffold and A is the cross-sectional area of the material sheared parallel to the applied force.

All samples selected for mechanical testing were cured for 24 h post cross-linking before removal from the moulds. For the as-prepared scaffolds, mechanical testing was carried out within 2 h of removal from moulds. Scaffolds were immersed in deionised water and incubated at 37 ºC for a period of 7, 14 and 28 days. The reaction solutions were refreshed every 7 days and changes in the scaffolds' Young's modulus (E) and maximum shear stress (τ_{max}) over time were determined. Prior to testing, the surface moisture of the sample was removed using blotting paper to avoid slippage during testing. The results represented the mean and standard deviations of at least three samples ($n \geq 3$; ± SD).

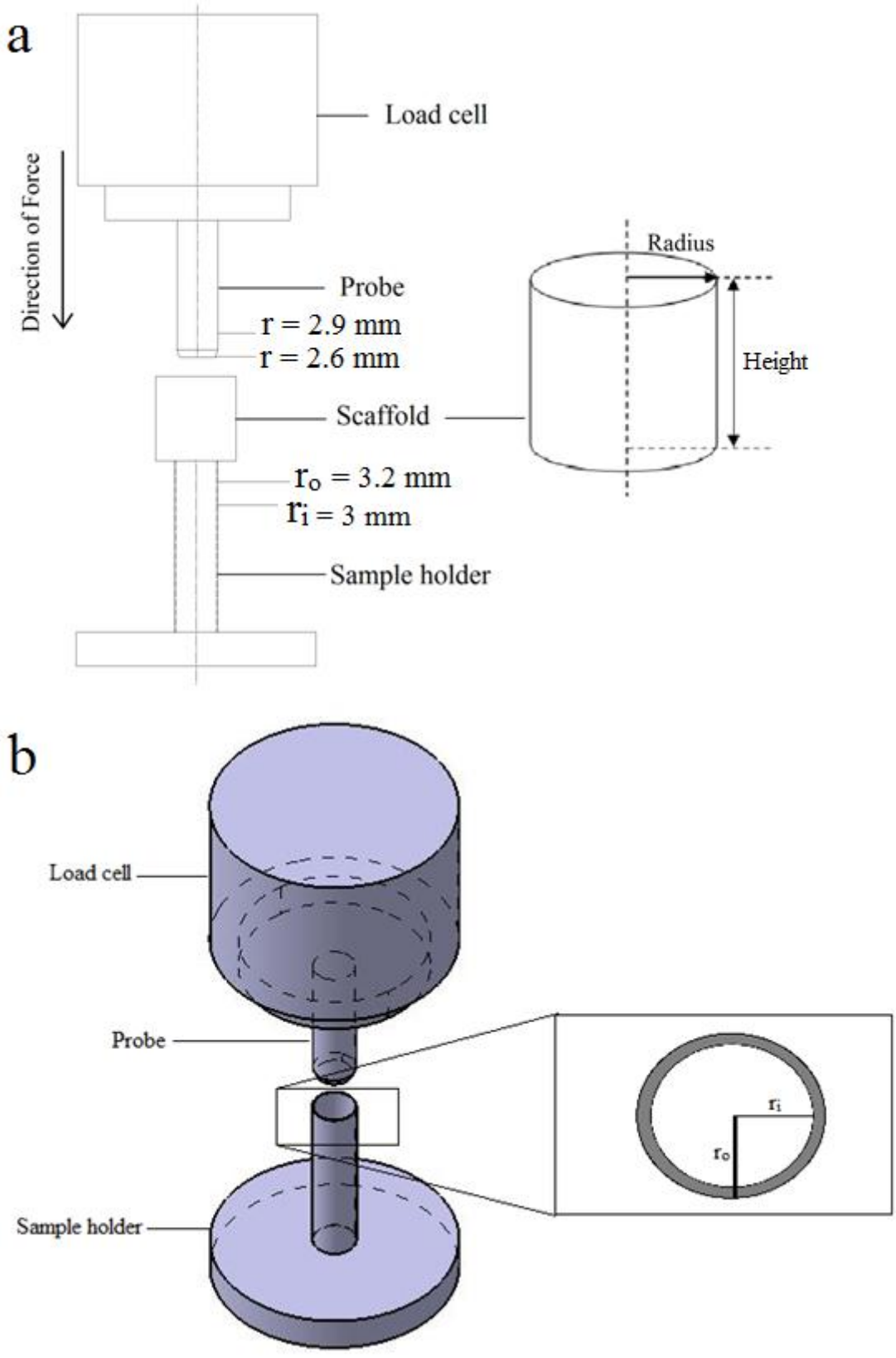

Figure 3. 4: Experimental setup of puncture test showing (a) the geometry of the probe and scaffold; (b) 3D representation of the setup and the inner radius (r_i) and outer radius (r_o) of the sample holder.

Chapter 4

Synthesis and characterisation of mesoporous bioactive glass nanoparticles

4.1 Introduction

Bioactive glass nanoparticles have been widely applied in the biomedical field. In particular, its mesoporous properties have been extensively researched on in areas extending from enhanced solubility and bioactivity, to multifunctional usage with antibacterial, protein and drug delivery capabilities [14, 15, 173, 176]. The synthesis of sol-gel bioactive glass nanoparticles follows the sequence of: sol mixing → ageing and drying → heat treatment [125]. At each stage, changes in experimental parameters, such as the composition and pH of the sol, drying methods and heat treatment temperatures could affect the final bioactive glass nanoparticle morphology.

Bioactive glass nanoparticle morphology, to include specific surface area (SSA), pore size, pore volume and pore shape of a nanoparticle, has been shown to be influenced by its composition. Specifically, glasses containing higher levels of silica had a larger SSA while glasses with higher calcium contents contained larger pores [180, 205, 206]. Additionally, changes in the pH conditions of the sol were found to affect the growth of the silicate network [138].

Furthermore, one important stage in sol-gel processing of bioactive glasses is the drying stage, where liquid (pore liquor) is removed from the gel upon condensation. This has been carried out by evaporation under ambient conditions [8], heating in a drying oven [159] or sublimation via freeze drying [10, 71]. Studies have shown that this drying stage is critical in establishing the final gel macrostructure, crucial for the production of porous scaffolds, films and membrane structures [140, 156, 159, 207]. However, identification of the effects of the drying stage on nanostructure are few and far in between [154]. For the processing of bioactive glass nanoparticles, grinding or milling bulk glasses into a fine powder is most commonly used [17]. Typically, this leads to a heterogeneous distribution of nanoparticle shape and sizes [134, 135].

Recently, some work has been carried out on the removal of pore liquor through freeze drying, producing a monodispersed powder and simultaneously eliminating the grinding step [155, 164]. Lastly, heat treatment has also been found to affect the pore size of the nanoparticles. Studies have shown that an increase in the maximum sintering temperature led to a reduction in pore size and caused densification of the nanoparticles [208].

Therefore, in this chapter, the effects of varying glass composition, pH conditions, drying procedures and heat treatment regimes on bioactive glass nanoparticle morphology were investigated. The aim of this chapter was to understand the morphological differences between nanoparticles of different silicon and calcium content. Bioactive glasses were also prepared from the sol-gel (acidic) route and the multi-step (alkali) route, to examine the effects of pH conditions on nanoparticle morphology. This was done by producing glasses of the same chemical composition. Concurrently, the control of nanoparticle morphological using sol-gel derived and multi-step derived bioactive glasses through different drying methods was investigated, to establish a protocol which reduced the processing time and effort in nanoparticle synthesis. Heat treatment regimes of the dried nanoparticles were also varied and changes to nanoparticle morphology evaluated. This study should provide a better understanding of how these changes fundamentally affect the final nanoparticle morphology, in order to provide a platform for further studies carried out in Chapters 5 and 6 of this thesis.

4.2 Nanoparticle synthesis

The effects of different glass composition on nanoparticle morphology were studied using bioactive glass nanoparticles of the ternary system SiO_2 – CaO – P_2O_5 with varying silicon and calcium content (BG35, BG50, BG65 and BG80), summarised in Table 4.1.

The effects of different pH (acid and alkali) processing conditions and different drying procedures (Route A, B and C) on nanoparticle morphology were studied through two types of bioactive glasses derived from the sol-gel route (BG65) and the multi-step

route (nBG65). Both types of glasses were of the ternary system 65% SiO_2 – 30% CaO – 5% P_2O_5 (wt. %). A summary of the drying parameters set for each drying procedure is provided in Table 4.2.

Additionally, the effects of different heat treatment regimes (maximum sintering temperatures) on nanoparticle morphology were studied using BG50 and BG65 bioactive glasses, subjected to different maximum sintering temperatures of 150 °C, 400 °C, 500 °C and 680 °C (Table 4.3). Details of the synthesis of these bioactive glasses were described in Section 3.2.

Table 4. 1: Sample code and corresponding composition of the various bioactive glasses.

Sample	Glass composition (wt. %)
BG35	35%SiO_2 – 60%CaO – 5%P_2O_5
BG50	50%SiO_2 – 45%CaO – 5%P_2O_5
BG65	65%SiO_2 – 30%CaO – 5%P_2O_5
BG80	80%SiO_2 – 15%CaO – 5%P_2O_5

Table 4. 2: Sample code, synthesis pH conditions and drying parameters set for the bioactive glasses.

Sample	pH conditions	Route	Description of method
BG65OD	Acidic	A	Oven dried at 150 °C for 24 h.
BG65VC	Acidic	B	Vacuum dried at ambient temperature for 24 h.
BG65FD	Acidic	C	Freeze dried at 100 mTorr at -25 °C for 24 h.
nBG65OD	Alkali	A	Oven dried at 150 °C for 24 h.
nBG65VC	Alkali	B	Vacuum dried at ambient temperature for 24 h.
nBG65FD	Alkali	C	Freeze dried at 100 mTorr at -25 °C for 24 h.

Table 4. 3: Sample code, corresponding composition and sintering temperature of the various bioactive glasses.

Sample	Glass composition (wt. %)	Sintering temperature (°C)
BG50 150°C	50%SiO_2 – 45%CaO – 5%P_2O_5	150
BG50 400°C	50%SiO_2 – 45%CaO – 5%P_2O_5	400
BG50 500°C	50%SiO_2 – 45%CaO – 5%P_2O_5	500
BG50 680°C	50%SiO_2 – 45%CaO – 5%P_2O_5	680
BG65 150°C	65%SiO_2 – 30%CaO – 5%P_2O_5	150
BG65 400°C	65%SiO_2 – 30%CaO – 5%P_2O_5	400
BG65 500°C	65%SiO_2 – 30%CaO – 5%P_2O_5	500
BG65 680°C	65%SiO_2 – 30%CaO – 5%P_2O_5	680

The composition of the different bioactive glasses were analysed by energy dispersive X-ray spectroscopy (EDX). Additionally, X-ray fluorescence (XRF; LSM Analytics, UK), a technique which identifies the characteristic energy (secondary X-ray) released by electron movement from a higher level to the lower level due to the ejection of electrons by X-rays, was used to confirm the composition of the nanoparticles. The functional groups of the different composition nanoparticles was analysed by Fourier transform infrared spectroscopy (FTIR), while the crystal structure was analysed by X-ray diffraction (XRD) and high resolution transmission electron microscopy (HRTEM) with fast Fourier transform (FT) analysis, according to the protocols described in Chapter 3.

Nitrogen (N_2) sorption techniques were used to obtain isotherms of the nanoparticles of interest. The specific surface area (SSA) of the nanoparticles was measured using the Brunauer – Emmett – Teller (BET) theory while pore size and pore volume distribution measurements were carried out using the Barrett – Joyner – Halenda (BJH) method. The nanoparticle structure was characterised using a transmission electron microscope (JEOL 1010 TEM) at an accelerating voltage of 100 kV.

4.3 Bioactive glasses of different composition

4.3.1 Compositional analysis

EDX analysis of the different silica and calcium content of the four compositions of ternary sol-gel derived glasses (BG35, BG50, BG65, BG80) is shown in Figure 4. 1. As expected, the increasing silica and decreasing calcium content shown from BG35 to BG80 is correspondent to the nominal compositions (Table 4. 1). Table 4. 4 summarises the XRF measured composition of each glass. It shows consistency in the composition of each glass, where a proportionate change was recorded for the compounds of SiO_2 and CaO, while P_2O_5 remained close to the designed 5 wt. % nominal composition. However, across each glass type, CaO recorded an approximate decrease of 7 wt. % from the intended nominal values.

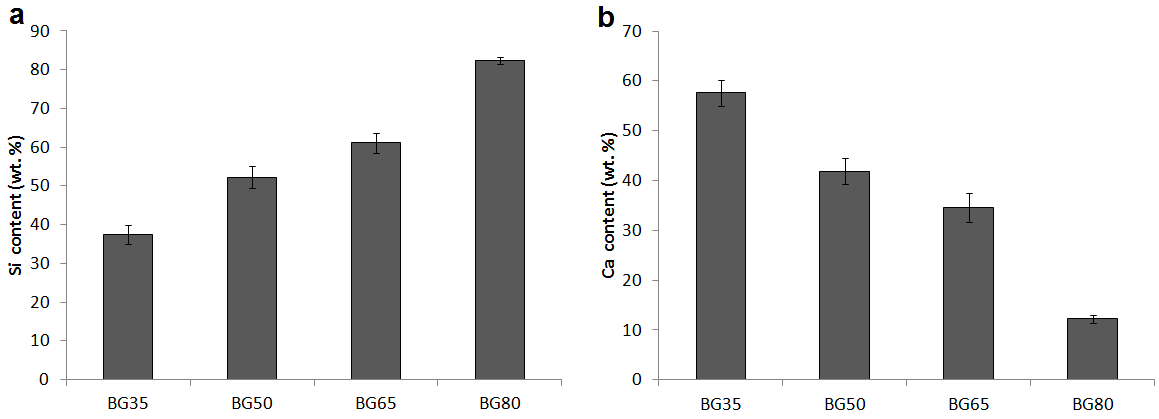

Figure 4. 1: The distribution of (a) silica content and (b) calcium content of the various bioactive glasses analysed using EDX. Data represents the mean ± SD, n = 5.

One explanation for this reduction could be due to the lost of calcium nitrate within the pore liquor which is the by-product of the gel condensation reaction. During the sol-gel process, calcium is not introduced into the silicate network until heat treatment is carried out, and thus remains largely within the pore liquor of the gel [131, 144, 159]. The decrease in CaO has also been observed in other studies, wherein variations of up to 25% were recorded [131]. This decrease in CaO content as compared to the theoretical value was attributed to the leaching of cations during the aging and drying stages [131, 158]. Although much care had been taken during the removal of the gel

from the moulds for heat treatment, some residue liquor could have been lost, resulting in the decrease of calcium.

Table 4. 4: XRF measurements of experimental nanoparticle compositions (wt. %)

Sample		SiO_2 (wt.%)	CaO (wt.%)	P_2O_5 (wt.%)
BG35	Nominal	35.00	60.00	5.00
	Experimental	33.60	53.66	5.56
BG50	Nominal	50.00	45.00	5.00
	Experimental	49.18	38.18	5.96
BG65	Nominal	65.00	30.00	5.00
	Experimental	63.56	23.42	5.28
BG80	Nominal	80.00	15.00	5.00
	Experimental	76.12	9.86	5.64

4.3.2 Functional groups within different bioactive glasses

The FTIR spectra of the four bioactive glasses with different composition are shown in Figure 4. 2. The silicate was found to be represented by a few bands; Si – O – Si stretching between 1040 cm^{-1} and 1200 cm^{-1}, Si – O – Ca stretching around 950 cm^{-1}, O – Si – O stretching at around 810 cm^{-1} and the Si – O – Si bending at 460 cm^{-1} [131, 134, 152, 159, 164, 189, 209, 210]. Further analysis of the broad band between 1040 cm^{-1} and 1200 cm^{-1} showed that as calcium content decreased, broadening of this band took place. Studies have shown that this broad band could be decovoluted into 5 separate bands, occurring at around 1040 cm^{-1}, 1080 cm^{-1}, 1100 cm^{-1}, 1160 cm^{-1} and 1200 cm^{-1}. Each of these bands corresponded to the asymmetric stretching of Si – O – Si, with 1080 cm^{-1} and 1200 cm^{-1} bands belonging to a cyclic or branched-like structure while 1040 cm^{-1}, 1100 cm^{-1} and 1160 cm^{-1} belonging to a linear structure [162, 210].

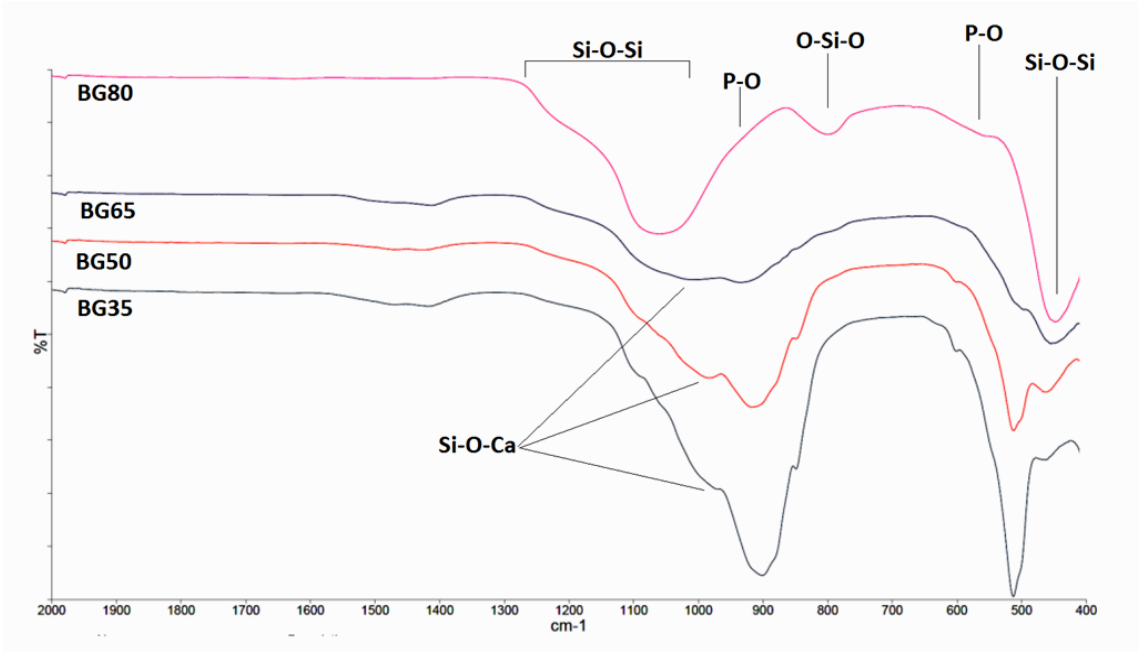

Figure 4. 2: FTIR spectra of ternary bioactive glasses with varying composition.

As discussed in the literature, the polymer formation of sol-gel derived silica-based glass can be synthesised into linear or branched-like polymer clusters depending on the pH conditions during synthesis [125]. Therefore, it is possible that, although all these glasses were derived under acidic conditions, both types of structures could be found. However, the band occurring at 1200 cm^{-1} was not profound in BG35, BG50 and BG65 spectra, pointing towards a more linear-structured silica-based glass, which was in agreement with the literature [125]. As silica content within the glass increased, these bands merged to form the broad band observed in the BG80 spectrum, indirectly confirming the high silica composition of BG80 bioactive glass.

Studies have suggested that for glasses with a low calcium content, there are high numbers of Si – O^{-1} species (Q^3) which hold the Ca^{2+} ions loosely. Only when the calcium content is high, the Ca^{2+} ions can be incorporated into the network, forming Si – O – Ca – Si – O [7, 131, 135]. Hence, the Si – O – Ca band which was observed present in all samples except BG80 could be explained by the decrease in calcium available to form bridging bonds with the Si – O^{-1} species. Furthermore, the presence of the O – Si – O band around 950 cm^{-1} in BG80, and less prominent in the other glasses corroborate with previous studies which showed a decrease in this band intensity as calcium content increased [8, 131]. The band at 470 cm^{-1}, which

corresponded to the bending mode of this group was present in all samples, with the intensity of the band increasing as silica content within the glass increased [131, 159].

Phosphate bands (P – O) were present in all samples at positions of 570 cm^{-1} and 960 cm^{-1}, corresponding to the υ_4 and υ_1 vibration of this group, respectively [152, 211]. Studies have shown that the υ_4 band can be separated into two discrete bands centred at 570 cm^{-1} and 600 cm^{-1}. However, due to the low concentration (5 wt. %) of phosphorous within the glass system, the presence of these bands were found to be low. The rather indistinguishable bands in the low calcium BG80 glass has been suggested to be due to the influence of the network modifier calcium, which is less in the BG80 sample, since the introduction of calcium promotes the isolation of orthophosphate [189].

4.3.3 Crystal structure

The effects of varying silica and calcium content on glass structure was analysed using XRD. The crystal structure of the bioactive glasses play a significant role in its degradation when introduced into a physiological environment, and hence might have an effect on the biological consequences, since bioactivity and biocompatibility of these glasses are reliant on the ionic release rates [164]. Figure 4. 3 shows the four spectra obtained from BG35, BG50, BG65 and BG80. Both BG35 and BG50, showed some form of crystalinity, with 2 peaks identified at $2\theta = 31.7^{o}$ and 32.1^{o}. This could be attributed the calcium-phosphate crystalline phase detected within the glass, since, BG35 and BG50 contained high levels of calcium [8, 131].

Separately, a broad band was observed between the 2θ angles of $20^{o} – 40^{o}$, with no noticeable diffraction maxima in the XRD patterns of BG65 and BG80, thus suggesting the amorphous nature of the bioactive glass samples. This broad band was more prominent in the BG80 pattern, characteristic of silica-based glasses due to incipient SiO_2 crystalline phases [8, 134, 142, 152, 206].

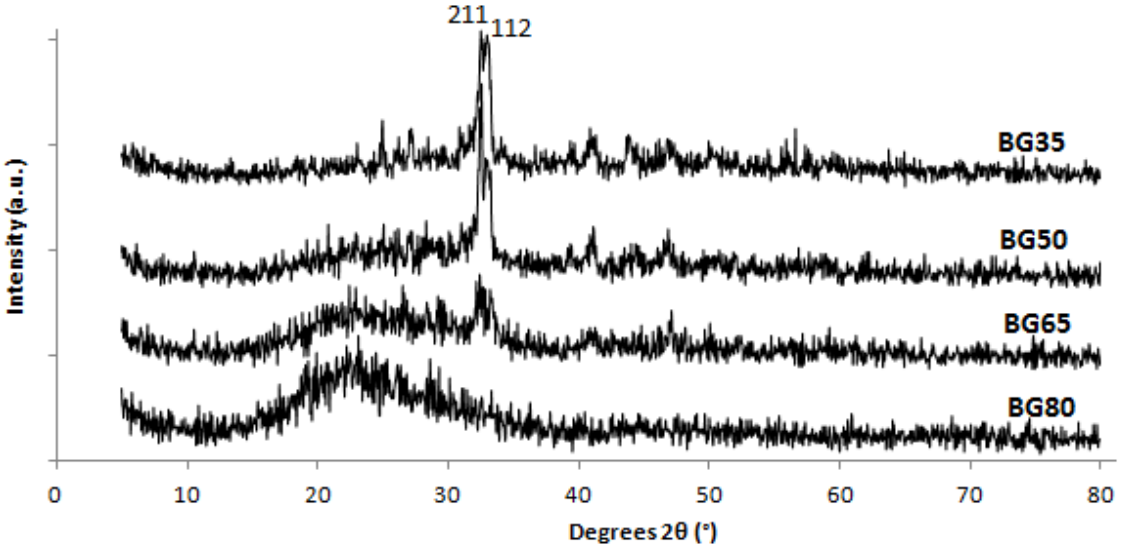

Figure 4. 3: XRD patterns of BG35, BG50, BG65 and BG80.

The results of XRD were further verified by HRTEM, with the lattice fringe spacing (d) measured using the Fourier transform (FT) patterns of the corresponding areas. Figure 4. 4 shows the HRTEM image of BG35 in which regions of highly ordered structures and regions with random arrangements were observed. The area of interest, a1 and a3 showed lattice fringes, corresponding to an ordered structure which consisted of a 2.8 Å lattice spacing. The different direction associated with the lattice fringes in a3, was deduced to be of the same crystalline material, since the diametric arrangement of the FT bright dots were equidistance (2.8 Å), and therefore correspond to repetitive frequencies [189]. The area of interest, a2 showed a disordered arrangement, thus suggesting the amorphous nature of this region [167, 180-182]. Similarly, the HRTEM image of BG50 (Figure 4. 5) also showed regions of amorphous disordered structures (area of interest a2) interjected with nanocrystallites (area of interest a1 and a3). The measured lattice fringe distance was found to be 2.8 Å and 2.9 Å respectively.

Figure 4. 6 shows the HRTEM image of BG65, which was largely dominated by amorphous regions. The area of interest a1, showed an area where some lattice fringes could be identified. The FT pattern of a1 showed a diametric arrangement of vague dots, each having a d-spacing of 0.27 nm. The other areas of interest (a2 and a3) showed no form of order, which was further evidenced by the FT patterns, which showed no observable dots [182]. Applying Bragg's Law (Equation 3.1) to the 2θ angles measured in XRD where the peaks of 2θ = 31.7º and 32.1º occurred, the lattice spacing (d) was calculated to be 2.8 Å and 2.7 Å respectively, thus in agreement with the distances measured from the FT patterns of the lattice fringes which were between 2.7 – 2.9 Å.

Using the standard card of hydroxyapatite (HA) (JCPDS 09-0432), wollastonite (JCPDS 43-1460) and cristobalite (JCPDS 39-01425), the d-spacing corresponding to peaks in HA were 2.8 Å and 2.78 Å, wollastonite were 3.09 Å and 2.78 Å, and cristobalite 2.84 Å respectively. Saravanapavan *et al.* [131] showed that for glasses containing a high calcium content (> 50 wt. %), wollastonite was the major crystalline phase, with traces of cristobalite. However, no mention of a calcium-phosphate phase was noted in that study, since the glasses studied were of the binary composition (SiO_2 – CaO). Nevertheless, in this study, ternary glasses containing phosphate was produced, confirming the trace amounts of HA detected within the glasses.

The results from XRD and HRTEM demonstrated that glasses which have higher amounts of calcium contained crystalline phases, consistent with previous studies. Based on the d-spacing measured, the presence of a calcium-silicate crystalline phase in the form of wollastonite with trace amounts of a calcium-phosphate (HA) crystalline phase and crystalline SiO_2 in the form of cristobalite can be found within the sol-gel glasses synthesised [131, 212, 213].

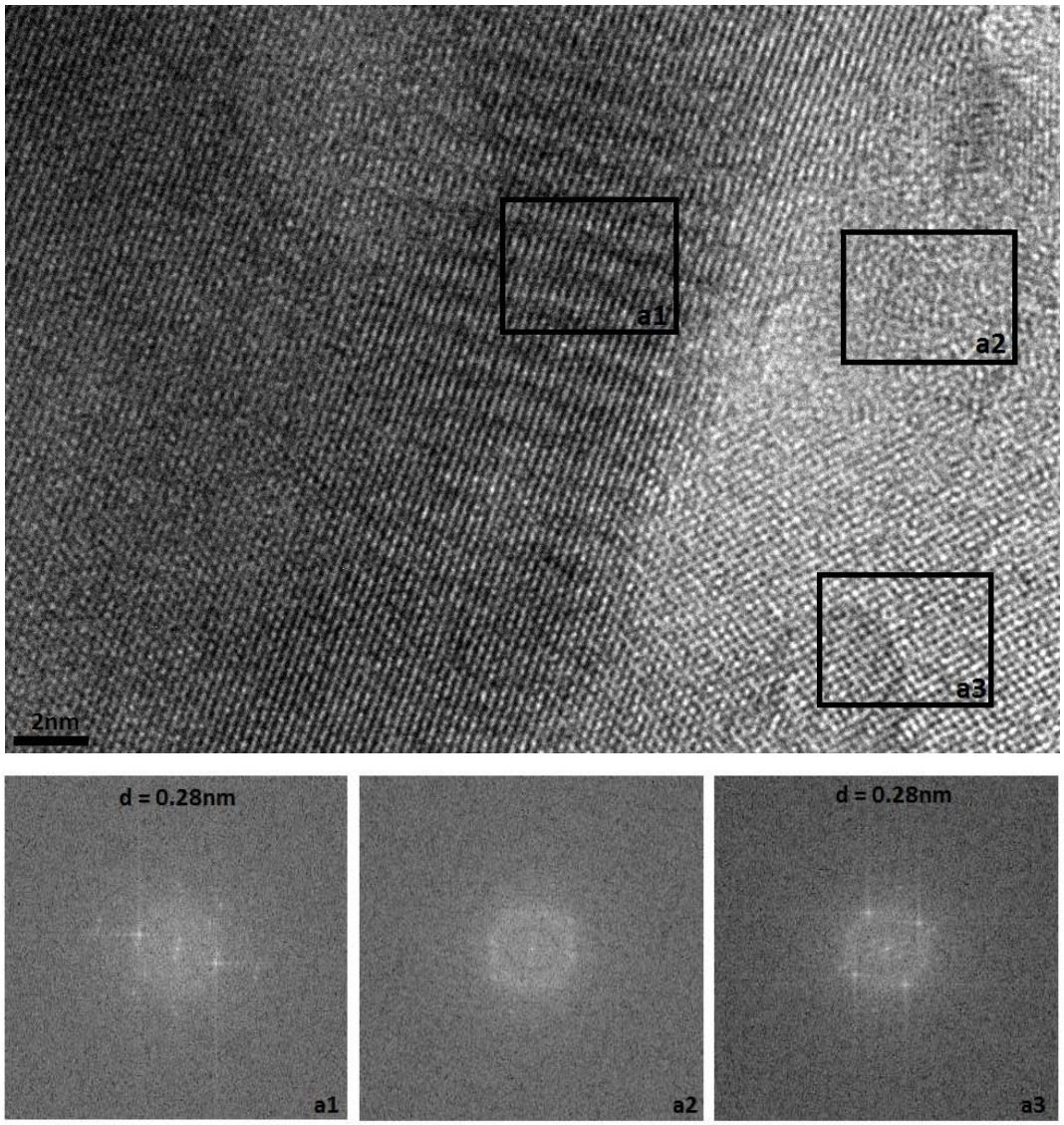

Figure 4. 4: HRTEM micrograph of BG35 with FT patterns and lattice fringe spacing corresponding to the areas of interest a1, a2 and a3.

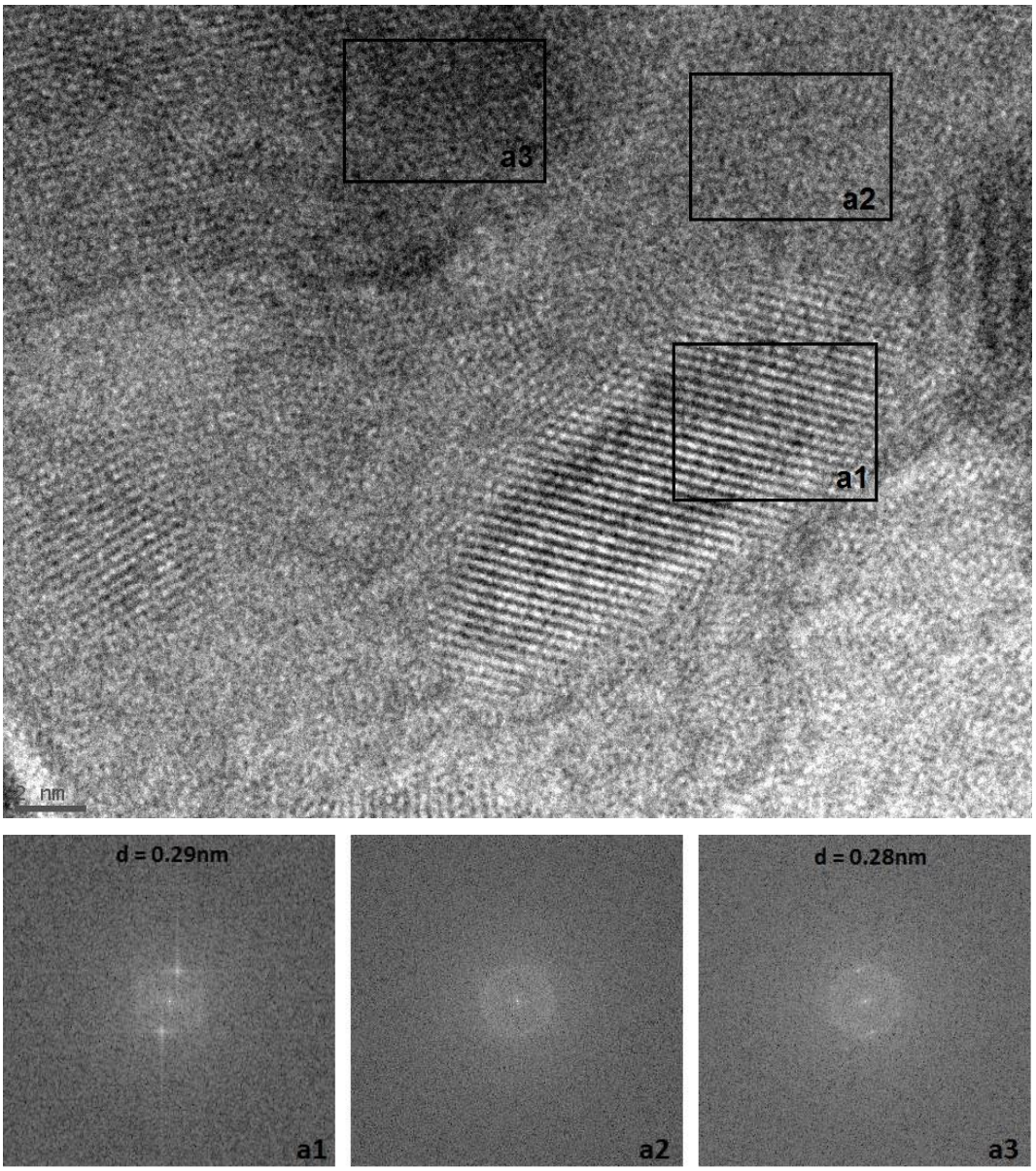

Figure 4. 5: HRTEM micrograph of BG50 with FT patterns and lattice fringe spacing corresponding to the areas of interest a1, a2 and a3.

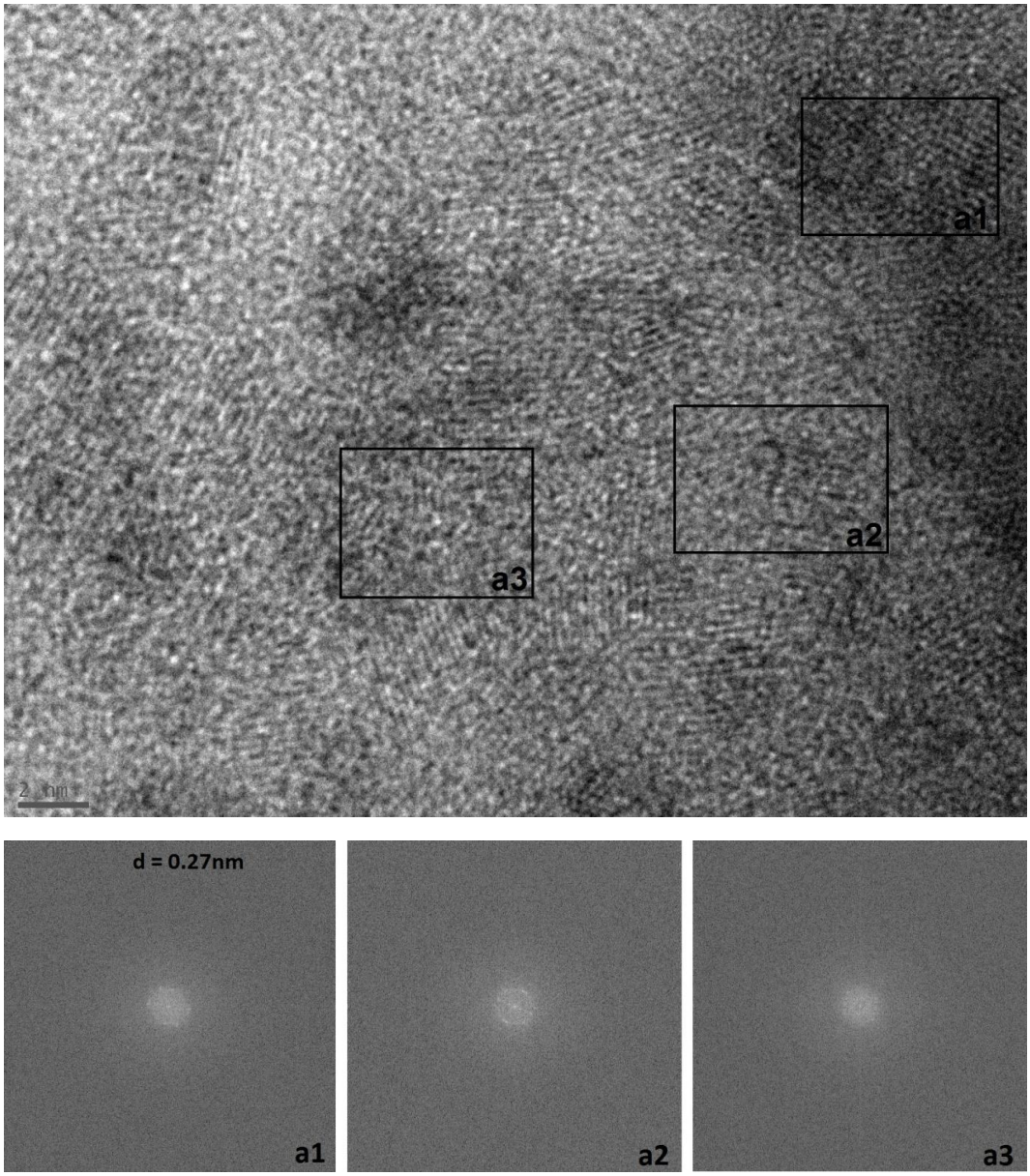

Figure 4. 6: HRTEM micrograph of BG65 with FT patterns and lattice fringe spacing corresponding to the areas of interest a1, a2 and a3.

4.3.4 Morphology

Nitrogen (N_2) sorption was performed on the synthesised bioactive glasses of different composition (BG35 – BG80) to determine its specific surface area, pore size, pore volume and pore shape. Figure 4. 7a shows the isotherms for these four ternary glass compositions produced. Each isotherm was irreversible, and found to represent the Type IV isotherm, based on the six idealised isotherms described in the IUPAC classification. To distinguish it from other isotherms, Type IV isotherms demonstrate an initial concave reversible adsorption and desorption branch to the relative pressures (P/P_0) axis [191]. The irreversibility of these isotherms, characteristic by the presence of a hysteresis loop, suggested the nanoparticles contained pores.

Each isotherm clearly occurs at a different level of adsorbed N_2 volume and show different hysteresis loops. Both BG35 and BG50 isotherms displayed a H1 loop, ascribed to cylindrical and open-ended pores [171, 191]. The H1 loop is defined by a near-parallel and almost vertical adsorption and desorption branch without the distinct steep drop in the desorption branch. However, the long sloping hysteresis loop over a broad range of relative pressures further point towards a wide distribution of pore width [134]. BG65 demonstrated a H3 and H4 hysteresis loop, defined by a sloping desorption branch, without the long plateau observed in the upper regions of P/P_0. H3 loops are distinguished by a steeper, vertical-like loop, while the H4 loop is shorter and horizontal-like, and occurs at the upper regions of P/P_0. Both these loops are associated with wedge- or slit-shaped pores, with pores of a H4 loop being found in the micropore range [169, 171, 191]. BG80, which contained the highest silica content and lowest calcium content among the different glasses, was defined by a H2 hysteresis loop. Characteristic of the H2 loop is the steep, non-parallel desorption branch occurring at the lower closing end of the hysteresis loop. The long plateau in the upper regions of P/P_0 and a narrow hysteresis loop with an irreversible desorption branch between 0.4 – 0.7 P/P_0 suggested that the BG80 nanoparticles contained pores which were not well interconnected and were extremely small micropores (< 2 nm), due to the complete filling of these micropores with N_2 occurring at lower relative pressures [169, 191].

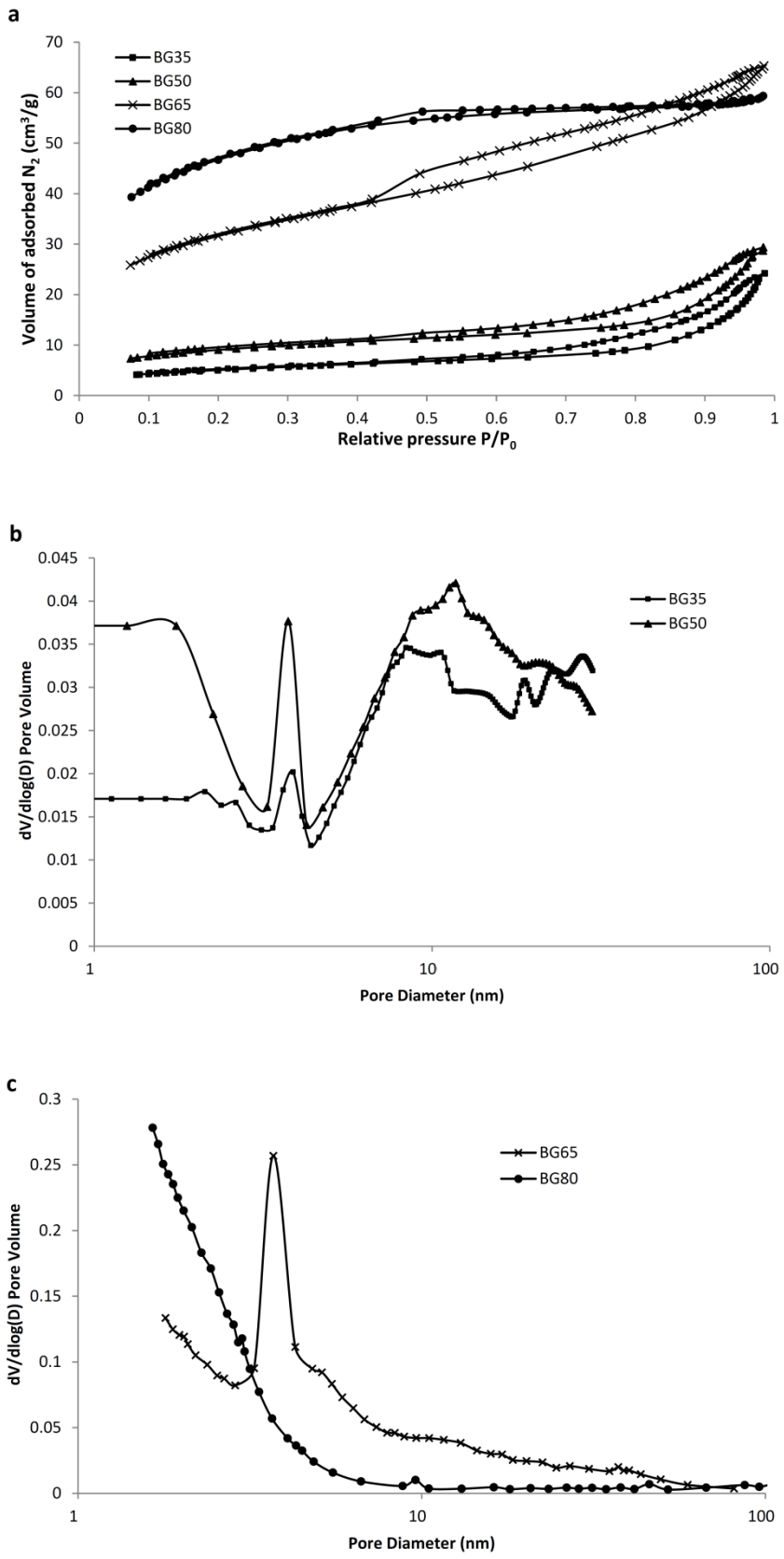

Figure 4. 7: (a) Nitrogen sorption isotherms of sol-gel derived bioactive glass nanoparticles with different compositions; pore size distribution for sol-gel derived (b) BG35 and BG50 nanoparticles and (c) BG65 and BG80 nanoparticles.

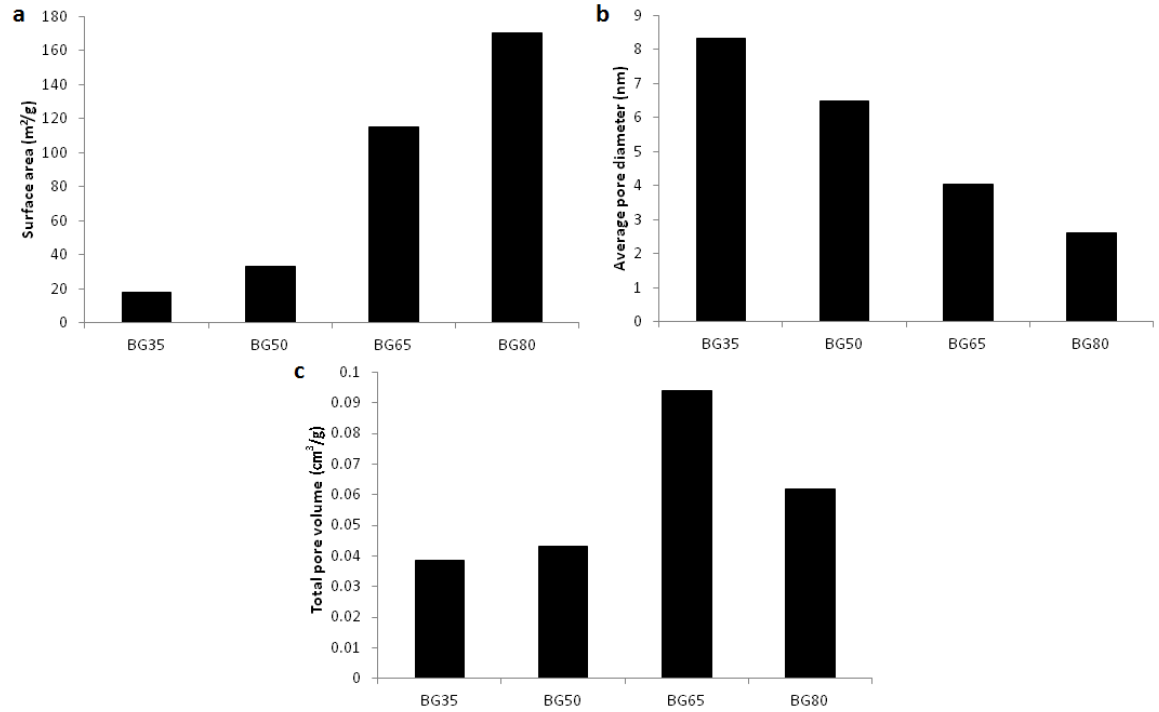

Figure 4. 8 : The (a) specific surface area, (b) average pore diameter and (c) total pore volume of bioactive glass nanoparticles with different composition.

Figure 4. 7b and c show the pore diameter distribution for BG35, BG50 and BG65 and BG80 bioactive glasses respectively. Both BG35 and BG50 glasses displayed a similar pore diameter distribution in which two distinctive pore types were observed. The nanoparticles contained micropores (< 2 nm), and a range of mesopores with a modal value at 3.7 nm and between 9 – 30 nm. The pore diameter distribution of BG65 showed a narrower distribution of pores centred around 3.7 nm, making up a large proportion of pore volume. A small proportion of micropores were also present, illustrated by the increase in pore volume for pore diameters of less than 2 nm. The pore diameter distribution of BG80 nanoparticles showed an increase in pore volume for pore diameters less than 10 nm, suggesting BG80 contained a narrow distribution of extremely small pores, with the majority being micropores.

Figure 4. 8a shows an increase in the specific surface area (SSA) of the bioactive glass nanoparticles with an increase in silica content while Figure 4. 8b clearly shows the inverse relationship between increasing silica content and decreasing average pore sizes. The total pore volume, which translates to the porosity of the nanoparticles, as seen in Figure 4. 8c, showed the total pore volume of BG65 nanoparticles being the

highest. BET analysis showed that a decrease in CaO and an increase in SiO_2 led to the overall increase in SSA of the nanoparticles, but an overall decrease in pore size. Such trends have been observed previously in both binary and ternary glass systems [15, 131, 181, 206].

One explanation for this occurrence can be provided by considering the presence of non-bonding oxygen atoms in the silicate network. Calcium when introduced into the glass network acts as a network modifier, and therefore an increase in calcium would increase its interaction with the silicate network, consequently leading to an increase in the number of non-bonding oxygen atoms. The quantity of micropores formed from these voids therefore increases, coalescing to form mesopores, and thus decreases the SSA but increases the pore size of the nanoparticles [205]. Interestingly, the relationship between glass composition and pore volume was not obvious, with BG65 nanoparticles determined to be most porous, recording the highest total pore volume amongst the four compositions.

Although studies have shown that an increase in the silica content would lead to a decrease in pore volume, due to the reason similar to the influence of composition on pore size as discussed above, the high pore volume of BG65 nanoparticles could be attributed to the susceptibility of the network to the effects of freeze drying (which will be discussed in Section 4.3.7). Briefly, it was observed that the mesopores of BG65 nanoparticles followed the shape of ice crystals, creating slit- or wedge-like shaped pores while BG35, BG50 and BG80 nanoparticles were not readily influenced by the effects of ice crystal formation, due to crystalline phases present in these nanoparticles, which hindered ice crystal growth.

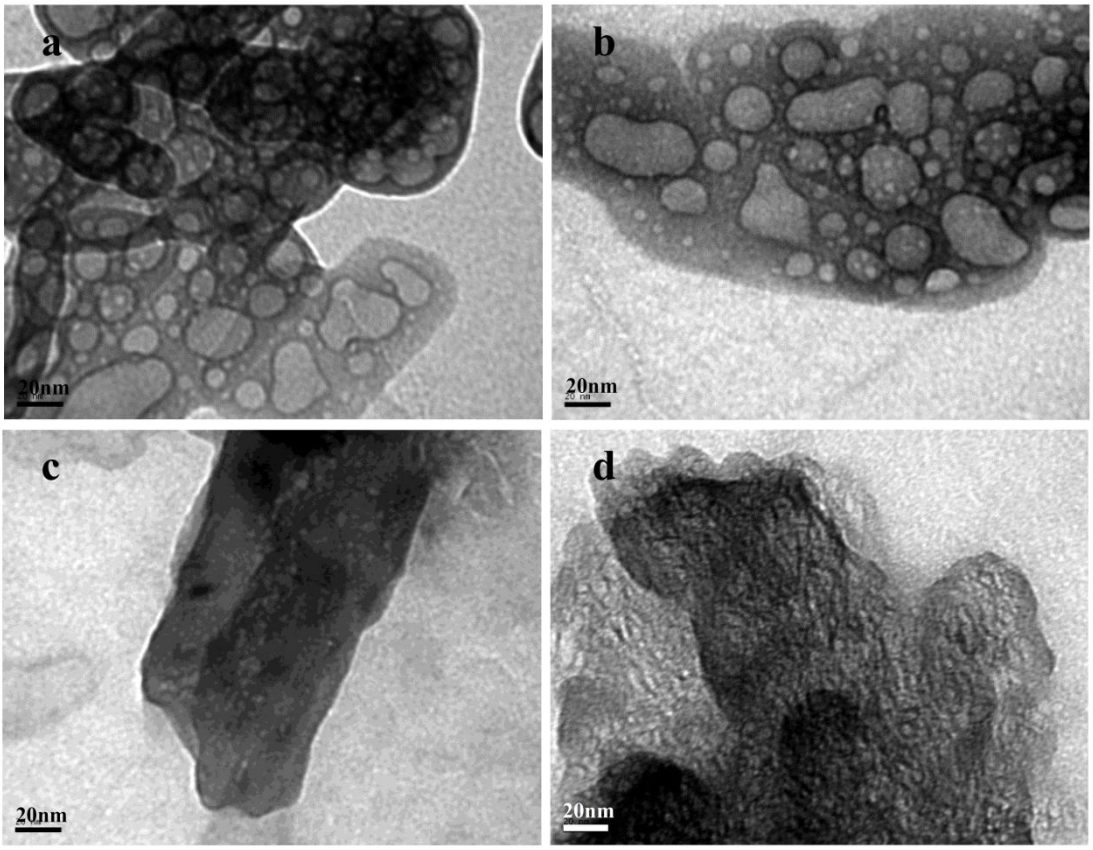

Figure 4. 9: TEM micrographs of sol-gel derived bioactive glass nanoparticles of the composition (a) BG35, (b) BG50, (c) BG65 and (d) BG80.

TEM was used to study the effects of different silicon and calcium content on the nanostructure of the bioactive glass nanoparticles. The nanostructure of the ternary glasses BG35, BG50, BG65 and BG80 are shown in Figure 4. 9. Both BG35 and BG50 reveal a similar nanostructure consisting of elongated plate-like particles with a broad range of sizes (30 – 100 nm in width). Both nanoparticle types were found to contain mainly spherical micropores and mesopores. BG65 revealed porous elongated nanoparticles, containing slit-like mesopores, while BG80 which had the highest silica content, showed an undefined structure of agglomerated nanoparticles packed together in a chain-like cluster conformation, similar to pure silica nanoparticles derived from a similar sol-gel route [161]. Closer inspection of the nanostructure suggests the existence of micropores within the nanoparticles.

Changes in the nanostructure of these various bioactive glasses due to compositional variation have been studied using gas sorption techniques [8, 131, 134, 181, 214]. When Li *et al*. [8] studied a range of glasses containing SiO_2 (50 – 90 mol %),

changes in SSA and porosity were noticed, in which an increase in silica content led to an increase in overall pore volume and SSA. Unfortunately, the effects of these changes were not corroborated visually with the aid of microscopes. To date, not much work has been carried out to verify the findings using both techniques [135], and hence, this work intends to explore the use of TEM as a means of substantiating the results of the N_2 sorption test performed.

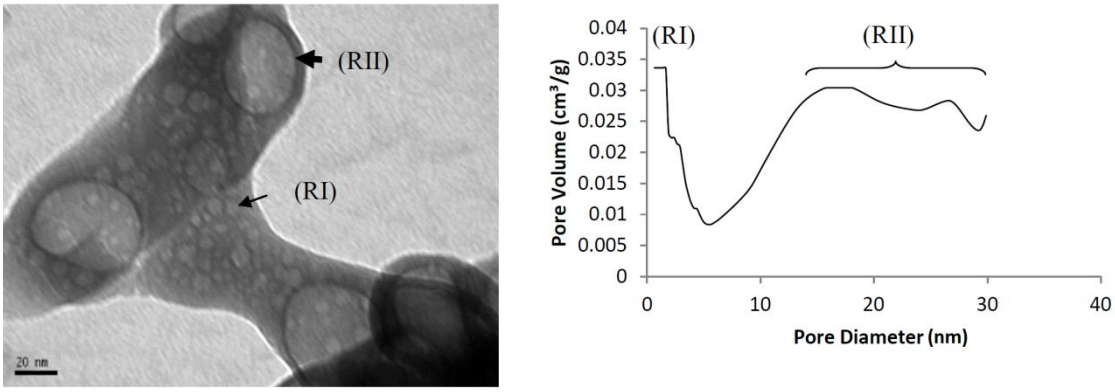

Figure 4. 10: TEM micrograph showing the existence of a dual-pore nanostructure in BG35 and BG50 nanoparticles and verification through N_2 sorption analysis.

Figure 4. 10 shows the corroborated evidence of this unique occurrence in which the BG35 and BG50 nanoparticles synthesised possessed a mixture of micropores and mesopores. The first region (RI), verified by N_2 sorption analysis of the pore volume, showed an increase in pore volume for pore diameters less than 5 nm, with a peak pore volume (0.034 cm^3/g) corresponding to pore diameters of less than 2 nm. The limitation of the equipment provides for a sensitivity of up to 1.7 nm, and hence, pore sizes smaller than this threshold cannot be quantified accurately [215]. However, the peak in pore volume for pore diameters less than 2 nm is sufficient to draw a conclusion that the pores can be categorically characterised as micropores based on the IUPAC classification [191]. The second region (RII), showed peak pore volumes (0.025 – 0.03 cm^3/g), corresponding to pore diameters between 15 – 35 nm, classified as mesopores [191]. Both pore regions (RI and RII) indicated on the TEM micrograph in Figure 4. 10 were spherical, with a pore diameter range of 2 – 5 nm for RI type pores and between 20 – 50 nm for RII type pores.

A dual-modal pore structure in mesoporous bioactive glasses was described by Yan *et al*. [150] in which pore diameters centred at 5 nm and approximately 20 nm were recorded. The formation of this pore structure was attributed to the interconnection of these smaller mesopores into larger mesopores. Interestingly, the study goes on to show the enlargement of these pores when the nanoparticles were soaked in water, attributed to the leaching of the inorganic Ca and P species from the wall framework. Thus, from the TEM and BJH analysis carried out, the dual-modal pore structure observed in the higher CaO component glasses of BG35 and BG50 could be induced by the leaching of inorganic species during aging into the liquor, causing the creation of voids, observed as the micropores and the coalescing of these voids to form the larger mesopore structures.

4.4 Acidic and alkali derived bioactive glasses from different drying procedures

4.4.1 Physical characterisation

Understanding the effects of different drying procedures on nanoparticle morphology was carried out by studying three different drying routes. Figure 4. 11a and d demonstrates the outcome of oven drying (Route A), in which gels have shrunk and were compacted into a dense cake of bioactive glass material. Figure 4. 11b and e also shows a similar outcome in the final product from vacuum drying (Route B). Route A followed the more common method of oven drying [8, 139, 151, 152, 214], whereby the loss of pore liquor through evaporation caused a rise in capillary pressure within the network, causing it to contract and shrink [156].

Conversely, Route B was intended to mitigate the situation of high external pressure by removing the pressure altogether through the creation of a vacuum in the drying chamber. It was expected that, by creating a vacuum, the driving force of shrinkage due to external pressure would be avoided. However, at low pressures, the pore liquor which consisted of a mixture of water and ethanol as the by-products of condensation, boiled due to a drop in the boiling point and then froze from the loss of energy in the liquor from boiling [197]. This phenomenon caused a significant rise in capillary

pressure as the liquor rapidly evaporated, and intensified the shrinkage of the solid network [156].

Figure 4. 11c and f show fine bioactive glass powder obtained via freeze drying (Route C). This route was designed in which the capillary pressure of the liquor within the pores was reduced to zero, as liquid surface tension became nullified ($\gamma = 0$). Hence during the drying stage, the pore liquor which had been solidified was sublimated into gas, without transiting through the liquid phase, resulting in no shrinkage or contraction of the gels. Through the acceleration of the drying rate, the rapid flow and diffusion of vapour within the gel caused cracking of the xerogel, which eventually led to the collapse of the structure to form bioactive glass powder.

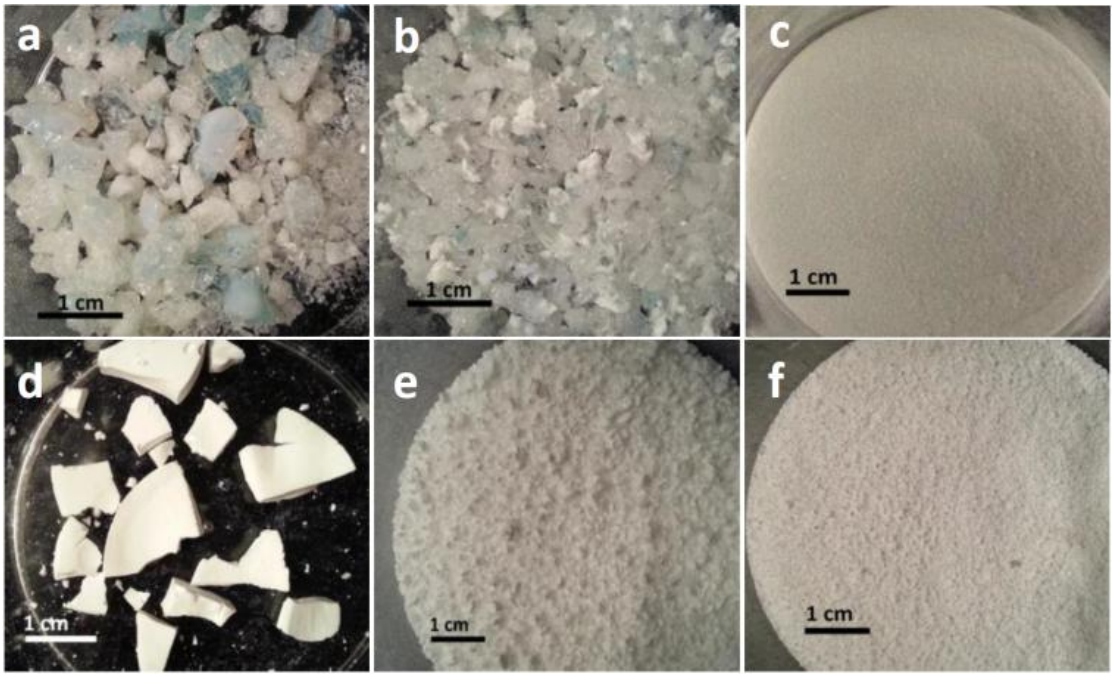

Figure 4. 11: Synthesised bioactive glasses from the sol-gel method prepared by (a) oven drying, (b) vacuum drying and (c) freeze drying; the multi-step method prepared by (d) oven drying, (e) vacuum drying and (f) freeze drying.

In the ternary glass system, the gel, an intermediate between a solid and a liquid [160], is formed by a silicate network of discrete colloidal particles, surrounded by calcium and phosphate groups, and would contain voids in-between the network which are

filled by liquid [135, 159]. This liquid trapped within the voids of pores in the silicate network creates a capillary pressure (P) [125].

$$P = \frac{2\gamma cos\theta}{r} \qquad \text{Equation 4.1}$$

where γ is the liquid surface tension, θ the contact angle between liquid-solid interface and r is the radius of the pore within the network.
During the final stages of drying in which capillary pressure is at the maximum (> 760 kTorr), it has been found that the extent of shrinkage of the dried network due to the exertion of capillary pressure establishes the final pore volume and pore size of the solid structure on a macroscale [156].

One strategy of overcoming this is by freeze drying, whereby the liquor within the network transits from solid ice directly into vapour without passing through the liquid phase [65, 71]. Under such a condition, no surface tension exists, hence eliminating capillary pressure altogether. Considering the way at which the liquor is removed from the gel during the drying stage is essential in providing distinct conditions which would influence the bioactive glass gel. Through freeze drying, the time consuming step of milling often employed to obtain ultra-fine powder is significantly reduced, since freeze drying of gel monoliths removes liquor within the gel without undergoing much shrinkage to produce xerogels, which can be easily crushed into powder [7, 125]. Furthermore, freeze drying of the precipitants can easily form monodispersed ultra-fine nanoparticles without even the need of grinding [165]. From this work, the ease of obtaining ultra-fine bioactive glass powder through freeze drying was demonstrated which extended to both the sol-gel and multi-step routes.

4.4.2 Composition homogeneity evaluation

Table 4. 5 shows the elemental concentration of the sol-gel and multi-step derived bioactive glasses dried via oven, vacuum and freeze drying, obtained using EDX. The theoretical composition of the glass was 65% SiO_2 – 30% CaO – 5% P_2O_5 (wt. %), however, some difference in the actual elemental concentrations were observed. Notably, multi-step derived glasses achieved a closer experimental content than those

synthesised by the sol-gel method. Separately, comparing the effects of the various drying routes on final glass composition, no significant variation was observed. This was expected as no loss of precursors would have occurred during the drying process.

Table 4. 5: Elemental composition of the bioactive glasses synthesised. All values represents the mean ± SD, n = 5.

Synthesis route	Sample	Elemental concentration (wt. %)		
		Si	Ca	P
Sol-gel	**BG65OD**	60.5±4.1	35.4±4.6	4.0±0.6
	BG65VC	59.7±3.3	35.4±4.9	4.8±0.9
	BG65FD	61.1±2.6	34.7±2.9	4.2±0.4
Multi-step	**nBG65OD**	64.7±1.2	28.6±1.4	6.8±0.6
	nBG65VC	64.8±1.1	28.8±1.0	6.4±0.3
	nBG65FD	64.7±0.4	28.3±1.3	7.0±0.9

The standard deviation recorded in Table 4. 5 is representative of some batch-to-batch variation, since manufacturer guidelines suggests an accuracy with a relative error of less than 2% should be considered when standardisation is carried out [185]. Analysing the standard deviation of each element, a larger standard deviation for the elements of Si and Ca was recorded for glasses derived from the sol-gel route, particularly sol-gel glasses processed by oven drying and vacuum drying (BG65OD and BG65VC). During the condensation of the sol, Ca which is present from the soluble precursor of calcium nitrate used and the element P which is present within the sol as an orthophosphate becomes homogenously distributed as the gel network forms [7, 135]. Throughout drying, migration of Ca occurs due to capillary diffusion, while the orthophosphate, isolated in its own form, remains randomly distributed throughout the dried network. Hence, heterogeneity between samples tested can be attributed to the migration of cation species [7, 130, 159]. Additionally, a reduction in the standard deviation of samples processed via freeze drying, which would suggest improvements in compositional homogeneity of BG65FD powders were attributed to the reduction of the effects of capillary diffusion, which hindered cation migration.

4.4.3 Morphology

Fundamental changes to the internal nanostructure of a single particle, brought about by the different drying processes should be characterised, pertinent to the establishment of a path towards better morphological control on a nanoscale. The possibility of tailoring bioactive glass nanostructures is vital for delivery applications. Therefore, the effects of different drying procedures on bioactive glass nanoparticle morphology from both the sol-gel (acidic) route and the multi-step (alkali) route were investigated.

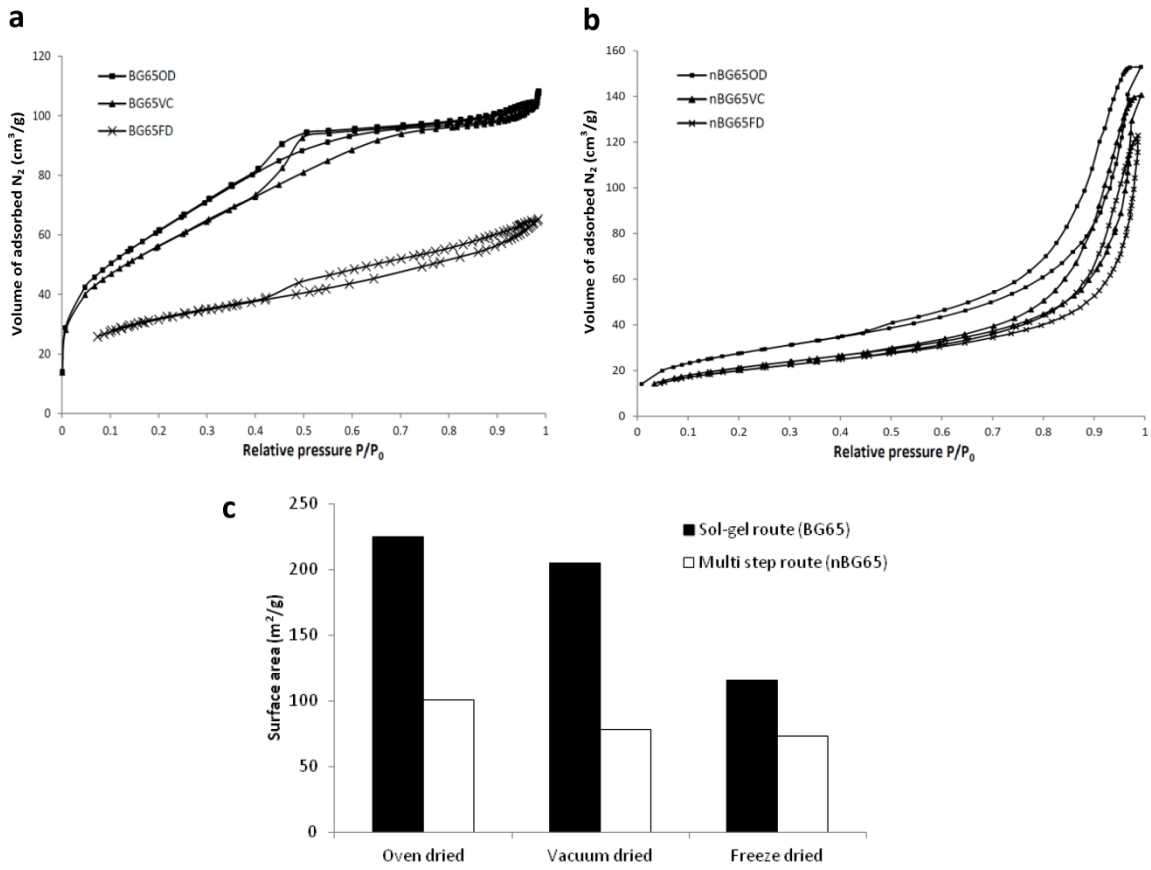

Figure 4. 12: The adsorption and desorption isotherms for (a) sol-gel derived and (b) multi-step derived bioactive glass nanoparticles; (c) effects of various drying procedures on SSA and the difference in SSA between the two synthesis routes.

N_2 sorption was performed on all samples produced from Route A, B and C drying procedures. Figure 4. 12a shows the adsorption and desorption isotherms for sol-gel derived bioactive glass nanoparticles. All three isotherms were irreversible, and corresponded to the Type IV isotherm, as seen in Figure 4. 12a [191]. Both

nanoparticles derived from oven drying and vacuum drying (BG65OD and BG65VC) displayed a H2 hysteresis loop [171, 191, 194]. This type of hysteresis loop correspond to pores of non-perfect cylindrical shape with a 'bottleneck', because pores of a certain radius will be filled by liquid N_2 at a higher relative pressure during adsorption than when it is emptied during desorption. The emptying of N_2 in the wider section of the pore is thus hindered by the narrow neck leading to the steep desorption branch observed [169, 171]. This Type IV, H2 isotherm is typically found in oven dried mesoporous bioactive glasses derived from the sol-gel route [134, 158].

Interestingly, the hysteresis loop of the freeze dried sample (BG65FD) was different. Correlating the shape of the loop to the five idealised types of hysteresis in the IUPAC, this loop corresponded to a H4 hysteresis loop. The pores from a H4 loop is measured as the spaces between parallel plates, primarily suggesting the pores were slit-shaped [169, 191]. However, typical H4 hysteresis loops are defined by its horizontal adsorption and desorption branches which are near-parallel, and stretch a wide range of relative pressures. Since, the loop observed Figure 4. 12a is slightly sloping, it could be suggested that the hysteresis loop of BG65FD was a combination of H3 and H4 type loops, pointing towards wedge- or slit-shaped pores, formed through the aggregation of plate-like particles, tapering at an end [171, 191].

Figure 4. 12b shows the isotherms obtained for nanoparticles derived from the multi-step route. It is evident that all three isotherms are similar and correspond to Type IV, with a H1 hysteresis loop [191]. The H1 loop suggested that pores found within the multi-step derived nanoparticles were cylindrical and open-ended [134, 169]. The sloping of the hysteresis loop, unlike the vertical loop described in an idealised example, suggests that the pores come in a variety of sizes. The interconnectivity of the pores within the nanoparticles, measured by the width of the loop, and the shape of pores between all three drying routes are rather similar, demonstrating that the method of drying bioactive glasses from the multi-step route has no effect on the final nanoparticle nanostructure.

One possible reason for this is due to the synthesis of the multi-step bioactive glass, which employs the use of a morphological catalyst to advance the rate of

polycondensation, thus forming a more tightly packed silicate network which is less susceptible to changes. The repelling of material from the ice front was shown to become more difficult as the viscosity and particle size of the material increased, because of the increased interaction between material content. Thus, the effects of ice crystal formation on pore architecture are less profound [19, 216] .

The specific surface area (SSA) of the bioactive glass nanoparticles derived from the three drying methods was compared and shown in Figure 4. 12c. The SSA of the bioactive glass nanoparticles derived from the sol-gel route and the multi-step route showed that oven drying produced nanoparticles with the highest SSA, while freeze drying produced nanoparticles with the lowest SSA. However, it is clear that nanoparticles derived from the sol-gel route had a significantly higher SSA than those derived from the multi-step route. For instance, the SSA of BG65OD with a SSA of 224.6 m^2/g was 2.2 times larger than the SSA of nBG65OD.

Changes in nanoparticle morphology between the sol-gel and multi-step derived glasses due to different drying routes is depicted in Figure 4. 13. Comparing both synthesis routes, it was evident that the sol-gel route produced nanoparticles with a narrow pore diameter distribution, with modal pore diameters of 3 – 4 nm across all drying routes (Figure 4. 13a), while a wide pore diameter distribution was observed for nanoparticles synthesised from the multi-step route, notable in Figure 4. 13b. Figure 4. 13c and d show the average pore diameter and total pore volume of each nanoparticle type, calculated using the BJH method. The pore sizes of the nanoparticles derived from the multi-step route were on average three-fold larger than sol-gel derived nanoparticles across all drying procedures, in agreement with the pore diameter distribution plots (Figure 4. 13b), wherein multi-step derived nanoparticles had a broad distribution of pore diameters.

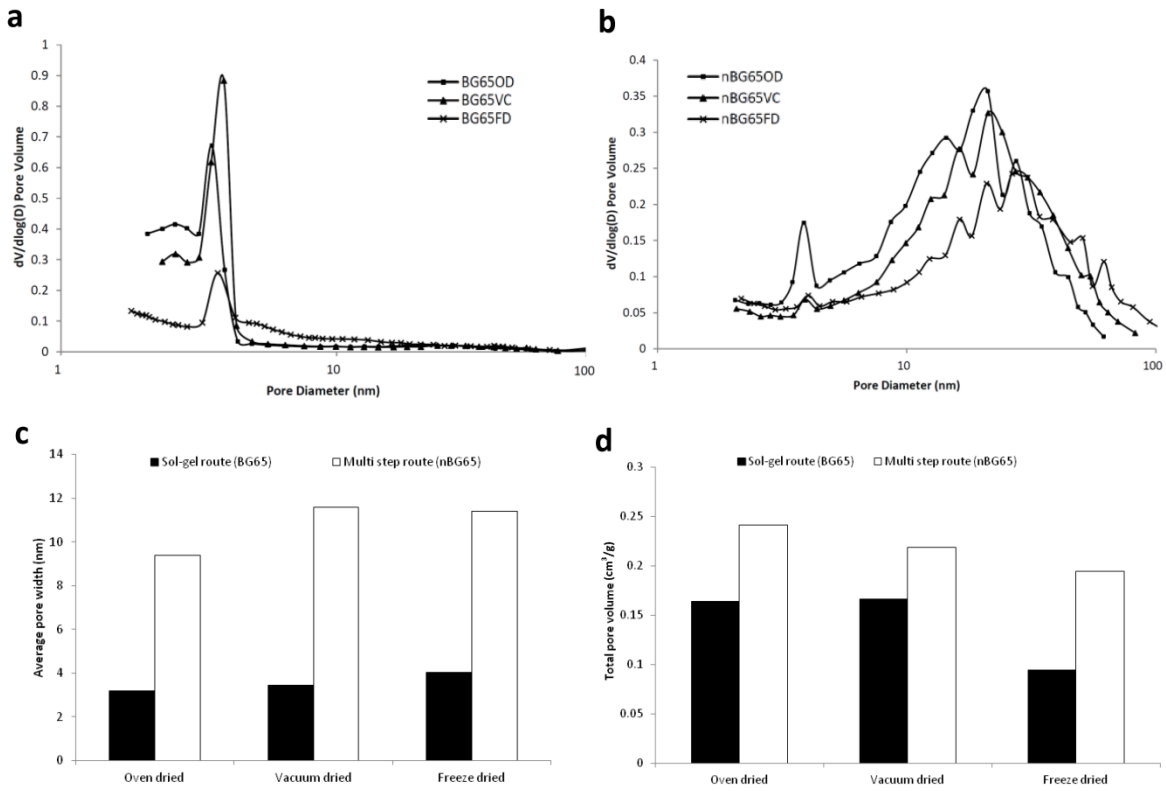

Figure 4. 13: Pore size distribution for (a) sol-gel derived nanoparticles and (b) multi-step derived nanoparticles, dried by different routes. The effects of synthesis method and various drying routes on (c) average pore diameter and (d) total pore volume.

Figure 4. 13d shows that across the three drying routes, the total pore volume of multi-step derived nanoparticles were higher than the sol-gel derived nanoparticles. The total pore volume is an indicator of the porosity of these nanoparticles, thus suggesting the multi-step route produced bioactive glass nanoparticles which were more porous [217]. This could be attributed to the larger pores found in the multi-step derived nanoparticles, which take up a larger proportion of the total nanoparticle volume. It is worth noting that ternary sol-gel glasses have been found to contain pore volumes in the region of 0.13 – 0.25 cm^3/g, therefore, suggesting that, although both the processing condition of the sol and drying procedures have an effect on the total pore volume of the nanoparticles, this influence is not profound [150, 182].

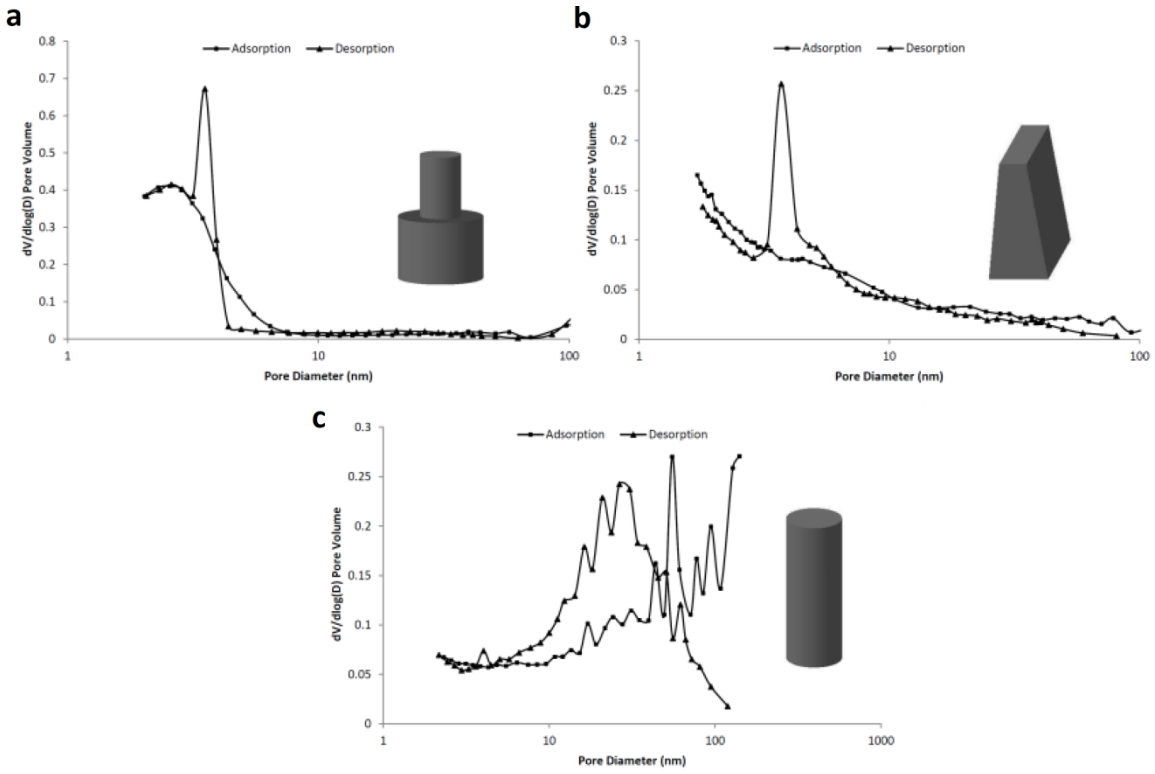

Figure 4. 14: BJH adsorption and desorption pore diameter distribution with corresponding schematics of proposed unit pore geometry of (a) oven dried, (b) freeze dried sol-gel bioactive glass and (c) freeze dried multi-step bioactive glass.

Analysis of the hysteresis loops pointed towards the existence of different pore shapes within the nanoparticles. To further ascertain these findings, comparisons of BJH pore size distribution between the adsorption and desorption branch was carried out to determine the geometric structure of the pores. Figure 4. 14a and b show the comparison between the adsorption and desorption pore size distribution for oven dried (BG65OD) and freeze dried (BG65FD) sol-gel bioactive glass nanoparticles respectively. Differences are apparent between both branches. The adsorption branch of BG65OD showed a broader distribution, with the modal pore diameter at 2.6 nm, while the desorption branch showed a narrow distribution, with a modal pore diameter of 3.7 nm. Pore size distribution from the adsorption branch corresponds to the cavity size of the pore, whereas the desorption branch corresponds to the throat size of the pore, due to the difference in N_2 volumes during filling and emptying of pores at given P/P_0, as previously described [125, 171]. Therefore, these results indicated that the mesopores have a varied cavity size, with a more consistent throat size. This also confirms that the unit shape structure of these mesopores is a non-perfect cylinder,

with a narrow neck and wide body, taking the shape of an ‘ink bottle’, as proposed in the schematic [134, 171].

Separately, the pore diameter distribution of BG65FD from the adsorption branch was broader, with modal pore sizes less than 1.8 nm, while the desorption branch showed a similar narrow size distribution of 3.7 nm. Based on hysteresis analysis and the difference between the adsorption and desorption modal pore sizes, the micropores within BG65FD nanoparticles are interpreted to be a mixture of open-ended tapered and wedge-shaped, formed by the spaces between plates of agglomerated tertiary particles [169, 191]. As for all bioactive glass nanoparticles synthesised from the multi-step route, in each case, both the adsorption and desorption branches showed a wide distribution of pore sizes. Figure 4. 14c depicts the pore size distribution of nBG65FD. Considering the modal diameter of the throat was less than half the modal cavity diameter ($\frac{26\ nm}{55\ nm} < 0.5$), the geometry of these mesopores was suggested to be approximately cylindrical [134, 169, 218].

One explanation for the occurrence of slit- or wedge-shaped pores found within BG65FD nanoparticles is due to the rearrangement of the 3D gel network consisting of water and the many units of the SiO_4 tetrahedron linked by oxygen atoms during freezing. In the gelled state, the secondary particles are entangled in a matrix which consists of water and ethanol [135]. When the gel monolith begins to freeze, the interface between the base of the gel monolith and the cooling plate begins to freeze first, forming ice crystals within the 3D gel network. As freezing progresses upwards, ice crystal formation would grow along the progressing cold front upwards, forming elongated rod like ice crystals, expelling the polymer phase to the edges [216]. Upon sublimation, these ice crystals which have acted as templates are removed, leaving a pore architecture consisting of elongated channels or parallel plates of material.

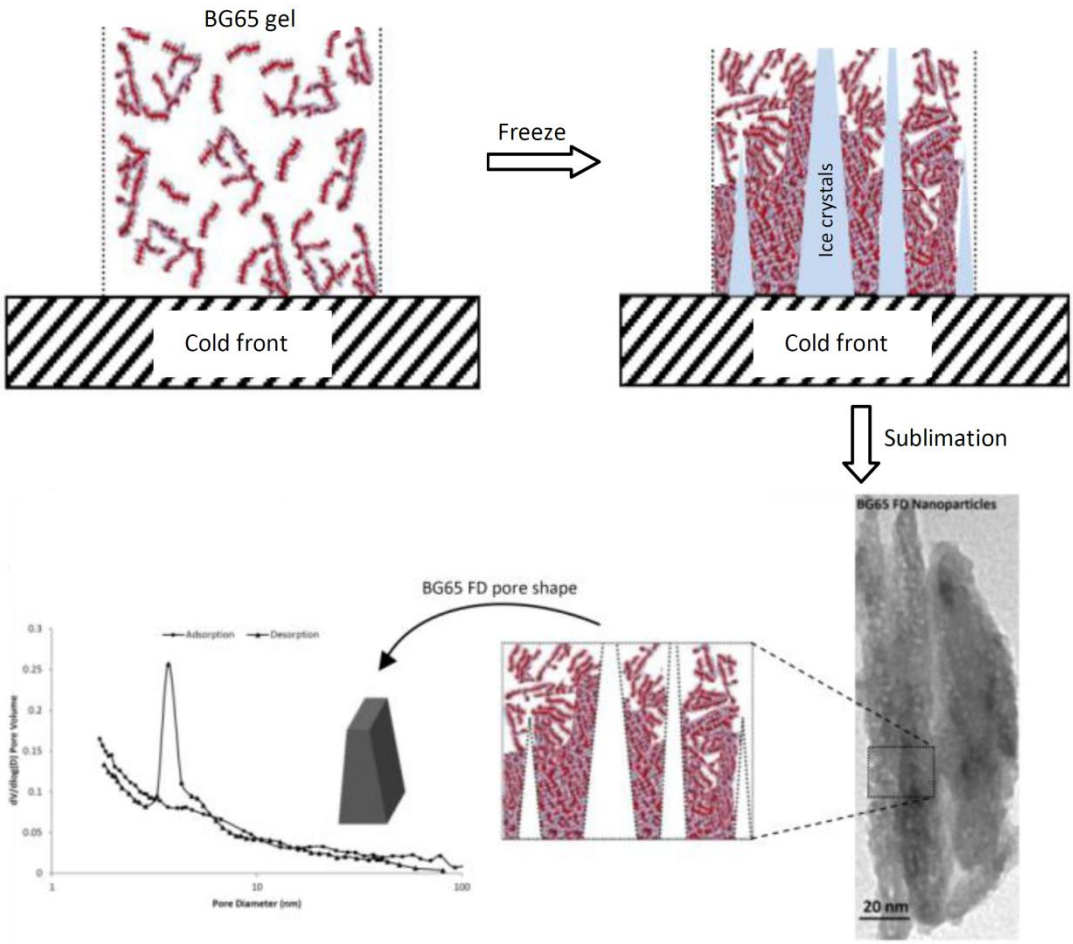

Figure 4. 15: Schematic representation of the ice crystal formation and subsequent templating (wedge-like shape) of nanoparticle pore shape via the sublimation of ice.

This model of unidirectional freezing is widely replicated for tailored hydrogel scaffold manufacture at the macroscale level [19, 66, 67]. However, in this instance, the same model is applied to the nanoscale level, to explain the occurrence of these slit- or wedge-shaped pores within the nanoparticles (Figure 4. 15). The application of this model is based on the fact that, in a gelled state, the sol-gel derived nanoparticles themselves contain water which are held together by linked SiO_4 tetrahedron chains [140]. Hence, the directionality of ice crystal formation will in effect realign these chains when freezing, hence, forming the slit- or wedge-shaped pores within the nanoparticles.

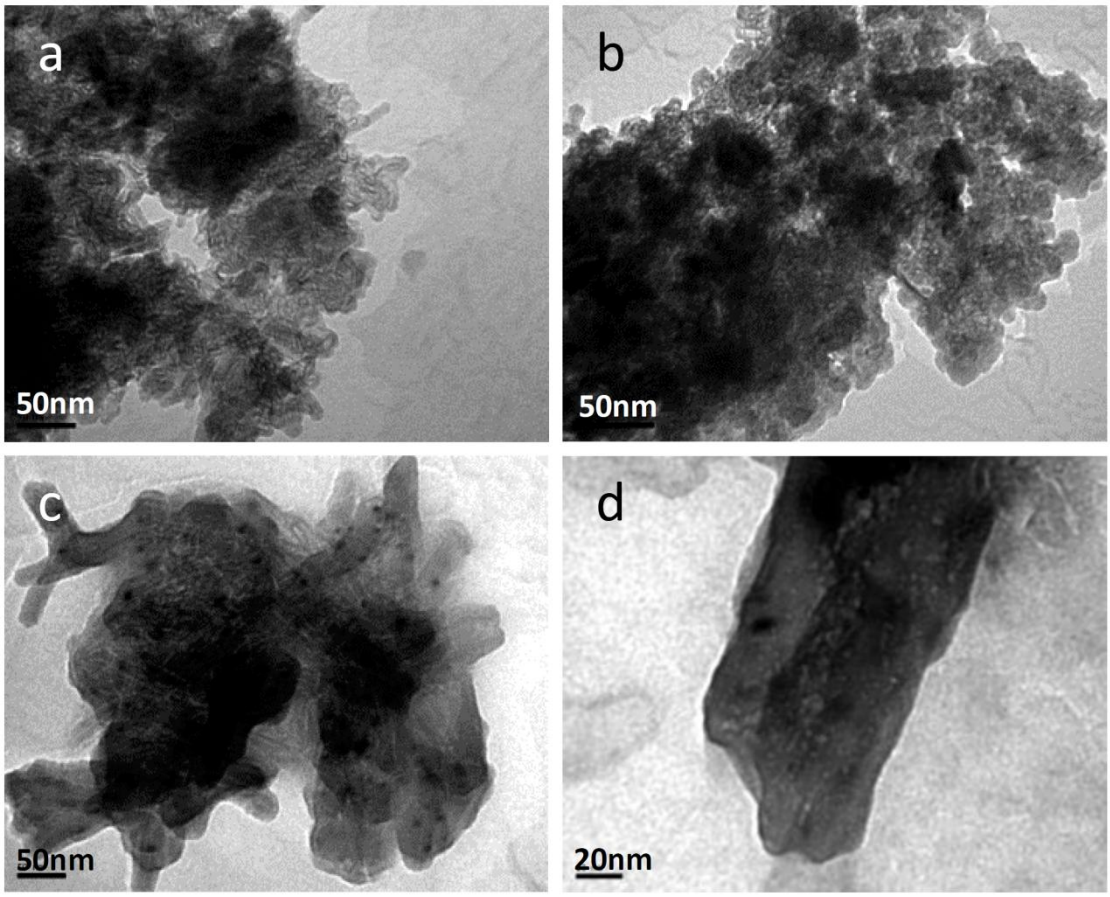

Figure 4. 16: TEM micrographs of sol-gel derived bioactive glass nanoparticles from (a) oven drying, (b) vacuum drying, (c) and (d) freeze drying.

Figure 4. 16 shows TEM micrographs of sol-gel derived bioactive glass nanoparticles dried via Route A, B and C. The nanoparticles produced by Route A and Route B (Figure 4. 16a and b) were heterogeneous in size and shape, with some interstitial spaces between the tertiary particles. The nanoparticles derived from Route C showed a rough surface texture, with an ordered mesoporous structure seemingly aligned to a single axis. Measurements revealed elongated rod-like particles of 10 – 30 nm in diameter with a mean length-to-width aspect ratio of 2.3. Conversely, TEM examination of the nanoparticles synthesised by the multi-step route (Figure 4. 17) revealed spherical shaped nanoparticles with a diameter mainly ranging from 30 – 90 nm. All multi-step derived nanoparticles revealed rather spherical mesopores of various sizes. No significant distinction could be made of the three drying routes on nanoparticle morphology.

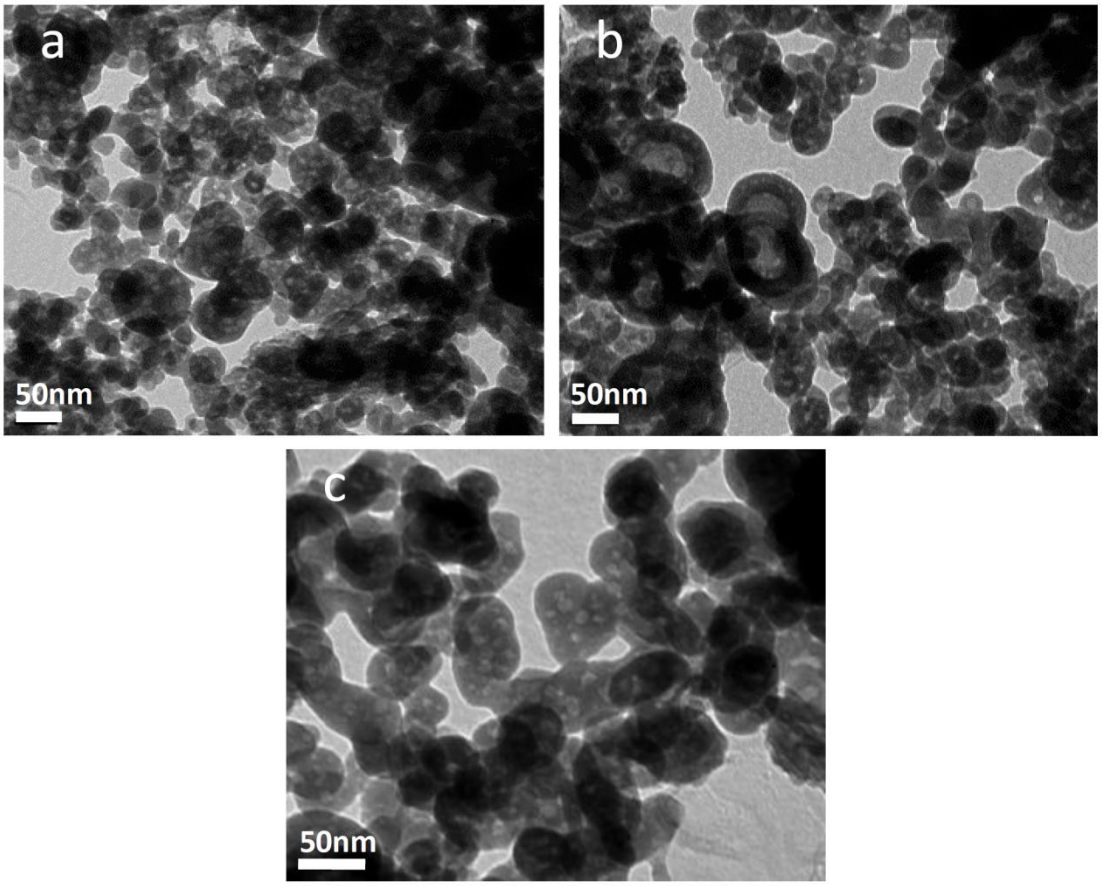

Figure 4. 17: TEM micrographs of multi-step derived bioactive glass nanoparticles from (a) oven drying, (b) vacuum drying and (c) freeze drying.

From TEM observation, some form of order is evident in the morphology of the nanoparticles. Primarily, the shape of the nanoparticles from this study was highly influenced by the synthesis method (sol-gel or multi-step), rather than affected by the drying process. However, nanoparticles prepared via freeze drying (Figure 4. 16c) showed a difference in nanoparticle surface texture and alignment in the agglomerated tertiary particles. Furthermore, cylindrical mesopores observed within the multi-step derived bioactive glasses are in agreement with reports that pore shape and size homogeneity within nanoparticles existed, based on isotherm and hysteresis loop analysis from gas sorption test [8, 134, 150]. TEM examination from this study further confirmed these findings.

By using glasses of a similar composition (65% SiO_2 – 30% CaO – 5% P_2O_5; wt. %), this study provides an insight into the effects of sol-gel (acidic) and multi-step (basic) synthesis on the final morphology of bioactive glass nanoparticles. Moreover, this

comparison also clearly showed that the drying procedure of bioactive glasses prior to heat treatment has a profound effect on nanoparticle specific surface area, pore shape, size and volume. Through the concomitant use of N_2 sorption and TEM techniques, a more conclusive result on the effects of synthesis methods on nanoparticle morphology can be drawn.

4.5 Bioactive glasses of different sintering regimes

4.5.1 Morphology

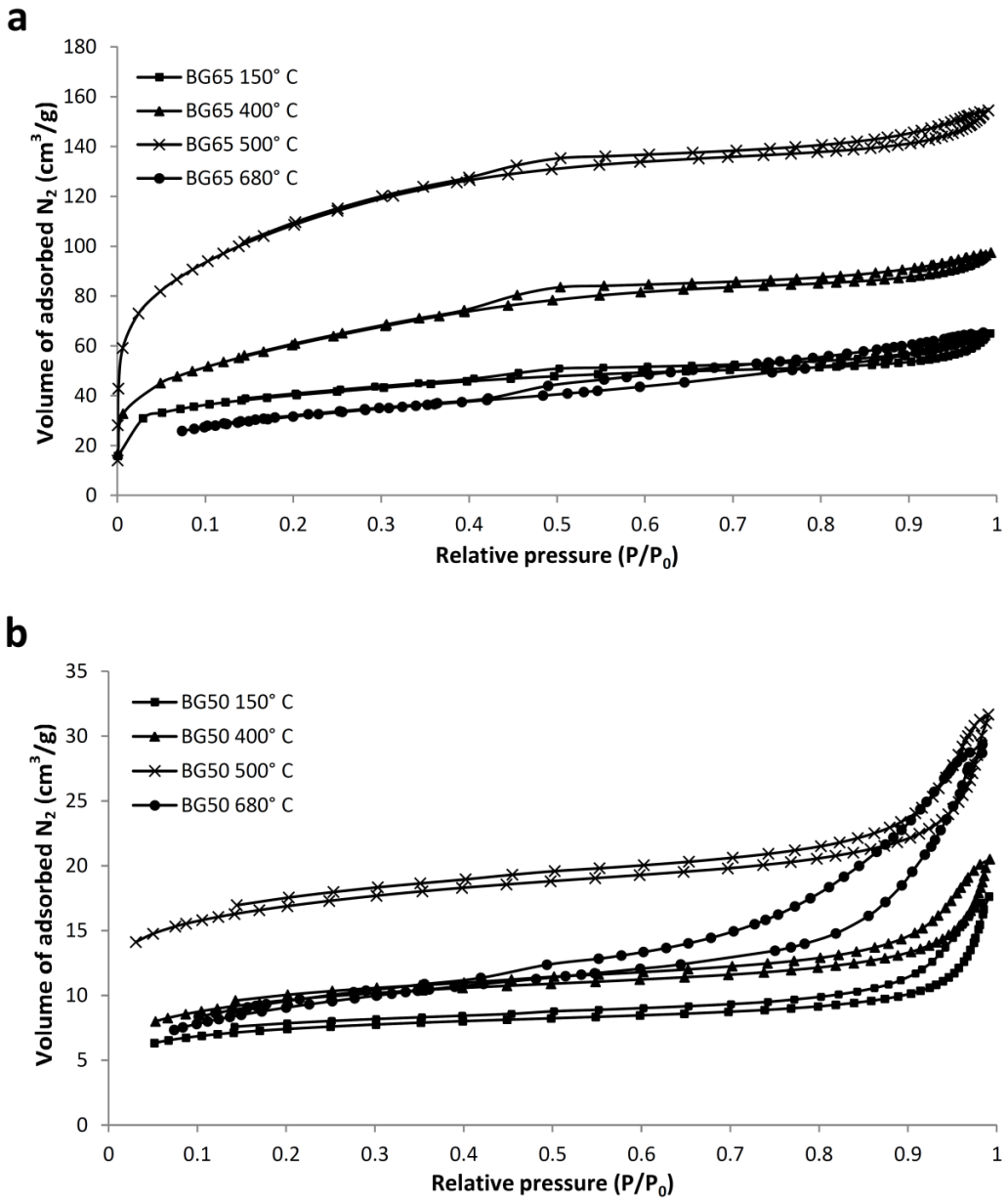

Figure 4. 18: Adsorption and desorption isotherms of (a) BG50 nanoparticles and (b) BG65 nanoparticles, heat treated at different temperatures.

Figure 4. 18a and b show the isotherms for bioactive glasses of two compositions (BG50 and BG65) heat treated at temperatures of 150 °C, 400 °C, 500 °C and 680 °C. Comparing both compositions, all four isotherms of BG50 (Figure 4. 18) fall into the category of Type IV with a H1 hysteresis loop [191]. The pores for this category are open-ended tubes or cylinders. The long near-horizontal loop which stretches across a broad range of relative pressures suggested the nanoparticles contained wide range of pore diameters. Figure 4. 18b shows the collection of isotherms for heat treated BG65, which all correspond to Type IV isotherms with H4 hysteresis loops. This is evidenced by the non-limiting adsorption at high pressures [171, 191]. As previously discussed, pore shapes identified with this hysteresis were slit-shape, lamellar pores tapered at an end. Upon closer inspection of Figure 4. 18a, it is interesting to note that apart from the BG50_680°C sample, the other isotherms display a non-closing desorption branch at low pressure. This phenomenon, known as low pressure hysteresis, occurs in non-rigid porous structures which have swelled during adsorption [191]. The reasons for this occurrence are, the possibility of irreversible N_2 uptake into pores which are about the same size as the N_2 molecule or a chemical reaction between N_2 and BG50 [191].

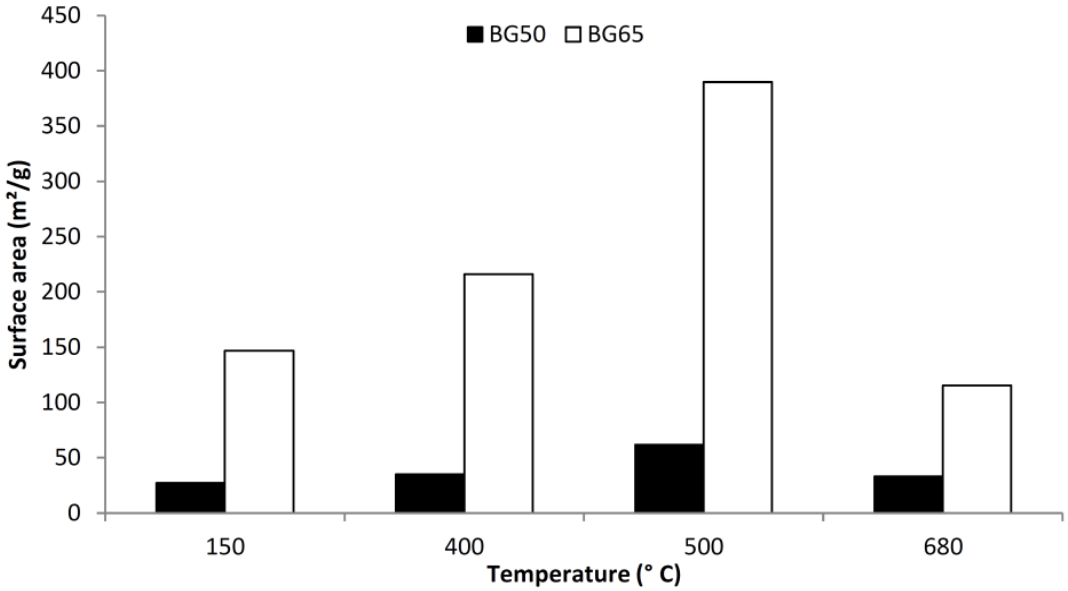

Figure 4. 19: Effects of heat treatment temperature on SSA and the difference in SSA between BG50 and BG65 nanoparticles.

Changes in specific surface area (SSA) of the bioactive glasses with respect to temperature is shown in Figure 4. 19, where an increase in temperature from 150 °C to 500 °C led to an increase in SSA. Since the BET method calculates the SSA based on a monolayer coverage of adsorbate on the surface, it is possible that, as temperature increases, the voids left by the removal of impurities, and the fusion of calcium into the silicate network as network modifiers, is filled by N_2 and therefore is considered as an increase in SSA. At a heat treatment temperature of 680 °C, the SSA decreases, which is in-line with the fusion of the secondary particles [150].

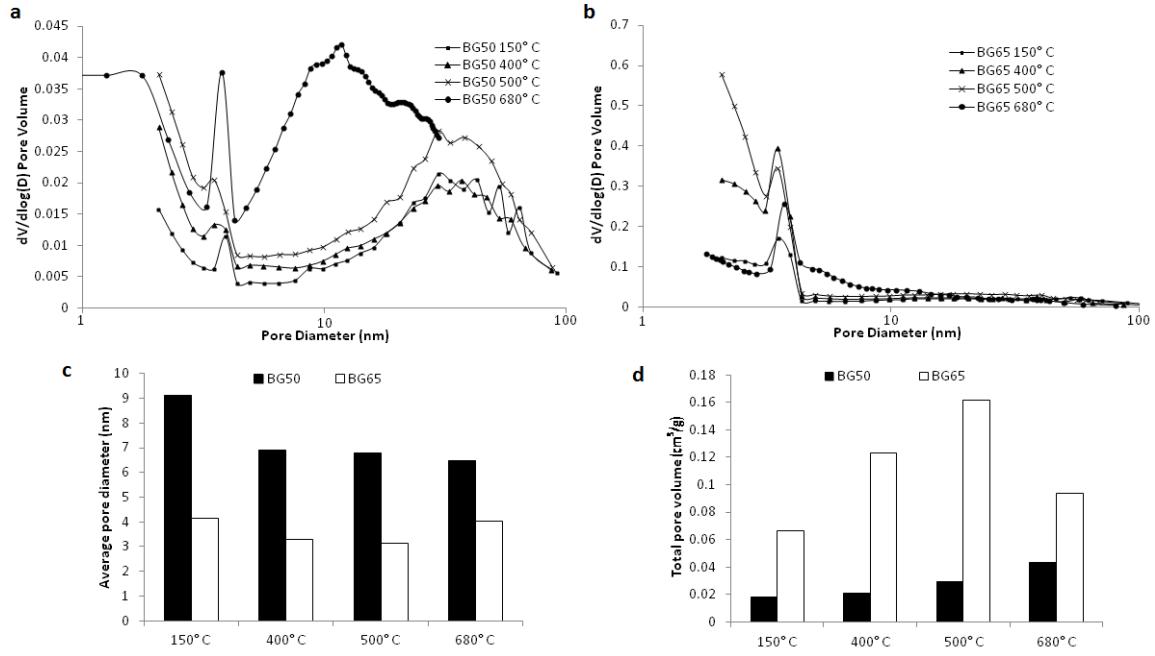

Figure 4. 20: The effects of heat treatment on pore size distribution for (a) BG50 nanoparticles and (b) BG65 nanoparticles; (c) average pore diameter and (d) total pore volume of BG50 and BG65 nanoparticles.

The effects of temperature on the both BG50 and BG65 glasses are similar, wherein, between 150 °C and 680 °C, not much difference in pore distribution is observed, apart from BG50_680°C, which shows a shift in pore diameter distribution from peaks centred around 30 – 40 nm to two distinct peaks at 3.7 nm and 11.7 nm, as seen in Figure 4. 20a and b. Comparing the effects of heat treatment on the average pore diameters and total pore volume of the nanoparticles (Figure 4. 20c and d), a decrease in average pore diameter while an increase in total pore volume was observed as heat

treatment temperature increased. However, for nanoparticles heat treated at 680 °C, total pore volume decreased.

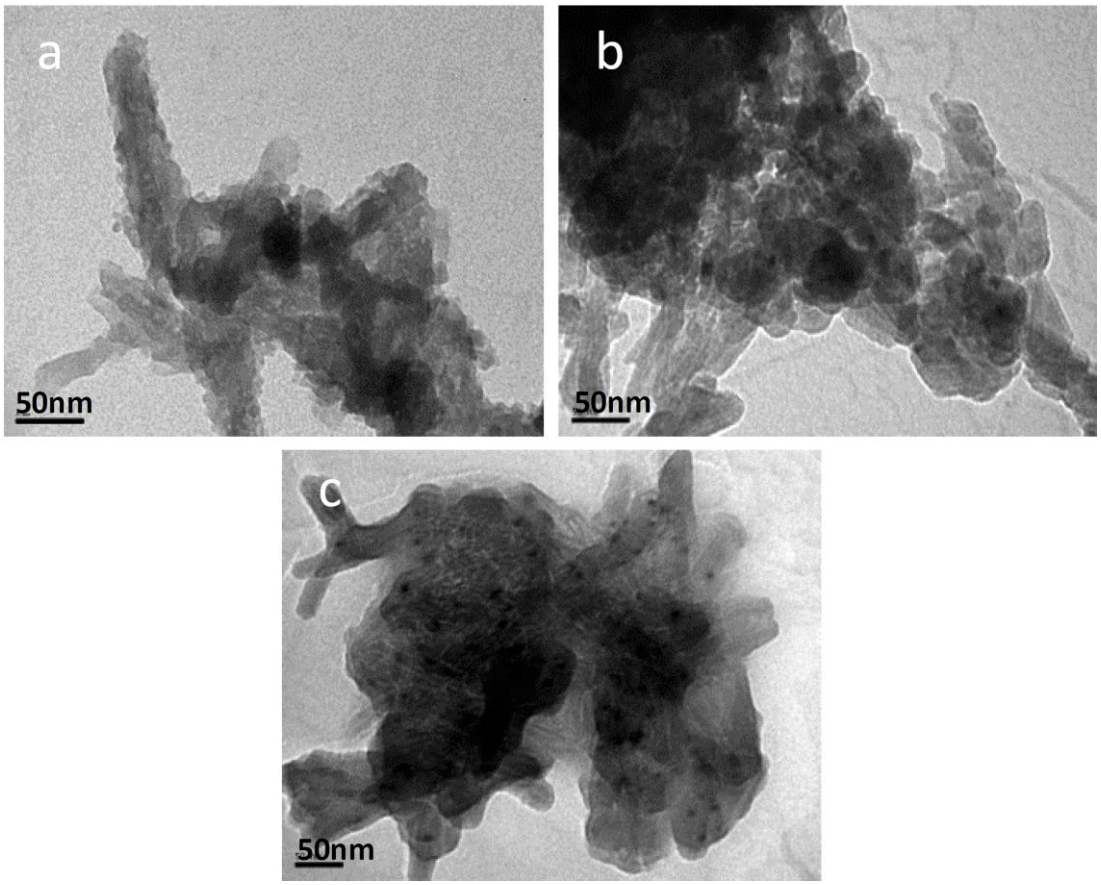

Figure 4. 21: TEM micrographs of BG65 sol-gel derived bioactive glass nanoparticles heat treated to (a) 150 °C, (b) 500 °C and (c) 680 °C.

Changes in BG65 nanoparticle morphology was examined using TEM, as shown in Figure 4. 21. The heat treated sample of BG65 at low temperature (150 °C) (Figure 4. 21a) showed needle-like nanoparticles with a rough surface texture. Closer examination revealed that the nanoparticles consisted of an agglomeration of smaller particles approximately 5 nm in diameter. These particles, termed secondary particles, were consistent with the evolution of structural units during the sol-gel synthesis of bioactive glass, whereby at low heat treatment temperatures, these secondary particles, which maintain their dimensions from early on in the condensation stages, agglomerated under drying to form the larger needle-like nanoparticles observed [135].

Figure 4. 21b and c showed heat treated BG65 nanoparticles at a temperature of 500 °C and 680 °C respectively. The nanoparticles appeared to have a smoother surface texture without defined secondary particles aggregation. A temperature of at least 400 °C is required to cause viscous flow between the secondary particles, fusing to become larger tertiary particles [134, 208]. Therefore, the nanoparticles observed in Figure 4. 21b and c represent tertiary particles, which would appear to be slightly larger than the nanoparticles heat treated at 150 °C due to the fusion of secondary particles. Figure 4. 21c show nanoparticles which appear to be denser, corroborating with the N_2 sorption results, which suggested a reduction in the interstitial spaces between the agglomerated secondary particles which form the pore size and pore volume of the tertiary particles due to higher sintering temperatures [135, 181].

The selection of different heat treatment temperature was done based on critical stages in the bioactive glass evolution. Briefly, 150 °C was selected as the minimum temperature required for N_2 sorption sample preparation. Previous studies on the effects of sintering on bioactive glass structure and calcium distribution have shown that sol-gel derived bioactive glasses must be heat treated to above 400 °C for the incorporation of calcium into the silicate network and above 600 °C for the complete removal of nitrate but above 800 °C, crystallisation of the glass takes place [7, 135, 142, 163]. Hence, at 150 °C, it was expected that no changes in the silicate network would have occurred at this stage. At 400 °C and 500 °C respectively, calcium would have entered the silicate network to form Si – O – Ca bonds and nitrates would have started to decompose. Thus, for both compositions (BG50 and BG65), as heat treatment temperature increased from 150 °C to 500 °C, the total volume of N_2 adsorbed increased (Figure 4. 18). This increase was also matched with an increase of total pore volume, which was in agreement with the removal of nitrate and other impurities, creating more interstitial voids in-between the network of secondary particles [135, 142].

The maximum sintering temperature of the bioactive glasses was limited to 680 °C because studies have shown that glasses treated at this temperature, network connectivity was the lowest with the highest content of Si – OH groups, which would promote bioactivity, due to the favourable negative surface charge of silinol which

induces the adsorption of calcium and phosphate ions, leading to the precipitation of apatite [142, 158, 181]. At temperatures of 680 °C, both BG50 and BG65 glasses exhibited a decrease in total pore volume, also seen by the isotherms with the lowest volume of adsorbed N_2. At this temperature, viscous flow of the secondary particles occurred, fusing together, reducing the interstitial spaces between the particles [208]. These results highlight the effects of heat treatment temperatures on the evolution of bioactive glass nanostructure, thus providing further understanding on the control of bioactive glass nanoparticle morphology.

4.6 *In vitro* studies

To reveal the effects of changes in glass composition on the ionic release of Ca^{2+} ions, ISE measurements were carried out on the supernatants containing the respective nanoparticles, as shown in Figure 4. 22. Results indicated a burst ionic release within the first 2 h of immersion, with BG35 releasing the highest concentration of Ca^{2+} ions, followed by BG50, BG65 and the lowest release was recorded from BG80 nanoparticles. As the immersion of the nanoparticles proceeded, the cumulative amounts of ionic release by each nanoparticle type increased, reaching a maximum concentration at day 7. After 7 days, the total concentration of Ca^{2+} ions detected in the supernatants decreased.

Comparing the release concentration between each bioactive glass variant, a direct relationship could be drawn between the release concentration and glass composition. Through the dissolution of the glass network, glasses with a higher content of calcium would lead to a larger proportion of Ca^{2+} ions being released. Such results were also noted by Martinez *et al*. [206], in which higher calcium containing binary glasses released greater amounts of calcium ions into its surroundings after 24 h. Furthermore, it was established that the decrease of calcium concentration in the immersion fluid was attributed to the consumption of calcium and phosphate ions through the growth of apatite nuclei [206]. Zhong *et al*. [159] also demonstrated that continued immersion in a controlled environment led to the precipitation of calcium and phosphate ions which were released from the network, forming an apatite structure, thus causing a decrease in the calcium ion concentration from the surrounding fluid.

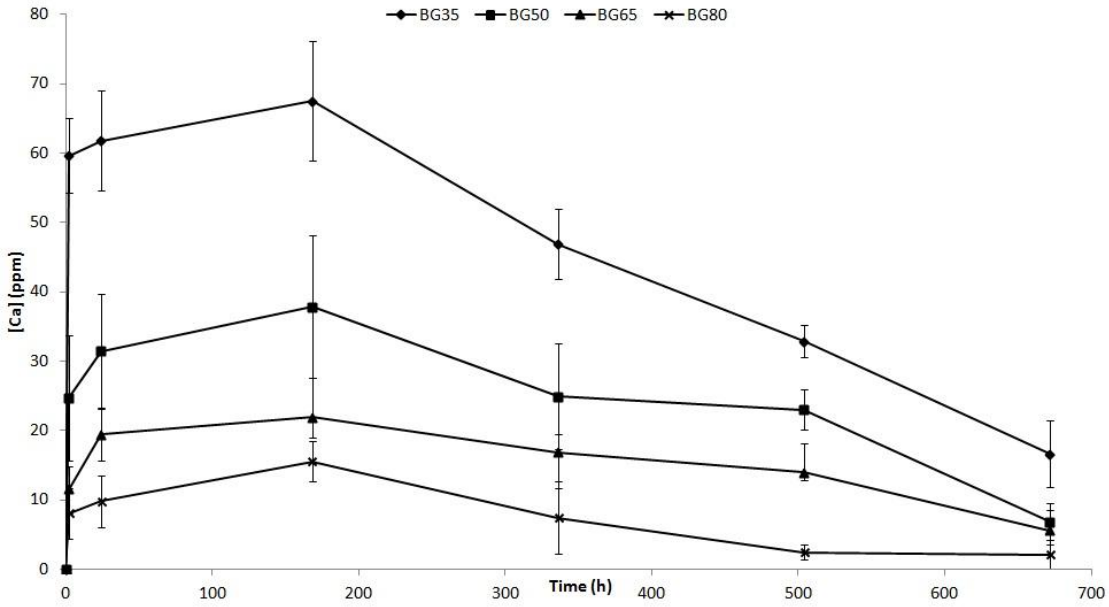

Figure 4. 22: The cumulative release concentration of calcium ions from the different bioactive glass nanoparticles over time in deionised water.

The dissolution of glass begins with the exchange of Ca^{2+} ions with H^{+}, causing the hydrolysis of silicate groups to form silinols (Si – OH). The Si – O – Si bonds of the silicate network is then attacked due to the increase in hydroxyl concentration in the supernatant, creating more silinol groups on the surface of the glass, while releasing soluble $Si(OH)_4$. Continued immersion would then lead to the condensation and repolymerisation of the silinol groups on the surface, forming a silica-rich layer low in cation species. The released Ca^{2+} and PO_4^{3-} groups from the glass are attracted towards this silica-rich layer, re-precipitating to form an apatite structure. As the results shown in Figure 4. 22 represent the cumulative amounts of Ca^{2+} ion release by each nanoparticle type, the decrease in the calcium ion concentration of the supernatants was indicative of the precipitation of calcium and phosphate ions, resulting in a net decrease in the calcium ionic concentration of the supernatant.

The bioactive response of the nanoparticles, observed through the rate of hydroxy-carbonate apatite (HCA) formation, was determined using the SBF model [195]. The FTIR spectra of the sol-gel derived bioactive glass nanoparticles before and after immersion in SBF at various time points are illustrated in Figure 4. 23 Before immersion (0 h), a strong band between the region of 1080 – 1200 cm^{-1} was identified as the asymmetric stretching modes of Si – O – Si, while the band at 470 cm^{-1} was

identified to correspond to the bending mode of Si – O – Si [131, 210, 219]. Another broad band observed at 890 cm^{-1} corresponded to the Si – O – Ca bond, suggesting that after heat treatment at 680 °C, the calcium was successfully introduced into the glass network as a network modifier, forming non-bridging oxygen bonds [131, 152, 159, 164].

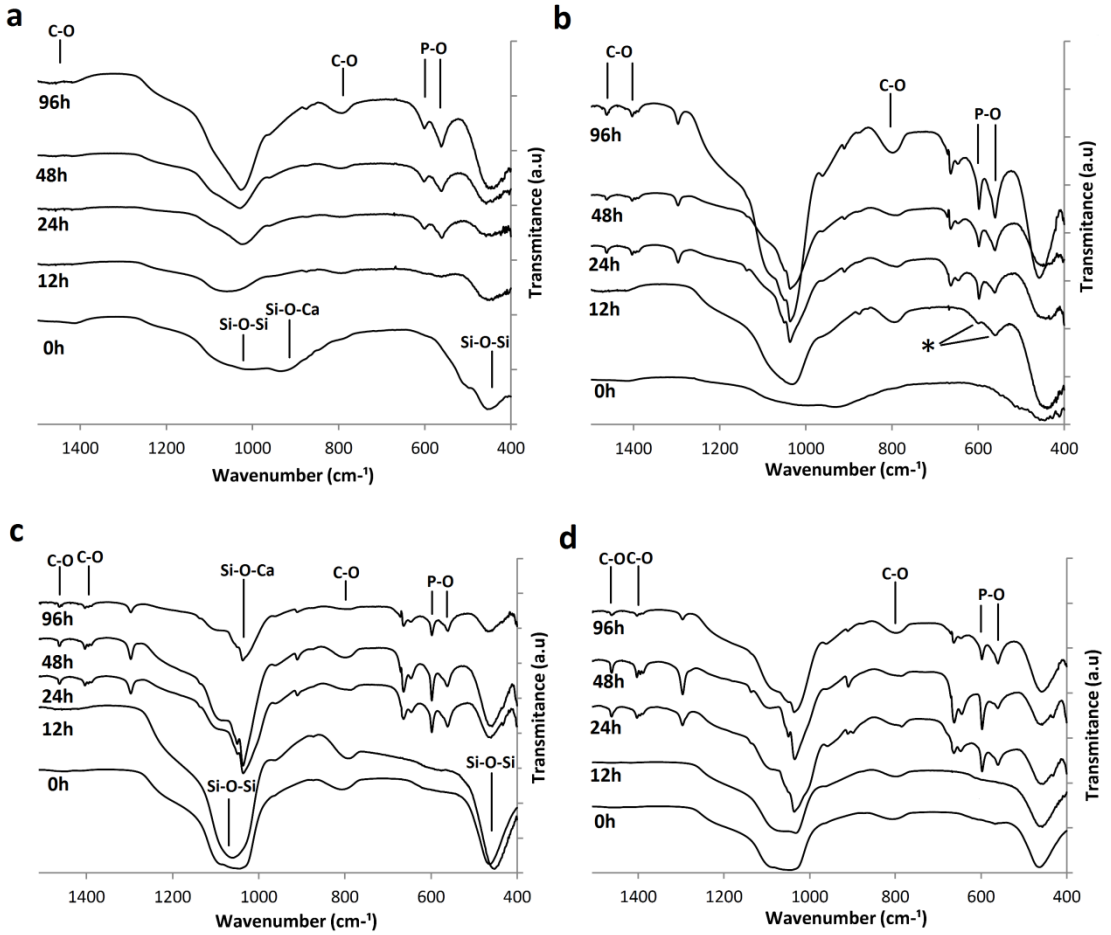

Figure 4. 23: FTIR spectra of BG65 bioactive glass nanoparticles from (a) oven drying and (b) freeze drying; nBG65 bioactive glass nanoparticles from (c) oven drying and (d) freeze drying. Asterisks (*) highlights the rapid appearance of P – O bonds within 12 h

After 12 h of immersion in SBF, a weak twin band in the FTIR spectrum of BG65FD nanoparticles (Figure 4. 23b) was observed to have formed at the wave number 600 cm^{-1} and 570 cm^{-1}. This twin band is associated with the υ_4 antisymmetric bending mode of P – O bonds in the amorphous calcium phosphate [107, 165, 220]. Interestingly, this twin band was not observed in the BG65OD nanoparticle spectrum at this early time point, demonstrating the rapid formation of HCA of within 12 h from

the sol-gel bioactive glass nanoparticles derived from freeze drying. As incubation progressed, the twin bands at 600 cm^{-1} and 570 cm^{-1} appeared on the BG65OD samples, while they intensified on the BG65FD samples. Other sets of peaks also formed, which corroborated with the formation of HCA, and thus indicated the bioactivity of the nanoparticles. Peaks formed at 1460 cm^{-1} and 1420 cm^{-1} after continued immersion was attributed to the formation of C – O bonds. These C – O bonds are from the υ_3 vibration mode of carbonate ions, which have undergone peak splitting [107, 164, 219]. A separate C – O bond was identified at the wave number 780 cm^{-1}, which corresponded to the υ_2 vibrational mode of this bond [211, 219].

Table 4. 6: Detected infrared band positions for HCA over time.

Peak assignment (cm^{-1})	BG65OD		BG65FD		nBG65OD		nBG65FD	
	12 h	24 h	12 h	24 h	12 h	24 h	12 h	24 h
Carbonate υ_3	-	-	-	1460	-	1460	-	1460
Carbonate υ_3	-	-	-	1420	-	1420	-	1420
Carbonate υ_2	-	780	780	780	780	780	780	780
Phosphate υ_4	-	-	-	660	-	660	-	660
Phosphate υ_4	-	-	-	640	-	640	-	640
Phosphate υ_4	-	600	600	600	-	600	-	600
Phosphate υ_4	-	570	570	570	-	570	-	570
Phosphate υ_2	-	470	470	470	-	470	-	470

The FTIR spectra of the nBG nanoparticles before and after immersion in SBF are shown in Figure 4. 23c and d. Prior to immersion (0 days), a strong band in the region of 1080 – 1200 cm^{-1} and at 890 cm^{-1} was observed, which corresponded to the asymmetric stretching modes of Si – O – Si, whilst the band at 470 cm^{-1} corresponded to the bending mode of this group [134, 210, 219]. A Si – O – Ca bond was observed at 960 cm^{-1} [134, 152, 159], suggesting that after thermal treatment at 680 °C, the calcium was introduced into the glass network as a network modifier, forming non-bridging oxygen bonds [135].

After 24 h immersion in SBF, a twin band was observed around the wave number 600 cm^{-1} and 570 cm^{-1} for both nBGOD and nBGFD samples, which corresponded to the υ_4 antisymmetric bending mode of P – O bonds in the amorphous calcium phosphate

[107, 220]. Another set of peaks formed at 1460 cm^{-1} and 1420 cm^{-1} after immersion was attributed to the formation of C – O bonds. These C – O bonds are from the υ_3 vibration mode of carbonate ions, which have undergone peak splitting [136, 219]. The presence of P – O and C – O bonds suggests the formation of HCA and indicates the bioactivity of the nanoparticles [134, 219, 221].

The formation of HCA was further verified by EDX analysis. Figure 4. 24 shows the EDX curves of the bioactive glass nanoparticles before and after immersion in SBF at the 96 h time point. Initially, the curve showed a composition containing higher levels of the element silicon, followed by calcium and then phosphorous, which was in agreement with the composition of the glass. After immersion (Figure 4. 24b), all nanoparticles showed an increase in the elemental contents of calcium and phosphorous and a decrease in the silicon element. The results confirmed the formation of a calcium phosphate-rich phase on the surfaces of these nanoparticles [165, 221].

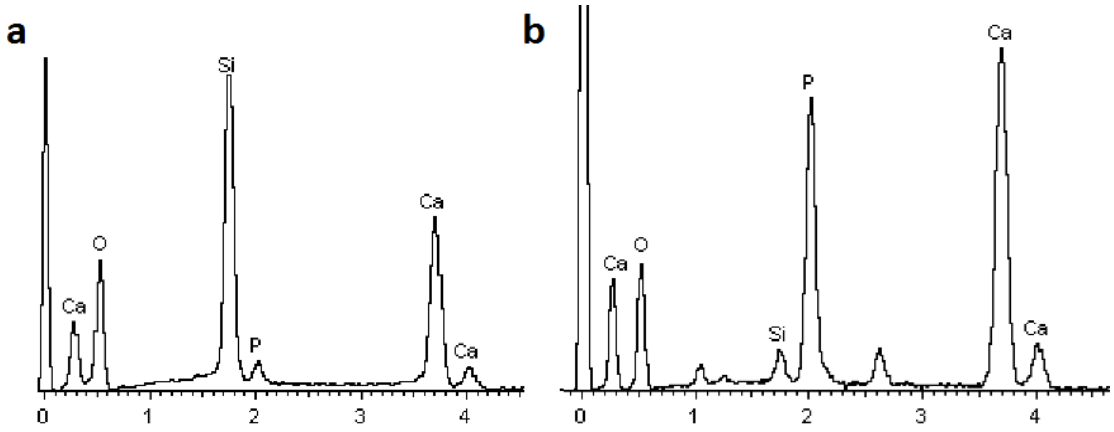

Figure 4. 24: EDX spectra of BG65FD nanoparticles (a) before immersion and (b) after 96 h immersion in SBF.

SEM micrographs presented in Figure 4. 25 show the progression of HCA crystallites growth on the surfaces of the bioactive glass nanoparticles. After 96 h of immersion in SBF (Figure 4. 25a), small cauliflower-like crystals were observed to have formed on the surfaces of the agglomerated bioactive glass nanoparticles. At 7 days (Figure 4. 25b), these cauliflower-like structures had increased in size, forming additional HCA crystallite branches from further nucleation of calcium phosphate.

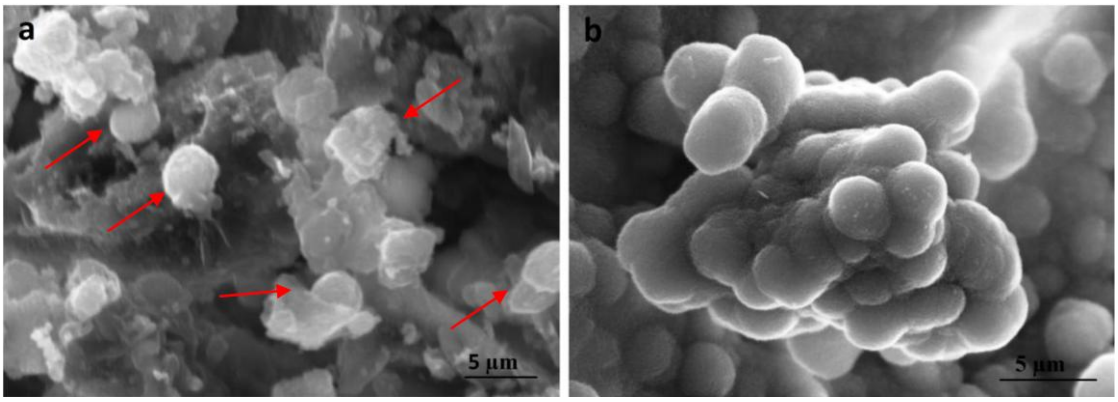

Figure 4. 25: The formation of HCA crystallites (marked by red arrows) on the bioactive glass nanoparticles after (a) 96 h immersion and (b) 7 days immersion in SBF.

The bioactive response of bioactive glass nanoparticles can be enhanced through a combination of composition and nanoparticle morphology [7, 15, 181]. In this study, glasses of the similar composition were studied, therefore, the improvements in the bioactive response can be correlated solely to changes in nanoparticle morphology. The specific surface area (SSA) and pore volume of BG65OD was found to be higher than BG65FD, which would suggest that BG65OD nanoparticles would have a greater glass-solution interface, accelerating its bioactive response [136]. Yet, BG65FD nanoparticles were found to have a faster HCA formation rate than BG65OD nanoparticles, as was summarised in Table 4. 6, which highlighted the detection of carbonate and phosphate bands after 12 h immersion for BG65FD nanoparticles.

One explanation for this could be due to the difference in pore shape and size of these nanoparticles. The larger pore sizes found within BG65FD nanoparticles, combined with the slit-like shaped pores could have improved the penetration of SBF, accelerating the ionic exchange process between the glass and the solution, leading to HCA formation on the surface and also within the nanoparticle [15, 182, 206]. Furthermore, the 'bottleneck'-like shaped pores, with small pore openings found within BG65OD would have hindered fluid flow, leading to poor ion transport. Whereas, the slit-like shaped pores of BG65FD would have created channels, allowing efficient ion transport and diffusion, thus contributing to rapid ionic exchange between the glass-solution interfaces [15, 66, 222]. The drying method did not affect the nanoparticle morphology of nBG65 glasses, with both nBG65OD and nBG65FD containing cylindrical pores. Hence, it was observed that the rate of CHA

formation was similar, in which carbonate and phosphate bands were only observed after 24 h immersion for both samples (Table 4. 6).

These results confirm the bioactive nature of the bioactive glass nanoparticles synthesised by the sol-gel route and the multi-step route, and successfully show an improvement in the HCA formation rate through changes in the nanostructure of these nanoparticles due to freeze drying. It is clear that the bioactive response of bioactive glasses is determined not only by their composition and SSA, but also by their pore shape and size.

4.7 Summary

Four compositions of ternary sol-gel derived glasses, namely BG35, BG50, BG65 and BG80 were synthesised. EDX results confirmed the different concentration of Si and Ca within each glass type, while XRF showed that the components of SiO_2 and P_2O_5 were close to the nominal values while CaO was on average 7 wt. % lower across all compositions than the nominal values. This was due to the leaching of Ca^{2+} ions during the aging and dry stages into the pore liquor. FTIR analysis further confirmed changes in the functional groups within the glasses through the merging of peaks around 1040 cm^{-1} to 1200 cm^{-1} and the absence of the Si – O – Ca bond in high silica content glass (BG80).

Nanoparticles containing higher amounts of calcium (BG35 and BG50) were found to contain crystalline phases, which were identified to be wollastonite and hydroxyapatite. An incipient amount of the SiO_2 crystalline phase of cristobalite was determined in the high silica content BG80 glass. The use of N_2 sorption and TEM analysis showed that both BG35 and BG50 nanoparticles contained dual-modal pore diameter morphology, with two distinct pore diameter regions of < 2 nm and 15 – 35 nm. The isotherms of these two glass types were classified as Type IV with a H1 hysteresis loop. This was correlated to be open-ended cylindrical pores, which was observed under TEM to be of a spherical shape, due to the two-dimensional projection of the images. The isotherms of BG80 were defined as Type IV with a narrow H2

hysteresis loop, which suggested the nanoparticles contained poorly connected, not well defined cylindrical micropores.

The direct comparison between sol-gel (acid) derived and multi-step (alkali) derived bioactive glass of similar composition (BG65 and nBG65 respectively) revealed that the polymerisation stages during synthesis play an important role in the final nanoparticle shape and nanostructure. Sol-gel derived nanoparticles were heterogeneous in shape, while multi-step derived nanoparticles were spherical with diameters ranging from 30 – 90 nm. The difference in nanoparticle shape was due to the difference in polymer growth during the hydrolysis and condensation of the sol. The progression of polymer growth under acidic conditions are of a linear form, while under basic conditions, the growth becomes highly branched and clustered.

Oven, vacuum and freeze drying were employed to process these nanoparticles with results suggesting that different drying methods can alter the final nanoparticle morphology. This was especially evident in sol-gel derived bioactive glass nanoparticles, whereby isotherm analysis showed that the nanoparticle morphology of freeze dried nanoparticles (BG65FD) was profoundly different that those of oven (BG65OD) and vacuum dried (BG65VC) nanoparticles (Type IV, H3/H4 and Type IV, H2 respectively). This suggested BG65FD contained pores formed from the aggregate of plate-like particles while both oven and vacuum dried nanoparticles contained less defined cylindrical-'ink bottle'-like shaped mesopores. Additionally, the unit pore geometry within individual nanoparticles was determined by comparing the BJH adsorption and desorption branches. The results indicated that the mesopores of BG65OD had a consistent throat size, with differently sized 'bodies', akin to bottles of different sizes but with similar necks. BG65FD revealed slit- or wedge-like shaped mesopores. Changes in mesopore shape were attributed to the ice-crystal formation process, during which pore shape was tailored from the direction of the cold front. The SSA of BG65FD were also found to be half that of BG65OD.

A decrease in pore size and pore volume was observed with the increase in maximum sintering temperature, attributed to the densification of the network from the fusion of secondary particles. However the viscous flow and fusion of these smaller secondary

particles (5 – 8 nm) into tertiary particles did not affect the final mesopore shape of the nanoparticles.

Through *in vitro* bioactivity testing, the differences in nanostructure from the effects of freeze drying improved the reactivity of BG65FD to SBF. The formation of hydroxy-carbonate apatite (HCA) was noticed after 12 h immersion, while HCA formation on BG65OD occurred only after 24 h. The collective difference in average pore size of BG65FD (4 nm) to BG65OD (3.1 nm) and pore shape (slit-like shaped pores of BG65FD) was found to improve the penetration and fluid flow of SBF within BG65FD nanoparticles. This led to increased glass-solution contact, promoting faster ionic exchange between Ca^{2+} and H^{+} in SBF, thus rapidly initiating the bioactivity mechanism. Since the drying stage did not influence the nanoparticle morphology of nBG65 nanoparticles, HCA growth was only detected after 24 h for both oven and freeze dried nBG65 nanoparticles. This confirmed the effects of changes in nanoparticle morphology, and specifically pore shape and size on the bioactive response of nanoparticles.

These findings suggest that changes in glass composition and heat treatment regimes affected the crystal structure and morphology of the nanoparticles. Furthermore, the pore shape was found to replicate ice crystal formation, which was evident in BG65 nanoparticles. Therefore, although it was possible to alter the pore shape through freeze drying, the effects of composition also played a vital role in the control of nanoparticle shape. The influence of heat treatment was also significant with changes seen on pore size and volume; however, the shapes of the pores remained unchanged.

Chapter 5

Mesoporous bioactive glass nanoparticles as ionic cross-linker nanocarriers for composite scaffold synthesis

5.1 Introduction

Alginate hydrogels are widely used in tissue engineering research due to its low cost and biocompatible nature [46, 86]. Typically, ionic cross-linkers, such as calcium chloride or calcium sulphate are used for the synthesis of hydrogels [47]. However, the gelation kinetics is difficult to control due to the rapid gelation induced by these cross-linkers, resulting in poor structural uniformity and a varying degree of cross-linking within the hydrogel [82]. Controllability is essential for the development of scaffolds for tissue engineering because, a controlled gelation rate will allow for structural homogeneity. This is crucial to ensure uniform pore sizes, porosity and interconnectivity as well as improved mechanical properties of the scaffold. Furthermore, the consistency and reproducibility of uniform scaffolds would warrant a successful application in bone tissue engineering, which requires nutrient uptake and transport, structural integrity and mechanical predictability.

In the literature survey, the affinity of different divalent ions towards alginate, and its effects on final hydrogel properties was discussed [90, 96]. Furthermore, the therapeutic properties of divalent ions such as strontium and copper ions were reviewed. Briefly, strontium was highlighted for its ability to stimulate bone formation, while copper is known for its antimicrobial properties [102, 109].

In this chapter, mesoporous bioactive glass nanoparticles have been employed as ionic cross-linker nanocarriers to deliver divalent ions required to cross-link alginate for the synthesis of alginate-bioactive glass composite scaffolds. This study was stimulated by the notion of using bioactive glass nanoparticles as a source of Ca^{2+} ions for the ionic cross-linking of alginate. In Chapter 4, it was discussed that the diffusion of calcium into the glass network required a sintering temperature of at least 400 °C.

Thus, the first objective was to study the effects of the different sintering temperatures of the bioactive glass nanoparticles on the gelation characteristics of alginate solutions.

Since the synthesis of consistent and reproducible homogenous scaffolds is vital, the overall aim of this chapter was to devise a strategy in which the gelation kinetics of alginate could be controlled. Derived mesoporous bioactive glass nanoparticles of various compositions (BG35, BG50, BG65 and nBG65) demonstrated different nanoparticle morphology. For instance, BG35 and BG50 contained a dual-pore size morphology, while BG65 and nBG65 recorded the highest specific surface area (SSA) and largest pore diameter respectively.

Therefore, one aim was to study the effects of nanoparticle morphology on its ability to uptake divalent ions for its role as nanocarriers to cross-link alginate. Additionally, the divalent ions of strontium and copper, with calcium as the control, were studied with respect to their effects on gelation kinetics. It was hypothesised that three individual variables would affect the gelation kinetics of alginate: I) heat treatment of bioactive glass nanoparticles, II) nanocarrier morphology, III) type of cross-linker ion. These were investigated in this chapter.

5.2 Composite material fabrication

The feasibility of employing bioactive glass nanoparticles produced through the sol-gel route (BG35, BG50, BG65) and the multi-step route (nBG65) discussed in Chapter 4, as nanocarriers for the ionic cross-linking of alginate was investigated by using 2 – 6 (wt. %) alginate solutions. 0.05 – 1 M concentration of strontium chloride ($SrCl_2$), copper chloride ($CuCl_2$) and calcium chloride ($CaCl_2$) ionic cross-linking solutions were prepared and their physical properties (density, surface tension and viscosity) measured, according to the protocols described in Section 3.8. The bioactive glass nanoparticles used as nanocarriers were loaded through impregnation with ionic cross-linking solutions of $SrCl_2$, $CuCl_2$ and $CaCl_2$, using a nanocarrier to solution ratio of 10 mg/mL [223]. For a typical experiment, 0.5 g BGX (X = Sr, Cu, Ca) was mixed with 50 mL of the ionic solution (XCl_2). The mixture was then vortexed for 2 min before

filtration. The filtered solids were then dried and ground to a fine powder. The impregnation efficiency (uptake concentration) of the nanocarriers was determined using energy-dispersive X-ray (EDX). The different impregnated nanocarriers, containing the respective ions (Sr^{2+}, Cu^{2+}, Ca^{2+}) is summarised in Table 5. 1.

Table 5. 1: Nanocarrier designation, corresponding to the properties of the different bioactive glass nanoparticles, produced via impregnation with different cross-linking solutions.

Nanocarrier	Properties	Loading concentration (M)
BGSr	BG65 impregnated with $SrCl_2$	0.05 – 1
BGCu	BG65 impregnated with $CuCl_2$	0.3 – 1
BGCa	BG65 impregnated with $CaCl_2$	0.1 – 1
BG0.5Sr	BG65 impregnated with $SrCl_2$	0.5
BG0.5Cu	BG65 impregnated with $CuCl_2$	0.5
BG0.5Ca	BG65 impregnated with $CaCl_2$	0.5
BG35CL-Ca	BG35 impregnated with $CaCl_2$	0.1 – 1
BG50CL-Ca	BG50 impregnated with $CaCl_2$	0.1 – 1
nBG65CL-Ca	nBG65 impregnated with $CaCl_2$	0.1 – 1

Composite hydrogels were ionically cross-linked using the variously loaded nanocarriers, compiled in Table 5. 1. The typical preparation for a cylindrical scaffold is described as follows. In a clear vial with a diameter of 15 mm, BGX (X = Sr, Cu, Ca) was weighed and suspended in 1 mL deionised water using a sonicator (Branson 250) for 20 s. 1 mL of the alginate solution was then pipetted into the vial, and the mixture vigorously stirred until homogenous. Gelation time was determined when the mixture no longer flowed when the vial was tilted at 45º [47]. The gelation of the alginate was carried out under ambient conditions and the averages and standard deviations (SD) of triplets were reported. Table 5. 2 summarises the different scaffold compositions studied.

Table 5. 2: Weights used for the synthesis of composite scaffolds with different glass nanocarrier (G) to alginate solution (A) ratios.

G/A ratio	Weight concentration of BGX (wt. %)	Weight concentration of alginate solution (wt. %)	Total volume of composite slurry (mL)
40:60	4	6	2
60:40	6	4	2
80:20	8	2	2

5.3 Interaction between alginate and differently sintered bioactive glasses

The influence of BG35, BG50, BG65 and nBG65 bioactive glass nanoparticles processed by different heat treatment regimes on the gelation kinetics of alginate was investigated. Two interdependent variables were studied: I) the effects of bioactive glass composition and nanoparticle morphology and II) the effects of maximum sintering temperature of the bioactive glasses.

Figure 5. 1 shows the gelation time of alginate solutions by different bioactive glass nanoparticles sintered at 150 °C, 400 °C and 500 °C. No specific trends were observed in the gelation rate of alginate, with complete gelation occurring within 5 min across all bioactive glasses sintered between 150 °C and 400 °C. Glasses sintered at 500 °C showed some differences, with nBG65 nanoparticles requiring the longest time to cross-link the alginate solution.

Initially, it was expected that the time taken to complete gelation would have decreased as the calcium content of the bioactive glasses increased, from BG35 to BG65. However, results indicated that the composition of the glass was not solely a determining factor in the gelation rate of alginate. One explanation for this was attributed to a balance between specific surface area (SSA) and calcium content. Nanoparticles with a higher SSA would increase the glass-alginate interfacial contact and consequently, higher amounts of Ca^{2+} ions would come into contact with the alginate, thus leading to rapid cross-linking [15, 135]. BG35 was found to have the

highest calcium content with the lowest SSA while BG65 had the lowest calcium content but the highest SSA (Table 5. 3). Hence, the net effect of SSA and composition on the cross-linking rate of alginate meant that both BG35 and BG65 (sintered at 500 °C) cross-linked the alginate within the shortest time.

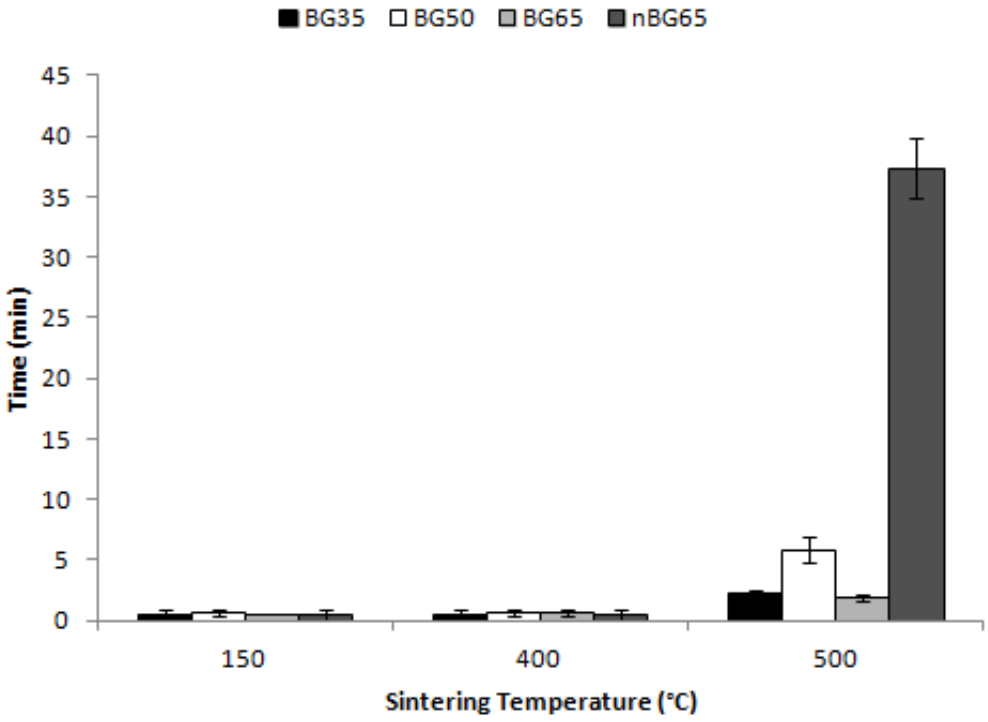

Figure 5. 1: Gelation time of alginate across 3 sintering temperatures for BG35, BG50, BG65 and nBG65 respectively. Data represents the mean ± SD, n = 3.

Interestingly, Figure 5. 1 showed that the gelation rate of alginate by BG65 and nBG65 was different, even though both were of similar composition. Since nBG65 had a lower SSA than BG65 (Table 5. 3), it would suggest that nanoparticle SSA was a contributing factor to the gelation rate of alginate. Furthermore, another reason could be attributed to the stability of nBG65. Results from Chapter 4 had pointed towards a tightly packed, highly branched silicate polymer network. Therefore, this could explain the differences in gelation time of alginate between BG65 and nBG65, owing to the stability of the silicate network, which in turn controls the release of Ca^{2+} ions through dissolution [136, 214].

The effects of BG65 nanoparticles sintered at temperatures between the ranges of 50 – 680 ºC on alginate gelation time is shown in Figure 5. 2. The corresponding Ca^{2+} ionic concentration, released from the bioactive glass nanoparticles sintered within that temperature range was also measured. The results indicated that an increase in sintering temperature led to a decrease in Ca^{2+} ionic concentration, while a sharp rise in gelation time (from 5 min to 5 h) was recorded between the temperatures of 500 – 560 ºC, with alginate being partially gelled after extended periods (> 5 h) of exposure to the bioactive glass nanoparticles.

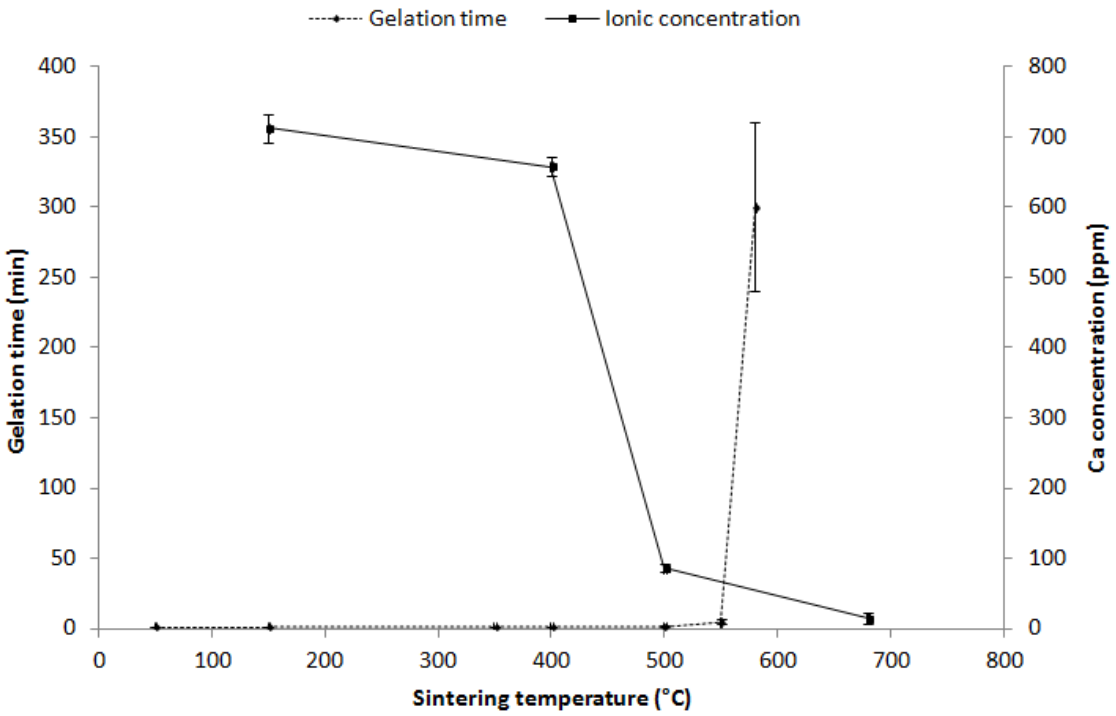

Figure 5. 2: The gelation rate of alginate solution and corresponding calcium ion concentration measured of BG65 nanoparticles sintered at various temperatures. Data represents the mean ± SD, n ≥ 3.

Table 5. 3: The SSA, pore width and pore volume of the various nanoparticle carriers synthesised.

Sample	BG35	BG50	BG65	nBG65
SSA (m^2/g)	17.9	33.2	115.7	73.0
Pore diameter (nm)	8.3	6.4	4.0	11.3
Pore volume (cm^3/g)	0.04	0.04	0.09	0.19

The diffusion of calcium into the silicate network of sol-gel bioactive glasses occurs at temperatures above 400 °C while a temperature above 560 ºC is required for the decomposition of nitrate [135, 163]. Prior to diffusion, the loose Ca^{2+} ions are deposited on the surface of the silicate network, and hence easily soluble when introduced in water. The rapid gelation (< 5 min) of alginate for temperatures below 500 ºC can be attributed to a large proportion of pre-diffused calcium in BG65, while the rapid loss in cross-linking ability above 560 ºC is likely due to the decomposition of nitrate, resulting in the complete diffusion of calcium into the glass network [7, 135]. The significant decrease of Ca^{2+} ions from 700 ppm to less than 100 ppm between the temperatures of 150 ºC and 500 ºC, shown in Figure 5. 2, confirms the mechanism of Ca^{2+} ion diffusion into the silicate network.

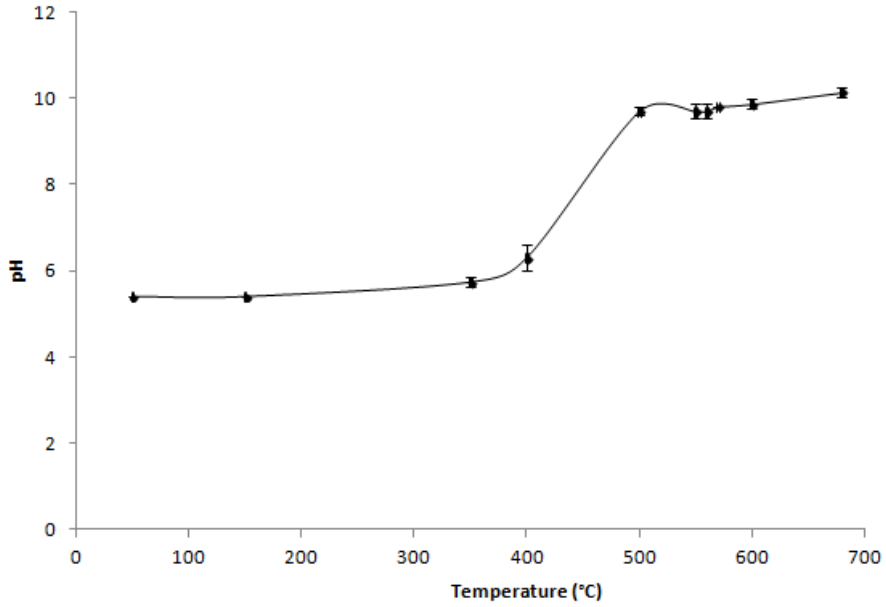

Figure 5. 3: pH levels of the supernatant containing BG65 nanoparticles sintered at various temperatures in deionised water sampled after 1 h incubation. Data represents the mean ± SD, n = 3.

Figure 5. 3 shows that pH levels of the supernatant (containing BG65 nanoparticles in deionised water) remained relatively acidic (≈ pH 4) for nanoparticles sintered at temperatures below 400 °C, with an increase in pH from acidic to alkali observed between 400 °C and 500 °C. This results would suggest changes in the silicate network with diffusion of calcium firstly occurring followed by the decomposition of

nitrate, since the lost of nitrate ions (NO_3^-) causes the number of free H^+ ions to decrease [135, 163].

Studies have demonstrated that a controlled release of Ca^{2+} ions led to improved hydrogel structure integrity and uniformity, which were found to improve the mechanical properties of the overall alginate hydrogel [47]. The increase in gelation time between 500 ºC and 560 ºC (Figure 5. 2) initially pointed towards the possibility of tailoring gelation rates through temperature control. Therefore, the sintering temperature of the nanoparticles was increased step-wise, at 10 ºC increments, to systematically record the gelation responses of alginate. However, the results indicated that gelation kinetics was uncontrolled beyond the sintering temperature of 500 ºC.

Nevertheless, the concept of using bioactive glass nanoparticles for ionic cross-linking was further developed through its application as a nanocarrier for the delivery of cross-linking ions. Instead of relying on the leaching of Ca^{2+} ions which were loosely bound to the glass network as the source for cross-linking alginate, sintered bioactive glass nanoparticles to the optimised temperature of 680 ºC [142], were impregnated with cross-linking ions. The feasibility of using this novel method for the gelation of alginate was subsequently studied.

5.4 Nanocarrier impregnation

5.4.1 Loading analysis

Mesoporous bioactive glass nanoparticles (BG35, BG50, BG65 and nBG65), termed nanocarriers were impregnated with cross-linking ions of Sr^{2+}, Cu^{2+} and Ca^{2+}. Two parameters were studied, which were hypothesised to affect impregnation: I) cross-linker ion type and II) morphology of the nanocarriers.

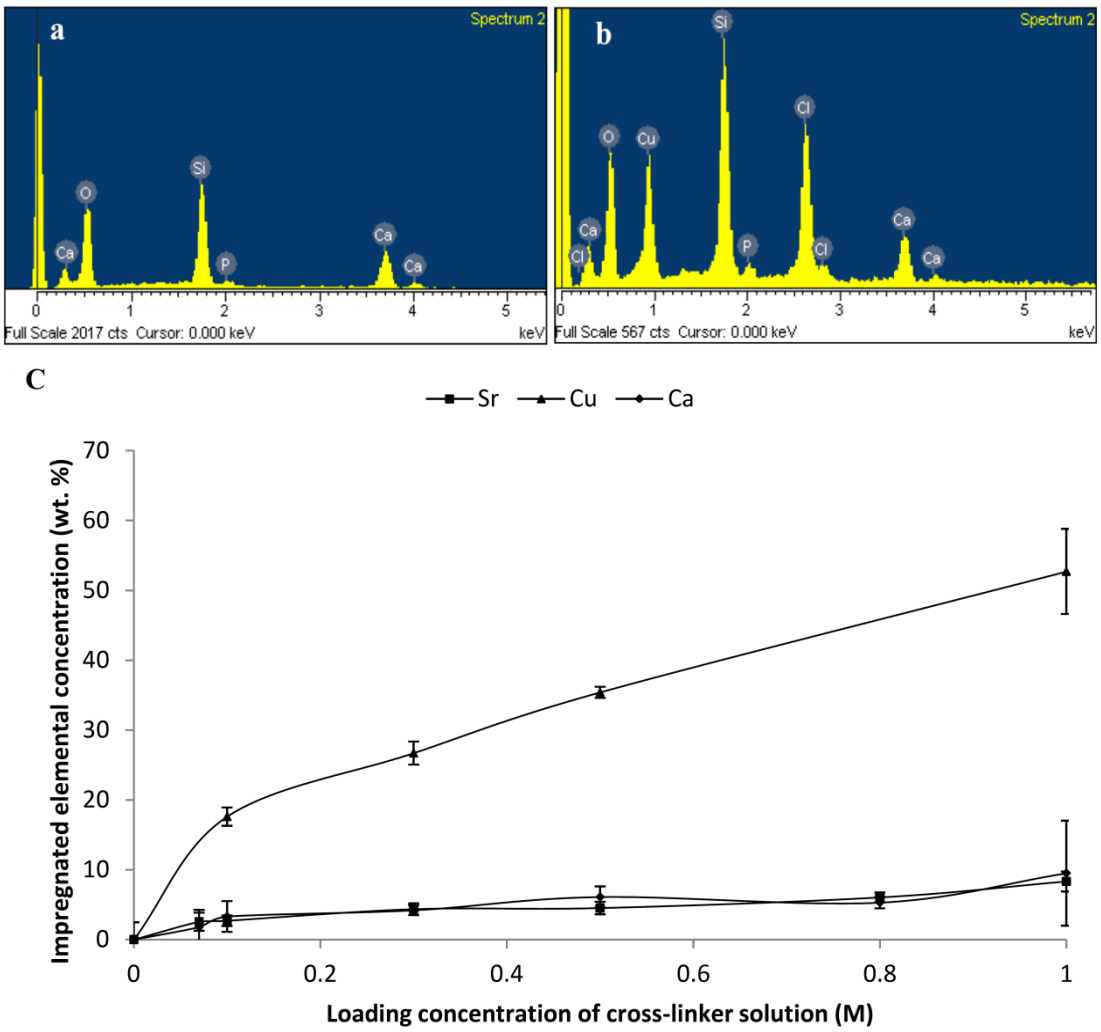

Figure 5. 4: EDX spectra of (a) unloaded nanocarrier, (b) the presence of copper and chloride elements after impregnation with 0.5 M of $CuCl_2$ solution and (c) the corresponding EDX measured elemental concentration of the impregnated cross-linking ions of strontium (Sr), copper (Cu) and calcium (Ca) at various initial cross-linker solution loading concentration. Data represents the mean ± SD, n = 5.

The loading of the nanocarriers with the specific cross-linker solutions of $SrCl_2$, $CuCl_2$ and $CaCl_2$ was measured by EDX and shown in Figure 5. 4. A comparison of spectra between the nanocarrier (BG65 nanoparticles) before and after impregnation with $CuCl_2$ solution (Figure 5. 4a and b), demonstrated that the elemental peaks of Si, Ca and P, corresponding to the nanocarrier composition, was present in both spectra, with the additional presence of the loaded ions Cu and Cl peaks, respectively after impregnation. Quantitative EDX analysis of the loaded nanocarriers in Figure 5. 4c revealed an increase in the elemental concentration of Sr, Cu and Ca, respectively, with an increase in the loading concentration of the cross-linker solution. This was

expected as final loading capacity of a carrier is dependent on loading concentration, since a higher concentration would permit more ions to come into contact with the surfaces of the carrier for a given area [15, 173]. Interestingly, the amount of Cu adsorbed was significantly higher. For instance, at similar impregnation concentrations of 0.5 M, the impregnated element of Cu was recorded to be 8 times higher than both Sr and Ca.

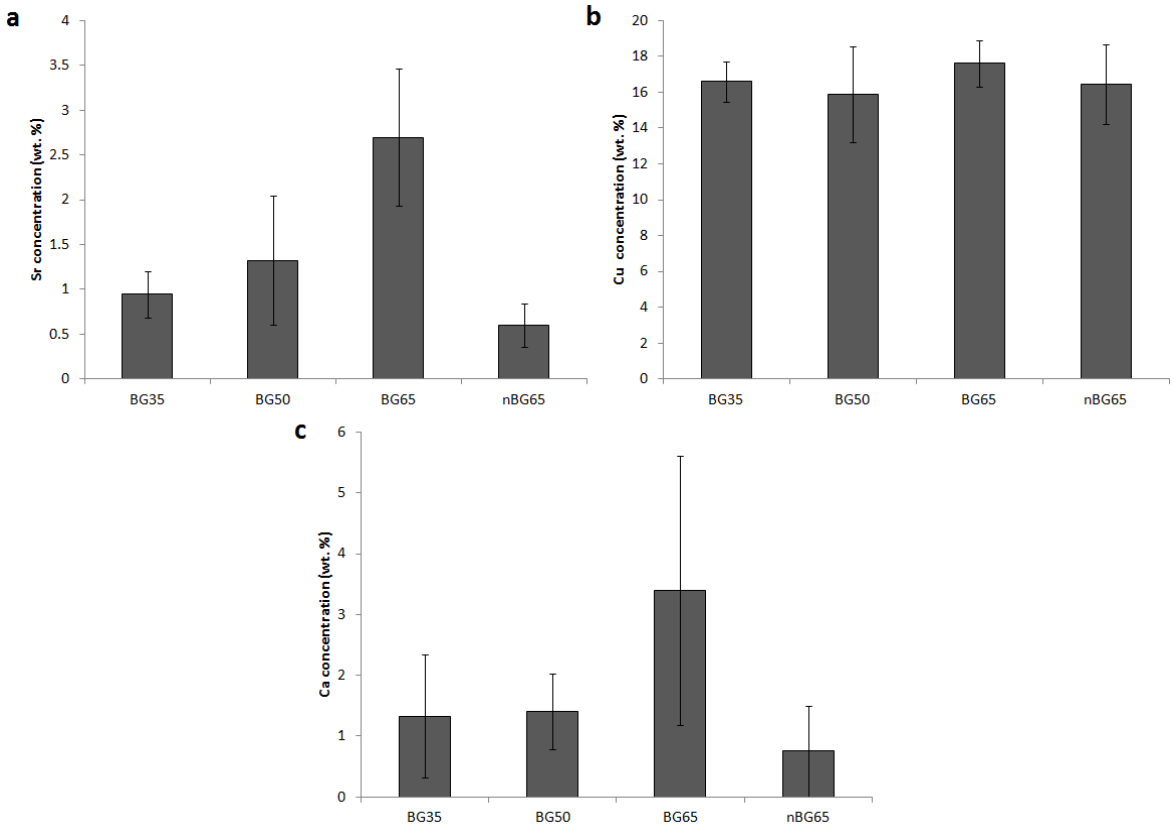

Figure 5. 5: Loading efficiency of BG35, BG50, BG65 and nBG65 nanoparticle carriers measured by EDX, through the initial loading of 0.1 M cross-linker solutions a) $SrCl_2$, b) $CuCl_2$ and c) $CaCl_2$. EDX measurements of Ca loaded nanocarriers have been normalised against respective unloaded nanocarrier Ca elemental concentrations. Data represents the mean ± SD, n = 5.

The effects of nanocarrier textural features on ionic loading capabilities were examined through a standard impregnation concentration of 0.1 M of the ionic cross-linking solution. Figure 5. 5 shows the loading efficiency of Sr^{2+}, Cu^{2+} and Ca^{2+} ions onto the four nanocarrier types (BG35, BG50, BG65 and nBG65 respectively) analysed using EDX. Results showed that BG65 nanocarriers were incorporated with

the highest concentration of cross-linking ions, while the impregnation efficiency of nBG65 nanocarriers was the lowest.

The mechanisms of loading dictate that without specific tailoring of the carrier to the intended load, such as through functionalisation of the surfaces to improve the interactions between the carrier and the host molecule, generally, the loading capacity of the nanocarrier is dependent on SSA and pore volume [15, 173]. Studies on the impregnation efficiency of mesoporous nanocarriers suggests that higher SSA and pore volumes would increase the contact surface between the porous matrix and the intended load molecule, thus allowing large quantities of the intended load to be incorporated into the carrier by adsorption onto the pore walls, increasing the loading amount [14, 168, 176, 223]. BG65 nanocarriers were found to have the highest SSA (Table 5. 3), which would explain its ability to uptake the largest quantity of ions as seen in Figure 5. 5.

In order to understand the reason behind the differences in impregnation efficiency between the different ions and the nanocarrier, fundamental physical properties of the cross-linking solutions were examined. Table 5. 4 summarises the density, dynamic viscosity and surface tension of $SrCl_2$, $CuCl_2$ and $CaCl_2$ at various concentrations. Similar trends were observed across all cross-linker types, whereby, increases in solution concentration led to an overall increase in density, dynamic viscosity and surface tension. An increase in ionic concentration meant that more solutes were dissolved per volume, hence an increase in cross-linker concentration led to a proportional increase in density of the fluid [198].

Dynamic viscosity, which is the measure of resistance of the cross-linker solutions to shear force, is a function of density and the velocity of the fluid flow through a restricted cross-section [198]. Since an increase in concentration led to an increase in density as well as an increase in the time taken for the fluid to flow through the restricted cross-section of the viscometer, dynamic viscosity was found to increase. Surface tension was measured through the capillary rise method and is a function of density of the fluid and the change in height of the fluid within a capillary tube [197]. Similarly, increases in cross-linker concentration led to an increase in overall surface

tension of the fluid. Therefore, the behaviour of the different cross-linker solutions observed through changes in dynamic viscosity and surface tension with changes in concentration were comparable, and thus would not have attributed to the differences in loading efficiency.

Table 5. 4: Density, dynamic viscosity and surface tension of cross-linker solutions. Data represents the mean ± SD, n = 3.

Cross-linker concentration (M)	Density (kgm^{-3})			Dynamic viscosity (Pa.s) $\times 10^{-3}$			Surface tension (Nm^{-1}) $\times 10^{-3}$		
	$SrCl_2$	$CuCl_2$	$CaCl_2$	$SrCl_2$	$CuCl_2$	$CaCl_2$	$SrCl_2$	$CuCl_2$	$CaCl_2$
0.1	1025	1011	1009	1.0 ± 0.0	1.0 ± 0.0	1.0 ± 0.1	76.9 ± 4.7	85.3 ± 2.7	70.9 ± 1.5
0.5	1131	1065	1053	1.2 ± 0.0	1.2 ± 0.1	1.1 ± 0.2	79.5 ± 2.4	89.9 ± 2.9	88.8 ± 3.0
1.0	1265	1132	1109	1.5 ± 0.1	1.4 ± 0.1	1.3 ± 0.2	83.0 ± 5.1	95.5 ± 3.0	109 ± 3.0

Table 5. 5: Elements of the cross-linkers, its corresponding symbol, ionic charge and radius [224].

Element name	Symbol	Ionic charge	Ionic radius (nm)
Strontium	Sr	2+	0. 118
Copper	Cu	2+	0.73
Calcium	Ca	2+	0.1
Chlorine	Cl	1-	0.167

The ionic radii of the cross-linker ions was also considered to establish if any influence on loading efficiency was due to ionic movement and diffusion within and out of the nanoparticle micropores. Table 5. 5 shows the ions used in the cross-linker solutions and its corresponding ionic radius. The values indicated that copper had the smallest ionic radii among the three ions used for cross-linking. The average pore size of the nanocarrier (BG65) was found to be 4 nm in diameter. However, isotherm analysis showed that BG65 also contained micropores (< 1.7 nm in diameter). Although all the ions used had diameters smaller than these pores, the mobility of ions

is influenced by its size, and thus this suggested that copper ions were essentially more mobile [197]. Furthermore, copper is a transitional element, thus having an incomplete d-orbital, and is known to form ligands when exposed to water through hyberdisation in which, dative bonds from the water molecule fill in the incomplete d-orbital.

Up to a maximum of 6 water molecules can form dative bonds with a single copper ion, thus forming a large ligand structure [225]. Pore diameters have been found to influence the adsorption of molecules, whereby the pores act as size-selective barriers, allowing molecules of a certain size to be hosted [168, 173, 223]. Separately, the pores also act as reservoirs, allowing a selected volume and size of molecules to be successfully loaded [15, 176]. Based on the significantly high loading capacity of BGCu from EDX analysis (Figure 5. 4c), it was proposed that the mobility of the copper ions allowed for higher surface coverage throughout the micro and mesoporous structure of the nanocarrier, while the large copper ligands which formed would have occupied the micro and mesopore cavity and would be confined within the inner parts of the pores, particularly as ionic concentration increased.

5.4.2 Understanding the mechanisms of impregnation

A rinsing test was conducted to determine the loading mechanism involved when the nanocarriers were impregnated with the cross-linking solutions. Figure 5. 6 shows the EDX analysis carried out on BG0.5Sr and BG0.5Cu nanocarriers before and after rinsing. The results indicated that, prior to rinsing, higher concentrations of their respective impregnated ions was detected, while a decrease was noted upon rinsing. These results would suggest that a portion of the loaded salts would not have penetrated into the pores of the nanocarrier, and thus easily rinsed off from the exterior surfaces [168].

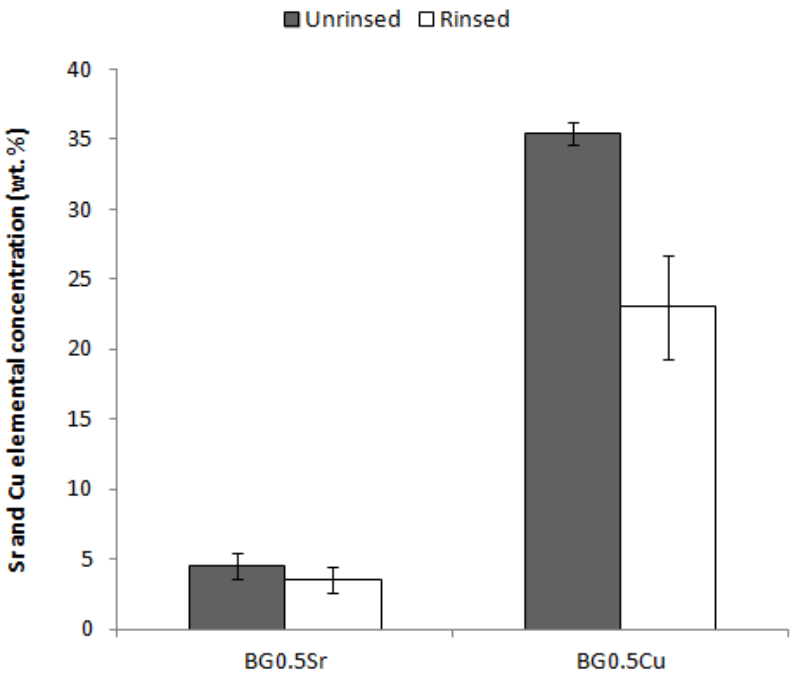

Figure 5. 6: EDX analysis of the loaded cross-linking ion concentration strontium or copper before and after rinsing with deionised water. Data represents the mean ± SD, n = 5.

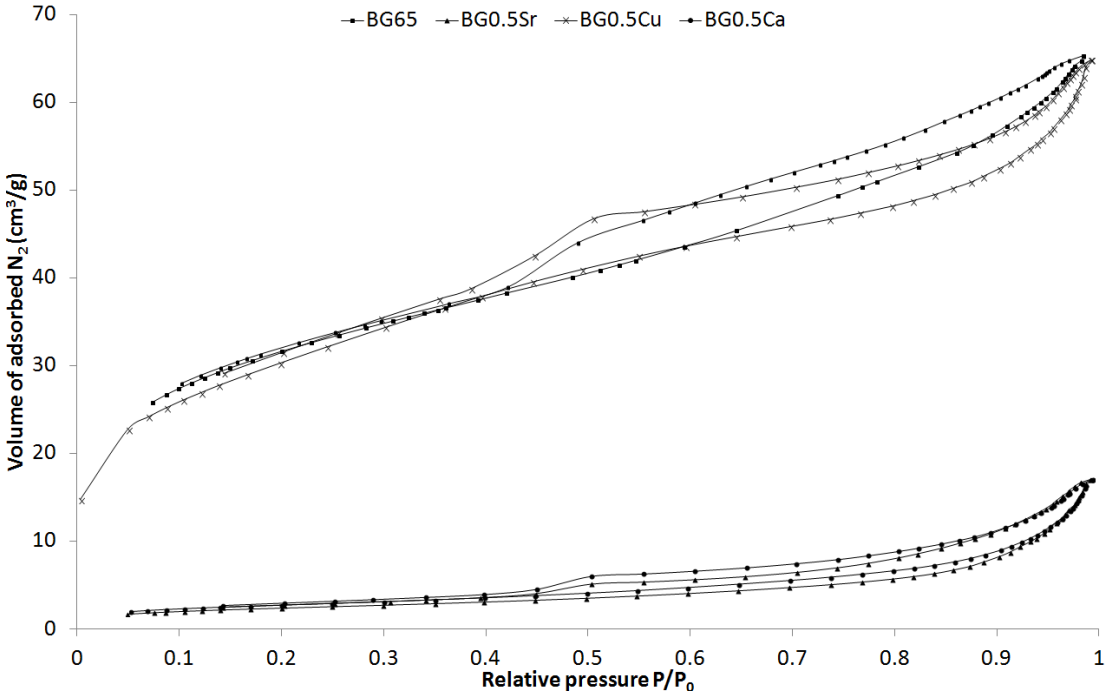

Figure 5. 7: Adsorption and desorption isotherms of the carrier BG65, and the variously loaded nanocarriers containing strontium, copper and calcium ions respectively.

The adsorption of different ions onto the surfaces of the nanocarrier was studied to obtain a better understanding of the loading mechanisms. Figure 5. 7 shows the comparisons between the isotherms of the loaded and unloaded nanocarrier (BG65). The isotherms reveal that the nanocarriers impregnated with $SrCl_2$ and $CaCl_2$ occur at low levels of adsorbed N_2 volumes, with small hysteresis loops, suggesting that the porous matrix (cavities) of the nanocarrier had been filled with the cross-linking salt molecules, thus forming a denser structure [191]. Interestingly, $CuCl_2$ loaded nanocarriers were found to exhibit similar levels of adsorbed N_2 volumes as the unloaded nanocarrier.

One possible explanation could be that the larger copper ligand structures are adsorbed as a monolayer onto the surfaces of the nanocarrier [176]. Due to its large structure as a ligand, further adsorption into the small cavities (micropores) of the nanocarrier is hindered by steric effects [222]. Therefore, monolayer coverage of the nanocarrier occurs when impregnated with $CuCl_2$ from aqueous solution. In addition, the high impregnation efficiency of copper onto the nanocarrier, even though monolayer coverage was observed, could be attributed to the silinol groups (Si – OH) present on the surfaces the nanocarriers attracting copper ligands to adhere. These silinols attract the hydrogen bonding molecules (water molecules) of the copper ligands, forming a strong molecule-substrate interaction [226, 227]. The ligands attracted to the accessible silinol would try to adhere to every available site on the surface, and in the process push together to form a tightly packed system of ligands [227]. It was therefore possible for BG65 nanocarriers to uptake the most Cu^{2+} ions compared to Sr^{2+} and Ca^{2+} ions, considering that the loading concentration of the cross-linker solutions were equal.

5.5 Gelation of composite scaffolds

The feasibility of using the impregnated nanocarriers as a delivery means for the ionic cross-linking of alginate, to synthesise alginate-based composite scaffolds, was studied. The underlying factors which could affect the gelation kinetics were identified to be: I) nanocarrier morphology, II) nanocarrier to alginate mixture ratio and III) type of cross-linking ion delivered.

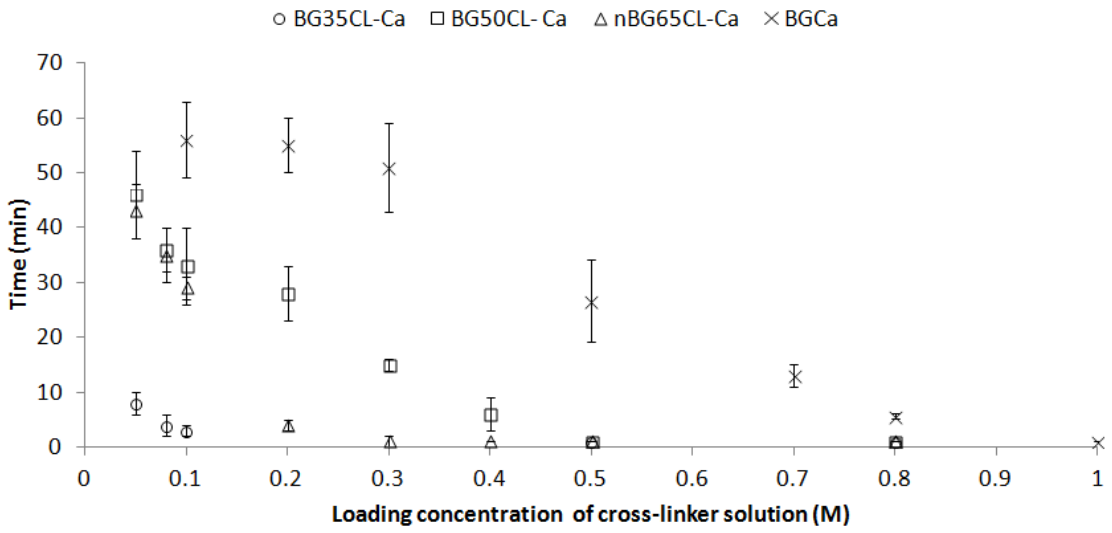

Figure 5. 8: Gelation time of alginate composites cross-linked by different nanocarriers. Data represents the mean ± SD, n ≥ 3.

The gelation time of the alginate-based composite slurry, cross-linked using different nanocarriers of BG35, BG50, BG65 and nBG65 impregnated with $CaCl_2$, is shown in Figure 5. 8. The gelation times of the slurry decreased when nanocarriers impregnated with higher loading concentrations of the cross-linking solution was used, because higher initial loading concentrations will allow for increased uptake by the carriers through the impregnation method [223]. Both BG35 nanocarriers formed hydrogel scaffolds within the shortest time, rapidly cross-linking even at low initial loading concentration (< 0.1 M). On the other hand, calcium loaded BG65 nanocarriers (BGCa) required the longest time to cross-link the slurry.

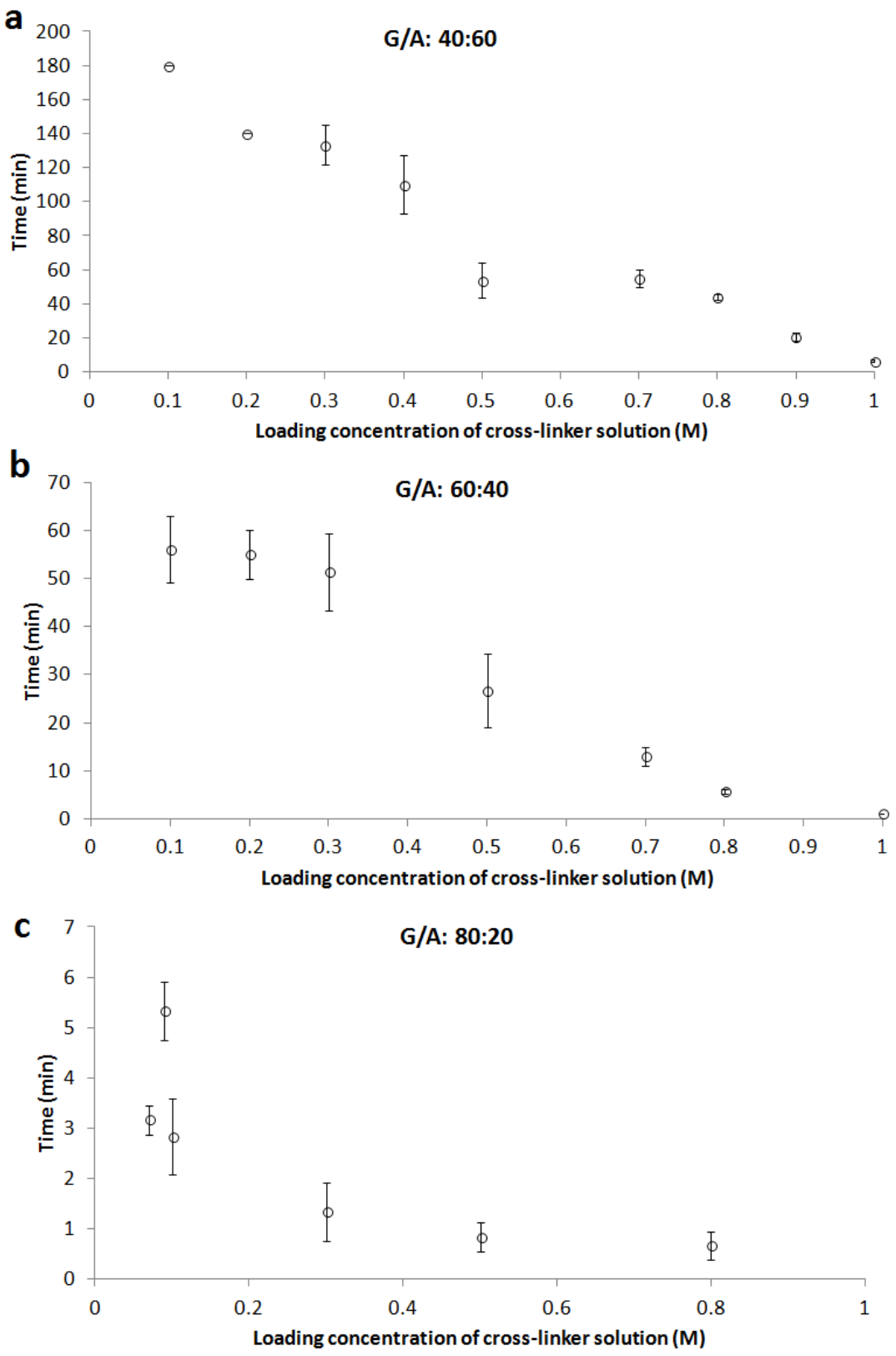

Figure 5. 9: Gelation time of composite slurry through BGCa cross-linking, using varying loading concentration of BGCa. (a) G/A ratio of 40:60; (b) G/A ratio of 60:40; (c) G/A ratio of 80:20. Data represents the mean ± SD, n ≥ 3.

Figure 5. 9 shows the gelation rate of the slurry as a function of impregnation concentration using BGCa, with G/A ratios of 40:60, 60:40 and 80:20. A similar relationship was drawn in which gelation rate increased with loading concentration and with an increase in the G/A ratio. An increase in the amount of nanocarriers (G) and consequently a decrease in alginate concentration (A) within the system led to faster gelation due to the availability of ions for cross-linking. Similarly, an increase in the availability of cross-linking ions impregnated on the carriers would directly result in an increase in the gelation rate, since more ions are readily available to cross-link the alginate.

The different gelation trends observed through the use of various nanocarriers were deduced to be affected by pore diameter, based on the N_2 sorption data tabulated in Table 5. 3. A direct comparison could be drawn in which, gelation rate was proportional to pore diameter; the larger the pore diameter, the faster the gelation rate. Trewyn *et al*. [13] compared the release rates of molecules between parallel hexagonal channels with that of disordered pores in mesoporous silica nanoparticles and firmly demonstrated that the former released molecules faster.

Interestingly, the observations drawn from the results above suggests otherwise. No direct link could be drawn between SSA with gelation time, which is an indicator of ionic absorption by the carriers with that of the ionic loading efficiency recorded by EDX (Figure 5. 6). In fact, as demonstrated in Figure 5. 8, BG65 which had the highest SSA, proved to be the least effective in cross-linking. For example, at a 0.3 M loading concentration of the cross-linker solution, nBG65CL-Ca and BG50CL-Ca cross-linked scaffolds recorded a gelation time of 3 min and 17 min, respectively, while BG65 required approximately 55 min. One explanation for this is, the intermolecular interaction between the cross-linking molecules within the pores increases with a decrease in pore diameter which in turn reduces the release rate of the cross-linking ions from the pores [173, 174]. The results suggest that the SSA of the nanocarriers influenced the loading capability and efficiency while pore width played a more important role in the release mechanism or diffusion of ions from the nanocarriers, consequently has a greater significance on the gelation kinetics of alginate.

These results indicate that specific control over gelation time can be achieved by varying the type of nanocarrier, the impregnation concentration of the cross-linker solution as well as the G/A ratio of the composite slurry. Such control over gelation time was found pertinent to the overall scaffold structure, as illustrated in Figure 5. 10. Three gelation regions: I) rapid gelation, II) controlled gelation and III) slow gelation, were identified and categorised based on the final physical appearance of the composite hydrogel.

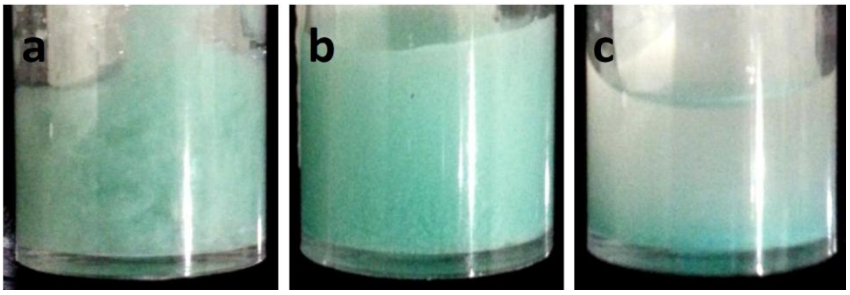

Figure 5. 10: The effects of gelation rate on scaffold structure. (a) Rapid gelation, (b) controlled gelation and (c) slow gelation. Images of scaffolds depicted were cross-linked using BGCu.

As seen in Figure 5. 10a, rapid gelation of the slurry led to the aggregation of alginate composite lumps, which consisted of gels formed from the instantaneous gelation and encapsulation of nanocarriers. Rapid gelation was found to typically occur within 5 min of the introduction of loaded nanocarriers into the alginate solution. Figure 5. 10b shows a scaffold produced under controlled gelation. Scaffolds synthesised within this region were observed to be physically uniform, consisting of a homogenously dispersed mixture of nanocarriers and alginate throughout the scaffold. For scaffolds produced under slow gelation (Figure 5. 10c), material segregation was observed, forming a composite-based material concentration gradient. As the time taken for complete gelation was long (> 1 h), the nanocarrier which was denser than the polymer solution gradually sank to the bottom, initially creating a glass-based concentration gradient. Consequently, the concentrated nanocarriers at the base would gradually leach out ions. These ions would in turn attract additional uncross-linked alginate towards the cross-linking ion-polymer interface, thus increasing the localised concentration of composite material [47, 82].

It is worth mentioning that the images of scaffolds depicted in Figure 5. 10 were BGCu cross-linked scaffolds. In all instances, all three types of loaded nanocarriers followed similar scenarios, however, for clarity; BGCu cross-linked scaffolds were imaged.

The BG65 nanocarrier was selected as the most efficient and reliable nanocarrier since it was shown to uptake the highest concentration of cross-linking ions from impregnation tests, while the gelation rates of hydrogels using BG65 were controlled and consistent. Additionally, a G/A ratio of 60:40 was used for further studies because this composition mixture was found to have the broadest loading concentration of cross-linker solutions (0.1 – 1 M), for a reasonable gelation time of within an hour, to minimise the effects of nanocarrier sedimentation. Thus, expanding on its application as a nanocarrier, BG65 nanoparticles loaded with Sr^{2+}, Cu^{2+} and Ca^{2+} were introduced, to synthesise composite hydrogels with a G/A ratio of 60:40.

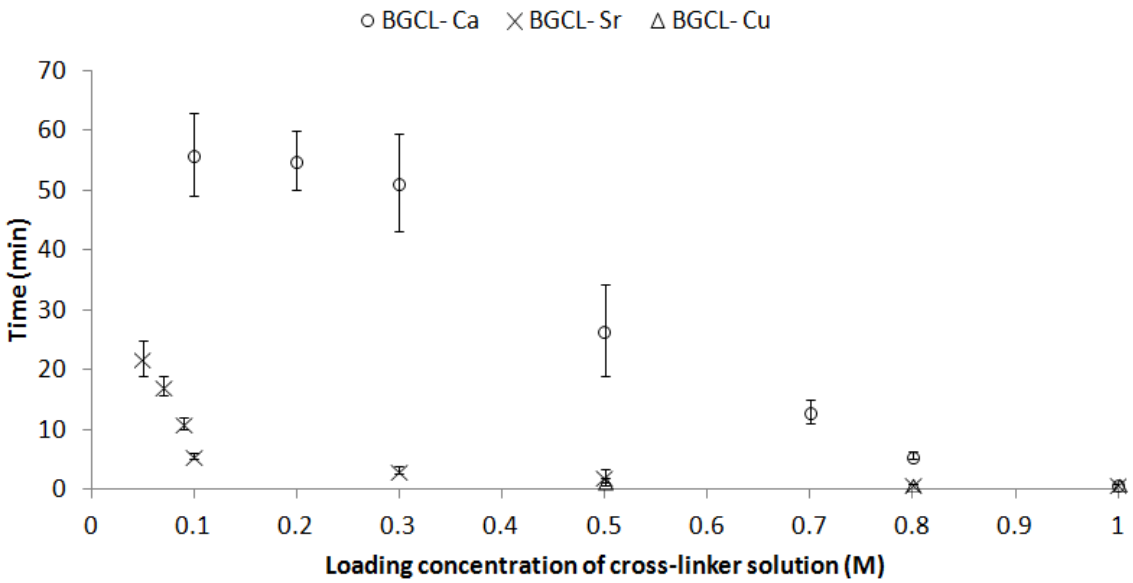

Figure 5. 11: Gelation time of composite alginate gels containing a G/A ratio of 60:40, cross-linked with BGSr, BGCu and BGCa respectively. Data represents the mean ± SD, n ≥ 3.

Figure 5. 11 shows the effects of ion type and initial nanocarrier ionic solution loading concentration on gelation time. The ionic concentration at which controlled gelation took place varied according to the type of ions the nanocarrier was loaded with. Controlled gelation occurred at a much lower concentration between 0.1 – 0.5 M

when cross-linked with BGSr, whilst a higher initial loading concentration of 0.5 – 0.8 M was required to uniformly cross-link the alginate using BGCa. Interestingly, the gelation rate of alginate scaffolds cross-linked with BGCu was sporadic, mainly occurring at a loading concentration somewhere between 0.3 – 0.5 M. For instance, gelation of the slurry using BGCu loaded with 0.3 M cross-linker solution required 180 min (not shown on graph), while BGCu loaded with 0.5 M cross-linker solution required less than 5 min.

Complete gelation of the alginate scaffolds which caused a visible concentration gradient was characterised as slow gelation. The threshold at which slow gelation became a controlled gelation followed a similar trend, whereby the initial loading concentration of BGCa was higher than BGSr.

The absorption efficiency of a nanocarrier is dependent on its chemistry and morphology, as discussed previously. In the above studies, BG65 was used as the carrier for the diffusion controlled delivery of cross-linking ions. Hence, the absorption efficiency of the carriers would remain unaffected by those factors, suggesting that the different gelation rates observed between Sr^{2+}, Cu^{2+}, Ca^{2+} was driven by the interaction between the divalent ions and the alginate. As discussed in the literature, only G-blocks are involved in the ionic binding of the polymer, with hydrogels forming from the assembly of polymer chains into larger complexes [79, 86]. Studies have indicated that the relationship between the affinity of the cross-linking ion to G-blocks is interdependent [89, 90, 101, 228].

Based on the affinity series of different ions to alginate (Table 2. 3), Cu^{2+} had a much greater affinity towards alginate than Sr^{2+} and Ca^{2+} which explains the rapid gelation of alginate when in contact with BGCu. The rapid gelation rate induced by BGCu was compounded by the high loading levels of Cu^{2+} onto the nanocarrier, which consequently led to burst releases of Cu^{2+} when introduced into the alginate solution. Observing the affinity series, the affinity of Sr^{2+} was found to be greater than Ca^{2+} [90]. In the experiments carried out, this was evident through measurements which showed that the required initial loading of BGSr to achieve similar rates of gelation as BGCa was considerably lower throughout.

5.6 Scaffold microstructure

The physical appearance and microstructure of the composite scaffolds synthesised by: I) nanocarriers impregnated with different cross-linking ions (Sr, Cu and Ca) and II) different nanocarrier types (BG35, BG50, BG65 and nBG65) were studied. The scaffolds studied were selected from the controlled gelation region.

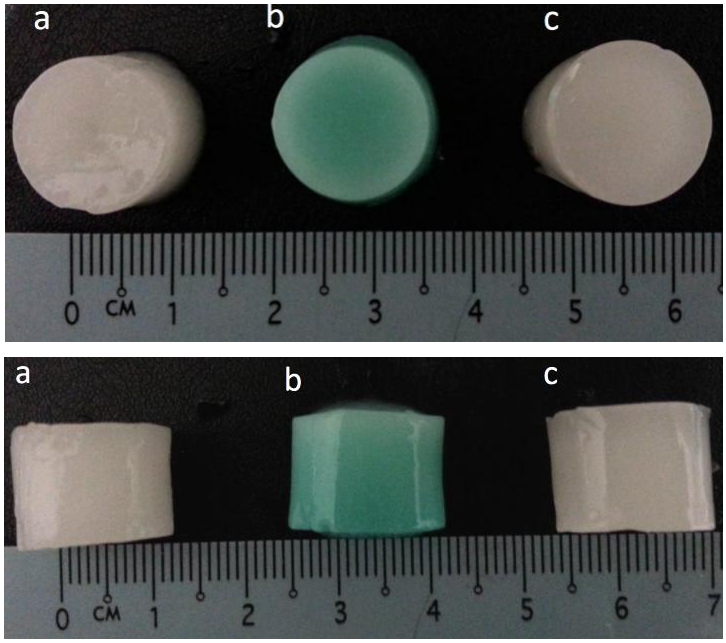

Figure 5. 12: Images of typical examples of scaffolds cross-linked with (a)BGSr, (b)BGCu and (c) BGCa under a controlled gelation rate.

Figure 5. 12 shows uniform cylindrical scaffolds synthesised by BGSr, BGCu and BGCa cross-linking. The physical appearances of the scaffolds produced within the controlled gelation region were three-dimensionally defined and homogenous, with no visible sedimentation of the nanocarriers. The distribution of composite material within the cross-linked scaffold matrix was determined using dry to wet weight ratios, as shown in Figure 5. 13 [47]. Both profiles of scaffolds cross-linked using BGSr and BGCa did not vary much across the three sections, indicating the distribution of composite material was homogenous throughout the scaffold matrix. However, for scaffolds produced through BGCu cross-linking, a difference in the dry to wet weight ratios between the slices were noted. The profile in Figure 5. 13 showed that slice

number 1, which represented the bottom slice, had a higher dry to wet weight ratio than the other two sections.

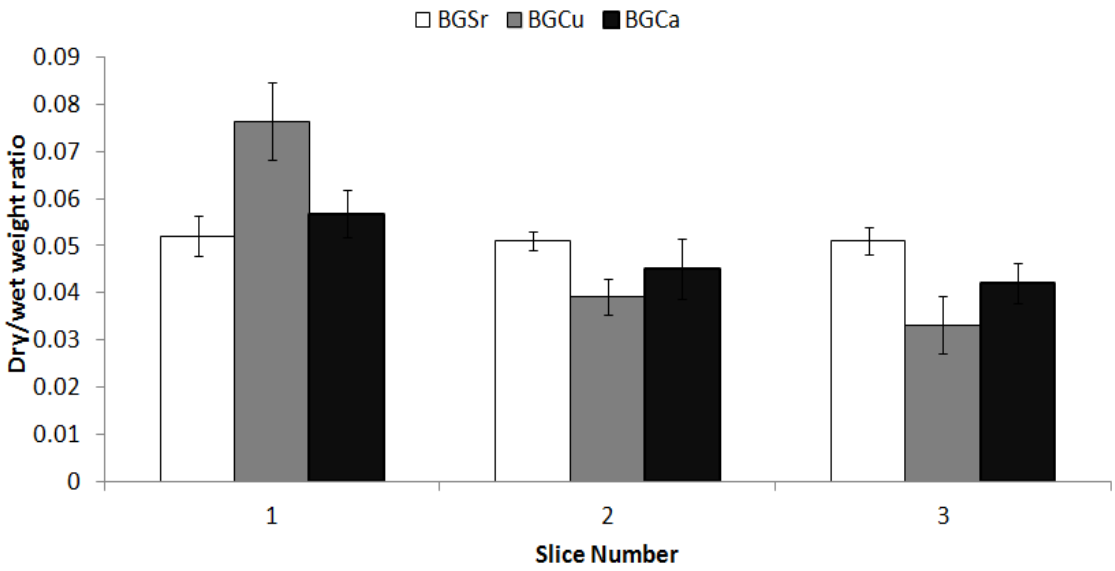

Figure 5. 13: Dry to wet weight ratios of scaffold slices cross-linked with BGSr, BGCu and BGCa, numbered 1 – 3, representing bottom, middle and top sections, respectively. Data represents the mean ± SD, n = 3.

Additionally, the dry to wet weight ratio method was employed to evaluate the distribution of composite material within scaffolds synthesised by different nanocarrier types, as shown in Figure 5. 14. The comparable profiles obtained between the scaffolds synthesised by different nanocarriers (BG35, BG50, BG65 and nBG65), suggested that, the type of nanocarrier employed to deliver cross-linking ions did not significantly affect scaffold homogeneity within controlled gelation regions, for the impregnation concentration ranges studied (Sr-system: 0.1 – 0.5 M; Ca-system: 0.5 – 0.8 M). Furthermore, the dry to wet ratios of scaffolds cross-linked using strontium loaded nanocarriers (Figure 5. 14a) were comparable across the three sections, indicating the distribution of composite material was homogenous throughout the scaffold. However, for scaffolds cross-linked using calcium loaded nanocarriers (Figure 5. 14b), a slightly decreasing dry to wet weight ratio was observed.

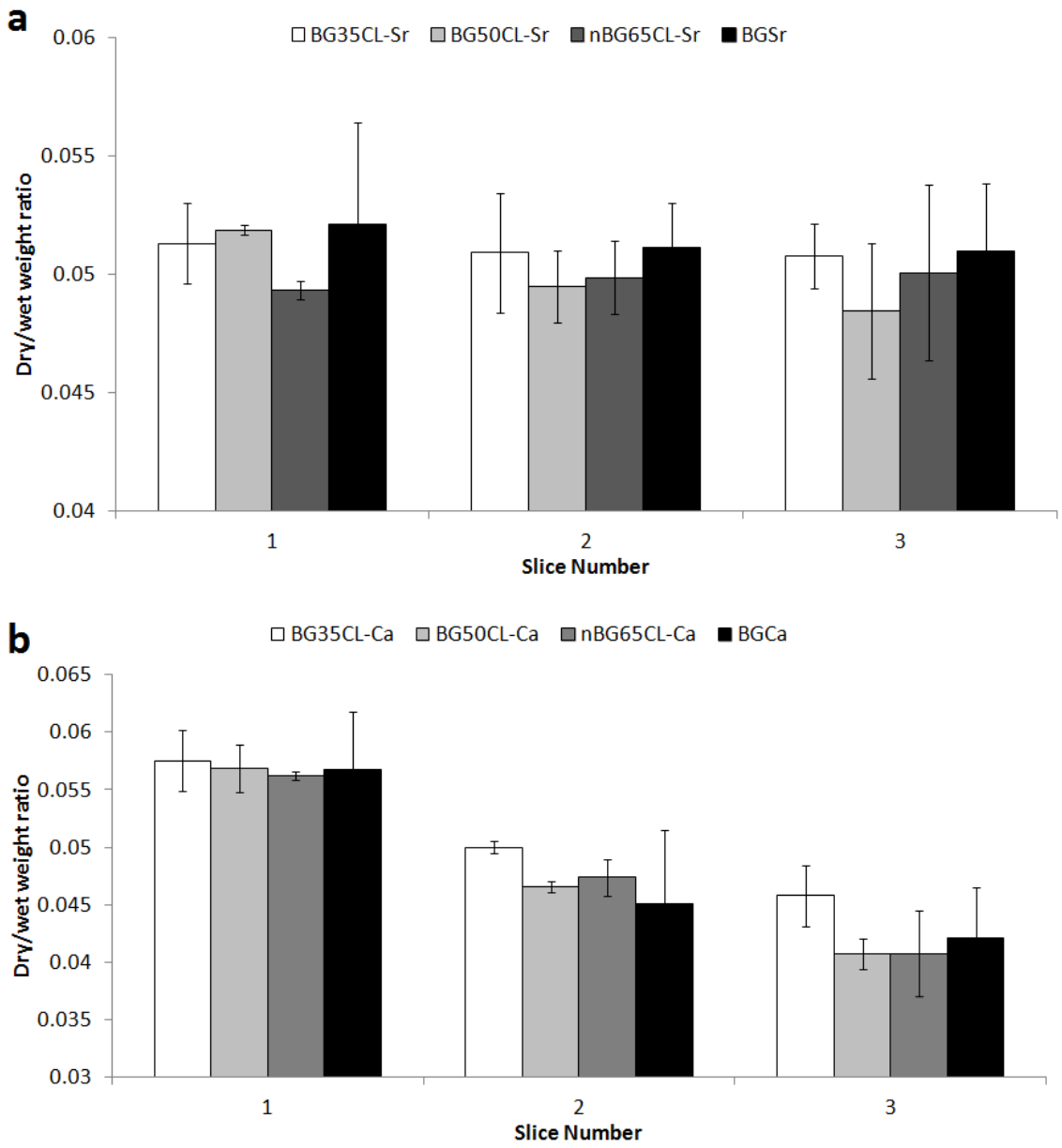

Figure 5. 14: Dry to wet weight ratios of scaffold slices cross-linked under a controlled gelation rate using various nanocarriers impregnated with a) strontium ions and b) calcium ions; numbered 1 – 3, representing bottom, middle and top sections, respectively. Data represents the mean ± SD, n = 3.

The dry to wet weight ratio method takes into account the amount of water trapped within the hydrogel, for a predetermined volume. Therefore, a higher dry to wet weight ratio points towards a higher concentration of composite material rather than water in that particular section [47]. The profile of BGCu cross-linked scaffolds (Figure 5. 13), which showed a large decrease of 0.04 in its dry to wet weight ratio between the middle and bottom sections, suggested that the bottom section contained

a higher concentration of composite material per volume than the middle and top sections. Likewise, for scaffolds cross-linked by various nanocarriers impregnated with calcium (Figure 5. 14b), a slight decrease in its dry to wet weight ratios (< 0.02) were observed across the three sections. This was indicative of a concentration gradient, largely due to sedimentation of the composite material and the adherence of the loaded nanocarriers to the bottom [19, 47].

Studying the gelation time of the composite gels in Figure 5. 11, it was difficult to attain a suitable loading concentration for the controlled gelation of BGCu cross-linked scaffolds. Hence, it is worth pointing out that the BGCu cross-linked scaffolds selected for dry to wet weight ratio profiling were chosen from a handful of samples which gelled within the controlled gelation region, but usually required close to 1 h for complete gelation. Therefore, this could explain the difference in the dry to wet ratios observed between the middle and bottom sections of BGCu scaffolds, due to the sinking effect of some composite materials as gelation took place over longer periods. Another possible explanation could be attributed to the mechanism in which gelation occurred. As mentioned in Section 5.3.5, the gelation time of BGCu scaffolds were rather sporadic. Thus, localised gelation could have occurred at the interface between the alginate and the nanocarriers at a rapid rate, causing these localised gelled composites to sink to the bottom rather than gradually leach out ions to homogenously cross-link the entire scaffold, as was noted predominantly in BGSr and BGCa cross-linked scaffolds.

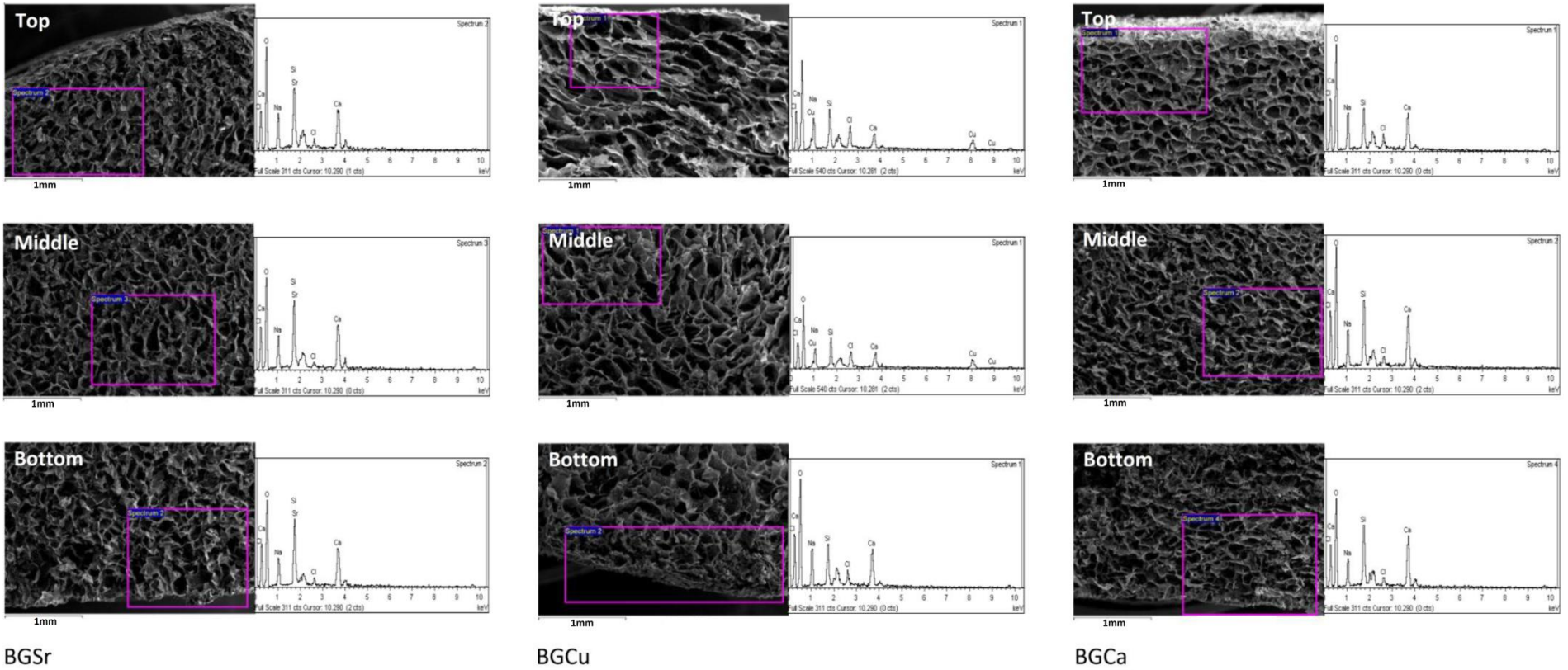

Figure 5. 15: SEM micrographs of the top, middle and bottom sections of the BGSr, BGCu and BGCa cross-linked composite scaffolds, showing the porous microstructure throughout the sections and EDX spectrum corresponding to the analysed section marked by a purple box, demonstrating the presence of the cross-linking ions and the nanocarrier.

Figure 5. 15 shows SEM micrographs of the top, middle and bottom sections of BGSr, BGCu and BGCa cross-linked scaffolds, with the corresponding EDX spectra for each respective section. EDX measurements of the three sections showed the homogeneous dispersion of BGSr and BGCa nanoparticles within the scaffold matrix from the detection of Si, Ca and their respective loaded cross-linking ions. Table 5. 6 shows the concentration of the elements strontium (Sr) and calcium (Ca) which were found to be rather consistent throughout the three sections, with the bottom sections measuring a slightly higher concentration. The element of copper (Cu) on the other hand was measured to be almost half the concentration in the top section as compared to the middle and bottom sections.

The consistency in the distribution of the cross-linking ions (Sr and Ca) detected across the top and middle sections of the scaffold matrix would suggest that nanocarrier was homogenously dispersed. The slightly higher elemental concentrations of Sr and Ca ($\leq$ 0.26 wt. %) observed in the bottom sections, was in agreement with the dry to wet weight ratios measured, which showed the presence of a concentration gradient, particularly for BGCa cross-linked scaffolds. For BGCu scaffolds, it was evident from the two-fold increase in the Cu elemental concentration detected between the top and the middle and bottom sections of the scaffold, a proportion of the nanocarriers sunk to the bottom, creating a more apparent concentration gradient, consistent with the wet to dry weight ratio results illustrated in Figure 5. 13.

Table 5. 6: Quantitative EDX analysis of the top, middle and bottom sections of scaffolds cross-linked with BGSr, BGCu and BGCa, under a controlled gelation rate. Data represents the mean ± SD, n = 5.

Scaffold section	Elemental concentration		
	Sr (wt. %)	Cu (wt. %)	Ca (wt. %)
Top	1.33 ± 0.52	2.86 ± 1.64	12.1 ± 0.91
Middle	1.29 ± 0.19	5.19 ± 0.28	12.4 ± 0.50
Bottom	1.55 ± 0.51	5.80 ± 0.41	13.5 ±0.65

SEM micrographs of the scaffolds shown in Figure 5. 15 revealed a porous network of interconnected pores held together by thin struts (< 10 µm) in between the pores. Table 5. 7 summarises the pore size distribution for each scaffold section. Both BGSr and BGCa cross-linked scaffolds observed a scattered distribution of pore sizes ranging from 120 – 200 µm. The measurements also showed that pore sizes decreased across the three sections, from the top to the bottom. BGCu scaffolds also demonstrated decreasing pore sizes from top to bottom, however, the distribution of pore sizes, particularly in the top section were heterogeneous, noted by the large standard deviation (± 153.7µm).

The microstructure of scaffolds synthesised by different nanocarriers (BG35, BG50 and nBG65 nanoparticles) loaded with strontium was also studied, as shown in the SEM micrographs of Figure 5. 16. Each scaffold showed consistent scaffold architecture, consisting predominantly of cellular pores separated by thin walls (struts), with a thickness of < 10 µm. The pore size distribution for the top, middle and bottom sections of the different scaffold types is tabulated in Table 5. 8. Similar to the results obtained in Table 5. 7, the pore sizes measured for each scaffold in Figure 5. 16 show a rather homogenous distribution of pore sizes between the top and middle sections, while overall smaller pore sizes were measured for the bottom section.

Table 5. 7: Pore size distribution of the top, middle and bottom sections of scaffolds cross-linked with BGSr, BGCu and BGCa, under a controlled gelation rate. Data represents the mean ± SD, n ≥ 50.

Scaffold section	Scaffold type/ pore size (µm)		
	BGSr	**BGCu**	**BGCa**
Top	172.0 ± 34.0	236.3 ± 153.7	195.5 ± 45.1
Middle	144.5 ± 35.3	183.6 ± 75.1	164.2 ± 34.9
Bottom	122.8 ± 24.3	152.5 ± 60.7	153.6 ± 36.7

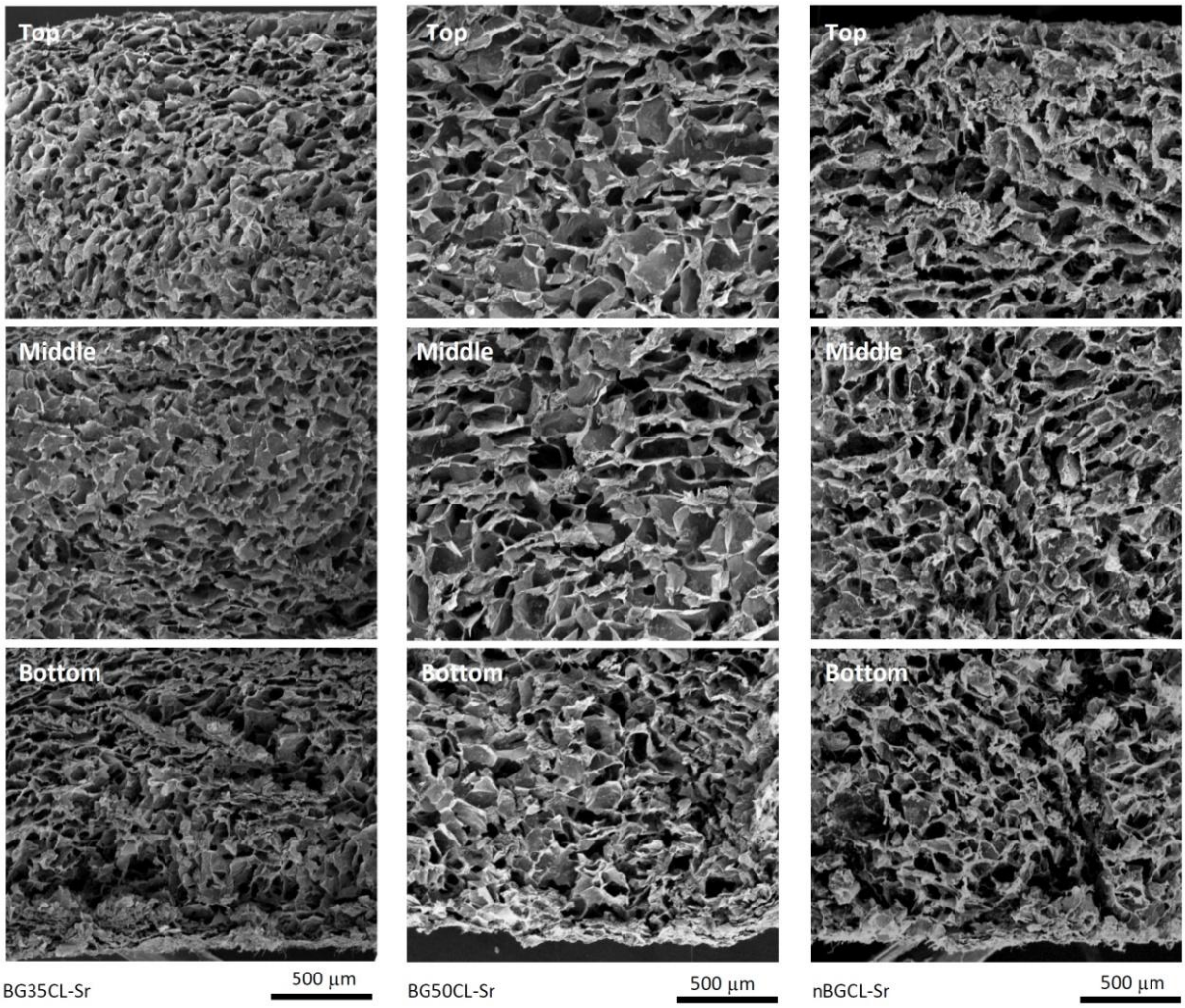

Figure 5. 16: SEM micrographs of the top, middle and bottom sections of BG35CL-Sr, BG50CL-Sr and nBG65CL-Sr cross-linked composite scaffolds.

Table 5. 8: Pore size distribution of the top, middle and bottom sections of scaffolds cross-linked with different nanocarriers impregnated with $SrCl_2$, under a controlled gelation rate. Data represents the mean ± SD, n ≥ 50.

Scaffold section	Scaffold type/ pore size (µm)		
	BG35CL-Sr	BG50CL-Sr	nBG65CL-Sr
Top	97.4 ± 31.9	170.3 ± 52.6	155.7 ± 50.8
Middle	95.5 ± 36.8	181.8 ± 59.4	147.5 ± 49.1
Bottom	94.0 ± 31.5	118.5 ± 37.7	137.1 ± 48.4

The differences in pore sizes between the sections have been observed in previous studies, attributed to the interdependencies between ice crystal formation and slurry concentration during the freeze drying process, since the microstructure of the scaffold is a replica of the sublimated ice [19, 65, 67]. The dry to wet weight ratio and EDX studies performed on the scaffolds confirmed the presence of a higher concentration of composite material in the bottom section. Therefore, during freezing, it becomes difficult for the ice crystals to repel the material as crystal growth progresses, eventually leading to the formation of smaller and segregated ice crystals [19]. Upon sublimation, this creates the smaller pores, as observed. Conversely, the upper sections of the scaffold, particularly that of BGCu scaffolds, had a lower concentration of composite material and more water trapped within the hydrogel. Therefore, ice crystal growth is less hindered, creating larger pores upon sublimation.

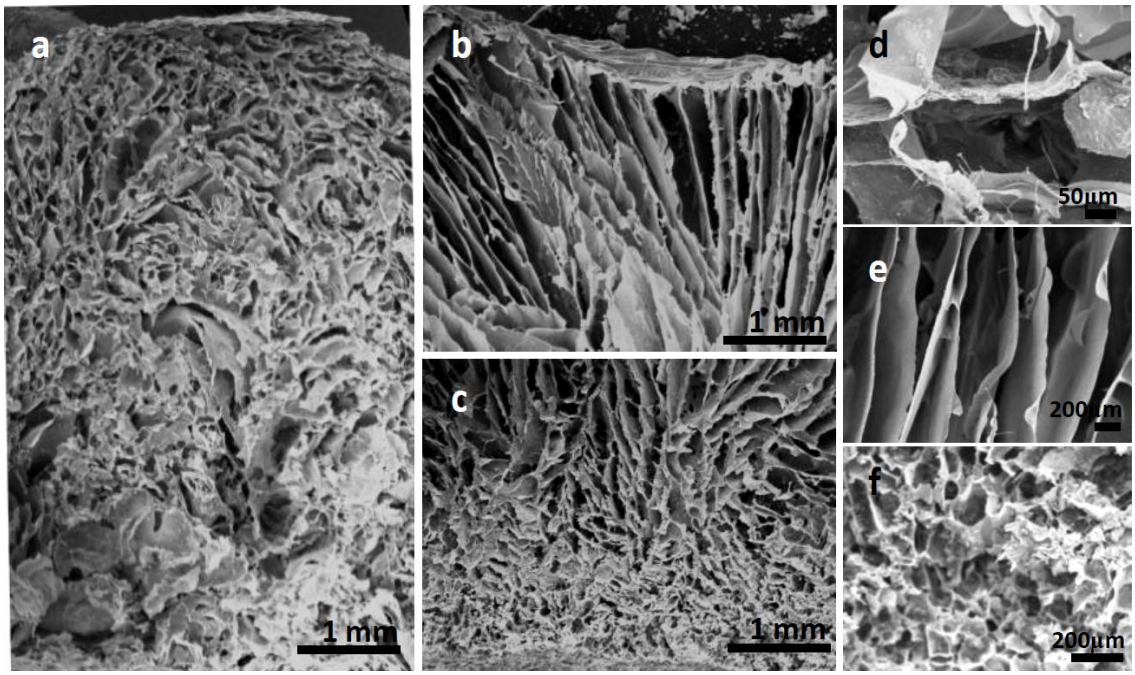

Figure 5. 17: SEM micrographs of the microstructure of BGCu cross-linked scaffolds. (a) Rapid gelation, (b) top section and (c) bottom section of slow gelation, (d) heterogeneous pores between lumps of alginate gel, (e) slow gelation; microchannels from the effects of freeze drying and (f) slow gelation; sedimentation of BGCu compacting at the base of the scaffold.

Three regions of gelation: I) slow gelation, II) controlled gelation and III) rapid gelation was identified in Section 5.3.4. Although the characterisation of scaffolds produced under controlled gelation have been presented, since, the physical

appearances of scaffolds produced from each region were distinct (Figure 5. 10), it was also important that the microstructure of scaffolds produced under slow and rapid gelation was characterised, to provide a better understanding of the correlation between gelation time and scaffold microstructure.

Figure 5. 17 shows SEM micrographs of scaffold cross-sections obtained from rapid gelation and slow gelation. Rapid gelation led to a heterogeneous alginate structure, consisting of lumps of alginate, observed in Figure 5. 17a. In-between these lumps, large pores in excess of 300 µm were recorded (Figure 5. 17d). Figure 5. 17b shows the upper section of a scaffold produced under slow gelation, in which microchannels with widths 150 – 400 µm were observed. The lower half of the scaffold (Figure 5. 17c) shows a completely different microstructure, in which pores, mainly cellular of 80 – 150 µm in diameter was observed. Figure 5. 17e and f shows the cross-section of a scaffold synthesised under slow gelation. As previously discussed, slow gelation led to the sinking of nanocarriers, which hindered ice crystal formation when the scaffold froze, thus leading to a dense microstructure of planar shaped pores. Conversely, the upper section, which contained less particles and polymer would have been susceptible to rearrangement of the polymer composite network by the ice [19]. Since the scaffolds were frozen in the direction from bottom up, the cold front would have gradually progressed upwards, forming elongated ice crystals, perpendicular to the cold front [19, 66]. Hence, in the upper section, when sublimation occurred, the ice which acted as a template would have shaped the polymer, leaving the microchannels observed (Figure 5. 17e).

The microstructural features of scaffolds produced under slow gelation provides an interesting perspective into the fundamentals of the physics of ice crystal formation. Specifically, in Figure 5. 17c, the transition of ice crystal morphology from planar to cellular to lamellar (microchannels) is observed. The progression of ice crystal growth begins at the cold front, at the base of the scaffold, which is the nearest surface to the freezing plate. Being closest to the cold source, the base of scaffold begins to rapidly freeze, forming small, heterogeneous and poorly connected ice crystals [19, 67]. This, collectively with the higher concentration of composite slurry led to the formation of small pores. It is difficult to determine the transition point between planar to cellular

pores, however, the transition between cellular to lamellar is clear. This morphological transition of ice crystals is attributed to cooling rate and composite slurry concentration. The transition occurs when the ice crystals, under gradual cooling rates are able to repel the composite material from the ice front, progressing into a steady lamellar growth. Additionally, gradual cooling rates are essential to allow the formation of large ice crystals through the coalescing of neighbouring crystals [19, 66, 67].

5.7 Summary

Composite scaffolds were synthesised using the novel method of internal diffusion cross-linking via ionically loaded mesoporous bioactive glass nanoparticles acting as nanocarriers. Mesoporous bioactive glass nanoparticles heat treated to a temperature below 680 ºC was found to be capable of cross-link alginate. This was attributed to the deposition of calcium on the surface of the silicate network upon drying, but unable to diffuse into the network, due the low sintering temperature (< 680 ºC). However, the uncontrolled nature of gelation made it difficult for the production of homogenous scaffolds.

Instead, mesoporous bioactive glass nanoparticles (BG35, BG50, BG65 and nBG65) derived in Chapter 4 were impregnated with various ions (Sr^{2+}, Cu^{2+}, Ca^{2+}), and used as nanocarriers, for the cross-linking of alginate. The impregnation efficiency of these nanocarriers was found to be influenced by both the specific surface area (SSA) of the nanocarrier and the type of impregnated ion. BG65 possessed the highest SSA, allowing it to be most efficiently impregnated by the various ions, while Cu^{2+} was most efficiently impregnated onto the nanocarriers due to the its small ionic radii, giving rise to increased mobility and permeability into the nanocarrier, but also through the interaction between copper ligands and the nanocarriers surface silinol groups, further encouraging the adherence of ligands onto the nanocarriers.

The gelation of alginate by the nanocarriers was found to be influenced by the initial loading concentration of the cross-linker solution, the G/A ratio and the morphology of the nanocarrier. An increase in the loading concentration led to faster gelation.

Similarly, an increase in the G/A ratio, wherein more nanocarriers per unit volume alginate were introduced, faster gelation was observed because of an increase in the availability of cross-linking ions within the system. Separately, pore size was found to affect the gelation rate, in which BG65 which contained the smallest pore size (4 nm) amongst the nanocarriers led to the slowest gelation rate. This was attributed to a reduction in the release rate of cross-linking ions due to increased intermolecular interaction of cross-linking molecules.

Based on the physical appearance of the synthesised scaffolds, the gelation rates of the scaffolds were separated into three regions; rapid gelation, controlled gelation and slow gelation. Rapid gelation typically occurred when the nanocarriers were loaded in an ionic solution concentration of more than 0.5 M for BGSr and BGCu and 1 M for BGCa. When introduced into the alginate solution, a huge burst of ions was released from the nanocarriers causing immediate gelation of the surrounding alginate, to form aggregated composite lumps. Slow gelation on the other hand led to the sedimentation of the nanocarriers over time, creating a concentration gradient within the scaffold. The scaffolds produced via controlled gelation were uniform in shape with no observable heterogeneity in material distribution.

Further microstructure analysis of scaffolds produced by controlled gelation showed that the composite material was well distributed throughout the scaffold matrix, with the exception of BGCu scaffolds. BGCu scaffolds showed evidence of an apparent concentration gradient through a two-fold increase in the elemental concentration of copper and a higher dry to wet weight ratio between the top and the middle, bottom sections. SEM characterisation of controlled gelating scaffolds was found to contain a homogenous microstructure consisting of interconnected cellular pores, separated by thin pore walls (< 10 μm). Conversely, slow gelating scaffolds revealed a porosity gradient, with fascinating pore architecture, consisting of three defined pore shape regions, beginning with planar pores at the base of the scaffold, followed by cellular pores and lastly lamellar pores (microchannels) in the upper sections of the scaffold. This pore architecture was influenced by the variation in slurry concentration (material-based concentration gradient) between the sections and ice crystal growth.

The development of hybrid composite scaffolds synthesised by the internal diffusion of ionically loaded mesoporous bioactive glass nanoparticles (nanocarriers) was demonstrated. Furthermore, the correlation between the various variables affecting the loading of the nanocarriers through to its implementation for scaffold synthesis was established. 3D scaffolds with uniform microstructures were observed, with the further discovery of scaffolds containing porosity gradients and interesting pore architecture.

Chapter 6

Structural and biological response of hybrid cross-linked scaffolds

6.1 Introduction

A crucial aim of this thesis was to develop a novel method of ionic cross-linking which would improve the structural integrity and mechanical properties of alginate and bioactive glass composite scaffolds. Thus, the importance of controlling parameters such as water absorption and swelling, and improving on the scaffolds' intrinsic mechanical properties, such as its Young's modulus and shear stress when introduced over time in a physiological environment formed the final objective of this study. Additionally, an ideal scaffold should be bioactive and provide a responsive platform for cells to adhere. This chapter proceeds to investigate the *in vitro* biomineralisation and cellular response of the synthesised alginate and bioactive glass composite scaffolds from Chapter 5, to determine the suitability of these scaffolds for use in bone tissue engineering.

The results from this study should ultimately pave the way for a new and improved method of ionically cross-linking alginate hydrogels, with enhanced structural and biological properties with the added element of dual-functionality, benefiting from both the ability to ionically cross-link alginate but also the ability to disseminate sustained biological action from the release of strontium, copper and calcium ions as the scaffold degrades.

The studies conducted in this chapter used alginate and bioactive glass composite scaffolds (glass to polymer ratio 60:40) derived from ionic cross-linking using BGSr and BGCa (Table 6. 1). Energy dispersive X-ray (EDX) analysis was carried out to verify the composition of the scaffolds, while scanning electron microscopy (SEM) and the dry to wet weight ratio measurements were used to confirm scaffold homogeneity. Details of the synthesis methods and characterisation of these scaffolds was described in Chapter 5. The control scaffolds of pure alginate (Alg; 2 wt. %) and

alginate-bioactive glass composite (AlgBG; G/A ratio: 60:40) were synthesised by external diffusion using 0.045 M calcium chloride ($CaCl_2$) solution based on the protocols mentioned in Section 3.9.

Table 6. 1: Scaffold designation corresponding to the cross-linker type and method employed for scaffold synthesis.

Scaffold	Cross-linker type	Cross-linking method
Alg	0.045M $CaCl_2$ solution	External diffusion
AlgBG	0.045M $CaCl_2$ solution	External diffusion
BG0.1Sr	BG65 impregnated with 0.1 M $SrCl_2$	Internal diffusion
BG0.5Sr	BG65 impregnated with 0.5 M $SrCl_2$	Internal diffusion
BG0.5Ca	BG65 impregnated with 0.5 M $CaCl_2$	Internal diffusion
BG0.8Ca	BG65 impregnated with 0.8 M $CaCl_2$	Internal diffusion

6.2 Effects of different impregnation concentration on scaffold mechanical properties

The Young's modulus (E) of composite scaffolds prepared via the internal diffusion of ions from nanocarriers impregnated with different concentrations of cross-linking solutions ($CaCl_2$ and $SrCl_2$), was evaluated. Figure 6. 1a shows the E values of various BGCa cross-linked scaffolds, in which E increased as the nanocarrier impregnation concentration increased. The E values of scaffolds synthesised with BG0.5Ca and BG0.8Ca (nanocarriers impregnated with 0.5 M and 0.8 M $CaCl_2$ solutions) were significantly higher ($p < 0.001$ and $p < 0.05$ respectively), while a large standard deviation was recorded for scaffolds cross-linked using BG1Ca (nanocarriers impregnated with 1 M $CaCl_2$ solutions). A similar increasing trend of E was observed with an increase in nanocarrier impregnation concentration for scaffolds cross-linked using the BGSr system (Figure 6. 1b). A maximum E was achieved for scaffolds cross-linked using BG0.1Sr, beyond that, no significant differences in E was observed ($p < 0.05$). At the highest nanocarrier impregnation concentration of 1 M $SrCl_2$ solution, a large variation in E was observed.

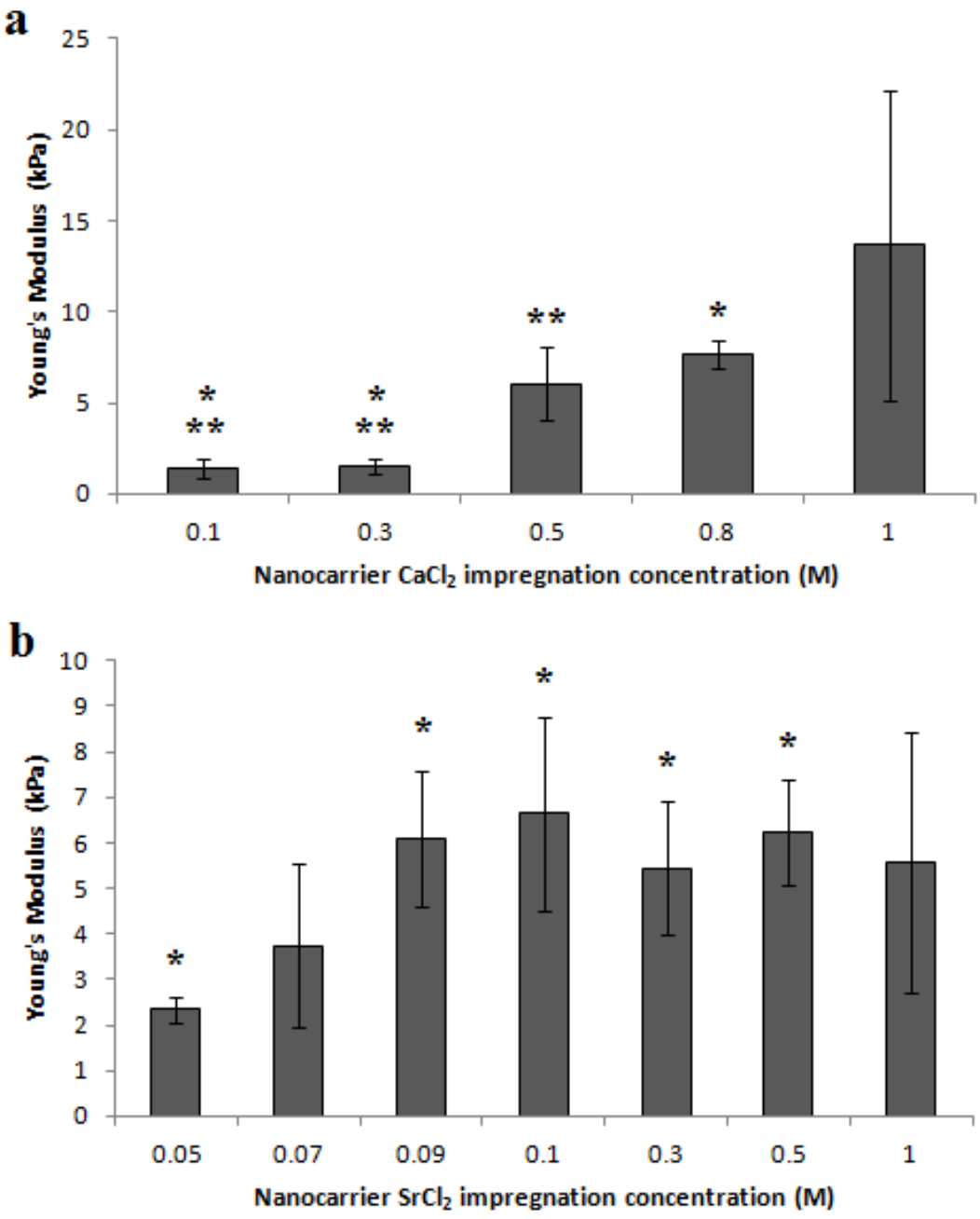

Figure 6. 1: The Young's modulus of bioactive glass and alginate composite scaffolds (glass to polymer ratio of 60:40) cross-linked by (a) BGCa against different nanocarrier impregnation concentrations; *: 0.8 M to 0.1 M, 0.3 M ($p < 0.001$), **: 0.5 M to 0.1M, 0.3 M ($p < 0.05$) and (b) BGSr against different nanocarrier impregnation concentrations; *: 0.05 M to 0.09 M, 0.1 M, 0.3 M, 0.5 M ($p < 0.05$). Data represent the means ± SD, $n \geq 3$.

These results were in agreement with published data, which demonstrated the reliance of the scaffold's stiffness (Young's modulus) on the degree of cross-linking, since an increase in the nanocarrier impregnation cross-linker concentration meant that there were more ions available to cross-link, thus increasing the cross-linking density of the scaffolds [47, 79]. At higher loading concentrations, a higher amount of cross-linking salts would be loaded onto the nanocarriers (demonstrated in Section 5.3.2). Hence, when the nanocarriers were introduced into the alginate solution, a larger reservoir of ions would be available to diffuse and cross-link the alginate. At the upper limits of impregnation concentration (1 M), the large standard deviations observed (Figure 6. 1) was attributed to inconsistent scaffold mechanical properties. The rapid gelation of the scaffolds under high loading concentrations resulted in structural heterogeneity, with voids in between the scaffold matrix. Under stress, these voids would coalesce, forming cracks, which in turn weakened the structure [117].

By comparing the two types of ions used for cross-linking (Figure 6. 1), it was evident that it required a lower impregnation cross-linker concentration for BGSr to cross-link scaffolds which could achieve similar levels of E as BGCa scaffolds. The highest E for BGSr scaffolds was achieved using 0.1 M of initial loading concentration while 0.8 M was required to achieve the similar E value (approximately 7 kPa) for the BGCa system. Since all other factors, such as alginate concentration, composition and molecular weight, which could influence the stiffness of the scaffolds remained constant, the factor which could explain this difference in E was the ion affinity towards alginate.

The ion affinity series describes Sr^{2+} ions having a greater affinity towards alginate as compared to Ca^{2+} ions, which results in the strengthening of the hydrogel due to the formation of more junctions between the G-blocks [90, 99]. Thus, the BGSr system provided ions which had greater affinity, resulting in scaffolds having a better resistance to deformation. In other words, the BGSr system was more efficient, requiring less cross-linking salts to achieve similar mechanical properties as its BGCa counterparts.

6.3 Nanocarrier ionic release concentration and rates

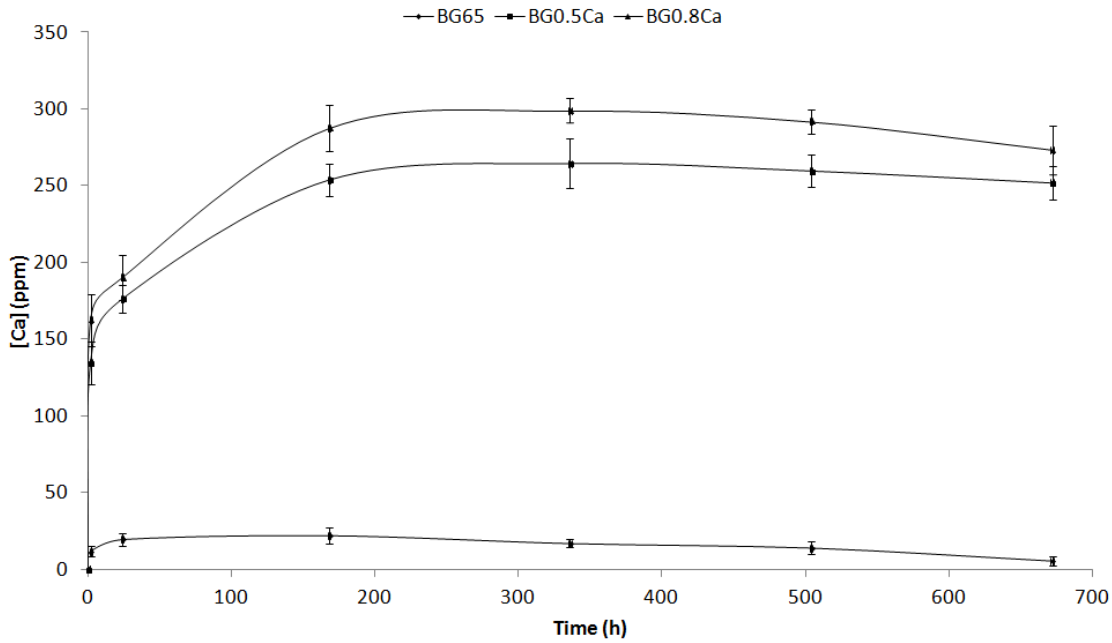

Figure 6. 2: The cumulative release concentration of calcium ions from the different initial loading concentrations of BGCa over time in deionised water.

Figure 6. 2 shows the release profiles of the nanocarrier BG65 and its loaded form of BG0.5Ca and BG0.8Ca respectively at time points of 2 h, 24 h, 168 h (7 days), 336 h (14 days), 504 h (21 days) and 672 h (28 days) measured by ion-selective electrodes (ISE). The results show that for the nanocarrier (BG65), a cumulative maximum concentration of approximately 20 ppm calcium ions was released after 7 days of immersion. Subsequently, a decrease in the calcium concentration sampled in solution was attributed to precipitation of the ions [159, 206]. The release of calcium ions from BG65 is concomitant with the gradual breakdown of the silicate network, thus simultaneously releasing silicate and phosphate ions into the surrounding water. The calcium and phosphate ions which are released from the network precipitates, forming HCA structures, thus decreasing the calcium ion concentration in the solution [159]. For both loaded nanocarriers of BG0.5Ca and BG0.8Ca, a burst release was recorded in both samples after 2 h of immersion, reaching a highest cumulative release of calcium ions after 7 days of immersion. Throughout the immersion period, BG0.8Ca nanocarriers released a higher amount of calcium ions than BG0.5Ca, with BG0.8Ca reaching a maximum in-solution concentration at approximately 300 ppm while

BG0.5Ca detected approximately 260 ppm. The higher release of ions by BG0.8Ca was expected, since, the impregnation concentration of BG0.8Ca was higher than BG0.5Ca nanocarriers.

The ionic release concentration from each system was evaluated once the known loading concentration which was able to cross-link the alginate gels within the controlled gelation region was established from the studies in Chapter 5. The burst release recorded by BG0.5Ca and BG0.8Ca nanocarriers after 2 h immersion could be explained from the loading mechanism of the nanocarriers. The impregnation method employed to load these nanocarriers meant that a proportion of the loaded salts ($CaCl_2$) would coat the surfaces of BG65 [173]. Hence, when exposed to a solution, these salts would dissolve readily, releasing a rapid burst of ions. The gradual decrease in calcium concentration after 7 days suggest that precipitation of the Ca^{2+} had occurred, however, excess calcium ions would remain in the solution due to the limited phosphate (PO_4^{3-}) ions available to re-precipitate.

6.4 Water absorption and degree of swelling of scaffolds

Based on the results drawn from Section 6.3.1, suitable scaffolds selected for further long term stability testing were chosen as BG0.1Sr and BG0.8Ca, which demonstrated significant ($p < 0.05$) improvements in the Young's modulus. Additionally, scaffolds cross-linked using similar amounts of cross-linker impregnation concentration of 0.5 M from both systems (BG0.5Ca and BG0.5Sr) were also studied. Changes in scaffold weight and size were monitored over 7, 14 and 28 days in deionised water. Scaffolds synthesised via the conventional method of using $CaCl_2$ (Alg and AlgBG scaffolds) were compared to scaffolds cross-linked with BGCa and BGSr with regards to changes in initial size and weight.

Noticeable differences in weight changes over time were observed between the two methods of cross-linking as shown in Figure 6. 3a and b. Both weights of Alg and AlgBG scaffolds increased linearly over time, with Alg scaffolds demonstrating the most rapid increase in weight over the 28 day period. After this incubation period, Alg

scaffolds were noted to have doubled (100% weight change) in initial weight while AlgBG scaffolds increased by 20% in weight over the same period.

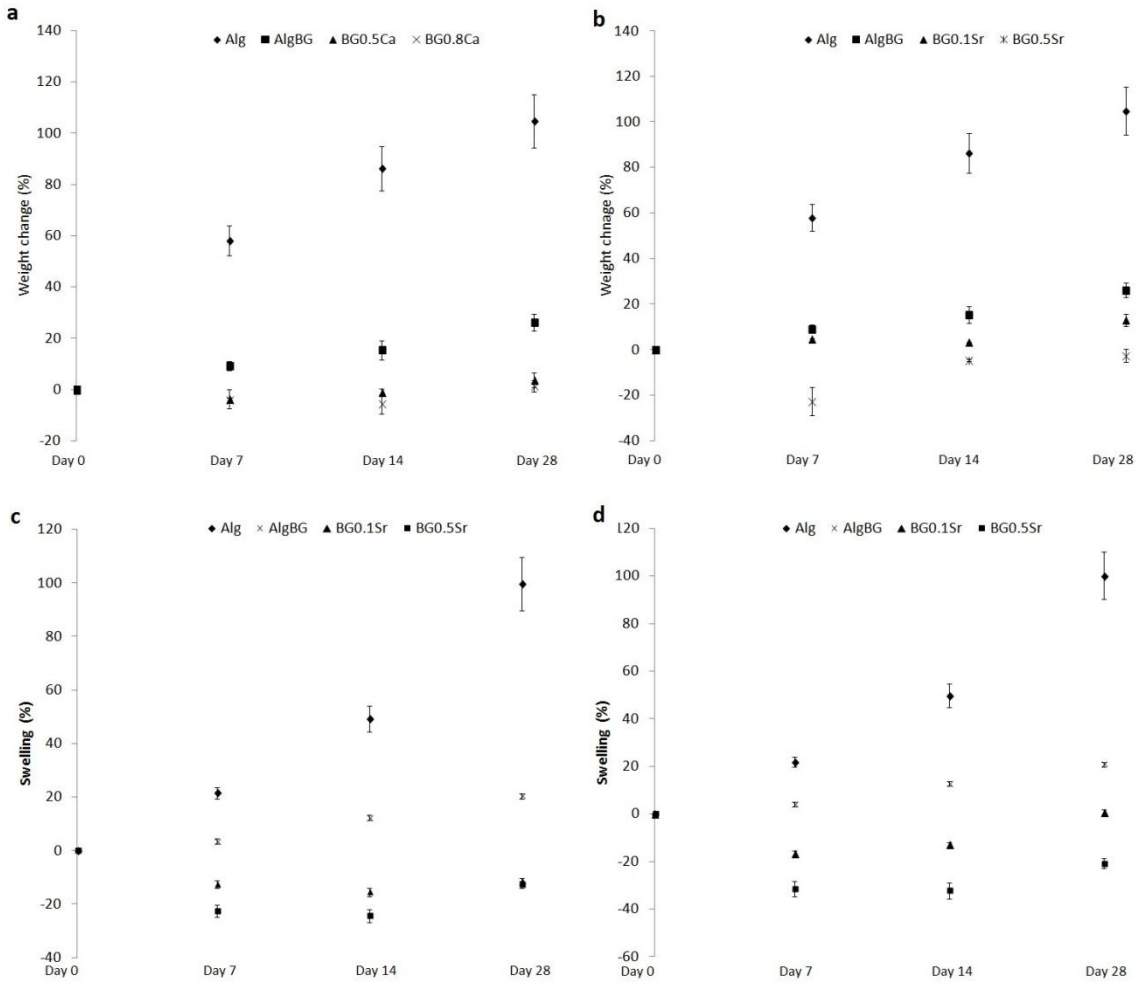

Figure 6. 3: Comparison of weight change between $CaCl_2$ cross-linked scaffolds (Alg and AlgBG) with (a) BGCa and (b) BGSr cross-linked scaffolds. Comparison of swelling properties between $CaCl_2$ cross-linked scaffolds (Alg and AlgBG) with (c) BGCa and (d) BGSr cross-linked scaffolds in deionised water at 0, 7, 14 and 28 days incubation. The deionised water was exchanged every 7 days and the weight measured after each exchange. Data represents the mean ± SD, n = 3.

Meanwhile, BGCa and BGSr cross-linked scaffolds showed trends of weight loss after 14 days of immersion, only increasing in weight after 28 days. Both BG0.5Ca and BG0.8Ca recorded a reduction in weight by approximately 10% after 14 days incubation, before returning to original weight (day 0). Similarly, BG0.1Sr (Figure 6. 3b) showed a small change in weight (< 5%) after 14 days of incubation, increasing to approximately 10% of initial weight after 28 days of immersion. Interestingly,

BG0.5Sr scaffolds showed an opposite effect of immersion in deionised water, which was a decreasing (negative) change in weight after 7 days of incubation by 20%. Subsequent time points of 14 and 28 days showed an increase in the scaffolds' weight but were overall still lower than the initial weight, suggesting that the scaffolds lost weight after 28 days of incubation.

This decrease in weight over time observed could be attributed to a phenomenon known as syneresis. Syneresis is the release of water and shrinkage of the gel over time, due to the further rearrangement and cross-linking of the gels when stored [76, 99]. This phenomenon was demonstrated in previous studies carried out by comparing changes in alginate composite hydrogel sizes through the use of cross-linker solutions ($CaCl_2$) with different concentrations. Size of the hydrogels decreased as cross-linker concentration increased, due to the shortening of polymers chains [203]. With higher cross-linker concentrations, a larger proportion of calcium ions become available to form cross-links. Hence, the inter and intra molecular interaction between the polymer chains in the alginate gel was enhanced, thus shortening the average distance between ionic cross links, leading to further shrinkage [47, 76].

Another parameter studied in terms of long term changes in scaffold morphology was its swelling capacity. Figure 6. 3c and d show the changes in scaffold size between the conventional method of using $CaCl_2$ (Alg and AlgBG scaffolds) with that of the BGSr and BGCa method of gelation respectively. The size of Alg and AlgBG scaffolds increased with immersion time, doubling in size (> 100% size change) with Alg scaffolds. These results corroborate with the weight changes, in which similar trends were observed. BGSr cross-linked scaffolds on the other hand showed a decrease in size after 7 days of immersion, with BG0.5Sr scaffolds shrinking up to 35% from original size (day 0). As immersion progressed, the size of both scaffold types increased, although still smaller than its original size even after 28 days of immersion in deionised water. Similarly, scaffolds cross-linked using BGCa also shrank in size after 7 days of immersion, but as opposed to the BGSr cross-linked scaffolds, both BG0.5Ca and BG0.8Ca scaffolds continued to decrease in size up till 14 days of immersion, with BG0.8Ca scaffolds shrinking by approximately 20%. After 28 days

of immersion, the size of both scaffold types increased, with both showing similar levels of shrinkage at approximately 15% of original size.

It was expected that the alginate-based scaffolds would swell when introduced in an aqueous environment due to osmotic exchange, which would affect the mechanical properties and encourage the break-down of the scaffold [90, 93]. Indirectly, the extent of size change is related to weight change and *vice versa* since, swelling of the scaffolds is the result of water uptake, which consequently means heavier scaffolds. However, the difference in the behavioural aspects between Alg and AlgBG with that of BGSr and BGCa cross-linked scaffolds from the effects of long term exposure in an aqueous environment is interesting. The increasing trend in both weight and size of Alg and AlgBG scaffolds over time is typical of alginate gels due to the permeation of water into the gel network through osmosis [90, 113]. An osmotic exchange occurs between the sodium rich alginate gels with the aqueous environment, allowing water to be absorbed into the polymer. As water is absorbed, swelling occurs (osmotic swelling), thus also increasing the size of the pores between the polymer chains. This encourages further permeation, which in turn further increases the swelling of the gels [90].

The lesser degree in swelling and weight gain observed in AlgBG scaffolds was probably due to the gradual release of Ca^{2+} ions from the dissolution of the bioactive glass nanofillers (BG65), as was shown in Figure 6. 2. From the onset of dissolution, these bioactive glass nanoparticles, which acted as nanofillers to AlgBG scaffolds, would provide a source of cross-linking ions, thus able to continuously supply ions to cross-link, slightly offsetting the effects of osmotic swelling as compared to pure alginate (Alg) scaffolds. The decrease in weight and size of BGSr and BGCa cross-linked scaffolds through syneresis could be attributed to a continuous release of ions from partly the nanocarriers, but also from the reservoir of ions stored within the mesopores of the nanocarrier. The greater amount of cross-linking ions from the nanocarriers would have offset the swelling and weight gain of the scaffolds through tightening of the gel network from an increased degree of cross-links. These densely packed gels would have reduced the permeability of the gel, making it difficult for water to be absorbed into the network.

6.5 Long term mechanical properties of scaffolds

The mechanical properties of BG0.5Ca, BG0.8Ca, BG0.1Sr and BG0.5Sr were further evaluated in terms of changes to its Young's modulus (E) over 7, 14 and 28 days of incubation in deionised water. The E values recorded were normalised against day 0 measurements which were taken to be 100 % (representing no change). The results demonstrated a remarkable difference in the E between BGCa and BGSr cross-linked scaffolds as compared to the conventional $CaCl_2$ cross-linked scaffolds of alginate (Alg) and bioactive glass-alginate (AlgBG) composite scaffolds. A decreasing trend in the relative E values as incubation progressed for Alg and AlgBG scaffolds while after 7 days incubation, both BGCa and BGSr cross-linked scaffolds recorded an overall increase in the relative E values, before decreasing as incubation progressed onwards of 14 days.

Changes in E for scaffolds cross-linked with BGCa were examined in Figure 6. 4a. The results showed that after 7 days of incubation, scaffolds cross-linked with nanocarriers impregnated 0.5 M and 0.8 M $CaCl_2$ solutions (BG0.5Ca and BG0.8Ca respectively) recorded significant improvements in its relative E, with both scaffold types breaching 200% of its day 0 E values. As incubation progressed, all scaffolds demonstrated a decreasing trend in its relative E values, although, BGCa cross-linked scaffolds still remained stiffer than the $CaCl_2$ cross-linked scaffolds of Alg and AlgBG even after 28 days incubation. Similarly, the relative E of scaffolds cross-linked with BGSr was studied, as shown in Figure 6. 4b. After 7 days incubation, scaffolds cross-linked using nanocarriers loaded with 0.5 M $SrCl_2$ (BG0.5Sr) showed a dramatic improvement in its relative E, increasing by almost 200%, while BG0.1Sr cross-linked scaffolds showed a slight overall improvement. Throughout 28 days of incubation, BGSr scaffolds remained stiffer than its original (day 0) E values (> 100%), while the E of conventionally cross-linked scaffolds decreased to less than half of its original stiffness. Interestingly, the relative E of BG0.1Sr scaffolds increased at day 14, achieving relatively similar levels to BG0.5Sr scaffolds, before subsequently decreasing at day 28.

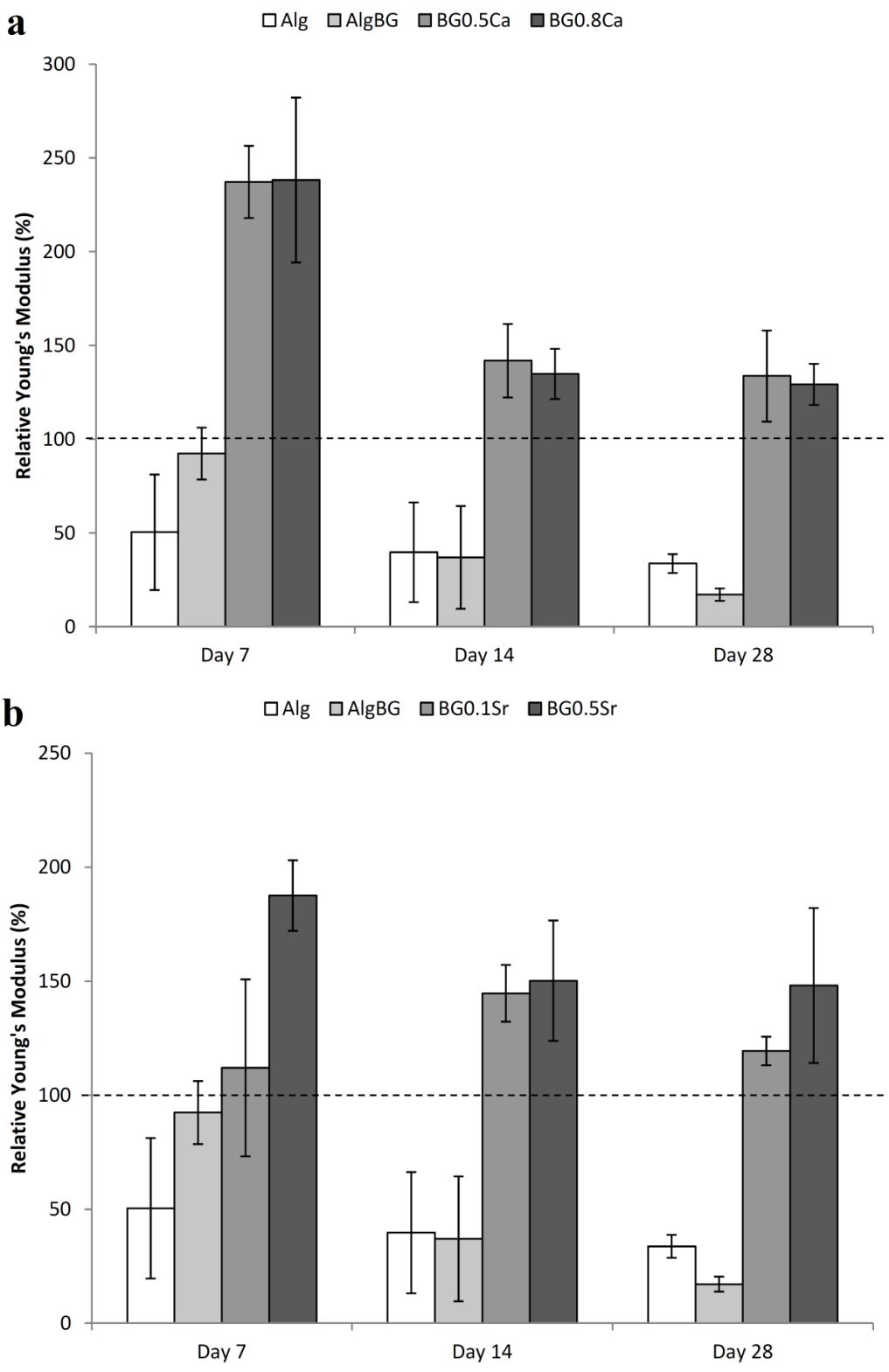

Figure 6. 4: The relative Young's modulus of alginate (Alg), alginate-bioactive glass composite (AlgBG) scaffolds cross-linked with $CaCl_2$ solutions compared against scaffolds synthesised from (a) the BGCa system and (b) the BGSr system over incubation time points of 7, 14 and 28 days in deionised water. The dotted line represents baseline (day 0) of E values. Data represents the mean ± SD, n ≥ 3.

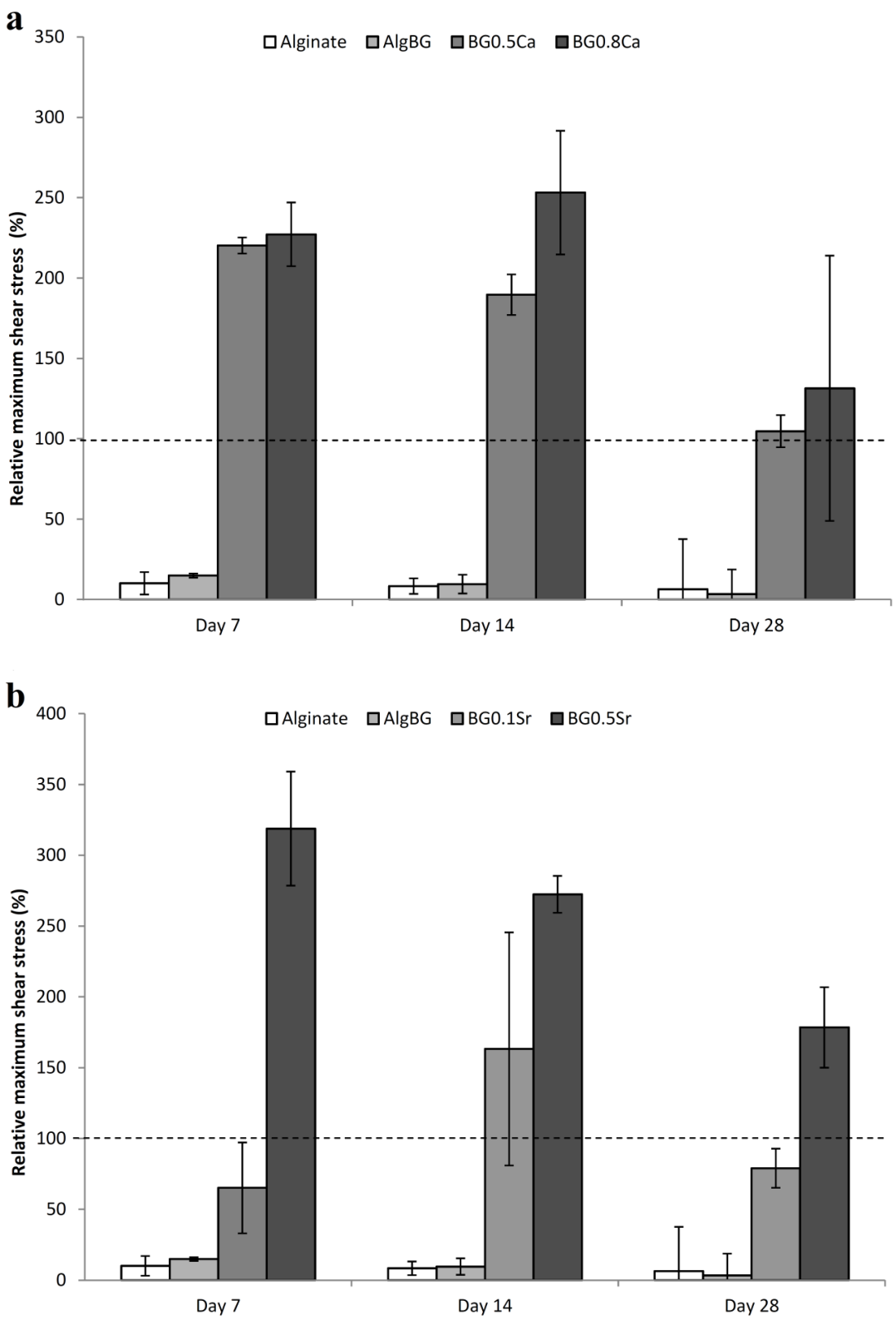

Figure 6. 5: The relative maximum shear stress for alginate (Alg), alginate-bioactive glass composite (AlgBG) scaffolds cross-linked with $CaCl_2$ solutions compared against scaffolds synthesised from (a) the BGCa system and (b) the BGSr system over incubation time points of 7, 14 and 28 days in deionised water. The dotted line represents baseline (day 0) of E values. Data represents the mean ± SD, n ≥ 3.

The maximum shear stresses (τ_{max}) of the variously cross-linked scaffolds were evaluated over 7, 14 and 28 days and normalised against day 0. The graphs in Figure 6. 5 compare the relative τ_{max} of scaffolds cross-linked using BGSr and BGCa with conventionally cross-linked Alg and AlgBG scaffolds. Huge differences in the τ_{max} were observed, in which both Alg and AlgBG scaffolds recorded a drastic decrease of more than 70% in original shear stress after 7 days of incubation. The maximum τ_{max} of both these scaffold types continued to decrease from its original day 0 values as incubation progressed. Meanwhile, in stark contrast to the Alg and AlgBG scaffolds, BGCa cross-linked scaffolds recorded a huge increase in τ_{max} (> 200% from original day 0 values) after 7 days of immersion in deionised water. As incubation progressed, BG0.5Ca scaffolds followed a decreasing trend in τ_{max} values, finally retaining its original shear stress (approximately 100%) after 28 days of incubation. Figure 6. 5a also shows the τ_{max} of BG0.8Ca scaffolds increased after 14 days of incubation, before decreasing at day 28. A large standard deviation noted in BG0.8Ca scaffolds at day 28 was likely attributed to scaffolds splitting at the sides from the onset of large deformation, causing each sample's maximum shear stress to vary.

Figure 6. 5b shows scaffolds cross-linked using BGSr. After 7 days of incubation, a decrease in the τ_{max} of BG0.1Sr scaffolds was observed, while a drastic increase by more than 300% compared to its original (day 0) shear stress was observed in BG0.5Sr scaffolds. After 14 days of incubation however, the relative τ_{max} of BG0.1Sr scaffolds increased, suggesting an improvement in its mechanical properties even after 14 days of immersion, while a decrease was noted for BG0.5Sr scaffolds. After 28 days incubation, the τ_{max} of both BGSr cross-linked scaffolds decreased with BG0.5Sr scaffolds still achieving a better overall τ_{max} than at day 0 while BG0.1Sr scaffolds retained more than 60% of its original τ_{max} values.

As opposed to Young's modulus testing, in which values of stress and strain were obtained from the linear elastic region of the scaffolds over small deformations (0.5 mm compression), the puncture test was carried out at large deformations, causing the scaffold material to slide relative to each other in the direction of the force, leading to shear. Therefore, the puncture test was conducted to determine the mechanical properties of the scaffolds under unacceptable levels of deformation or failure. The

results obtained from both tests demonstrate the superior long term mechanical properties of BGCa and BGSr cross-linked scaffolds. As compared to Alg and AlgBG scaffolds, the Young's modulus and maximum shear stress of both BGCa and BGSr cross-linked scaffolds improved over time. Typically, for alginate-based gels, research has demonstrated that long term exposure of the gels to an aqueous environment led to a decrease in mechanical properties due to the destabilisation of the polymer network from gradual loss of the ionic cross-links (osmotic exchange) [46, 90, 118]. This causes the gels to swell, as was observed in Figure 6. 3, which encourages further permeation of fluid, leading to the eventual disintegration of the scaffolds [76].

The lost in scaffold stiffness and shear stress observed in both Alg and AlgBG scaffolds over time were reminiscent of the destabilisation of the gel network. However, results indicated that the rate of decrease in overall mechanical properties of AlgBG scaffolds was slower than Alg scaffolds. This was because, AlgBG scaffolds were composed of a 60 to 40 percent ratio of bioactive glass nanoparticles (BG65) and alginate. Thus, during incubation, the BG65 would have leached calcium ions through the breakdown of the silicate network, providing small amounts of calcium ions to sustain the cross-links. Nevertheless, the release was insufficient to sustain the overall loss of Ca^{2+} into the aqueous environment from the gel network, therefore still resulting in a net reduction in ions to maintain scaffold mechanical properties.

On the other hand, scaffolds synthesised from BGCa and BGSr cross-linking systems were found to demonstrate remarkable improvements in mechanical properties over time. This was especially evident in the first 7 days of incubation, whereby increases of over 200% in Young's modulus and 300% in shear stress were recorded. One explanation for this occurrence could be attributed to the sustained release of cross-linking ions from the impregnated nanocarriers. This method was a novel internal diffusion method, in which the divalent-rich nanocarriers acted as reservoirs within the scaffold matrix to release cross-linking ions over time, thus sustaining the ionic cross-links in the gel [47, 92]. During gelation of the scaffold, the cross-linking salts impregnated during loading provided an outburst of cross-linking ions, largely from the surface of the nanocarriers. Subsequently, as incubation progressed, these nanocarriers would continue to release cross-linking ions trapped within the

mesoporous structure of the nanocarriers through its own dissolution. From the increase in mechanical properties observed, it can be postulated that there was an excess of cross-linking ions held by the nanocarriers, resulting in a net positive gain in ions available for sustaining and further cross-linking of the alginate-based scaffold.

6.6 Scaffold degradation and its effects on buffer pH

The degradation rate and pH changes of two scaffold types (AlgBG and BG0.8Ca) cross-linked via different routes, in phosphate buffer solution (PBS), is shown in Figure 6. 6. The complete dissolution of both scaffold types (100% weight loss) required approximately 10 h. During the initial 2 h, scaffolds were intact, with no weight loss recorded. After that, the scaffolds began to degrade, with a rather linear weight loss up until complete degradation at 10 h (Figure 6. 6a). Generally, scaffolds cross-linked with a higher concentration of cross-linking agent demonstrated a slightly slower degradation rate because, with higher concentrations meant an increase in the proportion of Ca^{2+} ions available to interact with the polymer chains to form more cross-links. Thus, this formed a tighter packing of the alginate polymer, slowing the penetration rate of phosphate ions into the scaffold matrix, reducing the chelating rate on Ca^{2+} ions [90].

The immersion of the scaffolds in phosphate buffer solution (PBS) led to rapid degradation due to the hypertonic nature of PBS which is 10 – 12 times (PBS:HBP; 1.0mM:12mM) the concentration of phosphate ions than in human blood plasma (HBP) [195]. It has been reported that ionically cross-linked alginate when exposed to a higher electron affinity ion such as phosphate, the chelating effect causes the ionic cross-links to break, as the Ca^{2+} ions become more attracted to the phosphate [46]. Hence, a rapid degradation of the sample was expected. However, this test was carried out to compare the rate of degradation between internally and externally cross-linked scaffolds as well as to monitor the onset of pH change in media due to scaffold degradation.

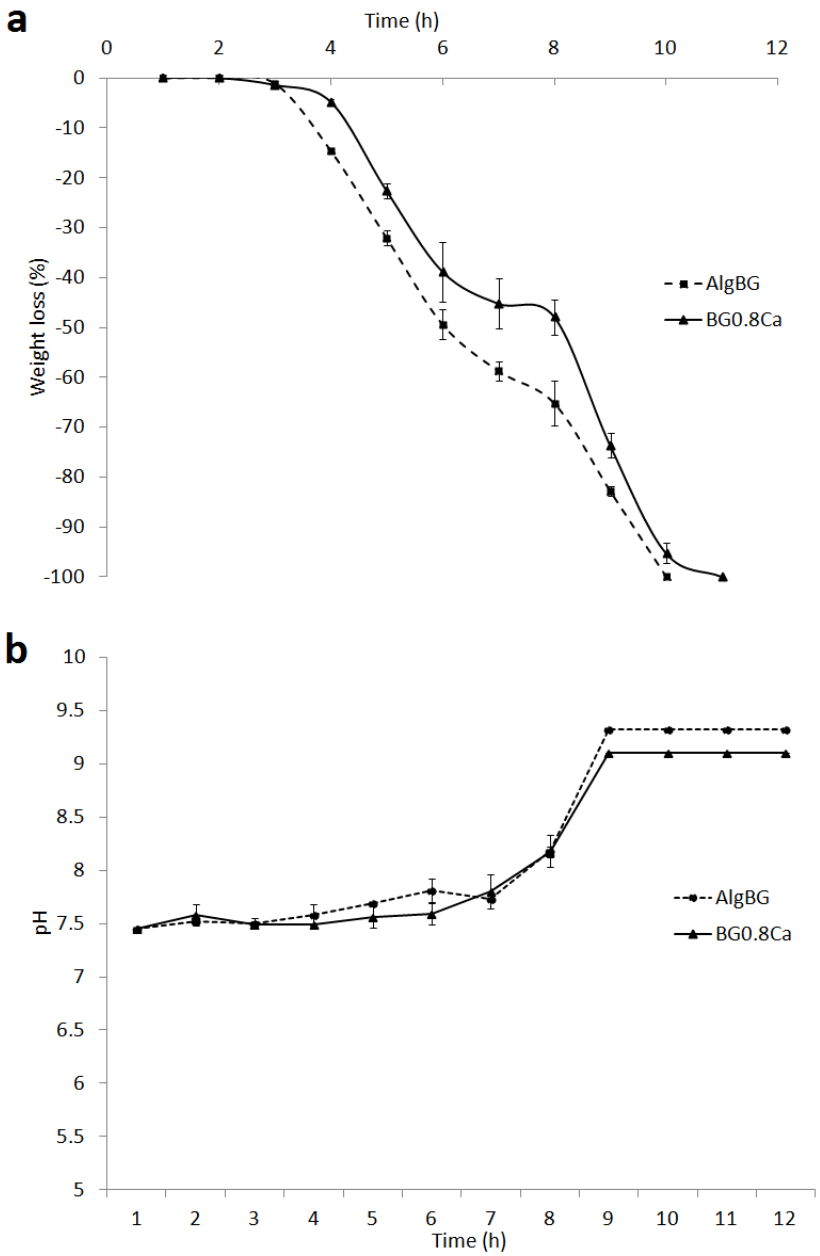

Figure 6. 6: Comparison in (a) weight loss through degradation and (b) pH change of the PBS over 12 h between conventionally cross-linked scaffolds using $CaCl_2$ and BGCa cross-linked scaffolds. Data represents the mean ± SD, n = 3.

The release of acidic or basic substances during the degradation of the scaffold plays an important role in determining if the scaffolds are viable or harmful towards cells. Figure 6. 6b shows a pH release comparison between AlgBG and BG0.8Ca scaffolds at hourly intervals. The graphs closely relate to the degradation state of the scaffolds, wherein, at initial 2 h, the pH levels remain relatively constant at pH 7.5, close to the

PBS solution prepared at pH 7.45. After that, as scaffold degradation ensued, pH levels in the buffer rose. It was noted that, BG0.8Ca scaffolds were slightly more alkali (approximately pH 0.5 higher) than AlgBG scaffolds. After 9 h, when the scaffolds were largely degraded, the final pH reached a plateau, with AlgBG scaffolds reaching a final pH of 9.5 while BG0.8Ca scaffolds recorded a pH of 9.

The reason for the difference in final pH levels was possibly due to the slightly acidic nature of BG0.8Ca nanocarriers which contained $CaCl_2$ salts in its mesopores. Ionic solutions ($SrCl_2$, $CuCl_2$, and $CaCl_2$) derived from salts containing a mixture of a weak base and a strong acid (HCL) when dissolved in water would tend to be acidic, with an increase in the acidity of the solutions as its concentration decreased, due to dilution which lowers the H^+ concentration in the solutions [225]. Therefore, the lower pH levels in the buffer solution recorded from the complete degradation of BG0.8Ca scaffolds concur with this finding.

This experiment showed that scaffolds synthesised through the internal diffusion of ions from the loaded BGCa nanocarriers was comparable to the conventional $CaCl_2$ cross-linked scaffolds, in terms of degradation rate and pH release levels. Although, it may seem that the pH levels of the scaffold were rather alkali, due to the rapid degradation rates and controlled environment (volume of 20 mL) in which this experiment was conducted, it would be expected that under a dynamic environment, for instance, *in vivo* models, the effects of pH would be significantly less.

6.7 *In vitro* bioactivity and biocompatibility of scaffolds

The FTIR spectra of the hybrid scaffold before and after immersion in simulated body fluid (SBF) at various time points are illustrated in Figure 6. 7. Before immersion (Day 0), a strong band between the region of 1080 – 1200 cm^{-1} was identified as the asymmetric stretching modes of Si – O – Si, while the band at 470 cm^{-1} was identified to correspond to the bending mode of Si – O – Si [134, 219]. Another broad band observed at 890 cm^{-1} corresponded to the Si – O – Ca bond, of which all stem from the BGCa within the matrix of the scaffold. Separately, a band in the region of 1600 –

1650 cm^{-1} was assigned to the carbonyl group (C – O – O bond), associated with the organic alginate [229, 230].

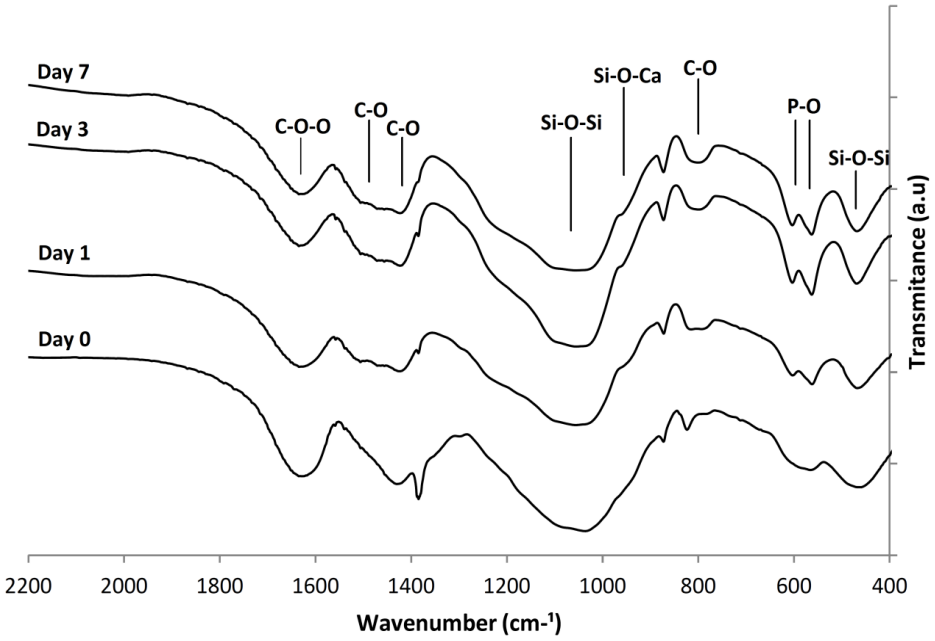

Figure 6. 7: FTIR spectra demonstrating no HCA formation at day 0 and then increasing HCA formation on the scaffolds immersed in SBF at time points of 1 day, 3 days and 7 days.

After 1 day of immersion in SBF, a weak twin band in the FTIR spectrum formed at the wave number 600 cm^{-1} and 570 cm^{-1}. This twin band is associated with the υ_4 antisymmetric bending mode of P – O bonds in the amorphous calcium phosphate [107, 165, 221]. As incubation progressed to 3 and 7 days, the twin bands at 600 cm^{-1} and 570 cm^{-1} appeared to intensify. Separately, a twin band at 1460 cm^{-1} and 1420 cm^{-1} formed 1 day of immersion was attributed to the formation of C – O bonds. These C – O bonds are from the υ_3 vibration mode of carbonate ions, which have undergone peak splitting [136, 164, 219]. A separate C – O bond was identified at the wave number 780 cm^{-1}, which corresponded to the υ_2 vibrational mode of this bond [219].

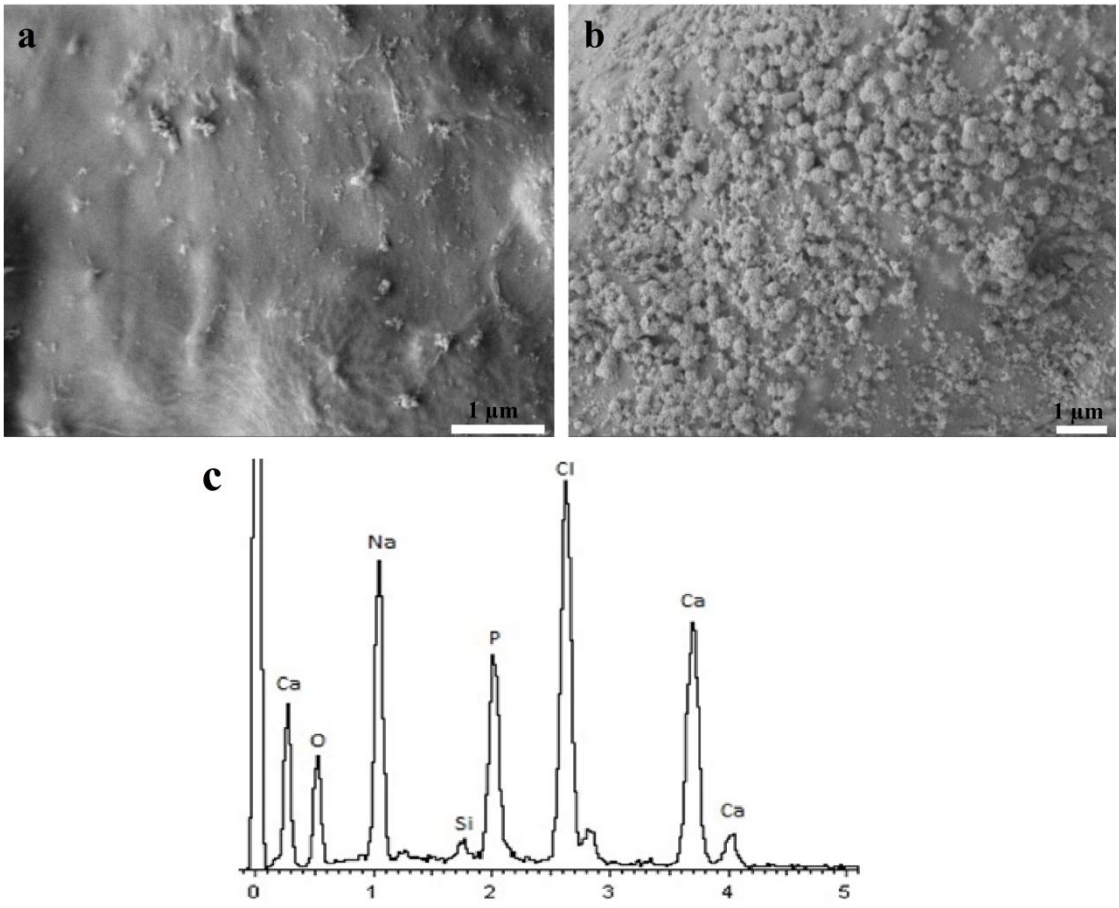

Figure 6. 8: The formation of HCA crystallites on the scaffold surfaces after (a) 3 days immersion and (b) 21 days immersion in SBF. (c) EDX spectrum of the HCA crystallites, confirming the high levels of Ca and P.

Figure 6. 8a and b show the SEM micrographs of a BGCa cross-linked scaffold post immersion in SBF at time points of 3 and 21 days. Figure 6. 8a shows the formation of small hydroxy-carbonate apatite (HCA) crystallites on the surfaces of the scaffold after 3 days incubation. After 21 days (Figure 6. 8b), these HCA crystallites had increased in size, covering the surface of the scaffold with pseudo-spherical (cauliflower-like) agglomerates of HCA crystallite, due to further nucleation of calcium phosphate. The identification of these HCA crystallites was carried out using EDX analysis. Figure 6. 8c shows the spectrum of a point EDX analysis of the crystallites demonstrating an elemental content rich in calcium (Ca) and phosphorous (P), confirming the formation of a HCA on the surfaces of the scaffolds. The sodium (Na) and chlorine (Cl) peaks detected in the spectrum were attributed to alginate, due to the penetrative depth of the X-ray beam between 5 – 10 µm, which would have penetrated beyond the HCA crystallites and into the scaffold [185]. Determining the

bioactivity of a material is crucial in deciding if the material will be able to bond to live bone tissue during *in vivo* implantation. This is determined by the HCA forming capability on the surface of the material when subjected to ionic buffer solutions, such as SBF [195]. Hence, the results which showed the formation of P – O bonds and C – O bonds upon immersion with SBF corroborated with both SEM and EDX evidence of the formation of HCA, and thus confirmed the bioactive nature of these scaffolds, pointing towards the possible use for further biological evaluation.

Human osteoblast bone cells (HOB) were seeded onto scaffolds for a period of 1, 4 and 7 days to establish the cytotoxic effects of BGCa cross-linked scaffolds on cells. Figure 6. 9 shows two-photon confocal micrographs of HOB cells stained with Cy3 cyanine dye anchored onto scaffold material after 24 h of culture. Dense clusters of cells were observed attached onto the scaffold (Figure 6. 9a) while Figure 6. 9b shows cells with stretched filopodia, suggesting healthy cells. SEM micrographs of cell coverage on scaffold material after 7 days of culture are shown in Figure 6. 10. The micrographs show cells covering the surface of the scaffold, forming a thick, healthy layer of cells. Closer examination of the cells (Figure 6. 10b and c) showed that the cells have anchored firmly to the surface with a fibroblast-like morphology and were well spread out with filopodia stretched out, suggesting that the cells have completely attached to the scaffold and are in the process of proliferating.

The anchoring of HOB cells on the scaffold after 24 h and the proliferation of HOB cells after 7 days culture confirmed the positive cellular response of the composite scaffolds on HOB cells, by creating a favourable microenvironment for cell proliferation and growth [221]. The initial contact of HOB cells to scaffold surfaces is crucial for successful osseointergration between the scaffold and native tissue [37, 52]. These preliminary results demonstrate the non-cytotoxic effect of the composite scaffolds. Although bioactive glasses and alginate have been shown to have no adverse effects to HOB cells, it was still important that this hybrid composite system was tested using the HOB cell model [7, 17, 46].

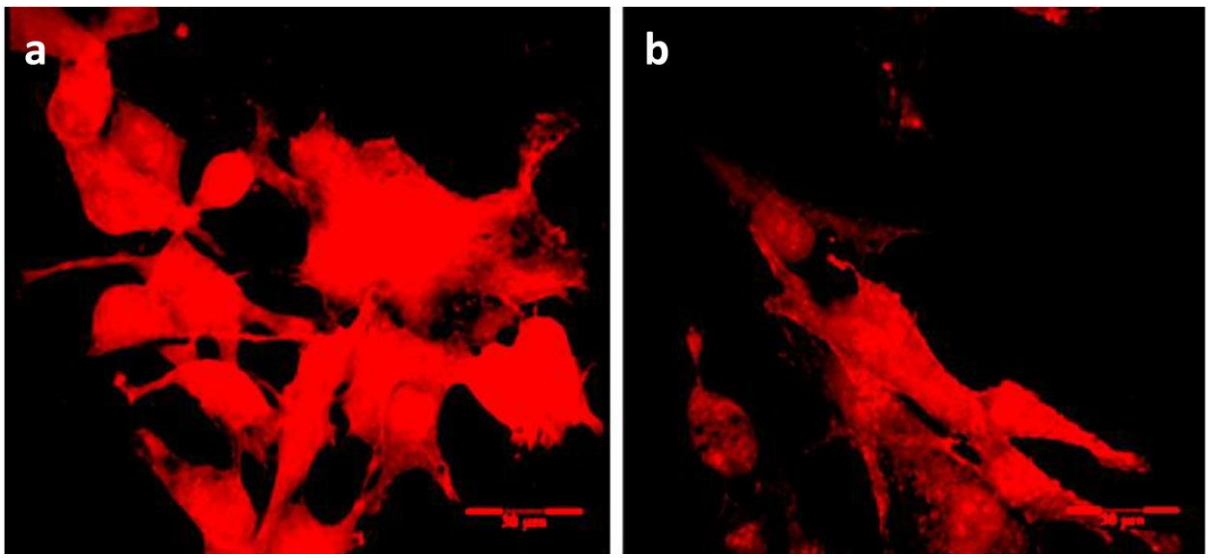

Figure 6. 9: Two-photon micrographs of HOB cells after 24 h seeding on a BGCa cross-linked scaffold.

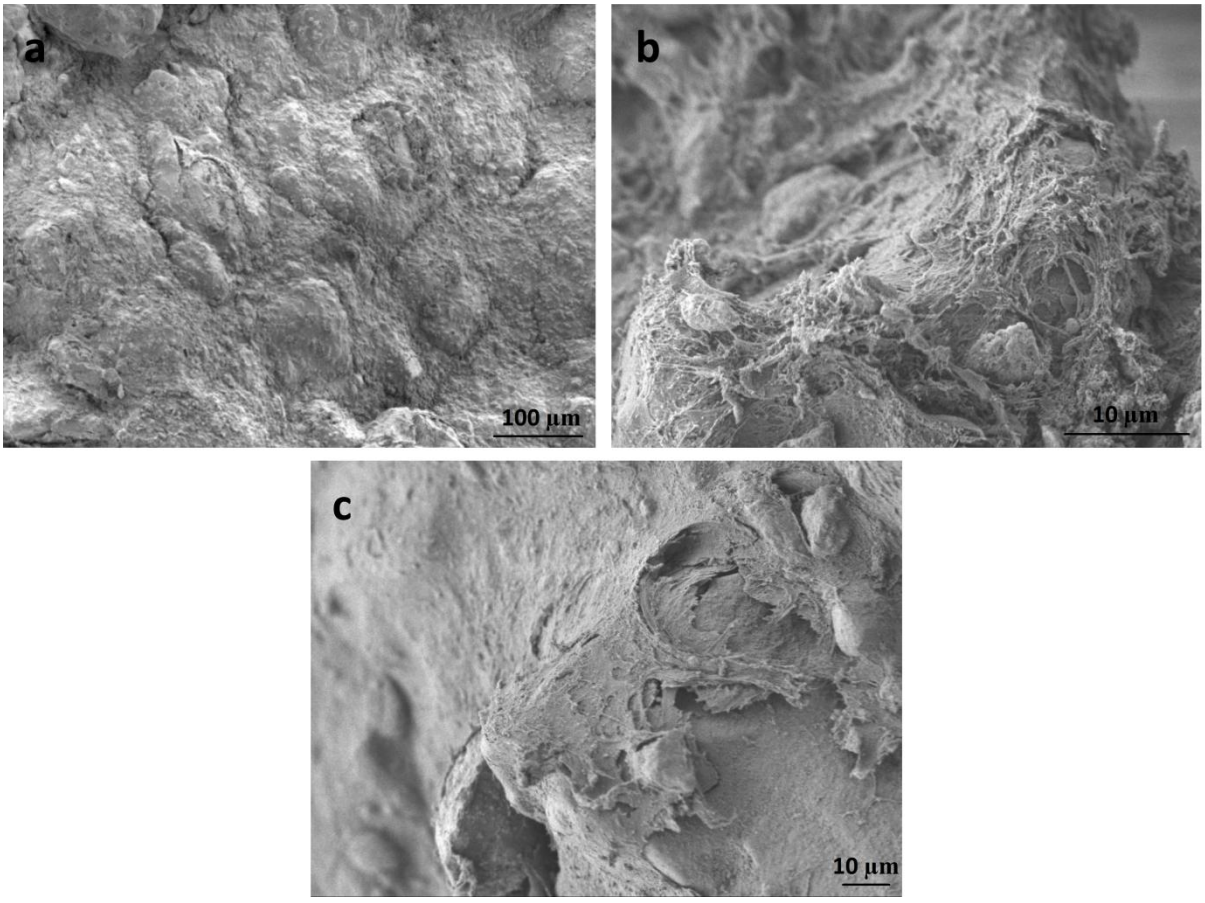

Figure 6. 10: SEM micrographs showing the proliferation of HOB cells on the surfaces of the BGCa cross-linked scaffold.

6.8 Summary

BGSr and BGCa cross-linked scaffolds were categorised as internally cross-linked, since the mechanism of cross-linking occurred through the diffusion of ions from the nanocarriers within the scaffold matrix. The conventionally cross-linked scaffolds using $CaCl_2$ solutions on the other hand were categorised as externally cross-linked, since the diffusion of ions occurred from the outside of the scaffold.

The Young's modulus (E) of scaffolds synthesised by BGSr and BGCa nanocarriers impregnated with different concentrations of cross-linker solutions showed that the E values of scaffolds increased as the impregnated cross-linker concentration increased, up until a critical concentration (0.8 M for BGCa and 0.5 M for BGSr systems), beyond which, the E values decreased and recorded large standard deviations. Higher impregnated concentrations increased the availability of ions to form cross-links with the alginate solution, however, poor structural uniformity due to uncontrolled gelation caused the weakening of the overall scaffold.

The release of calcium ions in deionised water from the nanocarrier (BG65) was investigated using ISE measurements. Throughout the 28 day testing period, the ionic release from nanocarriers impregnated in higher concentrations of cross-linker solutions recorded higher levels of calcium ion release (BG0.8Ca > BG0.5Ca nanocarriers). The ionic release by all nanocarrier types followed a similar profile of a burst release after 2 h immersion, proceeded by a steady increase, reaching a maximum cumulative release after 7 days of immersion. Subsequent immersion showed a decrease in the detected ions due to precipitation of calcium-phosphate ions.

The long term changes in weight and size of both internally and externally cross-linked scaffolds were monitored. Throughout the 28 day incubation period, the externally cross-linked scaffolds (Alg and AlgBG) showed an increasing trend in both weight and size due to osmotic swelling. Conversely, the internally cross-linked scaffolds (BG0.5Ca, BG0.8Ca, BG0.1Sr and BG0.5Sr) showed a decrease in weight and size after 7 days incubation. The continuous release of cross-linking ions was attributed to the offsetting of osmotic swelling, with further tightening of the gel

network through additional cross-links, thus contributing to the overall decrease in scaffold weight and size after incubation.

The comparison in mechanical properties between conventionally cross-linked scaffolds with BGSr and BGCa cross-linked scaffolds demonstrated the superior improvements in the long term E and maximum shear stress (τ_{max}) of the BGSr and BGCa scaffolds. Throughout incubation (28 days), the E and τ_{max} of Alg and AlgBG scaffolds decreased, where improvements in the E and τ_{max} of BGSr and BGCa scaffolds were observed. Looking specifically at the E values of each scaffold type, the scaffolds achieved a maximum relative E after 7 days of incubation, with the exception of BG0.1Sr scaffolds, which required 14 days. Remarkably, the maximum E of these scaffolds, which were higher than their original values, was recorded even after sustained periods of incubation in deionised water.

Additionally, the τ_{max} of BGSr and BGCa scaffolds also showed significant improvements over time, with for instance, BG0.5Sr scaffolds exhibiting a 300% increase in τ_{max} after 7 days incubation. Rather than losing its stiffness and shear resistance after long term exposure to an aqueous environment, both BGSr and BGCa scaffolds continued internally cross-linking, attributed to the sustained release of divalent ions from the loaded nanocarriers, thus driving this unprecedented improvement in mechanical properties.

Degradation rates of both the internally and externally cross-linked scaffolds were relatively similar. Complete degradation of both scaffold types required approximately 10 h, with the pH of the phosphate buffer solution (PBS) increasing concomitantly as the scaffold degraded, reaching a final pH 9 for BG0.8Ca cross-linked scaffolds and pH 9.5 for the AlgBG scaffolds. By using PBS, the degradation of the scaffolds was accelerated, due to the chelating effect of phosphate ions on calcium.

The *in vitro* bioactive and biological response of BGCa cross-linked scaffolds was investigated. The formation of hydroxy-carbonate apatite (HCA) on the surfaces of the scaffolds after 1 day of immersion in simulated body fluid (SBF), and the progression of HCA crystallite growth demonstrated the bioactive nature of the scaffolds.

Furthermore, the attachment of human osteoblast bone (HOB) cells on the surface of the BGCa cross-linked scaffolds suggested that these scaffolds were suitable for further biological studies despite the alkali nature of the scaffolds observed upon degradation.

The comparison between conventionally cross-linked scaffolds with the novel method of cross-linking via ionically impregnated nanocarriers is pertinent, to demonstrate the outstanding improvements to the mechanical properties of the composite scaffolds. Even though the data would suggests that these composite scaffolds are insufficiently strong for the direct use in load-bearing application for bone tissue replacement (kPa range as compared to MPa and GPa ranges [26, 29]), the vast improvements achieved through this method of cross-linking would certainly broaden its application as a temporary scaffold, providing a suitable site for the attachment and proliferation of osteoblast cells, which over time would lay an extracellular matrix, providing the mechanical integrity of the tissue naturally [37, 231].

Chapter 7

Conclusion and Future Work

7.1 General discussion

The objective of this thesis was to synthesise composite scaffolds for bone tissue engineering, employing the promising biomaterials of bioactive glass and alginate. To achieve this aim, the research was separated into three parts, with each part following a systematic sequence of study, beginning with: I) the development and characterisation of mesoporous bioactive glass nanoparticles, II) the synthesis of composite scaffolds using the tailored bioactive glass nanoparticles and III) evaluation of the alginate-bioactive glass composite scaffolds.

The synthesis of bioactive glass nanoparticles followed the order of sol, gel, drying and lastly sintering. In essence, variations in each stage had an effect on the structure of the bioactive glass nanoparticles. These effects were interlinked. The nanoparticle morphology of BG35 and BG50 glasses showed a dual-modal pore size distribution. These two glass types contained the lowest silica composition, with crystal structure analysis showing that these glasses contained crystal phases of wollastonite and hydroxyapatite (HA) in a largely amorphous matrix. The dual-modal pore size formation was attributed to the leaching of Ca species during the aging process of the gel, leading to the formation of micropores. The high calcium content of these glasses meant that more Ca species would have leached out, leading to further coalescing of the micropores into macropores.

Freeze drying was found to have affected BG65 nanoparticles, wherein, pore shape of BG65 was found to replicate ice crystals, through the templating effect of ice crystal formation on the silicate network. Interestingly, the influence of this was not observed in the other glass types studied (BG35, BG50, BG80 and nBG65) due to the crystal structure and the silica polymer chain type that was found. Trace amounts of wollastonite and HA within BG35, BG50, and incipient amounts of the SiO_2 crystalline phase (cristobalite) found within BG80 would have inhibited the effects of the ice crystal formation on pore shape change. Similarly, nBG65, produced by the

multi-step (basic) route, would have consisted of a tightly packed, clustered silicate polymer network, making it less susceptible to morphological change by freeze drying.

Apart from the investigation into the effects of different heat treatment regimes on nanoparticle morphology, the other studies conducted on the effects of changes in composition, pH and drying procedures on nanoparticle structure, involved nanoparticles which were heat treated to 680 °C, to ensure the incorporation of calcium into the silicate network, and from convention were termed tertiary particles. These tertiary particles were derived from the fusion of secondary particles (5 – 8 nm) during heat treatment, and hence was suggested that due to the uncontrollable nature of fusion, the shape and size of the pores produced within the nanoparticles would be random. The results of different sintering temperature showed that densification of the nanoparticles occurred, in which temperatures above 400 °C caused viscous flow of the secondary particles, reducing the interstitial spaces between them. However, these viscous flows were localised to within adjacent particles, and did not alter the final pore shape of these nanoparticles.

The evaluation of dissolution products from bioactive glass nanoparticles incubated in deionised water revealed that the precipitation of Ca and P species on the surface of the nanoparticles involved a complex mechanism of ionic exchange, condensation and polymerisation reactions. Results showed that the formation of apatite on different bioactive glass compositions can take place even in ion-deprived solutions. Nanoparticle morphology, specifically pore shape and size was important in improving the *in vitro* bioactive behaviour of the glasses. The hydroxy-carbonate apatite (HCA) formation on the surfaces of BG65FD after exposure to SBF was faster than conventionally dried BG65OD nanoparticles. This was attributed to the increased ionic transport efficiency of the channels created by the slit- or wedge-like mesopores. The mesopore channels would have promoted faster permeation of SBF throughout the nanoparticle, allowing greater glass-solution interfacial contact, thus increasing the rate of ionic exchange, rapidly initiating the HCA formation mechanism.

The feasibility of using the synthesised mesoporous bioactive glass nanoparticles (BG35, BG50, BG65, BG80 and nBG65) for the ionic cross-linking of alginate to produce alginate-based composite scaffolds was studied. The nanoparticles were sintered at different temperatures of 150 °C, 400 °C, 500 °C and 680 °C, and introduced into alginate solutions, to evaluate gelation kinetics. Results revealed that nanoparticles treated to temperatures below 680 °C caused rapid gelation of the alginate solutions. Indirectly, this result confirmed that, during the drying stages of the sol, calcium nitrate, as the precursor to the calcium component in the ternary glass system, was deposited onto the surfaces of the secondary silica particles. Therefore, at low sintering temperatures (< 680 °C), the calcium was unable to diffuse into the silicate network, and thus readily available to cross-link the alginate solutions.

Interestingly, it was discovered that the gelation kinetics of alginate solutions were jointly influenced by nanoparticle composition and its specific surface area (SSA). High calcium containing nanoparticles (BG35) led to rapid gelation of the alginate solution, while large SSA nanoparticles (BG65) similarly caused rapid gelation. This was because, for the high calcium content nanoparticles, a larger proportion of calcium would be available to provide cross-linking, while larger SSA nanoparticles would allow greater interfacial contact between the alginate solution and nanoparticles, thus providing larger contact areas for calcium to interact and cross-link the alginate. Specific control over gelation kinetics through systematic increments in sintering temperature was challenging, with large variations in gelation time (5 min to 5 h) between a 10 °C rise in sintering temperature.

Mesoporous bioactive glass nanoparticles, sintered to 680 °C were subsequently employed as nanocarriers for the ionic cross-linking of alginate. The nanocarriers were impregnated with cross-linking salts of $SrCl_2$, $CuCl_2$ and $CaCl_2$. The impregnation efficiency of $CuCl_2$ was 8 times more than the other two salts, attributed to Cu^{2+} ions having the smallest ionic radii, but also the unique property of copper as a transitional element, capable of forming water molecule-based ligand structures. The small ionic radii of Cu^{2+} ions would have allowed increased mobility of the ions during impregnation, enabling higher permeation into the cavities of the nanocarrier. Isotherm analyses of the nanocarriers after impregnation showed that the pores within

strontium and calcium loaded nanocarriers were filled with the cross-linking molecules. Interestingly, for copper loaded nanocarriers, no differences in isotherm characteristics were observed before and after impregnation. Monolayer coverage of the copper ligand structures was thus proposed, which adhered to the surfaces of the nanocarrier, and into pores sufficiently large to accommodate these ligands. The interaction between silinol groups present in the nanocarrier and the water-based copper ligands enabled high loading efficiency of copper onto the nanocarrier. Furthermore, this interaction drove the compaction of copper ligands adhered to the nanocarrier surfaces, leading to a closely packed system consisting of copper ligands, and thus explained the reason behind the high impregnation efficiency of copper, even though monolayer coverage was observed.

The loaded nanocarriers were subsequently introduced into alginate solutions, for the synthesis of composite scaffolds through internal diffusion of cross-linking ions. Gelation kinetics of the alginate, influenced by nanocarrier morphology, glass to alginate (G/A) ratio and cross-linking ion type, was defined into rapid gelation, controlled gelation and slow gelation, based on the physical appearance of the cross-linked gels. Although the formation of ice crystals played an important role in determining the final scaffold microstructure, its influence also relied on slurry concentration of the composite gel. For scaffolds produced through controlled gelation, a microstructure consisting of a narrow distribution of pore sizes was observed. This was because, under controlled gelation, the distribution of composite material was homogenous throughout the scaffold. Since, a gradual freezing rate was employed for the synthesis of scaffolds, ice crystal growth was controlled and thus the pores formed from the sublimation of ice was rather consistent in shape and size.

Similarly, a gradual freezing rate was employed for the drying of slow gelating scaffolds. However, a unique porosity gradient was observed, in which the shape of pores transited from planar, at the bottom section of the scaffold, towards cellular and finally into lamellar pores at the upper sections. This architectural feature observed was caused by a composite material-based concentration gradient, in which, the bottom sections contained a higher concentration of composite material. Hence, ice crystal growth at the bottom section was hindered, leading to the formation of small

discrete pores. Conversely, ice crystals in the upper section grew in the direction perpendicular to the cold front, unhindered by composite material, and thus formed unidirectional microchannels upon sublimation.

The mechanical properties of scaffolds produced via BGCa and BGSr cross-linking were evaluated. The gelation kinetics of the scaffolds, and its consequences on scaffold microstructure depended upon the cross-linker solution concentration in which the nanocarriers were loaded with. Therefore, it was unsurprising that the Young's modulus of the scaffolds increased as the nanocarrier cross-linker impregnation concentration increased. Conversely, nanocarriers loaded with high concentrations of the cross-linker solution (1 M) led to the rapid gelation of the composite slurry, which in turn caused the formation of aggregated gel lumps and an overall heterogeneous scaffold structure. This diminished the stiffness of the scaffold as the large voids in between the gel lumps were unable to resists compression, and thus collapsed under loading.

The relationship between the long term ionic release from the nanocarriers and the mechanical properties of the BGCa and BGSr cross-linked scaffolds was established. To describe this relationship, firstly, the concentration of calcium ions released from the nanocarriers was shown to increase over time, reaching a cumulative maximum concentration after 7 days of immersion in deionised water. Although subsequent immersion resulted in a decrease in the ionic concentration, which was attributed to the precipitation of calcium phosphate species, impregnated nanocarriers still recorded an excess of calcium ions (> 260 ppm) within the supernatant after 28 days, which could be used to enhance scaffold cross-linking.

In terms of swelling and weight change, scaffolds cross-linked by conventional means of using $CaCl_2$ solutions (Alg and AlgBG) were consistent in its behaviour of alginate-based gels being exposed to an aqueous environment. Both these scaffold types swelled and gained weight through osmotic exchange between the sodium rich alginate polymer and the deionised water. Remarkably, an opposite effect was observed for BGCa and BGSr cross-linked scaffolds. The release of cross-linking ions stored within the nanocarriers over time translated into a continuous internal cross-

linking process, providing for an increased degree of cross-linking, tightening and rearrangement of the gel network. Consequently, the scaffolds reduced in size and weight.

The mechanical properties of scaffolds were associated with these changes to its physical structure. The Young's modulus and maximum shear stress of Alg and AlgBG scaffolds decreased as immersion in deionised water progressed, due to the weakening of the scaffold as the polymer absorbs water. In contrast, the mechanical properties of both BGCa and BGSr cross-linked scaffolds improved over time, indicating that the internal diffusion of cross-linking ions was in progress, supplying a sustained source of ions to offset the effects of osmotic exchange. Nonetheless, the source of cross-linking ions stored within the nanocarriers is not limitless, and hence, a reduction in mechanical properties was observed as incubation of the scaffolds continued on to 28 days. Although the mechanical properties of BGCa and BGSr scaffolds were predominantly better off than its original day 0 properties (apart from BG0.1Sr scaffolds), the decrease in both the Young's modulus and maximum shear stress of the scaffolds at day 28 suggested that leaching of cross-linking ions from the nanocarriers decreased, and thus was unable to compensate for the effects of osmosis.

7.2 Conclusions

7.2.1 Comparison between sol-gel (acidic) route and multi-step (alkali) route

- Bioactive glass nanoparticles of the composition 65% SiO_2 – 30% CaO – 5% P_2O_5 (wt. %) were synthesised by a sol-gel route and a multi-step route.
- Nanoparticles from the sol-gel route (BG65), synthesised under acidic conditions (≈ pH 2) were heterogeneous in shape.
- Nanoparticles from the multi-step route (nBG65), synthesised under basic conditions (≈ pH 11) were spherical with diameters ranging from 30 – 90 nm.

7.2.2 Development of tailored mesoporous bioactive glass nanoparticles by varying composition

- Four sol-gel glass compositions (BG35: 35% SiO_2 – 60% CaO – 5% P_2O_5, BG50: 50% SiO_2 – 45% CaO – 5% P_2O_5, BG65: 65% SiO_2 – 30% CaO – 5% P_2O_5, and BG80 80% SiO_2 – 15% CaO – 5% P_2O_5; wt. %) were developed.
- BG35 and BG50 revealed interesting nanoparticle morphology of elongated plate-like particles between 30 nm and 100 nm in width while cylindrical and open-ended dual-modal size pores were observed within these nanoparticles.
- BG35 and BG50 showed crystalline phases through the identification of wollastonite and traces of hydroxyapatite within the amorphous matrix of the nanoparticles.
- BG65 and BG80 were amorphous with incipient crystalline phases of cristobalite.

7.2.3 Processing of bioactive glass nanoparticles through oven, vacuum and freeze drying

- The bioactive glass nanoparticles synthesised were subjected to three different types of drying processes: I) oven, II) vacuum and III) freeze drying.
- BG65 nanoparticles were susceptible to changes in nanoparticle morphology while nBG65 nanoparticles were not.
- Using BJH analysis of the adsorption and desorption branch, the unit pore shapes within oven dried nanoparticles were found to be ‘ink bottle’-like shaped mesopores.
- Freeze dried nanoparticles were found to contain slit- or wedge-like shaped mesopores.

7.2.4 Development of tailored mesoporous bioactive glass nanoparticles by varying sintering temperature

- Heat treatment did not affect nanoparticle pore shapes based on the similarities in the hysteresis loops across various maximum sintering temperatures of 150 °C, 400 °C, 500 °C and 680 °C, but affected SSA, pore size and pore volume.

- An increase in maximum sintering temperature led to an increase in nanoparticle SSA and pore volume, reaching a maximum at 500 °C before decreasing.
- Pore size decreased with an increase in sintering temperature.

7.2.5 Bioactive response of nanoparticles

- *In vitro* bioactivity test demonstrated an improvement in the bioactive response of freeze dried BG65 nanoparticles.
- Hydroxy-carbonate apatite (HCA) formation on freeze dried nanoparticles was detected after 12 h immersion in simulated body fluid (SBF).
- Conventional oven dried nanoparticles required 24 h of incubation for HCA formation.
- This study confirmed a nanostructure-bioactivity correlation, induced by changes in nanoparticle morphology through different drying methods.

7.2.6 Feasibility of using mesoporous bioactive glass nanoparticles for ionic cross-linking of alginate

- BG35, BG50, BG65 and nBG65 nanoparticles were employed to cross-link alginate.
- Correlation between sintering temperature and gelation time showed a region of rapid gelation (< 5 min) for treatment temperatures less than 500 °C.
- Gelation time of between 5 – 300 min for treatment temperatures between 500 – 560 °C.
- No gelation was observed for treatment temperatures above 560 °C.

7.2.7 Impregnation of mesoporous bioactive glass nanoparticles as nanocarriers

- Impregnation efficiency was related to SSA of the nanocarriers, whereby nanocarriers with the largest SSA showed the highest levels of impregnation efficiency.

- Impregnated BG65 nanocarriers showed that impregnation efficiency depended on ionic radii of the divalent ion, in which the smallest radii resulted in the highest uptake.
- Copper, through its ability to form ligand structures in water, was found to interact with the silinol groups on the surfaces of the nanocarrier, which promoted the uptake of copper onto the nanocarriers.

7.2.8 Gelation time of alginate by various nanocarriers

- Impregnated BG35, BG50, BG65 and nBG65 nanoparticles successfully cross-linked alginate within controlled gelation times.
- Nanocarriers cross-linked alginate through the diffusion of ions which were largely stored within its mesopores, because nanocarriers which recorded the highest impregnation efficiency had the smallest pore size which resulted in the slowest gelation time.
- The affinity of Sr^{2+} ions over Ca^{2+} ions to alginate was indicated by the faster gelation times of scaffolds cross-linked using $SrCl_2$ impregnated nanocarriers.

7.2.9 Dissolution of nanocarriers and impregnated nanocarriers

- The dissolution profile of Ca^{2+} ions from the nanocarriers showed a burst release after 2 h of immersion in deionised water, before reaching a cumulative maximum concentration at 7 days.
- The release concentration of the nanocarriers and impregnated nanocarriers were in line with their composition or impregnated concentration of calcium.

7.2.10 Mechanical properties of composite scaffolds

- Controlled water absorption and swelling levels of the composite scaffolds were observed through the novel use of impregnated nanocarriers as cross-linkers.
- Improvements in the scaffolds' Young's modulus and shear stress even after long term exposure to an aqueous environment were obtained. The continued diffusion of cross-linking ions from the nanocarriers within the scaffold matrix sustained

the cross-links within the scaffold, thus ensuring long term structural stability of the composite scaffolds.

7.2.11 Bioactive and biological response of composite scaffolds

- The composite scaffolds cross-linked by impregnated nanocarriers were bioactive, revealing HCA formation after 1 day of incubation in SBF.
- Cell culture studies on these scaffolds showed cell attachment and proliferation, suggesting its suitability for further biological studies.

7.3 Concluding remarks

This thesis showed the successful creation of an alginate-bioactive glass composite scaffold, employing a one-step cross-linking solution wherein, the mesoporous bioactive glass nanoparticles acted as a bioactive nanofiller and a divalent ionic nanocarrier. These synthesised scaffolds were bioactive, biocompatible towards HOB cells and demonstrated improvements in long term mechanical properties. Therefore, these scaffolds could potentially contribute greatly as an implant material for bone tissue engineering.

7.4 Future work

7.4.1 Tailoring of nanoparticle morphology

The composition of bioactive glass nanoparticles derived from the sol-gel route was varied, and changes in nanoparticle morphology was observed. Hence, the sol composition of the multi-step route could also be varied, to investigate the effects these changes towards its nanostructure.

Changes in nanoparticle morphology were observed when sol-gel bioactive glass nanoparticles were freeze dried, attributed to the ice crystal formation process. It is known that freezing rates affect ice crystal formation and crystal size [65, 66]. Therefore, further studies could be conducted to evaluate the effects of different freezing rates on nanoparticle specific surface area, pore size, volume and shape.

The role of pressure during the drying stage of sol-gel bioactive glasses could be further evaluated. In this thesis, a vacuum was applied during the drying of the gels, with the assumption that equilibrium between the capillary pressure acting within the gel network during drying with that of its environment was achieved. For future work, the gels could be subjected to various pressures during drying, to observe its effects on nanoparticle morphology.

Sandoval-Torres *et al.* [232] modelled changes in capillary pressure during the vacuum drying of wood. It would be interesting to investigate the evaporation mechanisms of liquid from the bioactive glass gel network using computational modelling, to further evaluate the pressures involved during the drying stages, and its effects on nanoparticle morphology.

7.4.2 Nanoparticle morphological effects on cells

The *in vitro* response of human osteoblast bone (HOB) cells to the multi-step derived bioactive glass nanoparticles has been conducted by Fan *et al*. [164], wherein the nanoparticles were found to be capable of supporting cell proliferation and differentiation. Therefore, the response of HOB cells to changes in bioactive glass nanoparticle morphology from the onset of variations in its sol composition, drying procedures and heat treatment regimes could be investigated further.

The multi-step derived bioactive glass nanoparticles have been found to enhance the osteogenic cell cycle, accelerating the sequence of cell proliferation to differentiation and finally towards mineralisation [164]. Comprehensive biological essays involving the study of cell alkaline phosphatase (ALP) enzyme activity and real-time qPCR analysis on the changes of bioactive glass nanoparticle morphology could be carried out, to establish that the other bioactive glass nanoparticles derived in this thesis are also capable of inducing cell differentiation and mineralisation.

7.4.3 Mesoporous nanoparticles as nanocarriers

In this thesis, the feasibility of employing bioactive glass nanoparticles for delivery of cross-linking ions was demonstrated. The cross-linking ions studied were Sr^{2+}, Cu^{2+},

Ca^{2+}. Other divalent ions, which could provide different therapeutic properties, could also be evaluated.

The carrier-delivery application of these mesoporous bioactive glass nanoparticles could be expanded towards drug delivery applications. These nanocarriers could be impregnated with various drug molecules or further functionalised to allow for the attachment of enzymes, antibodies and nucleic acids [176]. A multifunctional nanocarrier could also be developed with capabilities of cross-linking, sensing, targeting and delivery. These mesoporous bioactive glass nanoparticles could be loaded with cargo suitable of being imaged, such as fluorescent dyes or magnetic resonance imaging compounds and yet, simultaneously capable of delivering therapeutic molecules towards the targeted site.

7.4.4 Tailoring scaffold microstructure

Literature has shown that a rapid freezing rate leads to the formation of small and heterogeneous pores, while a gradual freezing rate leads to larger and more homogenous pores [67]. For the synthesis of hybrid composite scaffolds in this thesis, only one freezing regime was employed. Therefore, this could be expanded further, to evaluate the effects of different freezing rates on final scaffold microstructure. Furthermore, the benefits of unidirectional freezing could be explored. Wu *et al.* [66] described improvements towards the mechanical properties of gelatine-based scaffolds produced via freeze drying. An experimental setup could be further developed to synthesise bioactive glass-alginate composite scaffolds with tailored microstructures from unidirectional freeze drying [64].

Other fabrication routes could be investigated for the development of composite scaffolds with tailored microstructures. One possible route could be through the use of solid freeform fabrication (SFF), to deposit composite materials for the creation of 3D structures. Bioactive glass nanoparticles derived in this thesis could be coated with a polymeric glue substance such as PVA and dispensed in a controlled fashion, for the synthesis of highly reproducible and customised scaffolds. Apart from scaffolds, other composite structures could potentially be developed. The spinning of composite fibres

or the production of films should be explored, to widen the application of bioactive glass and alginate composite material.

7.4.5 Expansion on the evaluation of variously cross-linked scaffolds

The degree of cross-linking of the alginate-based scaffolds was determined by measuring swelling and volume changes to the scaffold. Mathematical modelling could be carried out by using the Flory interaction parameter on the degree of scaffold swelling, through which the cross-linking density could be calculated using the Flory-Higgins polymer-solvent interaction [233]. This would provide a numerical relationship between the nanocarrier impregnation concentration and the alginate to glass (G/A) ratio with that of cross-linking density.

The biological and mechanical properties of scaffolds synthesised by impregnated BG65 nanocarriers were studied in this thesis. However, other scaffolds synthesised by BG35, BG50 and nBG65 impregnated nanocarrier cross-linking, still remained untested. Therefore, a systematic study (based on the protocols outlined in this thesis) on the whole range of different scaffolds should be investigated, in order to obtain a broader understanding of the suitability of each scaffold type for bone tissue engineering applications.

The feasibility of using impregnated nanocarriers for the ionic cross-linking of other natural polysaccharides such as chitosan or the synthetic polymer poly [di(carboxylatophenoxy)phosphazene] could be investigated, to establish an even greater potential for this novel cross-linking method with other materials.

7.4.6 Evaluation of scaffold microstructure

Fascinating microstructural features were observed by scanning electron microscope (SEM), for scaffolds produced under slow gelation. In particular, the pore architecture of the scaffolds consisting of a transition from cellular to lamellar (microchannels) pores was observed. Mechanical testing can be carried out, to confirm the benefits suggested in the literature that pore orientation (aligned microchannels) can lead to an improvement in mechanical properties [65, 66].

Biological studies can be conducted to observe the response of cells, such as HOB cells towards the different pore shapes, and particularly, the benefits of the microchannels towards cell adhesion and proliferation. The interconnected microchannels, with widths in excess of 150 μm, is suitable for HOB cell in growth, and could be beneficial for improving nutrient transport [36, 37].

7.4.7 Anti-microbial properties of BGCu scaffolds

BGCu cross-linked scaffolds were synthesised in this thesis. Although the biocidal properties of copper have been established, the anti-microbial properties of the BGCu composite scaffolds produced can be studied [95, 109, 111]. Growth inhibition and bactericidal studies can be conducted using bacteria species such as Staphylococcus aureus, Staphylococcus epidermidis, Escherichia coli and Pseudomonas aeruginosa, which are known to be the cause of orthopaedic related infections [112].

7.4.8 Scale-up of nanoparticle and scaffold synthesis

Commercial use of the bioactive glass nanoparticles would warrant a scale-up of the production quantities currently manufactured in this thesis. For the sol-gel route glasses, larger volumes of the sol can be prepared; however, homogeneity in the sol must be ensured. For the synthesis of large batch multi-step glass nanoparticles, a system involving the use of multiple nozzles to drip the sols into the ammonium dibasic phosphate solutions could be proposed. This would allow for the rapid dispensing of sol, and therefore increasing the production rate.

Scaffolds fabricated in this thesis were of a single size and shape. Variations in scaffold size and shape could be explored, with the possibility of creating larger hydrogels which could consequently be fashioned into bespoke shapes and sizes, depending on the requirements of application.

References

[1] Stevens MM. Biomaterials for bone tissue engineering. Materials Today 2008;11:18-25.

[2] Wozniak P, El-Haj AJ. Bone regeneration and repair using tissue engineering. In: Boccaccini AR, editor. Tissue engineering using ceramics and polymers: CRC Press; 2007. p. 294-315.

[3] Langer R, Vacanti J. Tissue engineering. Science 1993;260:920-6.

[4] Huang J, Best SM. Ceramic biomaterials. In: Boccaccini AR, editor. Tissue engineering using ceramics and polymers: CRC Press; 2007. p. 3-27.

[5] Hench LL, Wilson J. An Introduction to Bioceramics: World Scientific; 1993.

[6] Hench LL, Polak JM. Third-Generation Biomedical Materials. Science 2002;295:1014-7.

[7] Jones JR. Review of bioactive glass: From Hench to hybrids. Acta Biomaterialia 2013;9:4457-86.

[8] Li R, Clark AE, Hench LL. An investigation of bioactive glass powders by sol-gel processing. Journal of Applied Biomaterials 1991;2:231-9.

[9] Arcos D, Vallet-Regí M. Sol–gel silica-based biomaterials and bone tissue regeneration. Acta Biomaterialia 2010;6:2874-88.

[10] Hong Z, Reis RL, Mano JF. Preparation and in vitro characterization of novel bioactive glass ceramic nanoparticles. Journal of Biomedical Materials Research Part A 2009;88A:304-13.

[11] Gupta R, Kumar A. Bioactive materials for biomedical applications using sol–gel technology. Biomedical Materials 2008;3:340-55.

[12] Kresge C, Leonowicz M, Roth W, Vartuli J. Ordered mesoporous molecular sieves synthesized by a liquid-crystal template mechanism. Nature 1992;359:710-2.

[13] Trewyn BG, Whitman CM, Lin VSY. Morphological control of room-temperature ionic liquid templated mesoporous silica nanoparticles for controlled release of antibacterial agents. Nano Letters 2004;4:2139-43.

[14] Slowing II, Vivero-Escoto JL, Wu C-W, Lin VSY. Mesoporous silica nanoparticles as controlled release drug delivery and gene transfection carriers. Advanced Drug Delivery Reviews 2008;60:1278-88.

[15] Vallet-Regí M, Izquierdo-Barba I, Colilla M. Structure and functionalization of mesoporous bioceramics for bone tissue regeneration and local drug delivery. Philosophical Transactions of the Royal Society A: Mathematical, Physical and Engineering Sciences 2012;370:1400-21.

[16] Sun C, Lee JSH, Zhang M. Magnetic nanoparticles in MR imaging and drug delivery. Advanced Drug Delivery Reviews 2008;60:1252-65.

[17] Gerhardt L-C, Boccaccini AR. Bioactive glass and glass-ceramic scaffolds for bone tissue engineering. Materials 2010;3:3867-910.

[18] Jones JR, Gentleman E, Polak J. Bioactive glass scaffolds for bone regeneration. Elements 2007;3:393-9.

[19] Deville S, Saiz E, Tomsia AP. Freeze casting of hydroxyapatite scaffolds for bone tissue engineering. Biomaterials 2006;27:5480-9.

[20] Ackerman LV, Spjut HJ, Abell MR. Bones and joints: Williams & Wilkins; 1976.

[21] Seal BL, Otero TC, Panitch A. Polymeric biomaterials for tissue and organ regeneration. Materials Science and Engineering: R: Reports 2001;34:147-230.

[22] Gibson LJ. The mechanical behaviour of cancellous bone. Journal of Biomechanics 1985;18:317-28.

[23] Rho J-Y, Kuhn-Spearing L, Zioupos P. Mechanical properties and the hierarchical structure of bone. Medical Engineering Physics 1998;20:92-102.

[24] Shea JE, Miller SC. Skeletal function and structure: Implications for tissue-targeted therapeutics. Advanced Drug Delivery Reviews 2005;57:945-57.

[25] Orlovskii VP, Komlev VS, Barinov SM. Hydroxyapatite and hydroxyapatite-based ceramics. Inorganic Materials 2002;38:973-84.

[26] Hollinger JO. Bone tissue engineering: CRC Press; 2005.

[27] Hernandez CJ, Beaupre GS, Keller TS, Carter DR. The influence of bone volume fraction and ash fraction on bone strength and modulus. Bone 2001;29:74-8.

[28] Nazarian A, von Stechow D, Zurakowski D, Muller R, Snyder BD. Bone volume fraction explains the variation in strength and stiffness of cancellous bone affected by metastatic cancer and osteoporosis. Calcified tissue international 2008;83:368-79.

[29] Rezwan K, Chen QZ, Blaker JJ, Boccaccini AR. Biodegradable and bioactive porous polymer/inorganic composite scaffolds for bone tissue engineering. Biomaterials 2006;27:3413-31.

[30] Lu HH, El-Amin SF, Scott KD, Laurencin CT. Three-dimensional, bioactive, biodegradable, polymer–bioactive glass composite scaffolds with improved mechanical properties support collagen synthesis and mineralization of human osteoblast-like cells in vitro. Journal of Biomedical Materials Research Part A 2003;64A:465-74.

[31] Report: The future of orthopedic implants, analysis and forecasts to 2016 - joint reconstruction and spinal implants creating growth opportunities. GBI-Research; 2010.

[32] Downey PA, Siegel MI. Bone biology and the clinical implications for osteoporosis. Physical Therapy 2006;86:77-91.

[33] Schmitz JP, Hollinger JO. The critical size defect as an experimental model for craniomandibulofacial nonunions. Clinical Orthopaedics and Related Research 1986;205:299-308.

[34] TÖrmälä P, Pohjonen T, Rokkanen P. Bioabsorbable polymers: Materials technology and surgical applications. Proceedings of the Institution of Mechanical Engineers, Part H: Journal of Engineering in Medicine 1998;212:101-11.

[35] Kaban LB, Mulliken JB, Glowacki J. Treatment of jaw defects with demineralized bone implants. Journal of Oral and Maxillofacial Surgery 1982;40:623-6.

[36] Rahaman MN, Day DE, Sonny Bal B, Fu Q, Jung SB, Bonewald LF, et al. Bioactive glass in tissue engineering. Acta Biomaterialia 2011;7:2355-73.

[37] Hutmacher DW. Scaffolds in tissue engineering bone and cartilage. Biomaterials 2000;21:2529-43.

[38] Liu X, Ma PX. Polymeric Scaffolds for Bone Tissue Engineering: 2nd Special Edition on Musculoskeletal Bioengineering. Guest Editor: Kyriacos A. Athanasiou. Annals of Biomedical Engineering 2004;32:477-86.

[39] Klawitter JJ, Bagwell JG, Weinstein AM, Sauer BW, Pruitt JR. An evaluation of bone growth into porous high density polyethylene. Journal of Biomedical Materials Research 1976;10:311-23.

[40] Bohner M. Resorbable biomaterials as bone graft substitutes. Materials Today 2010;13:24-30.

[41] Hench LL. The story of Bioglass. Journal of Materials Science: Materials in Medcine 2006;17:967-78.

[42] Hench LL. Genetic design of bioactive glass. Journal of the European Ceramic Society 2009;29:1257-65.

[43] Wei G, Ma PX. Polymeric biomaterials. In: Boccaccini AR, editor. Tissue engineering using ceramics and polymers: CRC Press; 2007. p. 32-47.

[44] Yu NYC, Schindeler A, Little DG, Ruys AJ. Biodegradable poly(α-hydroxy acid) polymer scaffolds for bone tissue engineering. Journal of Biomedical Materials Research Part B: Applied Biomaterials 2010;93B:285-95.

[45] Gombotz WR, Wee S. Protein release from alginate matrices. Advanced Drug Delivery Reviews 1998;31:267-85.

[46] Lee KY, Mooney DJ. Alginate: Properties and biomedical applications. Progress in Polymer Science 2012;37:106-26.

[47] Kuo CK, Ma PX. Ionically crosslinked alginate hydrogels as scaffolds for tissue engineering: Part 1. Structure, gelation rate and mechanical properties. Biomaterials 2001;22:511-21.

[48] Hatzistavrou E, Chatzistavrou X, Papadopoulou L, Kantiranis N, Kontonasaki E, Boccaccini AR, et al. Characterisation of the bioactive behaviour of sol–gel hydroxyapatite–CaO and hydroxyapatite–CaO–bioactive glass composites. Materials Science and Engineering: C 2010;30:497-502.

[49] Di Silvio L. Bone tissue enginerring and biomineralization. In: Boccaccini AR, editor. Tissue engineering using ceramics and polymers: CRC Press; 2007. p. 319-31.

[50] Misra SK, Boccaccini AR. Biodegradable and bioactive polymer/ceramic composite scaffolds. In: Boccaccini AR, editor. Tissue engineering using ceramics and polymers: CRC Press; 2007.

[51] Chen QZ, Efthymiou A, Salih V, Boccaccini AR. Bioglass®-derived glass–ceramic scaffolds: Study of cell proliferation and scaffold degradation in vitro. Journal of Biomedical Materials Research Part A 2008;84A:1049-60.

[52] Deb S, Mandegaran R, Di Silvio L. A porous scaffold for bone tissue engineering/45S5 Bioglass derived porous scaffolds for co-culturing osteoblasts and endothelial cells. Journal of Materials Science: Materials in Medicine 2010;21:893-905.

[53] Sepulveda P, Ortega FS, Innocentini MDM, Pandolfelli VC. Properties of highly porous hydroxyapatite obtained by the gelcasting of foams. Journal of the American Ceramic Society 2000;83:3021-4.

[54] Erol M, Mouriño V, Newby P, Chatzistavrou X, Roether J, Hupa L, et al. Copper-releasing, boron-containing bioactive glass-based scaffolds coated with alginate for bone tissue engineering. Acta Biomaterialia 2012;8:792-801.

[55] Dhara S, Pradhan M, Ghosh D, Bhargava P. Nature inspired novel processing routes for ceramic foams. Advances in Applied Ceramics 2005;104:9-21.

[56] Thomson R, Shung A, Yaszemski M, Mikos AG. Polymer scaffold processing. In: Lanza R, Langer R, Vacanti J, editors. Principles of tissue engineering: Academic Press; 2000. p. 251-62.

[57] Yuan H, de Bruijn JD, Zhang X, van Blitterswijk CA, de Groot K. Bone induction by porous glass ceramic made from Bioglass® (45S5). Journal of Biomedical Materials Research 2001;58:270-6.

[58] Almirall A, Larrecq G, Delgado JA, Martinez S, Planell JA, Ginebra MP. Fabrication of low temperature macroporous hydroxyapatite scaffolds by foaming and hydrolysis of an alpha-TCP paste. Biomaterials 2004;25:3671-80.

[59] Sachlos E, Reis N, Ainsley C, Derby B, Czernuszka JT. Novel collagen scaffolds with predefined internal morphology made by solid freeform fabrication. Biomaterials 2003;24:1487-97.

[60] Leukers B, Gulkan H, Irsen SH, Milz S, Tille C, Schieker M, et al. Hydroxyapatite scaffolds for bone tissue engineering made by 3D printing. Journal of Materials Science: Materials in Medicine 2005;16:1121-4.

[61] Kolan KCR, Leu MC, Hilmas GE, Brown RF, Velez M. Fabrication of 13-93 bioactive glass scaffolds for bone tissue engineering using indirect selective laser sintering. Biofabrication 2011;3:25004.

[62] Fu Q, Saiz E, Tomsia AP. Bioinspired strong and highly porous glass scaffolds. Advanced Functional Materials 2011;21:1058-63.

[63] Maquet V, Jerome R. Design of macroporous biodegradable polymer scaffolds for cell transplantation. Materials Science Forum: Trans Tech Publications; 1997. p. 15-42.

[64] Fan JP. Preparation of bioceramic and polymer composite scaffolds through freeze drying. Undergraduate Report: University College London; 2010.

[65] Deville S, Saiz E, Nalla RK, Tomsia AP. Freezing as a path to build complex composites. Science 2006;311:515-8.

[66] Wu X, Liu Y, Li X, Wen P, Zhang Y, Long Y, et al. Preparation of aligned porous gelatin scaffolds by unidirectional freeze-drying method. Acta Biomaterialia 2010;6:1167-77.

[67] Zmora S, Glicklis R, Cohen S. Tailoring the pore architecture in 3-D alginate scaffolds by controlling the freezing regime during fabrication. Biomaterials 2002;23:4087-94.

[68] Barley J. Basic principles of freeze drying. LyoLearn Educational Program. SP Industries;2009. p. 1-14.

[69] Cengel Y, Turner R. Fundamentals of thermal-fluid sciences: McGraw-Hill Professional; 2004.

[70] Lide DR. CRC Handbook of Chemistry and Physics, 85th Edition: Taylor & Francis; 2004.

[71] Minaberry Y, Jobbágy M. Macroporous bioglass scaffolds prepared by coupling sol–gel with freeze drying. Chemistry of Materials 2011;23:2327-32.

[72] Fu Q, Rahaman MN, Bal BS, Brown RF, Day DE. Mechanical and in vitro performance of 13-93 bioactive glass scaffolds prepared by a polymer foam replication technique. Acta Biomaterialia 2008;4:1854-64.

[73] Fu Q, Rahaman MN, Fu H, Liu X. Silicate, borosilicate, and borate bioactive glass scaffolds with controllable degradation rate for bone tissue engineering applications. I. Preparation and in vitro degradation. Journal of Biomedical Materials Research Part A 2010;95:164-71.

[74] Fu Q, Rahaman MN, Bal BS, Brown RF. Preparation and in vitro evaluation of bioactive glass (13-93) scaffolds with oriented microstructures for repair and

regeneration of load-bearing bones. Journal of Biomedical Materials Research Part A 2010;93:1380-90.

[75] Liu X, Rahaman MN, Fu Q. Oriented bioactive glass (13-93) scaffolds with controllable pore size by unidirectional freezing of camphene-based suspensions: Microstructure and mechanical response. Acta Biomaterialia 2011;7:406-16.

[76] Mørch YA. Novel Alginate Microcapsules for Cell Therapy–A study of the structure-function relationships in native and structurally engineered alginates Thesis: Norwegian University of Science and Technology; 2008.

[77] Gacesa P. Bacterial alginate biosynthesis - recent progress and future prospects. Microbiology 1998;144:1133-43.

[78] Stephen AM, Phillips GO. Food Polysaccharides and Their Applications: Taylor & Francis; 2010.

[79] Draget KI, Smidsrød O, Skjåk-Bræk G. Alginates from Algae. Biopolymers Online: Wiley-VCH Verlag GmbH & Co. KGaA; 2005.

[80] Shilpa A, Agrawal SS, Ray AR. Controlled delivery of drugs from alginate matrix. Journal of Macromolecular Science Part C: Polymer Reviews 2003;43:187-221.

[81] Smidsrød O, Glover RM, Whittington SG. The relative extension of alginates having different chemical composition. Carbohydrate Research 1973;27:107-18.

[82] Skjåk-Bræk G, Grasdalen H, Smidsrød O. Inhomogeneous polysaccharide ionic gels. Carbohydrate Polymers 1989;10:31-54.

[83] Stokke BT, Smidsrød O, Brant DA. Predicted influence of monomer sequence distribution and acetylation on the extension of naturally occurring alginates. Carbohydrate Polymers 1993;22:57-66.

[84] Dentini M, Rinaldi G, Risica D, Barbetta A, Skjåk-Bræk G. Comparative studies on solution characteristics of mannuronan epimerized by C-5 epimerases. Carbohydrate Polymers 2005;59:489-99.

[85] Shapiro L, Cohen S. Novel alginate sponges for cell culture and transplantation. Biomaterials 1997;18:583-90.

[86] Augst AD, Kong HJ, Mooney DJ. Alginate hydrogels as biomaterials. Macromolecular Bioscience 2006;6:623-33.

[87] Hartmann M, Dentini M, Ingar Draget K, Skjåk-Bræk G. Enzymatic modification of alginates with the mannuronan C-5epimerase AlgE4 enhances their solubility at low pH. Carbohydrate Polymers 2006;63:257-62.

[88] Birdi G, Bridson RH, Smith AM, Mohd Bohari SP, Grover LM. Modification of alginate degradation properties using orthosilicic acid. Journal of the Mechanical Behavior of Biomedical Materials 2012;6:181-7.

[89] Stokke BT, Smidsroed O, Bruheim P, Skjaak-Braek G. Distribution of uronate residues in alginate chains in relation to alginate gelling properties. Macromolecules 1991;24:4637-45.

[90] Mørch ÝA, Donati I, Strand BL. Effect of Ca2+, Ba2+, and Sr2+ on alginate microbeads. Biomacromolecules 2006;7:1471-80.

[91] Couperwhite I, McCallum M. The influence of EDTA on the composition of alginate synthesized by Azotobacter vinelandii. Arch Microbiol 1974;97:73-80.

[92] Pawar SN, Edgar KJ. Alginate derivatization: A review of chemistry, properties and applications. Biomaterials 2012;33:3279-305.

[93] Draget KI, Simensen MK, Onsøyen E, Smidsrød O. Gel strength of Ca-limited alginate gels made in situ. Hydrobiologia 1993;260-261:563-5.

[94] Place ES, Rojo L, Gentleman E, Sardinha JP, Stevens MM. Strontium- and zinc-alginate hydrogels for bone tissue engineering. Tissue engineering Part A 2011;17:2713-22.

[95] Heliopoulos NS, Papageorgiou SK, Galeou A, Favvas EP, Katsaros FK, Stamatakis K. Effect of copper and copper alginate treatment on wool fabric. Study of textile and antibacterial properties. Surface and Coatings Technology 2013;235:24-31.

[96] Haug A. The affinity of some divalent metals to different types of alginates. Acta Chemica Scandinavica 1961;15:1795.

[97] Thiele H, Schacht E. To process the order in the formation of ionotropic gels. Kolloid-Zeitschrift 1959;163:2-8.

[98] Smidsrød O, Grasdalen H. Polyelectrolytes from seaweeds. In: Bird C, Ragan M, editors. Eleventh International Seaweed Symposium: Springer Netherlands; 1984. p. 19-28.

[99] Smidsrod O. Molecular basis for some physical properties of alginates in the gel state. Faraday Discussions of the Chemical Society 1974;57:263-74.

[100] McDowell RH. Chemicals from seaweed. Third International Seaweed Symposium. Galway1958.

[101] Haug A, Smidsrod O. The effect of divalent metals on the properties of alginate solutions. Acta Chemica Scandinavica 1965;19.

[102] Gentleman E, Fredholm YC, Jell G, Lotfibakhshaiesh N, O'Donnell MD, Hill RG, et al. The effects of strontium-substituted bioactive glasses on osteoblasts and osteoclasts in vitro. Biomaterials 2010;31:3949-56.

[103] Canalis E, Hott M, Deloffre P, Tsouderos Y, Marie PJ. The divalent strontium salt S12911 enhances bone cell replication and bone formation in vitro. Bone 1996;18:517-23.

[104] Marie PJ, Hott M, Modrowski D, de Pollak C, Guillemain J, Deloffre P, et al. An uncoupling agent containing strontium prevents bone loss by depressing bone resorption and maintaining bone formation in estrogen-deficient rats. Journal of Bone and Mineral Research 2005;20:1065-74.

[105] Courthéoux L, Lao J, Nedelec JM, Jallot E. Controlled bioactivity in zinc-doped sol−gel-derived binary bioactive glasses. The Journal of Physical Chemistry C 2008;112:13663-7.

[106] Balamurugan A, Balossier G, Michel J, Kannan S, Benhayoune H, Rebelo AHS, et al. Sol gel derived SiO2-CaO-MgO-P2O5 bioglass system—Preparation and in vitro characterization. Journal of Biomedical Materials Research Part B: Applied Biomaterials 2007;83B:546-53.

[107] Saboori A, Rabiee M, Moztarzadeh F, Sheikhi M, Tahriri M, Karimi M. Synthesis, characterization and in vitro bioactivity of sol-gel-derived SiO2–CaO–P2O5–MgO bioglass. Materials Science and Engineering: C 2009;29:335-40.

[108] Hessle L, Johnson KA, Anderson HC, Narisawa S, Sali A, Goding JW, et al. Tissue-nonspecific alkaline phosphatase and plasma cell membrane glycoprotein-1 are central antagonistic regulators of bone mineralization. Proceedings of the National Academy of Sciences of the United States of America 2002;99:9445-9.

[109] Diaz-Visurraga J, Daza C, Pozo C, Becerra A, von Plessing C, Garcia A. Study on antibacterial alginate-stabilized copper nanoparticles by FT-IR and 2D-IR correlation spectroscopy. International journal of nanomedicine 2012;7:3597-612.

[110] Bellantone M, Williams HD, Hench LL. Broad-spectrum bactericidal activity of Ag2O-doped bioactive glass. Antimicrobial Agents and Chemotherapy 2002;46:1940-5.

[111] Allaker RP. The use of nanoparticles to control oral biofilm formation. Journal of Dental Research 2010;89:1175-86.

[112] Memarzadeh K, Vargas M, Huang J, Fan J, Allaker RP. Nano metallic-oxides as antimicrobials for implant coatings. Key Engineering Materials 2011;489:493-4.

[113] Thu B, Bruheim P, Espevik T, Smidsrød O, Soon-Shiong P, Skjåk-Bræk G. Alginate polycation microcapsules: I. Interaction between alginate and polycation. Biomaterials 1996;17:1031-40.

[114] Eiselt P, Lee KY, Mooney DJ. Rigidity of two-component hydrogels prepared from alginate and poly(ethylene glycol)−diamines. Macromolecules 1999;32:5561-6.

[115] Zhao X, Huebsch N, Mooney DJ, Suo Z. Stress-relaxation behavior in gels with ionic and covalent crosslinks. Journal of Applied Physics 2010;107:063509.

[116] Drury JL, G. DR, Mooney DJ. The tensile properties of alginate hydrogels. Biomaterials 2004;25:3187-99.

[117] Callister WD. Materials Science and Engineering: An Introduction: John Wiley & Sons Australia Limited; 2006.

[118] Martinsen A, Skjak-Braek G, Smidsrod O. Alginate as immobilization material: I. Correlation between chemical and physical properties of alginate gel beads. Biotechnology and bioengineering 1989;33:79-89.

[119] Mancini M, Moresi M, Rancini R. Mechanical properties of alginate gels: empirical characterisation. Journal of Food Engineering 1999;39:369-78.

[120] LeRoux MA, Guilak F, Setton LA. Compressive and shear properties of alginate gel: effects of sodium ions and alginate concentration. Journal of Biomedical Materials Research 1999;47:46-53.

[121] Abou Neel EA, Pickup DM, Valappil SP, Newport RJ, Knowles JC. Bioactive functional materials: a perspective on phosphate-based glasses. Journal of Materials Chemistry 2009;19:690-701.

[122] Hench LL. Bioceramics: From concept to clinic. Journal of the American Ceramic Society 1991;74:1487-510.

[123] Hench LL, Splinter RJ, Allen WC, Greenlee TK. Bonding mechanisms at the interface of ceramic prosthetic materials. Journal of Biomedical Materials Research 1971;5:117-41.

[124] Weinstein AM, Klawitter JJ, Cook SD. Implant-bone interface characteristics of bioglass dental implants. Journal of Biomedical Materials Research 1980;14:23-9.

[125] Brinker CJ, Scherer GW. Sol-Gel Science: The Physics and Chemistry of Sol-Gel Processing: Academic Press; 1990.

[126] Oonishi H, Hench LL, Wilson J, Sugihara F, Tsuji E, Kushitani S, et al. Comparative bone growth behavior in granules of bioceramic materials of various sizes. Journal of Biomedical Materials Research 1999;44:31-43.

[127] Oonishi H, Hench LL, Wilson J, Sugihara F, Tsuji E, Matsuura M, et al. Quantitative comparison of bone growth behavior in granules of Bioglass®, A-W glass-ceramic, and hydroxyapatite. Journal of Biomedical Materials Research 2000;51:37-46.

[128] Hench LL. Bioceramics. Journal of the American Ceramic Society 1998;81:1705-28.

[129] Albrektsson T, Johansson C. Osteoinduction, osteoconduction and osseointegration. European Spine Journal 2001;10 Supplement 2:S96-101.

[130] Pereira M, Clark A, Hench L. Calcium phosphate formation on sol-gel-derived bioactive glasses in vitro. Journal of Biomedical Materials Research 1994;28:693-8.

[131] Saravanapavan P, Hench LL. Mesoporous calcium silicate glasses. I. Synthesis. Journal of Non-Crystalline Solids 2003;318:1-13.

[132] Saravanapavan P, Jones JR, Pryce RS, Hench LL. Bioactivity of gel–glass powders in the CaO-SiO2 system: A comparison with ternary (CaO-P2P5-SiO2) and

quaternary glasses (SiO2-CaO-P2O5-Na2O). Journal of Biomedical Materials Research Part A 2003;66A:110-9.

[133] Hamadouche M, Meunier A, Greenspan DC, Blanchat C, Zhong JP, La Torre GP, et al. Long-term in vivo bioactivity and degradability of bulk sol-gel bioactive glasses. Journal of Biomedical Materials Research 2001;54:560-6.

[134] Saravanapavan P, L. Hench L. Mesoporous calcium silicate glasses. II. Textural characterisation. Journal of Non-Crystalline Solids 2003;318:14-26.

[135] Lin S, Ionescu C, Pike KJ, Smith ME, Jones JR. Nanostructure evolution and calcium distribution in sol-gel derived bioactive glass. Journal of Materials Chemistry 2009;19:1276-82.

[136] Sepulveda P, Jones JR, Hench LL. In vitro dissolution of melt-derived 45S5 and sol-gel derived 58S bioactive glasses. Journal of Biomedical Materials Research 2002;61:301-11.

[137] Sakka S, Kamiya K. Glasses from metal alcoholates. Journal of Non-Crystalline Solids 1980;42:403-21.

[138] Iler RK. The chemistry of silica: solubility, polymerization, colloid and surface properties, and biochemistry: Wiley; 1979.

[139] Balamurugan A, Balossier G, Kannan S, Michel J, Rebelo AHS, Ferreira JMF. Development and in vitro characterization of sol–gel derived CaO–P2O5–SiO2–ZnO bioglass. Acta Biomaterialia 2007;3:255-62.

[140] Martin RA, Yue S, Hanna JV, Lee PD, Newport RJ, Smith ME, et al. Characterizing the hierarchical structures of bioactive sol–gel silicate glass and hybrid scaffolds for bone regeneration. Philosophical Transactions of the Royal Society A: Mathematical, Physical and Engineering Sciences 2012;370:1422-43.

[141] Hill R. An alternative view of the degradation of bioglass. J Mater Sci Lett 1996;15:1122-5.

[142] Labbaf S, Tsigkou O, Müller KH, Stevens MM, Porter AE, Jones JR. Spherical bioactive glass particles and their interaction with human mesenchymal stem cells in vitro. Biomaterials 2011;32:1010-8.

[143] Lakhkar NJ, Lee I-H, Kim H-W, Salih V, Wall IB, Knowles JC. Bone formation controlled by biologically relevant inorganic ions: Role and controlled delivery from phosphate-based glasses. Advanced Drug Delivery Reviews 2013;65:405-20.

[144] Jones JR, Hench LL. Effect of surfactant concentration and composition on the structure and properties of sol-gel-derived bioactive glass foam scaffolds for tissue engineering. Journal of Materials Science 2003;38:3783-90.

[145] Elgayar I, Aliev AE, Boccaccini AR, Hill RG. Structural analysis of bioactive glasses. Journal of Non-Crystalline Solids 2005;351:173-83.

[146] Delahaye F, Montagne L, Palavit G, Claude Touray J, Baillif P. Acid dissolution of sodium–calcium metaphosphate glasses. Journal of Non-Crystalline Solids 1998;242:25-32.

[147] García A, Cicuéndez M, Izquierdo-Barba I, Arcos D, Vallet-Regí M. Essential role of calcium phosphate heterogeneities in 2D-hexagonal and 3D-cubic SiO2−CaO−P2O5 mesoporous bioactive glasses. Chemistry of Materials 2009;21:5474-84.

[148] Prasad SE. A review of: "Ultrastructure processing of ceramics, glasses and composites" edited by L.L. Hench & D.R. Ulrich John Wiley & Sons; 1984. Materials and Manufacturing Processes 1990;5:343-4.

[149] Wu C, Chang J. Mesoporous bioactive glasses: structure characteristics, drug/growth factor delivery and bone regeneration application. Interface Focus 2012;2:292-306.

[150] Yan XX, Deng HX, Huang XH, Lu GQ, Qiao SZ, Zhao DY, et al. Mesoporous bioactive glasses. I. Synthesis and structural characterization. Journal of Non-Crystalline Solids 2005;351:3209-17.

[151] Stöber W, Fink A, Bohn E. Controlled growth of monodisperse silica spheres in the micron size range. Journal of colloid and interface science 1968;26:62-9.

[152] Xia W, Chang J. Preparation and characterization of nano-bioactive-glasses (NBG) by a quick alkali-mediated sol–gel method. Materials Letters 2007;61:3251-3.

[153] Zhu Y, Wu C, Ramaswamy Y, Kockrick E, Simon P, Kaskel S, et al. Preparation, characterization and in vitro bioactivity of mesoporous bioactive glasses (MBGs) scaffolds for bone tissue engineering. Microporous and Mesoporous Materials 2008;112:494-503.

[154] Brinker CJ, Scherer GW. Sol → gel → glass: I. Gelation and gel structure. Journal of Non-Crystalline Solids 1985;70:301-22.

[155] Hong Z, Liu A, Chen L, Chen X, Jing X. Preparation of bioactive glass ceramic nanoparticles by combination of sol–gel and coprecipitation method. Journal of Non-Crystalline Solids 2009;355:368-72.

[156] Brinker CJ, Sehgal R, Hietala SL, Deshpande R, Smith DM, Loy D, et al. Sol-gel strategies for controlled porosity inorganic materials. Journal of Membrane Science 1994;94:85-102.

[157] Lee H-H, Yu H-S, Jang J-H, Kim H-W. Bioactivity improvement of poly(ε-caprolactone) membrane with the addition of nanofibrous bioactive glass. Acta Biomaterialia 2008;4:622-9.

[158] Jones JR, Ehrenfried LM, Hench LL. Optimising bioactive glass scaffolds for bone tissue engineering. Biomaterials 2006;27:964-73.

[159] Zhong J, Greenspan DC. Processing and properties of sol–gel bioactive glasses. Journal of Biomedical Materials Research 2000;53:694-701.

[160] Tanaka T. Gels. Scientific American 1981;1:124-36.

[161] Himmel B, Gerber T, Bürger H. X-ray diffraction investigations of silica gel structures. Journal of Non-Crystalline Solids 1987;91:122-36.

[162] Orcel G, Hench LL, Artaki I, Jonas J, Zerda TW. Effect of formamide additive on the chemistry of silica sol-gels II. Gel structure. Journal of Non-Crystalline Solids 1988;105:223-31.

[163] Ettarh C, Galwey AK. A kinetic and mechanistic study of the thermal decomposition of calcium nitrate. Thermochimica Acta 1996;288:203-19.

[164] Fan JP, Kalia P, Di Silvio L, Huang J. In vitro response of human osteoblasts to multi-step sol–gel derived bioactive glass nanoparticles for bone tissue engineering. Materials Science and Engineering: C 2014;36:206-14.

[165] Hong Z, Reis RL, Mano JF. Preparation and in vitro characterization of novel bioactive glass ceramic nanoparticles. Journal of Biomedical Materials Research Part A 2009;88:304-13.

[166] Lin AYM, Meyers MA, Vecchio KS. Mechanical properties and structure of Strombus gigas,Tridacna gigas, and Haliotis rufescens sea shells: A comparative study. Materials Science and Engineering: C 2006;26:1380-9.

[167] López-Noriega A, Arcos D, Izquierdo-Barba I, Sakamoto Y, Terasaki O, Vallet-Regí M. Ordered Mesoporous Bioactive Glasses for Bone Tissue Regeneration. Chemistry of Materials 2006;18:3137-44.

[168] Vallet-Regí M. Ordered mesoporous materials in the context of drug delivery systems and bone tissue engineering. Chemistry – A European Journal 2006;12:5934-43.

[169] Lowell S, Shields J. Powder surface area and porosity. Second edtion: Academic Press; 1984.

[170] Zgrablich G, Mendioroz S, Daza L, Pajares J, Mayagoitia V, Rojas F, et al. Effect of porous structure on the determination of pore size distribution by mercury porosimetry and nitrogen sorption. Langmuir : the ACS journal of surfaces and colloids 1991;7:779-85.

[171] Sing KSW. The use of gas adsorption for the characterization of porous solids. Colloids and Surfaces 1989;38:113-24.

[172] Suteewong T, Sai H, Hovden R, Muller D, Bradbury MS, Gruner SM, et al. Multicompartment mesoporous silica nanoparticles with branched shapes: an epitaxial growth mechanism. Science 2013;340:337-41.

[173] Manzano M, Vallet-Regi M. New developments in ordered mesoporous materials for drug delivery. Journal of Materials Chemistry 2010;20:5593-604.

[174] Charnay C, Bégu S, Tourné-Péteilh C, Nicole L, Lerner DA, Devoisselle JM. Inclusion of ibuprofen in mesoporous templated silica: drug loading and release property. European Journal of Pharmaceutics and Biopharmaceutics 2004;57:533-40.

[175] Kim J, Lee JE, Lee J, Yu JH, Kim BC, An K, et al. Magnetic fluorescent delivery vehicle using uniform mesoporous silica spheres embedded with monodisperse magnetic and semiconductor nanocrystals. Journal of the American Chemical Society 2006;128:688-9.

[176] Rosenholm JM, Sahlgren C, Lindén M. Towards multifunctional, targeted drug delivery systems using mesoporous silica nanoparticles–opportunities & challenges. Nanoscale 2010;2:1870-83.

[177] Li Z, Barnes JC, Bosoy A, Stoddart JF, Zink JI. Mesoporous silica nanoparticles in biomedical applications. Chemical Society Reviews 2012;41:2590-605.

[178] Menaa B, Miyagawa Y, Takahashi M, Herrero M, Rives V, Menaa F, et al. Bioencapsulation of apomyoglobin in nanoporous organosilica sol-gel glasses: influence of the siloxane network on the conformation and stability of a model protein. Biopolymers 2009;91:895-906.

[179] Choi S, Gray ML, Jones CW. Amine-tethered solid adsorbents coupling high adsorption capacity and regenerability for CO2 capture from ambient air. ChemSusChem 2011;4:628-35.

[180] Yan X, Yu C, Zhou X, Tang J, Zhao D. Highly ordered mesoporous bioactive glasses with superior in vitro bone-forming bioactivities. Angewandte Chemie International Edition 2004;43:5980-4.

[181] Yan X, Huang X, Yu C, Deng H, Wang Y, Zhang Z, et al. The in-vitro bioactivity of mesoporous bioactive glasses. Biomaterials 2006;27:3396-403.

[182] Arcos D, Vila M, López-Noriega A, Rossignol F, Champion E, Oliveira F, et al. Mesoporous bioactive glasses: mechanical reinforcement by means of a biomimetic process. Acta Biomaterialia 2011;7:2952-9.

[183] Mizutani M, Yamada Y, Yano K. Pore-expansion of monodisperse mesoporous silica spheres by a novel surfactant exchange method. Chemical Communications 2007:1172-4.

[184] Goldstein J. Scanning electron microscopy and X-ray microanalysis: Kluwer Academic/Plenum Publishers; 2003.

[185] Oxford-Intruments. INCA energy operator manual 2.1. Oxford Intruments Analytical; 2006.

[186] Fultz B, Howe J. Transmission electron microscopy and diffractometry of materials: Springer; 2007.

[187] Egerton RF. Physical principles of electron microscopy: an introduction to TEM, SEM, and AEM: Springer; 2005.

[188] Williams DB, Carter CB. Transmission Electron Microscopy: A Textbook for Materials Science: Springer; 2009.

[189] Aguiar H, Serra J, González P. Nanostructural transitions in bioactive sol–gel silicate glasses. International Journal of Applied Ceramic Technology 2011;8:511-22.

[190] PerkinElmer. Universal ATR sampling acessory user's guide. PerkinElmer, Inc.; 2011.

[191] Sing KSW. Reporting physisorption data for gas/solid systems. Pure and Applied Chemistry 1985;57:603-19.

[192] Brunauer S, Emmett PH, Teller E. Adsorption of gases in multimolecular layers. Journal of the American Chemical Society 1938;60:309-19.

[193] Barrett EP, Joyner LG, Halenda PP. The determination of pore volume and area distributions in porous substances. I. computations from nitrogen isotherms. Journal of the American Chemical Society 1951;73:373-80.

[194] Everett DH, Stone FS. The Structure and properties of porous materials: Butterworths; 1958.

[195] Kokubo T, Takadama H. How useful is SBF in predicting in vivo bone bioactivity? Biomaterials 2006;27:2907-15.

[196] Di Silvio L, Gurav N. Primary Mesenchymal Cells. In: Koller MR, Palsson BO, editors. Human cell culture Vol 5: Kluwer Academic Publishers; 2001.

[197] Breithaupt J. New understanding physics for advanced level: Stanley Thornes; 2000.

[198] Massey BS, Ward-Smith AJ. Mechanics of fluids. 8th edition: Taylor & Francis Group; 2006.

[199] Vargaftik N, Volkov B, Voljak L. International tables of the surface tension of water. Journal of Physical and Chemical Reference Data 1983;12:817.

[200] Kestin J, Sokolov M, A WW. Viscosity of liquid water in the range -8 C to 150 C. Journal of Physical Chemistry Reference Data 1978;7:941.

[201] European pharmacopoeia 5.0: Vol 2: Council of Europe; 2004.

[202] Sigma-Aldrich. Alginate low viscosity A2158. Product specification: Sigma Aldrich.

[203] Fan JP, Kalia P, Di Silvio L, Huang J. Development and characterisation of a novel bioglass-hydroxyapatite-alginate nanocomposite scaffold for tissue engineering. Conference paper: World Biomaterials Congress. Chengdu, China;2012.

[204] Radebaugh GW, Murtha JL, Julian TN, Bondi JN. Methods for evaluating the puncture and shear properties of pharmaceutical polymeric films. International Journal of Pharmaceutics 1988;45:39-46.

[205] Vallet-Regí M, Ragel CV, Salinas Antonio J. Glasses with medical applications. European Journal of Inorganic Chemistry 2003;2003:1029-42.

[206] Martínez A, Izquierdo-Barba I, Vallet-Regí M. Bioactivity of a CaO−SiO2 binary glasses system. Chemistry of Materials 2000;12:3080-8.

[207] Scherer GW. Recent progress in drying of gels. Journal of Non-Crystalline Solids 1992;147–148:363-74.

[208] Hench LL, West JK. The sol-gel process. Chemical Reviews 1990;90:33-72.

[209] Chen X, Guo C, Zhao N. Preparation and characterization of the sol–gel nano-bioactive glasses modified by the coupling agent gamma-aminopropyltriethoxysilane. Applied Surface Science 2008;255:466-8.

[210] Lenza RFS, Vasconcelos WL. Structural evolution of silica sols modified with formamide. Materials Research 2001;4:175-9.

[211] Rehman I, Karsh M, Hench L, Bonfield W. Analysis of apatite layers on glass–ceramic particulate using FTIR and FT-Raman spectroscopy. Journal of Biomedical Materials Research 2000;50:97-100.

[212] Olszta MJ, Cheng X, Jee SS, Kumar R, Kim Y-Y, Kaufman MJ, et al. Bone structure and formation: A new perspective. Materials Science and Engineering: R: Reports 2007;58:77-116.

[213] Shih SJ, Chou YJ, Chen CY, Lin CK. One-step synthesis and characterization of nanosized bioactive glass. Journal of Medical and Biological Engineering 2014;34.

[214] Skipper LJ, Sowrey FE, Pickup DM, Drake KO, Smith ME, Saravanapavan P, et al. The structure of a bioactive calcia-silica sol-gel glass. Journal of Materials Chemistry 2005;15:2369-74.

[215] MicromeriticsIntrument. TriStar 3000 V6.08: An operators manual. Micromeritics Instrument Corporation; 2007.

[216] Jackson CL, Shaw MT. The phase behaviour and gelation of a rod-like polymer in solution and implications for microcellular foam morphology. Polymer 1990;31:1070-84.

[217] Suzuki Y, Nishimura Y, Tanihara M, Suzuki K, Nakamura T, Shimizu Y, et al. Evaluation of a novel alginate gel dressing: cytotoxicity to fibroblasts in vitro and foreign-body reaction in pig skin in vivo. Journal of Biomedical Materials Research 1998;39:317-22.

[218] Cohan LH. Sorption hysteresis and the vapor pressure of concave surfaces. Journal of the American Chemical Society 1938;60:433-5.

[219] Rehman I, Knowles JC, Bonfield W. Analysis of in vitro reaction layers formed on Bioglass® using thin-film X-ray diffraction and ATR-FTIR microspectroscopy. Journal of Biomedical Materials Research 1998;41:162-6.

[220] Huang J, Best SM, Brooks RA, Rushton N, Bonfield W. In vitro evaluation of nanosized carbonate-substituted hydroxyapatite and its polyhydroxyethylmethacrylate nanocomposite. Journal of Biomedical Materials Research Part A 2008;87A:598-607.

[221] Huang J, Silvio LD, Wang M, Rehman I, Ohtsuki C, Bonfield W. Evaluation of in vitro bioactivity and biocompatibility of Bioglass®-reinforced polyethylene composite. Journal of Materials Science: Materials in Medicine 1997;8:809-13.

[222] Andersson J, Rosenholm J, Linden M. Mesoporous silica: An alternative diffusion controlled drug delivery system. In: Ashammakhi N, editor. Topics in multifunctional biomaterials and devices: E-book; 2008.

[223] Vallet-Regí M, Balas F, Arcos D. Mesoporous materials for drug delivery. Angewandte Chemie International Edition 2007;46:7548-58.

[224] Shannon R. Revised effective ionic radii and systematic studies of interatomic distances in halides and chalcogenides. Acta Crystallographica Section A: Crystal Physics, Diffraction, Theoretical and General Crystallography 1976;32:751-67.

[225] Briggs JGR. Level Course in Chemistry: Longman Publishing Group; 2002.

[226] Berendsen GE, Galan Ld. Preparation and chromatographic properties of some chemically bonded phases for reversed-phase liquid chromatography. Journal of Liquid Chromatography 1978;1:561-86.

[227] Ulman A. Self-assembled monolayers of alkyltrichiorosilanes: Building blocks for future organic materials. Advanced Materials 1990;2:573-82.

[228] Smidsrød O, Haug A. The effect of divalent metals on the properties of alginate solutions. I. Calcium ions. Acta Chemica Scandinavica 1965;19:329-40.

[229] van Hoogmoed CG, Busscher HJ, de Vos P. Fourier transform infrared spectroscopy studies of alginate–PLL capsules with varying compositions. Journal of Biomedical Materials Research Part A 2003;67:172-8.

[230] Lawrie G, Keen I, Drew B, Chandler-Temple A, Rintoul L, Fredericks P, et al. Interactions between alginate and chitosan biopolymers characterized using FTIR and XPS. Biomacromolecules 2007;8:2533-41.

[231] Yang S, Leong KF, Du Z, Chua CK. The design of scaffolds for use in tissue engineering. Part I. Traditional factors. Tissue engineering 2001;7:679-89.

[232] Torres Ss, Jomaa W, Puiggali J-R, Avramidis S. Multiphysics modeling of vacuum drying of wood. Applied Mathematical Modelling 2011;35:5006-16.

[233] Vera-Graziano R, Hernandez-Sanchez F, Cauich-Rodriguez J. Study of crosslinking density in polydimethylsiloxane networks by DSC. Journal of Applied Polymer Science 1995;55:1317-27.

Appendix A – Publications

A.1 Biological response of multi-step bioactive glass

A.2 Biological response of differently shaped nanoHA

A.3 Antimicrobial evaluation of metallic oxides